Therapeutic Microparticles and Biolistic Drug-Delivery to the Cornea

Thesis by

Benjamin J. Laccetti

In Partial Fulfillment of the Requirements for
the Degree of
Chemical Engineering

CALIFORNIA INSTITUTE OF TECHNOLOGY
Pasadena, California

June 26, 2020

Benjamin Laccetti
ORCID: 0000-0002-0399-1204

LIST OF THIRD-PARTY MATERIAL

- **Chapter 1**
  - Figure 1.2, reprinted with permission from: Ehlers & Hjortdal. The Cornea: Epithelium and Stroma. *Adv. Organ Biol.* **10**, 83–111 (2005).
  - Figure 1.4, reprinted with permission from: Zieman & Kass. Advanced Glycation Endproduct Crosslinking in the Cardiovascular System. *Drugs* 64, 459–470 (2004).

- **Chapter 2**
  - Figure 2.1, reproduced with permission from: Kiyama et al. Gelatine Cavity Dynamics of High-Speed Sphere Impact. *J. Fluid Mech*. **880**, 707–22 (2019).

ACNKNOWLEDGEMENTS

Attributing gratitude for all those who made this thesis possible is no trivial matter. I wish I could write a great song or paint a picture with strokes like Degas, but instead I have my words. I have my feelings and my memories. I have scars, physical remnants of battle… or perhaps they are just from old rollerblading accidents? I have heartache, and I have elation.

First of all, I thank Professor Kornfield for providing the opportunity to grow as an engineer at Caltech. You fought for me, you told me to persist, and you taught me how to stand up for my ideas. Professor Flagan, you are a model scientist and engineer. Your integrity, ability to deconstruct problems, and your creativity are inspiring. Some of our discussions were the most exciting of my young engineering career. Professor Ravichandran, thank you for providing valuable insight from the field of impact science, but more importantly, thank you for teaching me to believe in my own work. Professor Gao, thank you for your interesting input during our committee meetings; I wish we could have had time to study the impact of rod-like projectiles.

Professor Groisman at UCSD got us started on this project with his elegant technology, and I am grateful for his thoughtful discussions. Alex not only provided technology, but he taught us the fundamentals of microballistic device design. Thanks to Dennis Ko for starting this project and for bringing Alex's technology to campus.

Caltech research runs on the backs of talented engineers and machinists. Thanks to Jeff Groseth for assisting with sensor development when we had a very small budget. Tim Heitzman was integral in teaching me how to design circuits and to work at high voltage for a separate DOW

project. Mike Roy and Ricardo Zarazau, you produce meticulous work as machinists, and your patience is seemingly infinite. I am proud of the machining I did in the student shop, but I know I could not have done it without your willingness to teach and reteach.

To Kathy Bubash and Allison Kinard, thank you for making my degree progression work out so smoothly, for coordinating TA responsibilities, and for offering supportive words.

To my labmates: thank you for dealing with me when I was cantankerous and forlorn! In Julie's lab, we work on completely separate, barely overlapping projects, and yet there is a unanimous spirit in our group to learn from one another, to help out in any way possible, or just to listen when times are tough. Thank you for being my friends and my role models.

To the undergraduate students who worked with me, Nina Butkovich and Isabella Pestana, I extend my gratitude. These students contributed significantly to this research and made me remember how enjoyable it can be to attack scientific problems as a team.

To the Carrascos and the Kuriyamas, thank you for letting me be a part of your family while my own family members are so far away. I appreciate having the opportunity to get to know so many intelligent and warm people. David and Susan, you have taught me so much about literature, the world, and responsibility. Alan, your friendship is so dear to me. There are few people I would rather share a cup of coffee with. Sam - we met at the beginning of my time at Caltech. Since then, I have learned from you. We have created friendship, life, and love that is on our own

terms. We have grown up together. As we continue to grow and learn, our friendship will be a constant, and it will always feel like home.

Last, I thank my family members, who always have been there for me. To my brother, thank you for making me laugh and for being my best friend. To my father, thank you for the nights spent working late on extra credit math problems. Thank you for taking me to the science museum in Cambridge, MA. Thank you for working on engineering problems with me even before I knew what engineering was. To my mother, thank you for teaching me about different organs and tissues on the beach when I was a kid. Most importantly, thank you for supporting me. During all the times I thought about giving up, you were there to tell me to go just a little bit further.

ABSTRACT

The ability to deliver therapeutic compounds to the cornea using high-velocity microparticles is assessed and a method to synthesize therapeutic particles suitable for the cornea is demonstrated. Using a commercial gene gun (BioRad; PDS1000), a pneumatic capillary gun, and custom biolistic technology, microparticles were accelerated and made to embed in target materials: either homogeneous gels or corneal tissue. In homogeneous gels, penetration was shown to be directly proportional to particle size and density. In contrast, penetration of microparticles into the cornea is insensitive to particle size and density: varying the sectional density by 680% failed to penetrate beyond the epithelium (ca. 50 microns). The corneal epithelium exhibits two distinct kinetic energy thresholds that must be exceeded to first embed particles in the epithelium (rather than stopping on its anterior surface) and second to embed particles in the stroma (rather than stopping at the posterior surface of the epithelium). Penetration profiles show that the stroma is a highly effective stopping medium for high velocity microparticles. Despite the high water content of corneal tissue (76 w%) compared to the stratum corneum of skin (40 w%), the resistance to penetration of the cornea is comparable to literature values for skin. Ideal particles for drug delivery to the cornea would dissolve away completely, leaving no residue that might scatter light. With a vibrating orifice aerosol generator and a temperature-controlled column, 30-50 μm particles were composed of 1% Eosin Y with poly(ethylene glycol). Using low density polymer particles with a therapeutic agent payload, it was demonstrated that bulk material can be ballistically delivered to the central 1 cm^2 of the corneal epithelium rapidly, in an even, quantifiable layer.

TABLE OF CONTENTS

Page

LIST OF FIGURES

Figure *Page*

Chapter 1: Introduction

Chapter 2: Penetration Mechanics of Ballistic Microparticles in Homogeneous Hydrogel Substrates

Chapter 3: Ballistic Experiments In Ex Vivo Porcine Cornea

Chapter 4: Vibrating Orifice Generator Research and Therapeutic Microparticle Production

Chapter 5: Technology Developed and Experiments for the Future

Appendix A

Appendix B

Appendix C

Appendix D

LIST OF TABLES

Page

Chapter 1: Introduction

Chapter 2: Penetration Mechanics of Ballistic Microparticles in Homogeneous Hydrogel Substrates

Chapter 3: Ballistic Experiments In Ex Vivo Porcine Cornea

Chapter 4: Vibrating Orifice Generator for Therapeutic Microparticle Production

Chapter 5: Technology Developed and Experiments for the Future

Appendix A

Appendix B

Appendix C

Appendix D

LIST OF SYMBOLS

A_o…….orifice surface area

A_p…….particle surface area

A_K……..Kapton film surface area

C_D…… drag and discharge coefficients

C_V……...……volumetric concentration

D_p……....particle diameter

D_d……...….droplet diameter

D_j……...…….jet diameter

f…….vibrational excitation frequency

G…….shear storage modulus

g……...….gravity constant

L……. particle displacement/ acceleration barrel length

$\dot{m}$…….mass flowrate

m_p……...…….particle mass

m_K……..……Kapton film mass

M……..……gas molecular weight

p……pressure

R_p……..…….….particle radius

R……..resistance term in Poncelét Model

$\dot{Q}$……..…volumetric flowrate

u_o……...……impact velocity

U…….……gas velocity

v……...……particle velocity

Y_M……...……..……..Yield Modulus

z_{max}……max penetration during embedding

z_∞……..…ultimate penetration depth

α……..lensing factor: upstream radius divided by downstream radius

β……..orifice constriction factor

λ…….excitation wavelength

ρ_g……...…….. gas density

ρ_l……..liquid density

ρ_s…….……target substrate density

ρ_p……...……projectile density

$\Delta\rho$……density difference between target and projectile

μ……..……..dynamic viscosity

σ……surface tension

τ……... aerodynamic relaxation time

Chapter 1

INTRODUCTION

1.1 **The Impact of Corneal Disease and Relevant Corneal Anatomy**

The human eye functions due to the distinct optical elements shown in **Figure 1.1**. The pupil (an optical aperture) is controlled by muscles attached to the iris called the *sphincter pupillae*. Working in concert, the lens and the ciliary body (a self-correcting biconvex lens) provide final focusing touches in order to let us see near and far. Light is received in the retina (a sensor) by cells that transduce parcels of light into the miracle that is sight. This process depends on the cornea, a 550 micrometer thick, transparent tissue layer, which we depend on for the clarity of our world. The cornea is the eye's main refractory element and it provides over two-thirds of its focusing power.[1]

Unfortunately, pathologies of the cornea are common and can result in the loss of focus or worse. Prevalence of astigmatism is high. A recent study found that under 10% of pre-adolescents had astigmatism, while over 35% of adults over 45 years old had the condition.[2] The cornea is a sensitive optical component: micrometer-scale changes in the geometry of the anterior surface can produce visually significant changes on the order of several diopters. This can lead to astigmatism and sometimes myopia.

In countries where corrective eyewear can be prohibitively expensive, vision problems can translate to the inability to find gainful employment. Worse than this, the WHO estimates that 1.9 million people suffer from blindness from corneal opacity and tens of millions suffer from corneal blindness in one eye.[2] Seven percent of the world's cases of blindness are caused by corneal opacification and trachoma, completely preventable diseases if treated early enough with an effective medicine and drug-delivery regimen.[3] Preventing diseases that affect the cornea, put vision out of focus, or cause total blindness, is therefore an issue of great concern. Our research group is concerned with the mechanical properties of the cornea, which come from its distinct layered heterogeneity, and diseases that affect these properties.

The cornea is comprised of five main layers: the epithelium, Bowman's Layer, the stroma, Descemet's Membrane, and the endothelium (identified in **Figure 1.2**). The epithelium is on average 53 μm thick and sits on a 0.3-μm-thick basement membrane, which consists of collagen fibrils and laminin proteins. Beneath this, Bowman's Layer is a sheet of randomly oriented collagen fibrils that provides an outward toughness to the cornea. Next, the stroma constitutes most of the corneas' thickness. It is mainly acellular (1 keratocyte per 50,000 μm^3) and contains 200 collagen lamellae containing fibrils that radiate outwards at precise angles to give the cornea its transparency. The extracellular matrix consists of a mixture of peptidoglycans, glycosaminoglycans, fibronectins, and lamins.[4] The high content of peptidoglycans and glycosaminoglycans in the stroma gives the tissue a net negative charge. Finally, Descemet's Membrane is an acellular fibrous layer secreted by the endothelium monolayer below. The biomechanical strength of the cornea can be attributed to its inner stromal layer, since epithelial and endothelial cell layers lack any contiguous protein network. The interlamellar spacing

between collagen fibrils and constitutive properties between protein and peptidoglycan is what gives rise to a transparent tissue, similar in structure to tendon, that has considerable mechanical strength (**Table 1.1**).[5]

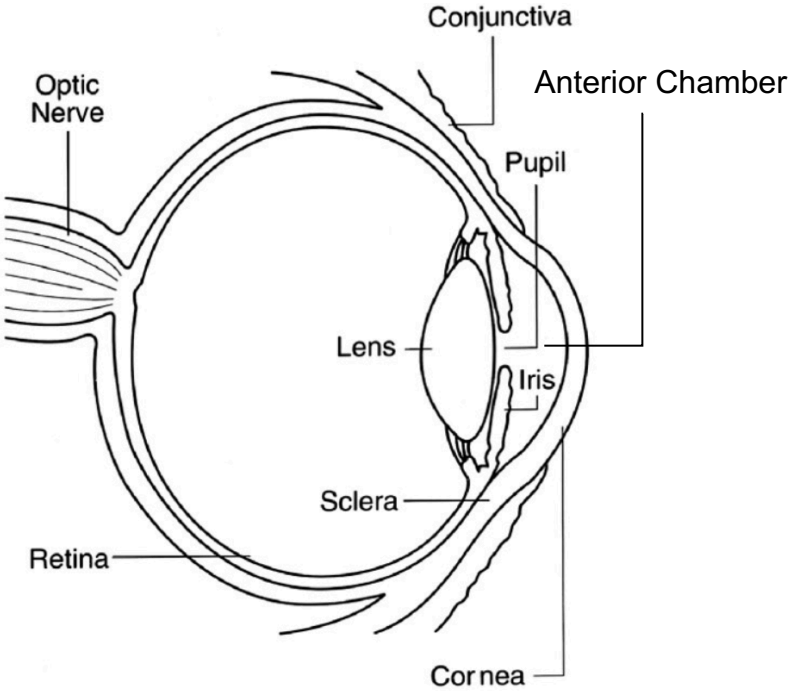

Figure 4.1 - Anatomy of the eye and positioning of basic optical elements. Reproduced from the National Eye Institute. National Institutes of Health.

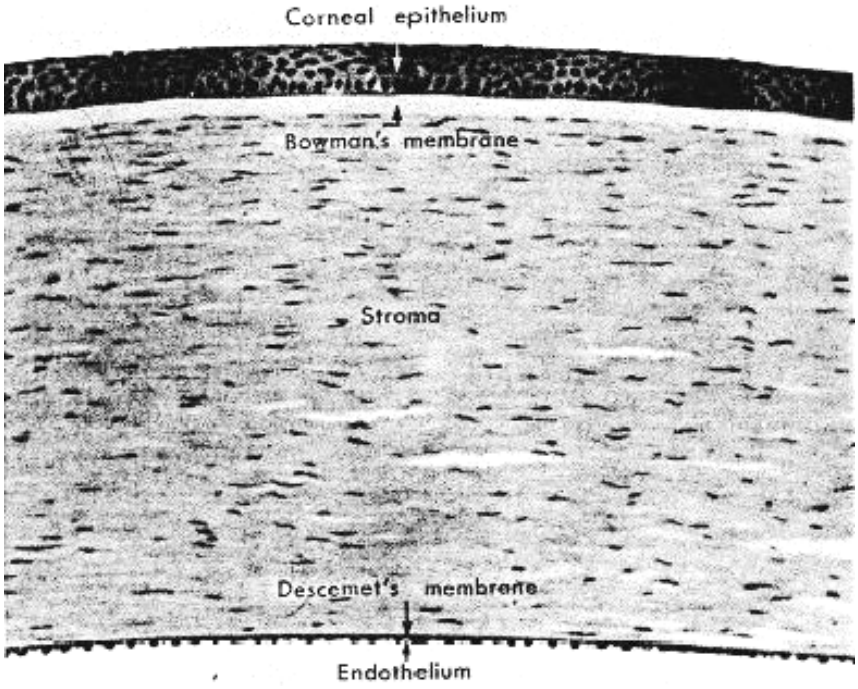

6

Figure 5.2 – Major layers of the cornea shown in H&E stained tissue section. Image reprinted from Ehlers and Hjortdal.[6]

Unfortunately, corneal tissue has biophysical properties related to layered heterogeneity that prevent the uptake of drug species. Precorneal barriers to drug delivery include solution drainage, blinking, and induced lacrimation. Most topically administered solutions are washed

away within 15–30 s after instillation, resulting in total tissue uptake rates as low as 5%.[7] Tear film with dissolved mucin forms a hydrophilic, negatively charged barrier, blocking hydrophobic materials or anions. Superficial epithelial cells are joined to one another by desmosomes and tight-junction complexes (*zonula occludens*). These structural elements stitch the anterior surface of the eye together and prevent the infiltration of bacteria and viruses, but also medicinal compounds. Corneal epithelial cells express an array of ATP-binding cassette efflux transporter pumps, which actively remove lipophilic molecules and organic anions from epithelial cytoplasm.[8] The corneal epithelium is lipophilic in nature - hydrophilic compounds that are delivered topically have low uptake rates. These characteristics impair the ability to deliver drugs to the cornea, and especially to underlying stromal tissue.

Strategies have been developed to overcome the anterior eye's ability to reject therapeutic compounds. Ophthalmic formulations such as suspensions, emulsions, ointments, gels, polymeric inserts, and colloidal systems have been investigated for topical administration to the eye with the goal of improving retention-time on the ocular surface.[9] In addition, dendrimers, cyclodextrins, nanoparticles, liposomes, and polymeric micelles have been investigated for enhanced drug uptake in the cornea. Novasorb is a patented FDA-approved cationic emulsion technology that can be used for drug delivery of lipophilic drugs. It binds to the mucin layer on the anterior surface.[10] Hydrogel-based, soft contact lenses are being investigated for their efficacy in achieving sustained release to the eye.[11] Iontophoresis, the use of an electrical gradient applied to tissue, allows for the transfer of charged therapeutics into tissue by electrophoresis and electroosmosis. A human cadaver tissue study, which used high-performance liquid chromatography to measure intrastromal concentration of riboflavin, found that

iontophoresis was able to increase riboflavin imbibition by a factor of two compared to epithelium-on absorption, but uptake was half as much compared to epithelium-off absorption.[12] Drug-delivery technologies are actively being pursued to treat deleterious pathologies of the cornea, and especially to enable subepithelial uptake of therapeutic compounds.

1.2 Biomechanical Pathology of the Cornea and Treatments

To focus light effectively, the cornea needs to maintain its shape under intraocular pressure. The average intraocular pressure of healthy human eyes is 15 mmHg, but short-acting influences including food or fluid intake, variations in systemic blood pressure, and heavy physical activity can double this pressure and submit the eye to stress-cycles.[13] Some combination of steady intraocular pressure and stress cycles can lead to creeping mechanisms if mechanical properties of the cornea deteriorate. As shown in **Table 1.1**, the cornea has significant stiffness, especially in Bowman's Layer and the stroma. Mechanical properties within the stroma can vary with depth. Regions where collagen lamellae are more interwoven (the anterior stroma) are consistently found to be stiffer than regions that are less interwoven (the posterior cornea). With aging come both composition and structural changes. Some collagens change level of expression and collagen fibrils increase in diameter with age as they show increased interfibrillar spacing. In general, the cornea is found to increase in stiffness roughly linearly with age while decreasing in viscous behavior.[4]

Certain pathologies can lead to distension, known as ectasia, in corneal tissue. The most common form of corneal ectasia is keratoconus. For over 30 years, it has been known that keratoconus is related to biomechanical weakening of the cornea, as is evidenced by strip extensiometry.[14]

Although etiology of the disease is unclear, it is known that keratoconus is a multifactorial disease of genetics and environment. The main biochemical changes to the cornea include altered expression of collagen VII, increased enzyme activity, and significant changes in lamellar organization.[4] The result of these changes is conical ectasia (distension shown in **Figure 1.3)**.

Table 1.1 – Mechanical properties of individual layers of the cornea. Data from Last et al. unless otherwise specified.*

Structure	Mechanical Properties Reported in Literature
Tear Film	Loss modulus (viscosity): 2.33 mPa [Human; Rheometry]**
Epithelium	Elastic Modulus: 0.57 kPa [Rabbit; AFM]
Epithelial Basement Membrane	Elastic Modulus: 7.5 kPa [Human; AFM]
Bowman's Layer	Elastic Modulus: 108.9 kPa [Human; AFM]
Stroma	Elastic Modulus: 33.1 kPa [Human; AFM]
Descemet's Membrane	Elastic Modulus: 50 kPa [Human; AFM]
Endothelium	Elastic Modulus: 4.1 kPa [Rabbit; AFM]***

* From Last et al.; 2005[15] ** From Gouveia et al.; 2005[16]

***From Thomasy et al.; 2014[17]

This viscoelastic creeping phenomenon leads to thinning of stroma and epithelial layers and presents high myopia and irregular astigmatism. In severe cases, the result can be edema and corneal scarring from decomposition, which can permanently degrade vision and lead to corneal blindness. Keratoconus is a major cause of corneal blindness worldwide, and its affects are geographically disproportionate.

For example, only 0.3/100,000 of people in the Russian population are at risk for keratoconus, while 53.5/100,000 are at risk in the United States. In significantly impoverished parts of the world, incidence of the disease is much higher. In central India, 2,300/100,000 people have the condition.[18,19] In most cases, the disease is unilateral, although in one study it was stated that after 16 years, 50% of cases show signs in the fellow eye as well.[20] Keratoconus typically progresses from teenage years to the third or fourth decade of life, when natural stiffening of the cornea with aging is thought to halt the disease. Nonetheless, this does not occur before severe degradation of visual acuity and patient quality of life.

For keratoconus patients, the timing of diagnosis is equally important as the treatment itself. Since the disease progresses from adolescence to middle age, the best-case scenario is to catch it in its earliest stages before any topographical changes to the cornea take place. It is suggested from computer modeling of the disease state that biomechanical changes precede topographical changes. Thus, a firm understanding of biomechanics may aid in diagnosis of early-stage keratoconus.[21] While *in vivo* characterization of biomechanical properties can be challenging, a suite of measurement techniques can help infer the strength of the cornea. Corneal hysteresis, an *in vivo* measurement of viscous dampening measured by ejecting a pulse of compressed air at the eye and measuring intraocular pressure from the mechanical response, has shown promise in predicting the onset of topological changes. Corneal response factor, a similar measurement to corneal hysteresis (made on the same machine), takes into account corneal central thickness. This measurement has even higher predictive power for topographical changes than corneal hysteresis.[22] Despite these new tools, pachymetry is still the gold-standard for keratoconus diagnosis. It works by measuring thickness of the central cornea using an ultrasound probe.[23]

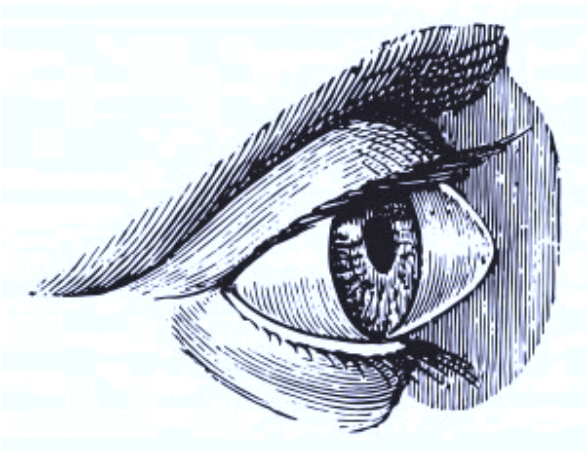

Figure 6.3 – Distension of the cornea seen in severe, untreated keratoconus. Cornea bulges outward, leading to high myopia and discomfort. Reproduced from Discovery Eye Foundation.

Treatments of the disease can be divided into presurgical and surgical measures. For patients with moderate myopia, spectacles can be used to improve visual acuity, but patients with irregular astigmatism are forced to wear hard contact lenses or even scleral contact lenses (lenses that cover a much greater proportion of the anterior surface than normal contact lenses). While effective in improving visual acuity, the lenses can be uncomfortable and can lead to corneal hypoxia if left in too long.[24] Intrastromal corneal ring segments (ICRS) are rings made of polymethyl methacrylate (PMMA) that are surgically implanted deep in the stroma to reduce the corneal curvature. In general, keratoconus patients in the moderate and severe stage of the disease who have no corneal scarring and cannot tolerate contact lenses are the best candidates for ICRS implantation. While effective, improper positioning of the ring can lead to

overcorrection or undercorrection and there is no promise that further progression of the disease will not nullify the existence of ring inserts.

Phakic intraocular lenses (PIOLs) are recommended for patients with high irregular astigmatism who are at least 21 years of age, who do not achieve sufficient correction with spectacles or contact lenses, and who are not suitable candidates for refractive surgery or excimer laser procedures. While effective, these lenses require surgical implantation into the anterior or posterior chamber of the anterior eye.[25] Conductive keratoplasty is a method that uses radio wave energy applied to the corneal stroma at 8-32 points. As a result of generated heat, permanent collagen shrinkage, corneal steepening in flat regions, and correction of refractive errors through corneal remodeling can occur. This technique is effective, but only for patients with low to moderate myopia.[26] For patients with severe corneal thinning or corneal opacity, the only treatment available is corneal transplantation. Keratoconus is a major indication for corneal transplantation in the Western world.[27] While effective, finding donor tissue can be challenging and tissue graft rejection-rates are high.

This leads to the gold-standard for keratoconus treatment, corneal cross-linking surgery (CXL). The original treatment, referred to as the Dresden Protocol, was pioneered by Dr. Gregor Wollensak. In 2003, he published a paper working with five enucleated cadaver eyes that showed that in just 30 minutes, the treatment resulted in an increase in Young's Modulus by a factor of four (measured with an Instron device).[28] Since then, Avedro Inc.'s CXL treatment has been approved by the FDA (April 2016). It builds on the Dresden Protocol, which involves using riboflavin (vitamin B) dissolved in the stroma to cross-link collagen fibrils with chemistry

depicted in **Figure 1.4**.[29] The Dresden treatment involves a dose of 370nm UV radiation that lasts for 30 minutes, while the Avedro protocol involves shorter exposure to higher intensity UV light. It is recommended for younger patients with high risk of ectasia progression as well as those who have a clear cornea with a minimum thickness of 400 μm. The treatment is frequently done in tandem with photorefractive keratectomy (PRK) and LASIK, or with the insertion of ICRS, to improve visual acuity before stiffening the cornea. In the Kornfield Lab, Dr. Joyce Huynh was able to demonstrate that Eosin Y could be used to perform CXL using green, visible light instead of UV light. The Eosin Y/visible treatment achieves comparable cross-linking with negligible phototoxicity.[30]

A major drawback of this invasive surgery is that it involves epithelial debridement in order to achieve sufficient riboflavin imbibition. This is a drawback for several reasons. First, it cannot be used on thin corneas with already severely degraded epithelial tissue. Second, it causes pain and temporarily reduced visual acuity. Third it can cause a haze that is likely to persist for one to twelve months. Last, it takes four-five days for the epithelium to regrow as cells migrate from the peripheral zones of the cornea, in which time the cornea is susceptible to infection.[31]

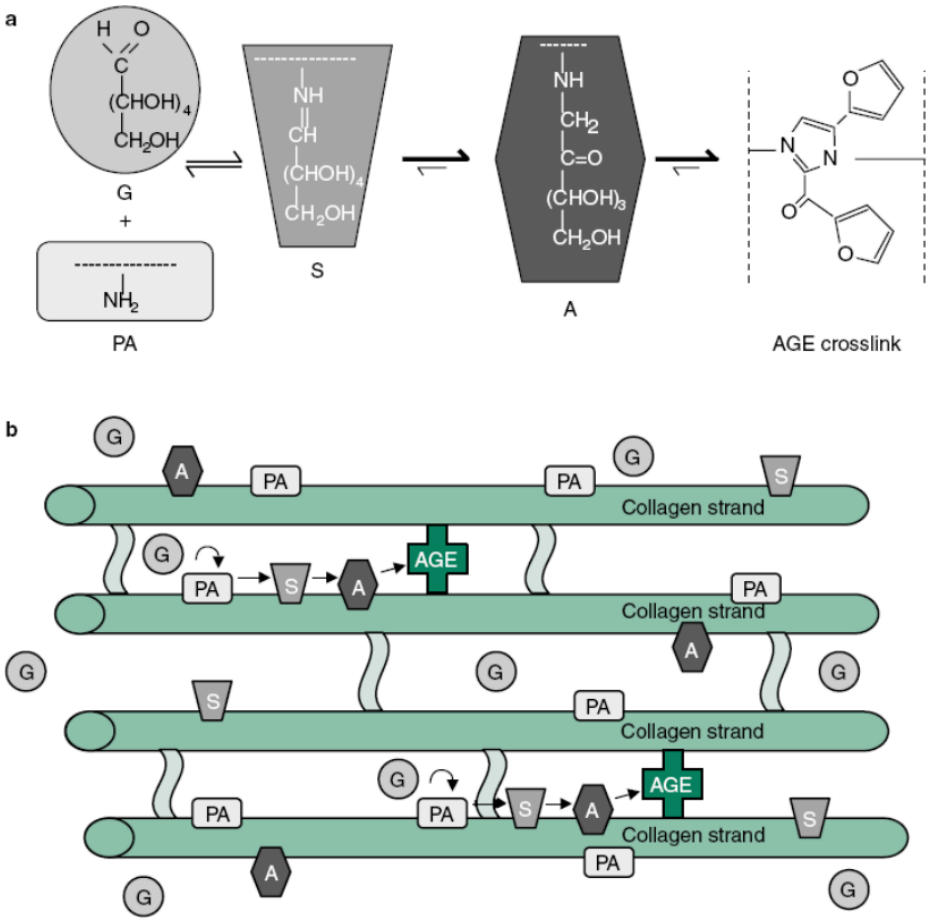

Figure 7.4 – The Maillard Reaction and its role in corneal cross-linking. (**a**) The Maillard reaction occurs when a reducing sugar (glucose) reacts with an amine group to form an unstable Schiff base that transforms to an Amadori product, which can further rearrange to form advanced glycation end products (AGEs) capable of crosslinking proteins. (**b**) Schematic of the formation of collagen-collagen AGE crosslinks. The Maillard reaction occurs in two places (arrows) to form AGE crosslinks (dark green) between strands of collagen, which are also functionally enzymatically crosslinked for strength (light green). A = Amadori product; G = glucose; PA = protein amine; **S** = Schiff base. Reproduced from Zieman and Kass.[29]

Some studies purport the efficacy of epithelium-on CXL. In Cifariello et al., epi-on CXL was performed with a solution of riboflavin 0.1%, dextran 15.0%, trometamol (Tris, a buffer component), and ethylenediaminetetraacetic acid. With this formula, researchers found that both epi-on and epi-off treatment modalities were equivalent in terms of results and related complications.[32] However, other studies have reported inferior post-surgical outcomes of epi-on CXL. In a recent study, it was found that after 24 months of treatment with the epithelium-off technique, 94.4% of eyes either showed less keratoconus or no worsening of the disease. On the other hand, only 66.6% percent of eyes treated with the epithelium-on technique showed less keratoconus or no worsening of the disease.[33] While iontophoresis (previously mentioned) has been used to increase imbibition, uptake is still half what was shown for epi-off CXL. Elastin-like polypeptide (ELP), an engineered protein that is easily purified and modified to carry drugs or therapeutic proteins, has shown promise in increase imbibition, but uptake is still lower than what is needed for CXL.[34] To reduce post-operative complications for patients with keratoconus, and to possibly make CXL a walk-in procedure, there is impetus to find ways of increasing the uptake of riboflavin, or Eosin Y, in stromal tissue.

1.3 Biolistics and the Ability to Treat Corneal Tissue

Biolistics involves the bombardment of tissues with microparticles containing therapeutic agents to transfer genes and materials of interest. Originally intended to transfect maize cells through their tough cell walls, this technology is now used to deliver genes to both plant and animal tissues, including corneal tissue.[35,36] For example, to improve the acceptance rates of corneal transplants, biolistic gene delivery has been used *in vivo* to enable epithelial cells to produce cytotoxic T-lymphocyte-associated protein 4. This gene therapy is meant to deal with the

problem of rejected corneal grafts in penetrating keratoplasty.[37,38] To deliver drugs, rather than genes, larger particles (20 to 40 μm dia) have been delivered biolistically to various tissues, including skin and mucosal tissue, but not to the cornea.[39,40]

Although therapeutic particle delivery through the epithelium to the corneal stroma, to the best of our knowledge, has not been investigated, there is a body of evidence that suggests that such penetration is possible. Corneal foreign bodies include objects that embed in superficial and underlying stromal tissues of the cornea, often related to wood and metal working or exposure to explosions in mining or warzones. After blast injuries, particularly improvised explosive device (IED) and mine-blast injuries, there are often multiple deep stromal foreign bodies in exposed corneal tissue.[41–43] While corneal injuries show penetration well past the corneal epithelium, there have been no biolistic therapies that have demonstrated penetration into the corneal stroma. To enable biolistic drug delivery, a detailed study is required to determine impact parameters (particle size, density, and velocity) that can lead to successful delivery of bulk therapeutics to the stroma.

This research investigates using biolistics to solve two problems: 1) low bioavailability of drugs delivered to the eye and 2) difficulty delivering photosensitizing agents to the stroma. There are several theories as to how the cornea prevents successful CXL therapy: (1) With the epithelium intact, it is thought that tight junctions and the composition of the epithelium prevent sufficient uptake of photosensitizing agents; (2) the epithelium acts as a mask absorbing some of the incoming ultraviolet light, possibly impeding the cross-linking therapy from penetrating as deeply as it should; and (3) oxygen is required to cross-link corneal tissue. With the epithelium

intact, oxygen diffusion may be slowed, thus affecting the depth of cross-link formation and the efficacy of CXL treatment.

Studies showing the attenuation of riboflavin uptake in the cornea with the epithelium intact, indicate that the first explanation given is the likely reason for the lack of efficacy of epi-on treatment.[12] Operating on this assumption, our original idea was to deliver solid microparticles composed of photosensitizing agent to the eye's anterior surface. If particles with a large volume fraction of drug were used, a sufficient dose might be provided biolistically with 6,000 particles of 30um diameter per cm^2, potentially in the blink of an eye.[30] However, the delivery of low-density ballistics to tissue lacks a precedence in the literature.

1.4 Project Objectives and Organization of Thesis

The objective of our work was to investigate a new form of rapid, quantifiable drug delivery to the cornea that uses ballistic microparticles. To do this, the size, velocity, and particle composition leading to a successful biolistic therapy had to be elucidated, for treatment of both the epithelial tissue and of the underlying stroma. Working with keratoconus as our target disease, a secondary goal of our work was to enable epithelium-on CXL by using high-velocity microparticles containing therapeutic compounds (Eosin Y). This work not only requires that particles are delivered deep enough in tissue, but also that damage to tissue is low. In Chapter 2, initial experiments are done delivering microparticles to a homogeneous reference material (ballistic gelatin). Ballistic devices that deliver particles to target substrates under vacuum and atmospheric pressure are investigated. Particles of different composition and density are used to demonstrate a range of kinetic embedding energies. As discussed in Chapter 3, the same range of

particles are delivered to porcine corneal tissue and penetration mechanics are elucidated. Thresholds are determined for delivery of particles to different layers of the cornea and significant toughness of the tissue is revealed. Therapeutic microparticles formed using the custom drying column are delivered to corneal tissue, suggesting a new way to deliver medicines to the cornea in high bioavailability. In Chapter 4, a vibrating orifice aerosol generator (VOAG) and a heated drying column were used to create therapeutic microparticles containing Eosin Y. The size-distributions using the VOAG with different solutions are studied in detail. Last, in Chapter 5, future experiments are discussed to study more effective delivery of microparticles to target substrates under atmospheric pressure. Experiments are proposed which investigate the effect of projectile shape on penetration and which assess immune response and toxicity of ballistic therapies.

1.5 References

1. Sridhar, M. Anatomy of cornea and ocular surface. *Indian J. Opthalmology* **66**, 190–94 (2018).
2. Hashemi, H. *et al.* The prevalence of astigmatism and its determinants in a rural population of iran: The "Nooravaran Salamat" Mobile Eye Clinic experience. *Middle East Afr. J. Ophthalmol.* **21**, 175–181 (2014).
3. Foster, A., Gilbert, C. & Johnson, G. Changing patterns in global blindness: 1988-2008. *Community Eye Heal. J.* **21**, 37–39 (2008).
4. Blackburn, B. J., Jenkins, M. W., Rollins, A. M. & Dupps, W. J. A review of structural and biomechanical changes in the cornea in aging, disease, and photochemical crosslinking. *Front. Bioeng. Biotechnol.* **7**, 1-16 (2019).
5. Marchini, M. *et al.* Differences in the fibril structure of corneal and tendon collagen. An electron microscopy and X-ray diffraction investigation. *Connect. Tissue Res.* **15**, 269–281 (1986).
6. Ehlers, N. & Hjortdal, J. The cornea: epithelium and stroma. *Adv. Organ Biol.* **10**, 83–111 (2005).
7. Ahmed, I. The noncorneal route in ocular drug delivery. in *Ophthalmic drug delivery systems* 335–63 (2003).
8. Gaudana, R., Krishna, H. & Mitra, A. Ocular Drug Delivery. *AAPS J.* **12**, 348–360 (2010).
9. Imtiazul, M. K. & Zafar Auniq, R. Bin. Emerging trends in ocular drug delivery: a review on recent updates. *J. Neoplasm* **02**, 14–17 (2017).
10. Lallemand, F., Daull, P., Benita, S., Buggage, R. & Garrigue, J.-S. Successfully improving ocular drug delivery using the cationic nanoemulsion, novasorb. *J. Drug Deliv.* **2012**, 1–16 (2012).
11. Ribeiro, A. M., Figueiras, A. & Veiga, F. Improvements in topical ocular drug delivery systems: Hydrogels and contact lense. *J. Pharm. Pharm. Sci.* **18**, 683–695 (2015).
12. Mastropasqua, L. *et al.* Corneal cross-linking: intrastromal riboflavin concentration in iontophoresis-assisted imbibition versus traditional and transepithelial techniques. *Am. J. Opthalmology* **157**, 623–630 (2014).
13. Phelps, C. D., Woolson, R. F., Kolker, A. E. & Becker, B. Diurnal variation in intraocular pressure. *Am. J. Ophthalmology.* **77**, 367–377 (1974).

14. Andreassen, T. Simonson, A. & Oxlund, H. Biomechanical properties of keratoconus and normal corneas. *Exp. Eye Res* **31**, 435–441 (1980).
15. Last, J. A., Thomasy, S. M., Croasdale, C. R., Russell, P. & Murphy, C. J. Compliance profile of the human cornea as measured by atomic force microscopy. *Micron* **43**, 1293–1298 (2012).
16. Gouveia, S. & Tiffany, J. Human tear viscosity: An interactive role for proteins and lipids. *Biochim. Biophys. Acta.* **1753**, 155–63 (2005).
17. Thomasy, S., Raghunathan, V. & Winkler, M. Elastic modulus and collagen organization of the rabbit cornea: Epithelium to endothelium. *Acta Biomater.* **10**, 785–91 (2014).
18. Jonas, J., Nangia, V., Matin, A., Kulkarni, M. & Bhojwani, K. Prevalence and associations of keratoconus in rural Maharashtra in Central India: The Central India eye and medical study. *Am. J. Opthalmology* **148**, 760–65 (2009).
19. Gorskova, E. Epidemiology of keratoconus in the Urals. *Vestn. Oftalmol.* **114**, 38–40 (1998).
20. Li, X., Rabinowitz, Y., Rasheed, K. & Yang, H. Longitudinal study of normal eyes in unilateral keratoconus patients. *Opthalmology* **111**, 440–46 (2004).
21. Roy, A. S. & Dupps, W. J. Patient-specific computational modeling of keratoconus progression and differential responses to collagen cross-linking. *Investig. Ophthalmol. Vis. Sci.* **52**, 9174–9187 (2011).
22. Johnson, R., Nguyen, M., Lee, N. & Hamilton, D. Corneal biomechanical [properties in normal, forme fruste keratoconus, and manifest keratoconus after statistical correction for potentially confounding factors. *Cornea* **30**, 516–23 (2011).
23. Ambrósio, R. *et al.* Novel pachymetric parameters based on corneal tomography for diagnosing keratoconus. *J. Refract. Surg.* **27**/, 753–758 (2011).
24. Pilskans, B., Fink, B. & Hill, R. Oxygen demands with hybrid contact lenses. *Optomology Vis. Sci. - Off Publ Am. Acad. Optom.* **29**, 1780–85 (2003).
25. Mohammadpour, M., Heidari, Z. & Hashemi, H. Updates on managements for keratoconus. *J. Curr. Ophthalmol.* **30**, 110–124 (2018).
26. Habibollahi, A., Hashemi, H., Mehravaran, S. & Khabazkhoob, M. Visual outcomes of conductive keratoplast to treat hyperopia and astigmatism after laser in situ keratomileusis and photorefractive keratectomy. *Middle East African J. Opthalmology* **18**, 238–42

(2011).

27. Kang, P., Klintworth, G., Kim, T., Carlson, A. & Adelman, R. Trends in the indications of penetrating keratoplasty. *Cornea* **24**, 801–03 (2005).
28. Wollensak, G., Spoerl, E. & Seiler, T. Stress-strain measurements of human and porcine corneas after riboflavin-ultraviolet-A-induced cross-linking. *J. Cataract Refract. Surg.* **29**, 1780–1785 (2003).
29. Zieman, S. & Kass, D. Advanced glycation endproduct crosslinking in the cardiovascular system. *Drugs* **64**, 459–470 (2004).
30. Huynh, J. Factors Governing Photodynamic Cross-Linking of Ocular Coat. (2011).
31. Jia, H. Z. & Peng, X. J. Efficacy of iontophoresis-assisted epithelium-on corneal cross-linking for keratoconus. *Int. J. Ophthalmol.* **11**, 687–694 (2018).
32. Cifariello, F. *et al.* Epi-off versus epi-on corneal collagen cross-linking in keratoconus patients: A comparative study through 2-year follow-up. *J. Ophthalmol.* **2018**, (2018).
33. Eraslan, M., Toker, E., Cerman, E., and Ozarslan. Efficacy of epithelium-on vs. epithelium-off corneal cross-linking in treating pediatric keratoconus. *Eye and Contact Lens*. **43**, 155-61 (2017).
34. Bidwell, G., Liu, H., Robinson, J., Marquart, M. & George, E. A corneal penetrating drug delivery system based on elastin-like polypeptide. *Fed. Am. Soc. Exp. Biol.* **28**, (2014).
35. Lu, W. N. *et al.* Gene transfer into corneal endothelial cells by Helios gene gun. *Nihon. Ganka Gakkai Zasshi* **107**, 189–195 (2003).
36. Tanelian, D. L., Barry, M. A., Johnston, S. A., Le, T. & Smith, G. Controlled gene gun delivery and expression of DNA within the cornea. *Biotechniques* **23**, 484–488 (1997).
37. Merediz, S. A. K., Zhang, E. P., Wittig, B. & Hoffmann, F. Ballistic transfer of minimalistic immunologically defined expression constructs for IL4 and CTLA4 into the corneal epithelium in mice after orthotopic corneal allograft transplantation. *Graefe's Arch. Clin. Exp. Ophthalmol.* **238**, 701–707 (2000).
38. Zhang, E. P. *et al.* Minimizing side effects of ballistic gene transfer into the murine corneal epithelium. *Graefe's Arch. Clin. Exp. Ophthalmol.* **240**, 114–119 (2002).
39. Kendall, M., Mitchell, T. & Wrighton-Smith, P. Intradermal ballistic delivery of micro-particles into excised human skin for pharmaceutical applications. *J. Biomech.* **37**, 1733–1741 (2004).

40. Mitchell, T., Kendall, M. & Bellhouse, B. A ballistic study of micro-particle penetration of the oral mucosa. *Int. J. Impact Eng.* **28**, 581–99. (2003).
41. Yudcovitch, L. *Corneal foreign body*. *Clinical Cases in Eye Care* (StatPearls, 2018).
42. Gumus, K., Karakucuk, S. & Mirza, E. Corneal injury from a metallic foreign body: An occupational hazard. *Eye Contact Lens Sci. Clin. Pract.* **33**, 259-260. (2007).
43. Scott, R. The injured eye. *Philos. Trans. R. Soc. B Biol. Sci.* **366**, 251–260 (2011).

Chapter 2

PENETRATION MECHANICS OF BALLISTIC MICROPARTICLES IN HOMOGENOUS GEL SUBSTRATES

2.1 – Theory Behind Microparticle Penetration in Homogeneous Gel Substrates

In homogeneous, isotropic gel targets, ballistic impacts of projectiles scale with a key dimensionless parameter: the Elastic Froude Number $\frac{\Delta\rho u_o^2}{G}$, where $\Delta\rho$ is the difference between target and projectile density, u_o is the impact velocity, and G is the shear storage modulus. When inertia is low or the stiffness of a gel is high, particles are likely to penetrate with low depth or even to rebound off of surfaces. When inertia is high or gel stiffness is low, penetration depends on the formation of smooth cavities, similar to those that form when penetrating low viscosity fluids. The Froude numbers of biolistic impacts dictate how resulting cavities form and seal during penetration. **Figure 2.1** shows data from another group's study in which different regimes of penetration/cavity formation for a range of Elastic Froude Numbers were observed.[1]

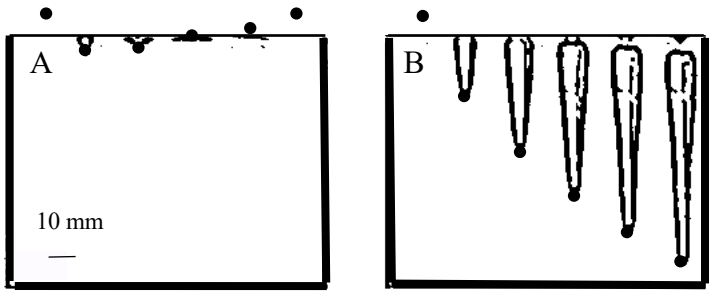

Figure 2.1 – Images of cavities from ballistic impact in sequence in 2% w/w gelatin (two different velocities). A) Rebound (u_o~1.3 m/s; Fr_e~1.8 x 10^1; Δt~8 $msec$.) B) Shallow seal cavity (u_o~30 m/s; Fr_e~4.0 x 10^4; Δt~1.2 $msec$). Reproduced with permission from Kiyama et al.[1]

Table 2.1 – Dimensionless groups relevant to ballistic impacts.

Dimensionless Group	Expression	Definition
Froude Number; Fr	$\frac{u_o^2}{gR}$	*inertial:gravitational forces*
Weber Number; We	$\frac{\Delta\rho R u_o^2}{\sigma}$	*intertial:surface tension forces*
Bond Number; Bo	$\frac{\Delta\rho g R^2}{\sigma}$	*gravitational force:surface tension forces*
Elastic Froude Number; Fr_e	$\frac{\Delta\rho u_o^2}{G}$	*Inertial:elastic forces*
Elastic Grashof Number; Gr	$\frac{\Delta\rho g R}{G}$	*gravitational force:elastic forces*

Dimensionless groups shown in **Table 2.1** dictate the physics of various impacts. In **Table 2.1**, g is the gravitational constant, R the particle radius, and σ is the substrate surface tension. Since gravitational forces and surface tension forces are small compared to the inertia of the particle and the resistance to deformation (elastic forces), penetration is expected to scale with the Elastic Froude Number for ballistic impacts. Numerous studies have been done with projectiles that are several millimeters up to 1-2 centimeters, and this is found to be true. In Akers and Belmonte, transient cavity length of steel spheres dropped in a micellar fluid was shown to scale with $Fr_e^{1/3}$.[2] In Swain et al, the penetration of steel spheres (7 to 11 mm) in ballistic gelatin was found to scale with $Fr_e^{1/2}$.[3] In Mrozek et al, the penetration of metal spheres in gels made of an ABA triblock copolymer (shear moduli of 60 to 630 kPa) was also found to scale with $Fr_e^{1/2}$.[4] One can write the following generalized expression for penetration in homogeneous materials:

(1)

$$\frac{z_\infty}{D_p} \sim \left[\frac{\Delta \rho u_o^2}{G}\right]^\gamma$$

where z_∞ is the final penetration depth, D_p is the diameter of the particle, and γ is a power which is usually found to be around $\frac{1}{2}$ in gel materials.

There are two main equations used when interpreting ballistics research. For shallow penetration in tough materials (e.g. microparticles embedding in skin), the cavity strength model is used. In this model, the impact pressure is assumed to be equal to the cavity strength during impact, which is about 3 times the yield strength.[5] Therefor, the cavity strength model is written:

$$dE = Fdx \quad \rightarrow \quad dE = 3Y_M A_p dx \tag{2}$$

where E is the energy of the particle, F is the force from impact, Y_M is the material yield strength, and A_p is the area of the projectile. This expression can be integrated and arranged into a predictive equation for penetration depth, which is proportional to $\rho r u_o^2$, a value that is used to plot shallow penetration of ballistics (the kinetic energy per unit cross-section):

$$z_\infty = \frac{\frac{1}{2} m_p u_o^2}{3Y_M A_p} = \frac{\rho_p R_p u_o^2}{6Y_M} \tag{3}$$

where z_∞ is penetration depth, u_o is the impact velocity, m_p is projectile mass, ρ_p is its density, and R_p is its radius. In Kendal-Wright Smith et al., it is shown that penetration in human cadaver skin fits well to a similar model, the fracture toughness model, for different particles sizes, densities, and impact velocities.[6] Skin is a useful tissue to compare the cornea to, because it is a heterogeneous material composed of tissue layers with different mechanical properties, similar to the corneal epithelium and the underlying stroma.

For deeper penetration with a clearly viscous component, a Poncelét model is typically used, like the one described in Veysset et al. and in Bellhouse et al.[7,8] This equation is formulated using a force balance. By Newton's Second Law, the rate of change of momentum is equal to the sum of all forces. For a microparticle penetrating tissue, there are three main force components: 1) friction, 2) acceleration of tissue at the particle head, and 3) resistance of the material to stretching/deformation. The Poncelét model assumes that friction is negligible compared to inertial and resistance terms. The resulting expression is shown below:[7]

$$m_p \frac{dv}{dt} = B_2 v^2 + B_o \tag{4}$$

$$B_2 = \frac{1}{2} C_D \rho_s A_p v^2 \quad and \quad B_o = AR$$

where A_p is the area of a particle, ρ_s is the target density, and R is a gel resistance term that is typically related to yield stress. Integrating this equation twice, using the impact speed as an initial condition, yields the following expression:

$$z(t) = \frac{m_p}{B_2}\left[\ln cos\left(\frac{\sqrt{B_2 B_o}}{m_p}(t_f - t)\right) - \ln cos\left(\frac{\sqrt{B_2 B_o}}{m_p} t_f\right)\right] \tag{5}$$

where t_f is the time that it takes for the particle to come to rest, given by:

$$t_f = \frac{m_p}{\sqrt{B_2 B_o}} \tan^{-1}\left(u_o \sqrt{\frac{B_2}{B_o}}\right). \tag{6}$$

Finally, the max penetration depth is given by the following expression:

$$z_{max} = \frac{2}{3}\frac{\rho_p D_p}{\rho_s C_D} \ln\left(\frac{\rho_s C_D u_o^2}{2R} + 1\right) \tag{7}$$

where z_{max} is the maximum penetration depth, ρ_p is the density of the particle, and C_D is a drag coefficient. The max penetration depth can be different than z_∞, the final resting point of the particle, due to recoil of particles embedding in elastic media.

The scaling relationship in Equation (1) and the result of the Poncelét Model in Equation (7) indicate the importance of particle density. If particle density is equivalent to the density of the substrate, penetration depth will be severely attenuated. While it is related to the yield strength, one must hesitate before equating the gel resistance to actual yield stresses, which are typically measured at low strain rates. In Veysset et al., resistance values of 2.5% w/w, 5.0% w/w, and 10.0% w/w ballistic gelatin samples are calculated from empirical data for low-density microparticles in the ballistic embedding process. With the Poncelét model, they calculate resistance values that are on the order of 2 to 30 MPa, as water content in the gels decreases.[7] These values are comparable to values measured in high strain-rate testing done by Kwon and Subhash, where compressive strength of a 10% ballistic gelatin sample increased from 3 kPa at a strain rate of around 0.0013/s to 6 MPa at a strain rate of around 3200/s.[9]

The work of Veysset et al. was a breakthrough in the field of microballistics. In their work, they use a set-up called laser-induced projectile impact testing (LIPIT) to accelerate microparticles (7.8 μm) to speeds as high as 1500 m/s. Using a highspeed camera with interframe spacing of 50 nanoseconds, the group was able to film impact events in ballistic gelatin. The work is significant for several reasons. First, this is one of the first bodies of research that studies low density microparticle (1.8 g/cc) penetration in ballistic gelatin for a broad range of impact velocities. Second, the work establishes minimum threshold velocities needed to embed particles

in gel material (in general, the velocities are high: >200 m/s). Third, the paper reports resistance values that allow our group to infer impact velocities from penetration depth data in ballistic gelatin. In **Figure 2.2**, predicted penetration depths are shown for two different particle compositions, using the Poncelét Model. The curves show expected penetration depth in three concentrations of gelatin, 2.5% w/w, 5.0% w/w, and 10.0% w/w. The data is produced by dividing Equation (7) by particle diameter and graphing the results. From experimental data in Veysset et al., resistances of 1.5 MPa, 6.0 MPa, and 21 MPa are used in the penetration equation for the previously mentioned respective concentrations.

The results of this analysis reinforce the importance of projectile density. In **Figure 2.2**, the expected penetration of a polymer particle with density of 1.1 g/cc and a stainless-steel particle are shown. At low density, particles require velocities of several hundred meters per second in order to achieve just a few diameters of penetration. In fact, the model equation predicts the maximum depth reached in gel and does not consider elastic rebounding of particles, which can further attenuate penetration depth. As gelatin concentration increases, it becomes harder and harder for the spheres to embed. When the particle is made of stainless steel, the minimum velocity needed to achieve significant penetration is much lower, and the penetration that is possible for the projectile is considerably higher. These figures show that by changing particle density, a broad range of penetration in gel substrates can be achieved.

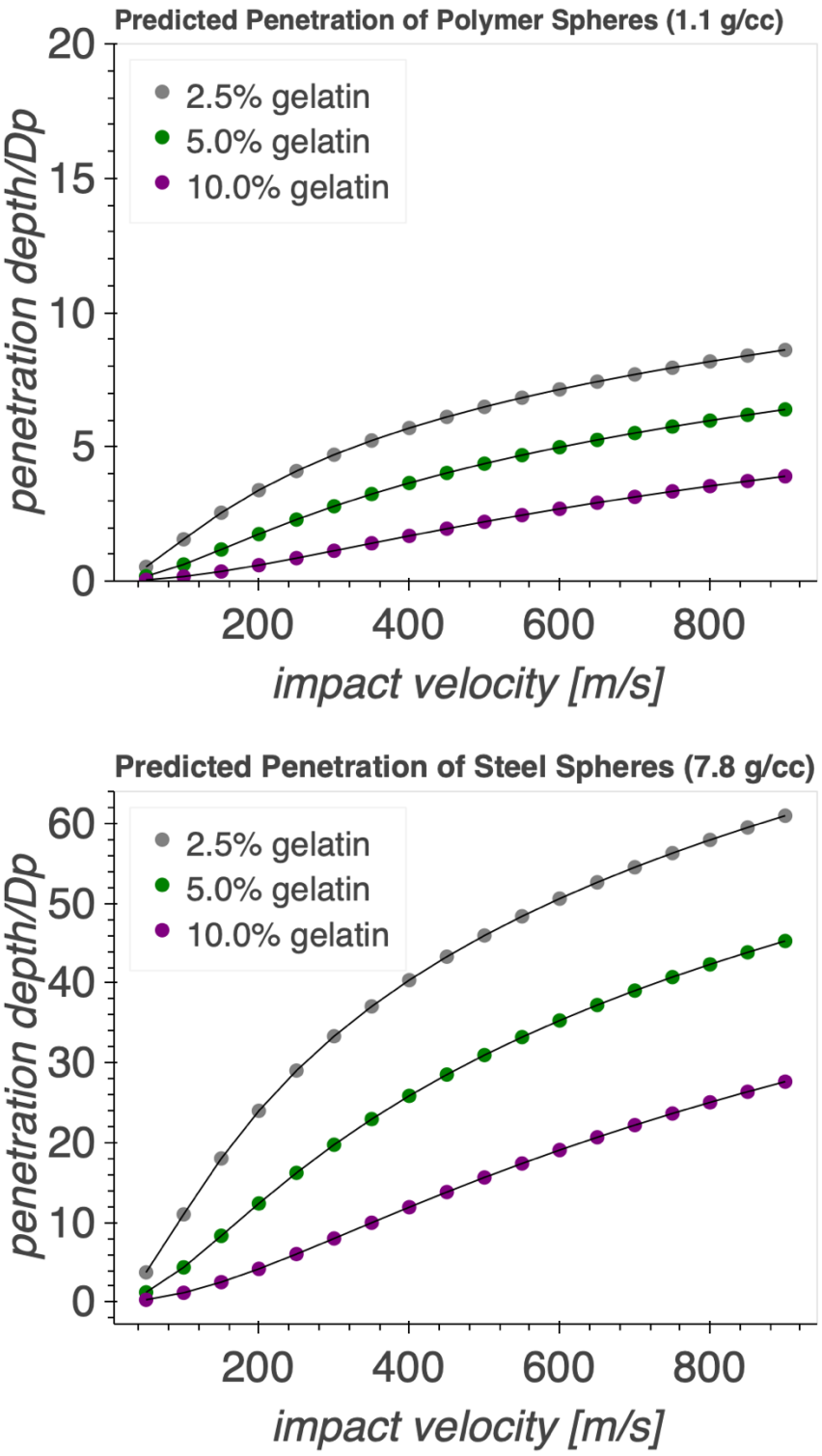

Figure 2.2 – Penetration depth of two different particle compositions in gelatin predicted by the Poncelét Model. Low density polyethylene and stainless steel in 2.5%, 5%, and 10% w/w ballistic gelatin. Data calculated using resistance parameters and model from Veysset et al.[7]

2.2 – Experiments Using Low-Density Ballistics and the Pneumatic Capillary Gun

2.2.1 – Performance of Alex Groisman's Pneumatic Capillary Gun in Literature

To begin our research, the group used a Pneumatic Capillary Gun (PCG) to deliver microparticles to tissue and gel samples. Professor Alex Groisman, at the University of San Diego, developed the PCG, a device which delivers microballistics to tissues with minimal damage from compressed gas. The key feature of the device is the use of vacuum suction to divert the highspeed flow of helium gas from the device nozzle. Within the device, helium injection gas is used to strip particles from an inserted mesh substrate. Particles are swept into an acceleration barrel with a carrier gas flowing through it and after picking up speed, they enter a cylindrical insert with a smaller cross-sectional area than the acceleration barrel. Some gas is diverted by this event, and the remaining gas is suctioned away by vacuum pulling on the barrel insert. Particles pass through two chambers in the barrel insert before exiting the device with high velocity. This process is depicted in **Figure 2.3** and **2.4**.

While compatible with polymeric particles, all published work with the device uses particle payloads of high density. In Simonnet et al., typical gene gun payloads are used, including 0.47± 0.15, 1.1± 0.1, and 1.27± 0.27 μm gold microparticles (19.3 g/cc). By firing particles into an atmosphere of hydrogen (due to its high speed of sound), velocity of these microparticles was estimated. This was done by changing gene gun stand-off distance until penetration in a soft 0.25% w/w agarose gel was prevented. With this max-standoff distance and assuming Stokes

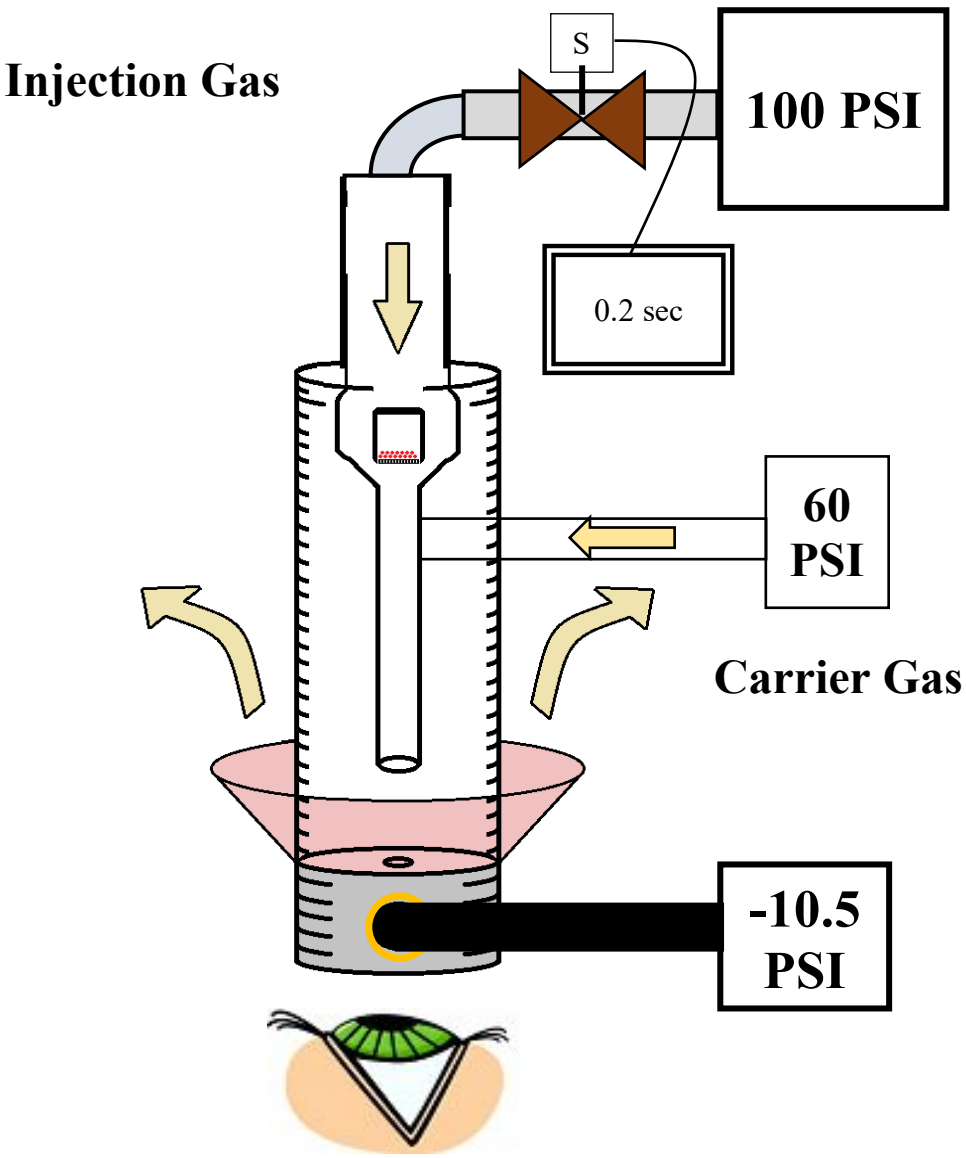

Figure 2.3– Schematic of Groisman capillary gun. The device has two pressurized connections: 1) is used to strip particles from mesh inserts and 2) is connected directly to the acceleration barrel. The first (injection gas) can be charged up to 100 PSI (6.8 bar) and the second (carrier gas) up to 60 PSI (4.1 bar). Particles are accelerated down the acceleration barrel and gas is diverted outside of the device and into the vacuum connection. Cartoon prepared by Nina Butkovich.

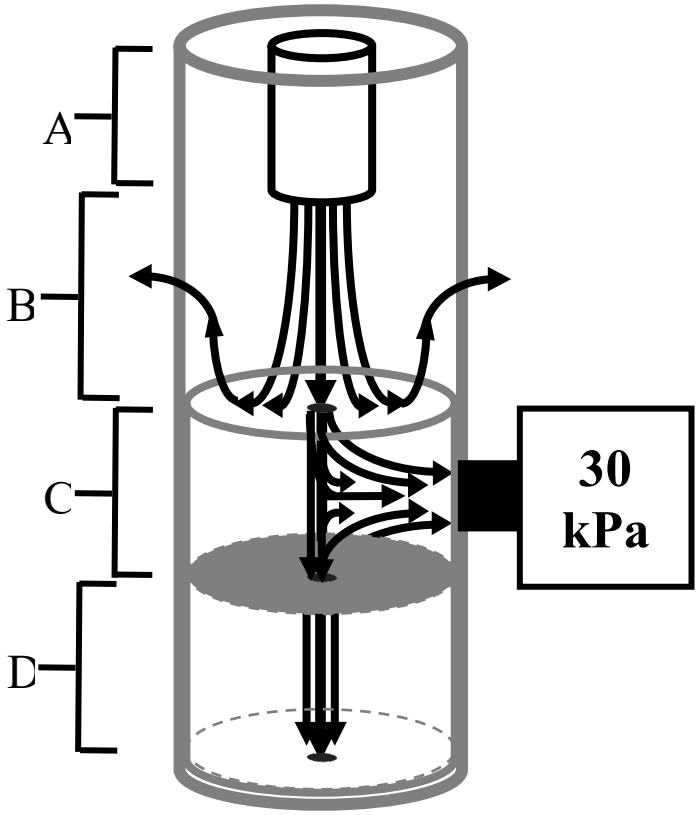

Figure 2.4 – Schematic of vacuum insert with approximated streamlines in Groisman capillary gun. A) Particles are accelerated in a 1.6 mm ID polyimide tube. B) Particles are released into a volume of the device above the vacuum insert. The insert has an opening with a diameter of just 0.8 mm. C) Particles travel through the first chamber in the device which is connected to the vacuum source. The pressure can be changed, but our experiments kept this suction at 30 kPa absolute pressure. D) Particles travel through a second chamber in the insert before exiting through an outlet with the same size as the inlet.

Drag on a particle, velocity for the three microparticles was estimated to be 400 m/s, 230 m/s, and 280 m/s.[10] Penetration depth profiles show a bimodal distribution, where particles cluster at the surface and at some mean penetration depth below the surface. In published work, 0.47 μm microparticles, were able to embed 25 μm in 3% w/w agarose, and 1.27 μm particles were able to embed 85 μm in the same gel. These penetration events indicate over 50 to 70 self-diameters of penetration in a stiff agarose gel (elastic modulus = 20 kPa).[10]

The Groisman device was used for one of the most successful ballistic experiments reported in literature. In Zilony et al., porous Si microparticles were fabricated with an electrochemical etching process. The plate-like particles (2-18 μm) were not only able to penetrate a 2% agarose gel by up to 2 mm, but they were also able to traverse 700 μm of excised porcine skin.[11] This study is highlighted because not only does it show how effective the PCG can be, but it also suggests the importance of particle shape. This work represents some of the greatest penetration depth achieved in literature (skin is notoriously difficult to penetrate), and it may not be coincidental that particles had pointed shapes with aspect ratios from two to three.

2.2.2 – Selection of Gel Substrate for Ballistic Experiments

Before testing the PCG, a convenient gel target was required that had similar mechanical properties compared to corneal tissue. Agarose gels can be prepared quickly and are transparent, which is a benefit for ballistics experiments. Based on previous work done by Professor Groisman, agarose was selected as the substrate material. Oscillatory shear rheology was performed on a range of agarose gels using an 8 mm diameter geometry. To make gels, agarose was dissolved in DI water by microwaving until boiling. Using a Pasteur pipette, the boiling solution was poured in between two acrylic plates clamped around 0.7 mm spacers with

rectangular slots for the solution to flow into. The gels were allowed to set at 4° C for two hours. The gels were cut into discs using an 8 mm biopsy punch. Tissue samples were prepared by dissecting the cornea from porcine eyes and punching out an 8 mm disc from the center of the tissue using a biopsy punch. When testing tissue, an 8 mm cleated geometry developed by our lab was used to prevent wall slip.[12,13] To test samples, the rheometer geometry was lowered onto samples until a normal force was registered. Strain sweeps were run on a stress-controlled rheometer (TA Instruments; AR1000) from 1 to 100 1/s with eight points per decade (at 25 °C).

The results of this testing are shown in **Figure 2.5**. The storage and loss modulus for 1.0 to 3.0% w/v agarose gels are plotted along with the data measured from corneal tissue. From this data, it can be found that the 1.0% w/v gels are the most similar compared to the corneal tissue. The outcomes of this experiment have to be considered along with the testing parameters. The strain rates measured in this experiment are very low. This is problematic, since it has been demonstrated that the mechanical properties of corneal tissue are heavily dependent on strain-rate.[14] Regardless, this data indicated the use of 1% w/v agarose gels for our initial ballistic testing. Agarose was chosen over ballistic gelatin, since agarose can be prepared much more quickly than ballistic gelatin. In later experiments, a switch was made to ballistic gelatin so that regressions fit to empirical data could be used to infer particle impact velocity.

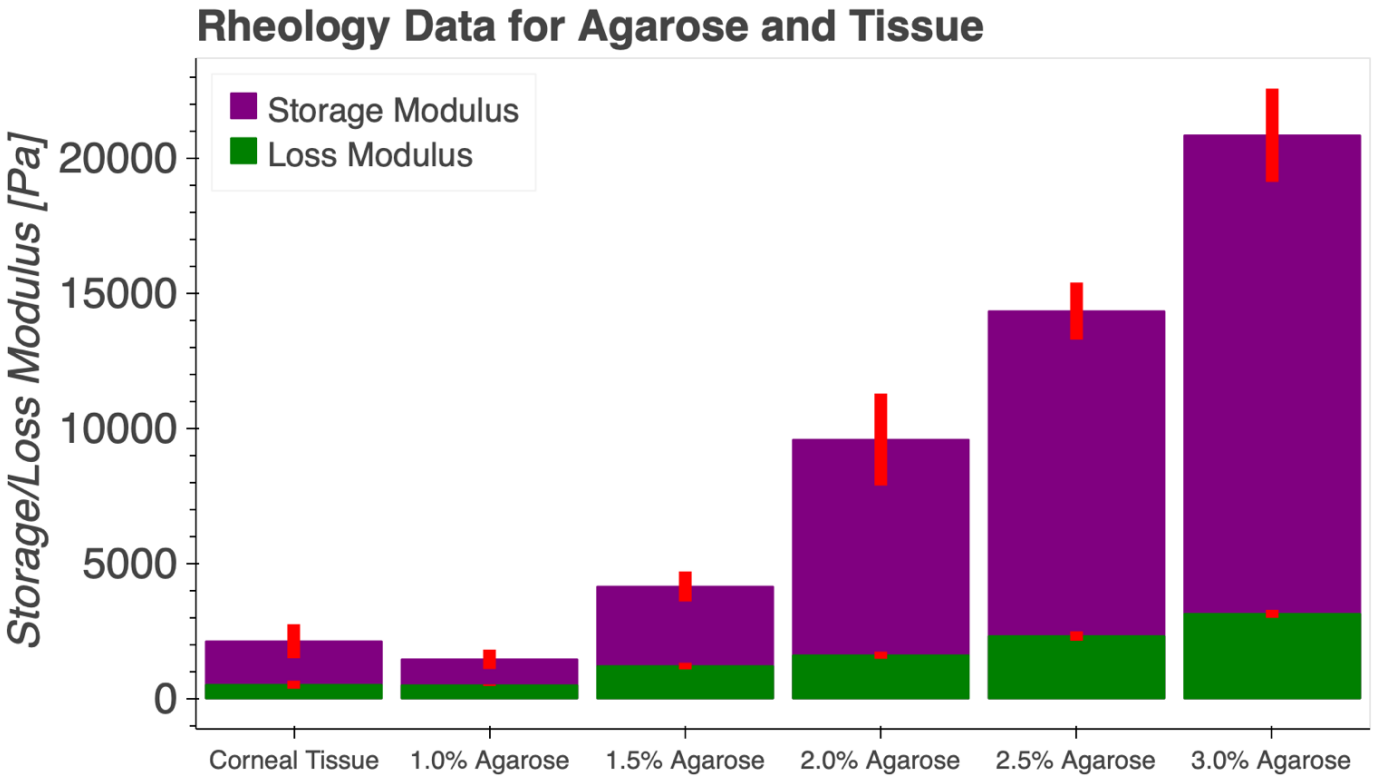

Figure 2.5 – Rheological data of agarose gels and corneal tissue. Storage and loss modulus taken as the average of reported values when doing frequency sweeps from 1 to 100 1/s. N = 6 measurements per sample. 95% confidence intervals shown.

2.2.3 – Kinematic Equations of Particle Motion and Expected Velocities of Particles

For a particle of radius R_p in the barrel of a gene gun, where the gas of viscosity μ flows with a speed v_o, the velocity of the bead changes with time as Stokes' Drag acts on the particle:

$$v(t) = v_0\left[1 - \exp\left(-\frac{t}{\tau}\right)\right] \tag{8}$$

$$\tau = \frac{2}{9}\frac{\rho_p R_p^2}{\mu} \tag{9}$$

where τ is a characteristic acceleration time. Integrating the equation $L(t) = \int_0^t v(t)dt$:

$$L(t) = v_o[t - \tau + \tau\exp(-t/\tau)]. \tag{10}$$

Now, if Equation 8 and Equation 10 are nondimensionalized using $\bar{L} = L/L_o = L/v_o\tau$, $\bar{t} = t/\tau$, and $\bar{v} = v/v_o$, Equation 8 becomes:

$$\bar{v} = 1 - e^{-\bar{t}} \tag{11}$$

$$\bar{t} = -\ln(1 - \bar{v}) \tag{12}$$

and Equation 10 becomes:

$$\bar{L}(\bar{t}) = \bar{t} - 1 + e^{-\bar{t}}. \tag{13}$$

By plugging Equation 12 into Equation 13,

$$\bar{L}(\bar{t}) = -\ln(1 - \bar{v}) - \bar{v} \tag{14}$$

producing the Taylor Expansion of this expression,

$$\bar{L}(\bar{t}) = \frac{\bar{v}^2}{2} + \frac{\bar{v}^3}{3} + \frac{\bar{v}^4}{2} \tag{15}$$

and truncating after the first term, an equation is created that relates ejection velocity to acceleration barrel length:

$$\bar{v}^2 \approx \sqrt{2\bar{L}(\bar{t})}. \tag{16}$$

Reintroducing dimensions produces the following useful relationship that predicts ejection velocity as a function of acceleration barrel length L:

$$v = v_o\sqrt{2L/L_0} = v_o\sqrt{2v_0L/\tau} = \sqrt{\frac{9v_0L\mu}{\rho_p R_p^2}} = \frac{\sqrt{9v_0L\mu/\rho_p}}{R_p}. \quad (17)$$

The characteristic acceleration time is a measure of how fast it takes for a microparticle to come to the velocity of the carrier gas. In **Table 2.2**, the characteristic acceleration time of a range of microparticles used in this study is shown. Also the expected velocity is calculated (using Equation 17) for microbeads accelerating in gas moving at the speed of sound in air through a 20 cm column (the length of the PCG barrel). Predicted ejection velocities are shown for polystyrene particles and steel particles.

Table 2.2 - Aerodynamic relaxation and expected ejection velocity assuming an acceleration barrel that is 20 cm long that is conveying air traveling at its speed of sound

Bead Diameter[μm]	**τ [msec]** ($\boldsymbol{\rho_p = 1\ \frac{kg}{m^3}}$])	**v [m/s]** ($\boldsymbol{\rho_p = 1\ \frac{kg}{m^3}}$])	**v [m/s]** ($\boldsymbol{\rho_p = 7.8\ \frac{kg}{m^3}}$])
10	0.3	343.0	242.0
20	1.2	338.0	121.0
30	2.8	225.3	80.7
48	7.1	140.8	50.4
108	36.0	62.6	22.4
165	84.9	20.0	14.7
265	216.7	25.5	9.1

This table shows that 10 to 20 μm plastic beads will have the same velocity as the speed of sound in air, assuming no collisions. Once particles get to be 30 μm, the velocity drops significantly.

The largest particles are only able to accelerate up to several tens of meters per second. The stainless steel microparticles show more pronounced reductions in expected ejection velocity. After particles are ejected from the PCG into still air, rapid deceleration can occur, based on aerodynamic relaxation time. After ejection, the rate of change of momentum is governed by:

$$m_p \frac{dv}{dt} = m_P g - \frac{1}{2}\rho_g C_D A(v)^2. \quad (18)$$

This equation was numerically integrated with an expression for C_D[15], assuming that particles are ejected with a velocity of 300 m/s, to determine favorable standoff distances between gene gun and target substrate. The results shown in **Figure 2.6** indicate how quickly plastic beads can decelerate in air. If particles are 10 μm or less in size, they lose velocity in about a centimeter. If beads greater than 20 μm are used, at least 100 m/s of impact velocity will be achieved if the standoff distance is 1 cm.

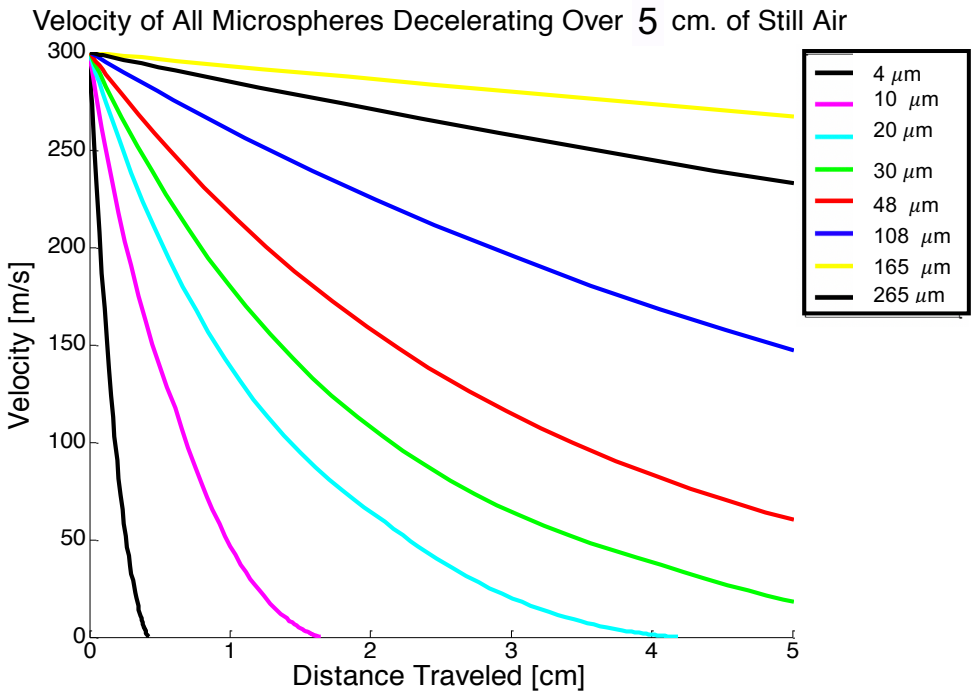

Figure 2.6 – Expected deceleration of plastic beads in air. The 165 μm bead is barium titanate with density of 4200 kg/m^3. Equation 18 was numerically integrated.

2.2.4 – Penetration of Polystyrene Beads in Agarose Gels

To test the penetration of plastic beads in gel using the PCG, 1% w/v agarose was prepared by heating in the microwave until boiling. Gels were poured into 6 cm diameter petri dishes to a thickness of about 5 millimeters and were allowed to solidify at 4° C for approximately two hours. To prepare cassettes for particle delivery, 3% w/w solutions of microparticles (Sigma Aldrich and Cospheric Inc.) were vortexed and pipetted into luer-lock cassettes. The cassettes had 2.5 μL droplets deposited onto mesh substrates, the cassettes were dropped into liquid N_2, and then they were exposed to rough vacuum (10 - 100 mtorr) for 1 hour. This produced dry clusters of particles with low-adhesion forces between particles and the mesh substrate (**Figure 2.9**). The particles were delivered using 4.8 bar injection pressure with 4.1 bar acceleration barrel pressure with vacuum suction on the end of the barrel of – 0.7 bar gauge pressure. Following delivery, penetration depth was measured using confocal microscopy (for fluorescent microparticles) or with visual microscopy on gels that were cut into blocks and flipped on their sides to reveal cross-sections.

Our group began testing 10 – 30 μm particles, with the aim that they would be undetectable to the human eye and would cause the lowest amount of damage (the acuity of the human eye is about 0.03 mm).[16] To test penetration, confocal and transmission microscopy was done. To find where the surface of the gel was in our confocal experiments, a mixture of two monodisperse particle solutions was delivered. 4 μm particles, which have a considerably low aerodynamic relaxation time (see **Figure 2.6**), were delivered with 10, 20, and 30 μm beads. This way, smaller particles mark the surface (due to low impact velocity), and larger particles can be seen

underneath the surface. The results of testing (**Figure 2.8**) demonstrate that 10 µm beads do not penetrate the surface, 20 µm beads just barely do, and 30 µm beads penetrate gel by 200 µm.

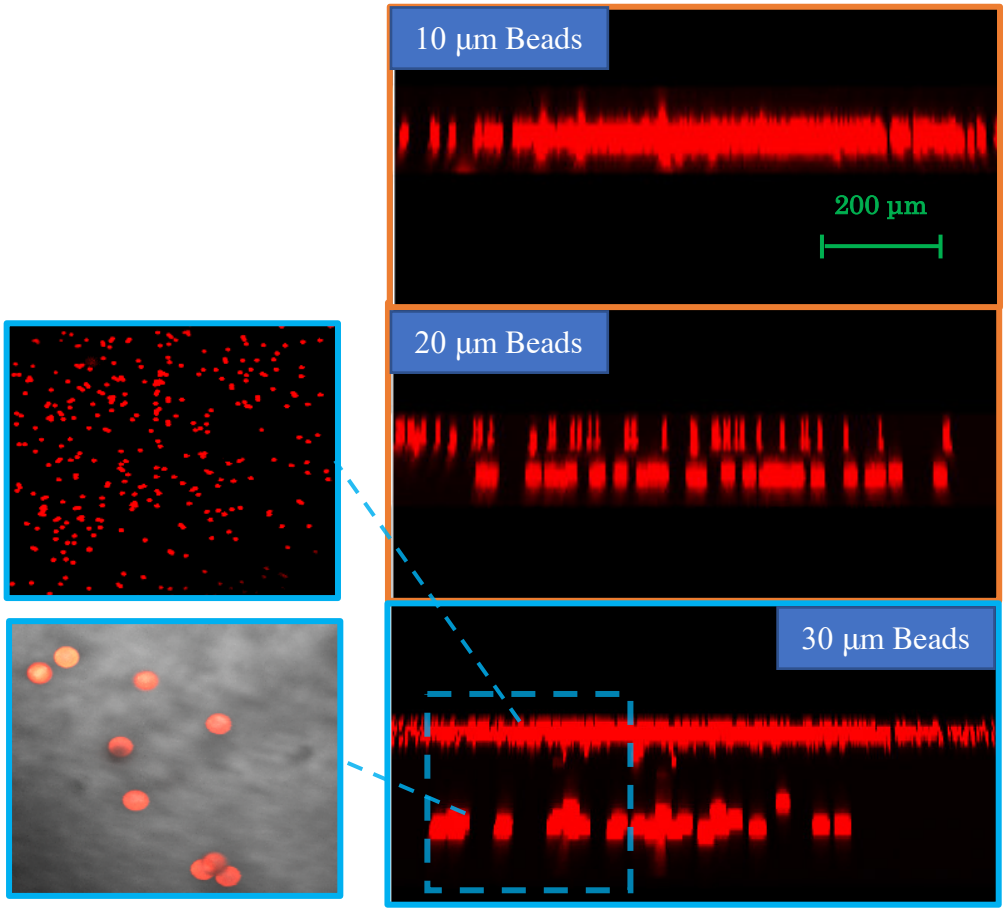

Figure 2.7 – Confocal microscopy of 1% w/v agarose gels treated with 10, 20, and 30 µm spheres. 4 µm spheres are at the surface of the gel, and larger particles are shown below.

This was a successful first demonstration of the ballistic device. The lack of penetration of 10 μm spheres is expected, since they decelerate so quickly in air (**figure 2.6**). The penetration of 30 μm spheres was promising, displaying almost seven diameters of penetration. One of the compelling facets of this data is that the penetration depth of particles is quite consistent – both the 20 and 30 μm spheres appear in roughly the same plane. This is a desirable result for our purpose of drug delivery. In these figures, some particles appear stretched in the z direction. This comes from the point-spread function of light coming from our particles not being optimized using the gain/threshold parameter of the confocal microscope. This stretching phenomenon was hard to avoid and fluorescent particles were not always available, so our group decided to use standard transmission microscopy to perform a quantitative ballistics experiment (by cutting out gels and imaging along the penetration axis).

To carry out ballistic experiments, a range of larger particle sizes was chosen (30, 48, 70, 108, and 250-280 μm polystyrene spheres). In addition, high-density, barium-titanate beads were used to show just how much penetration is possible when density is modulated. A 20X objective imaged cross sections of embedded microparticles in agarose. **Figure 2.9** shows representative micrographs of particles embedded in gel - as particle size increases in these figures, penetration increases proportionally. The result of penetration depth experiments, shown in **Figure 2.10**, demonstrate low variance in penetration depth as particles embed significantly in the gel medium (by up to 8 self-diameters). To see if particles penetrate in the gel with direct, linear proportionality to bead diameter (as predicted by Equation 1), the penetration depth of all particles tested was plotted against the mass:surface area ratio. This allowed us to incorporate the data for the 150 - 180 μm beads that had different density. This data (in **Figure 2.11)** reveals that

penetration for 30 to 108 μm beads increases linearly with particle diameter. The last two particles fail to fall on this curve, likely due to poor acceleration in the ballistic device. In **Table 2.1**, it is shown that these particles have lower predicted ejection velocities than the other particles. It is surprising that the data shows a linear relationship for the first four points, considering that expected ejection velocity decreases significantly from 30 to 108 μm diameters. It is possible that particles are hitting the surface with similar impact velocities in this size range.

With the PCG, promising penetration was achieved in a gel model of corneal tissue and rules were established for biolistically delivering low-density microparticles under atmospheric pressure (i.e. the effect of short aerodynamic relaxation time and high-particle density on penetration).

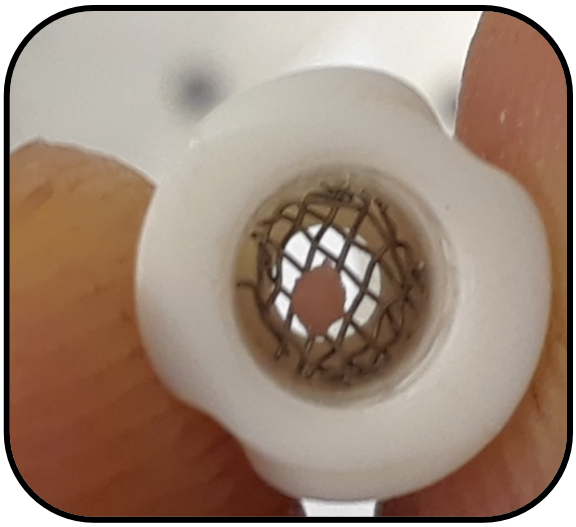

Figure 2.8 – Luer-lock cassette with polystyrene microparticles freeze-dried on mesh substrate. These cassettes are loaded into the PCG to deliver particles to gel.

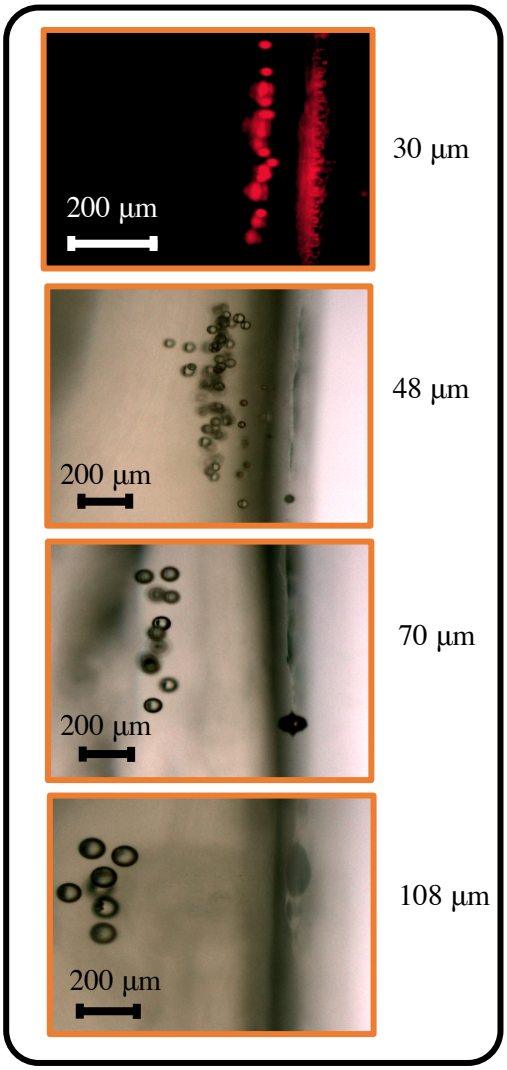

Figure 2.9 – Micrographs from a range of polystyrene microparticle sizes delivered to agarose gels. Penetration increases proportionally with particle size.

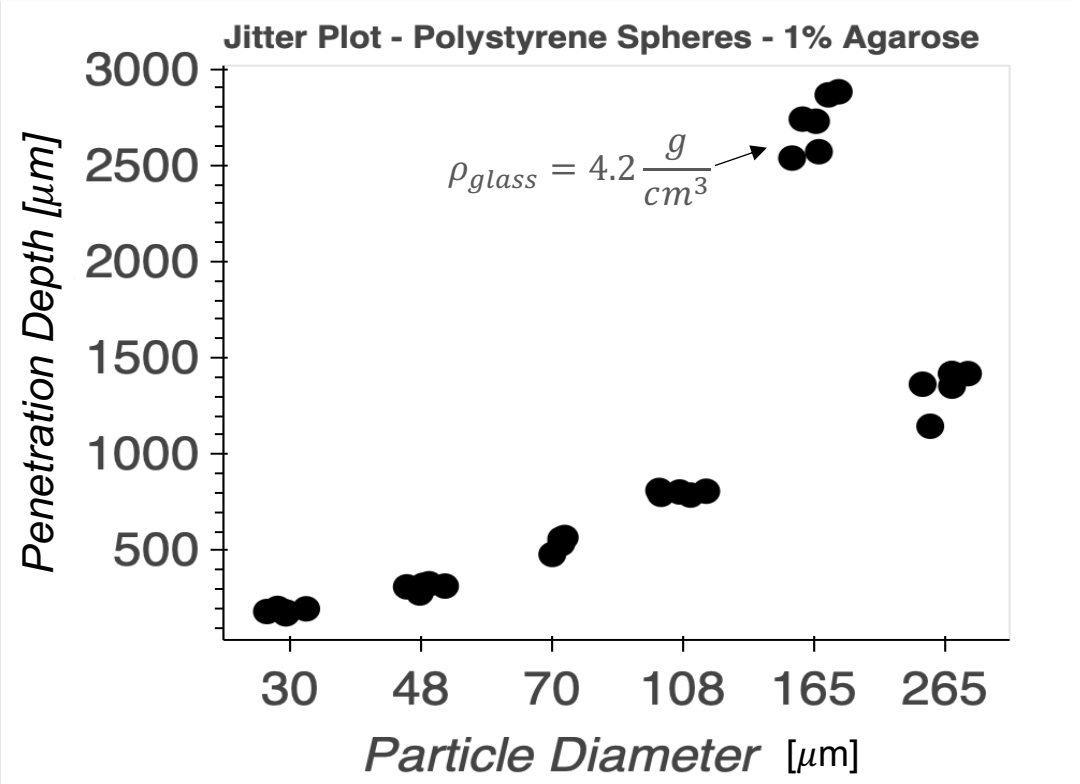

Figure 2.10 – Data from a range of polystyrene microparticle sizes delivered to 1% w/v agarose gels. Penetration increases proportionally with particle size.

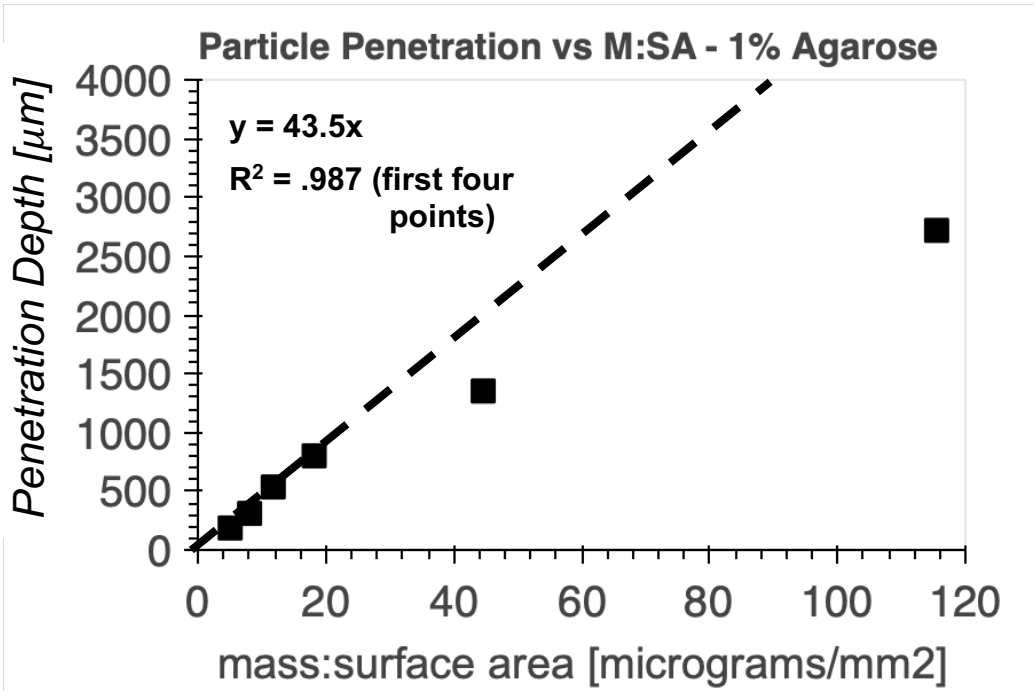

Figure 2.11 – Polystyrene microparticle penetration vs. mass to surface area ratio. First points are linear (marked with green). Last two points deviate from the linear trend.

2.2.5 Drawbacks of the Pneumatic Capillary Gun and Use of the PDS1000 Gene Gun

While the capillary gun was consistent in delivering microparticles to gel substrates, there were a few drawbacks to this device. 1) There would be difficulties delivering higher density microparticles at high velocity. **Table 2.1** indicates that as the density of the particle gets higher, the predicted velocity at the end of the 20 cm acceleration barrel drops. 2) The device delivers particles to a small area of target substrate due to the 0.8 mm diameter outlet. This was not a problem with gels because areas of gel could be identified under a microscope and then cut out using a razor blade. With corneal tissue, this presents an issue since beads will have to be located by sectioning bulk tissue. For these reasons, our group looked for a different ballistic device.

Ultimately, a PDS1000 gene gun, sold by BioRad (Catalog # 1652257), became available. The device not only covers a much wider section of the target substrate (approximately 4 cm^2), it is also compatible with higher density microballistics. The gene gun works by accelerating a Kapton disc with particles deposited on the surface. **Figure 2.12** shows the process. Helium is pumped into an acceleration tube sealed with a rupture disc. When the rupture disc breaks, the Kapton film, called a macrocarrier, is accelerated into a stopping screen and releases particles when it comes to a rapid stop. This method of acceleration is more compatible with denser microparticles because it is the light macrocarrier that is accelerated, not the individual beads. The Kapton disc has a high surface area and a short relaxation time given by:

$$m_K \frac{dv}{dt} = \Delta P A_K \tag{18}$$

where ΔP is the pressure above and below the macrocarrier. Note that this equation is incomplete, since there is a missing component of drag. However, we assume this component to

be small in the chamber held at rough vacuum and at low velocities, so it may be a useful approximation. With this equation nondimensionalized using v_o, the gas velocity, the time-constant is produced:

$$\frac{m_K v_o}{\Delta P A_K}\frac{d\bar{v}}{dt} = 1 \;\rightarrow\; \bar{\mathrm{v}}(\mathrm{t}) = \frac{\Delta \mathrm{PA_K}}{\mathrm{m_K} v_o}\mathrm{t} \quad\rightarrow\quad \tau = \frac{\mathrm{m_K} v_o}{\Delta \mathrm{PA_K}}\,. \tag{19}$$

In **Table 2.3**, the characteristic acceleration time of the Kapton disc is approximated, assuming that helium used in the device is expanding at sonic velocity (972 m/s). The characteristic time is plotted for the entire range of rupture discs offered by BioRad. In addition, the distance traveled by the Kapton disc moving the speed of sound propagating in helium for two characteristic times is shown. As can be seen, the characteristic acceleration time can be changed by up to 80% by switching rupture discs. The acceleration lengths reported are all greater than the actual path of acceleration in the device (1 cm), but not significantly. In addition, a conservative estimate was made by assuming such a high average gas expansion velocity. Since the short acceleration times of the macrocarriers would translate to high acceleration of microparticles, and the BioRad allowed for uniform coverage of target substrates, this device was used for the majority of our testing with corneal tissue.

Table 2.3 – Aerodynamic relaxation times of Kapton discs. The distance travelled over two acceleration times [$v_{avg} = 972\ m/s$]

$\boldsymbol{\Delta P}$ $[\boldsymbol{PSI}]$	$\boldsymbol{\tau = \frac{m_{kapt} v_o}{\Delta P A}}$ $[\boldsymbol{\mu sec}]$	$\boldsymbol{v_o * 2\tau}$ $[\boldsymbol{cm}]$
450	34.9	6.8
900	17.5	3.4
1350	11.6	2.3
1800	8.7	1.7
2250	7.0	1.4

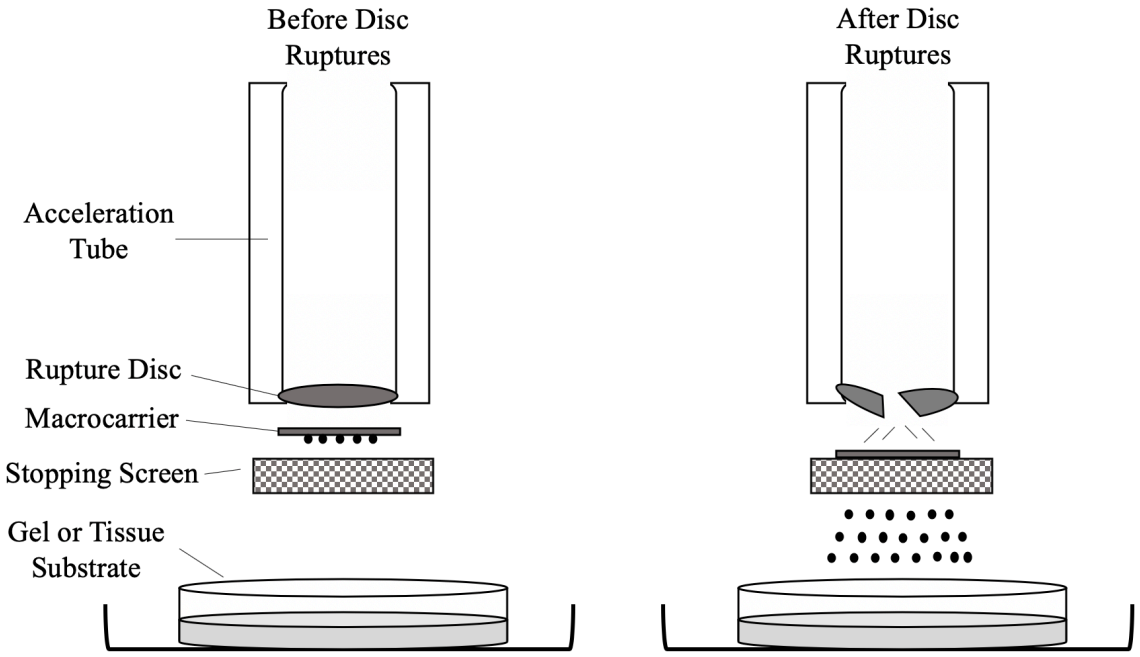

Figure 2.12 – Biolistic acceleration process employed by the PDS1000 gene gun. Reproduced from BioRad PDS1000 Instruction Manual.[21]

2.3 - Experiments Done in Ballistic Gelatin With PDS1000 Gene Gun

Ballistics research typically uses bovine or porcine gelatin as a target reference material. While there are many concentrations of ballistic gelatin used, the 10% w/w gelatin formulation is meant to best simulate muscle tissue.[17] Other works in literature develop scaling relationships with the Elastic Froude Number (previously mentioned) and characterize the elastic response of gelatin using high-speed imaging.[3,7] This is a rich area of research involving high-speed transient cavity dynamics. Our group switched to ballistic gelatin to be more in line with other ballistics research. In addition to this, since our group would have a very challenging time measuring penetration depth in the BioRad device, which contains microparticles in a sealed vacuum chamber, it was decided to switch to ballistic gelatin because we could use the Poncelét Model developed in Veysset et al. to estimate impact velocity.[7]

After testing penetration depth for particles of a single, low density in the pneumatic capillary gun, it was decided to expand the particles being tested to incorporate ballistics of different densities. Our group wanted to demonstrate a wide range of kinetic embedding energies before testing penetration in corneal tissue. The particles selected for this study are shown in **Table 2.4**. As can be seen, the particles all cover similar size ranges, but densities vary from 1.1 to 19.2 g/cc. If a power of 1/2 is used in Equation (1), the densest particle (tungsten) is expected to penetrate 13.5 times as deep in ballistic gelatin compared to polyethylene particles with the same impact velocity.

To run experiments, ballistic gelatin was prepared with a standard protocol, described in Jussila et al.[18] This protocol results in consistent mechanical properties and is used in many ballistics experiments.[19,20] In short, to prepare gels, half of the powdered gelatin (Sigma Aldrich; acid precipitated gelatin from porcine tissue) was dissolved in half of the required deionized water. This mixture was stirred for half an hour while the rest of the water was heated to 80 °C. The hot water was added to the gelatin mixture and was stirred for another 15 minutes. Gelatin was allowed to solidify at room temperature for 24 hours before storing in a refrigerator for 24 hours. To do ballistics testing, macrocarriers were loaded into the device along with the requisite rupture disc, gels were placed in the vacuum chamber, the space was pumped down to -737 mmHg (gauge pressure), and the acceleration tube was pressurized until the rupture disc broke and particles were delivered. To determine penetration depths, 5 mm cubes of gel were cut out in the center of the particle delivery zone. Gels were then flipped on their side and imaged with a transmission microscope to visualize the particle cross-section. An image processing pipeline was written to measure penetration depth (Appendix A.1).

Table 2.4 – Information about particles used in ballistics study

Particle Material	Particle Density	Size (Diameter) Range
poly(ethylene)	1.1 g/cc	10 – 29 μm
soda lime glass	2.5 g/cc	10– 22 μm
barium titanate glass	4.2 g/cc	5 – 22 μm
stainless steel	7.8 g/cc	5 – 22 μm
tungsten	19.2 g/cc	20 – 40 μm

2.3.1 – Penetrating 5% w/w Ballistic Gelatin with Microparticles of a Range of Densities

Direct linear proportionality between penetration depth and particle diameter was demonstrated using the PCG. From here, the effect of particle density on penetration depth was investigated. For testing, a 5% w/w gelatin substrate was selected. This concentration was chosen because it would allow the Poncelét Model to be used to infer impact velocity (using resistance values from Veysset et al.). In addition, the gel is stiff enough to be cut out while holding its shape, enabling reliable penetration depth measurement, but also the gel is not too stiff such that penetration is highly attenuated, making it difficult to discern differences in penetration when different impact parameters are used.

There were three goals to this study. First, it was designed to demonstrate a broad range of kinetic energy for particle embedding that could then be tested on our tissue model. Second, our group wanted to determine how penetration scales with particle density on the microscale (using the Elastic Froude Number). Third, it was desired to use this data to infer impact velocities from the Poncelét model.

To begin testing, low-density poly(ethylene) spheres were delivered to 5% w/w agarose. Representative micrographs of particle cross-sections are shown in **Figure 2.13** below. As can be seen, particles embed in the gel to a shallow extent, likely due to the low density of the particles. The overall penetration of particles is as high as two-three diameters. Referring back to **Figure 2.2**, this corresponds to an impact velocity of around 240 to 320 m/s. Since penetration depths were so low, quantitative penetration statistics were saved for denser particles that penetrate tissue to a greater overall extent.

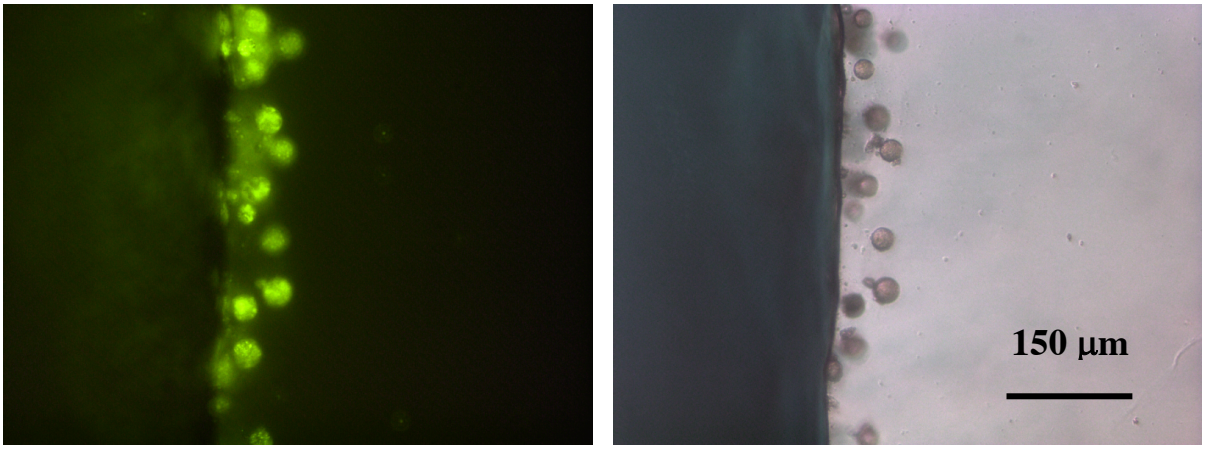

Figure 2.13 – 10 – 29 μm poly(ethylene) spheres embedded in 5% w/w ballistic gelatin. (Left) Particle field excited by blue light to emit green fluorescence. (Right) Particle field illuminated under bright field microscopy.

With higher levels of penetration (particles not just piled up at surface), our group was able to generate penetration statistics. The image processing pipeline used in this study was a manual process. Since many particles appear in cross-sections out of focus, our group relied on going through images and selecting particles in focus one-by-one. While thresholding software was written that would calculate penetration statistics, it was found that this software would include out-of-focus, blurred objects. The procedure chosen to measure penetration depths involved

selecting particles that were in focus, clicking on each side of the object, and then clicking on the point closest to the particle on the surface of the gel. Once these pixel coordinates were identified, the thresholding software automatically calculated particle diameter and penetration depth from the center of the particle to the surface of the substrate (pipeline described in Appendix A.1). This process was carried out for soda-lime glass, barium-titanate glass, and stainless-steel microparticles. Three shots of particles were delivered of each particle material and then enough micrographs were imaged to produce one-hundred statistical points per particle delivery.

The results of penetration studies in 5% w/w ballistic gelatin are shown in **Figures 2.14** through **2.16**. There are several features worth pointing out from this set of penetration statistics. First, the image processing pipeline produces particle sizes that are in the expected range based on the size distributions of the particles used. That being said, there are some particles that showed up as being larger than the expected size. For example, some particles show up as being greater than 22 μm in penetration statistics. This can be attributed to the fact that some particles were in fact out of focus, some particles actually were outside of the expected size distribution, or some of these statistics come from clicking errors. Second, the data appears binned as opposed to a continuous distribution of particle sizes. The reason for this is that the particles were around 10-30 pixels wide. Since clicking on discrete pixels was done in the image processing pipeline, the data shows up in this binned fashion. Third, it can be seen that the penetration depth increases as particle density is increased. Where soda-lime particles penetrate 100-150 μm in gelatin, stainless steel spheres penetrate up to 600 μm. This range of penetration depths is promising, because it ensures that there will be a wide range of kinetic energy for embedding that can be

accessed when testing penetration in the cornea. The last interesting feature to point out is that when penetration depth is normalized using particle diameter, the curve flattens out, so all particle sizes embed in gel at a similar overall extent.

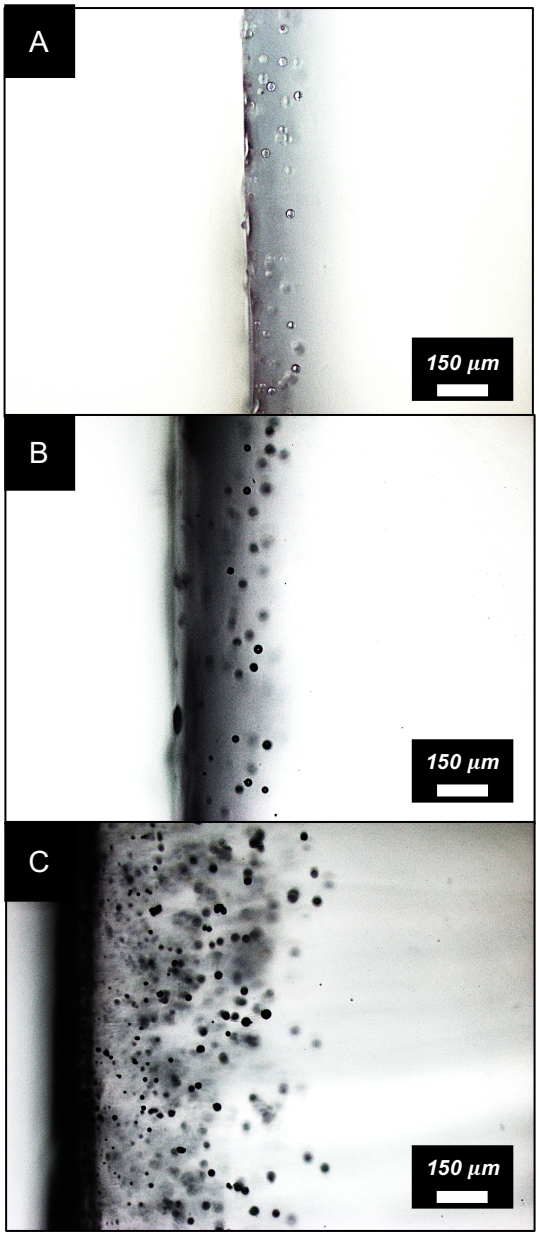

Figure 2.14 – Representative micrographs of three different compositions of microparticles penetrating 5% w/w ballistic gelatin. A) Soda-lime glass beads, B) barium-titanate glass beads, and C) stainless-steel beads penetrate a significant amount in the gel substrate.

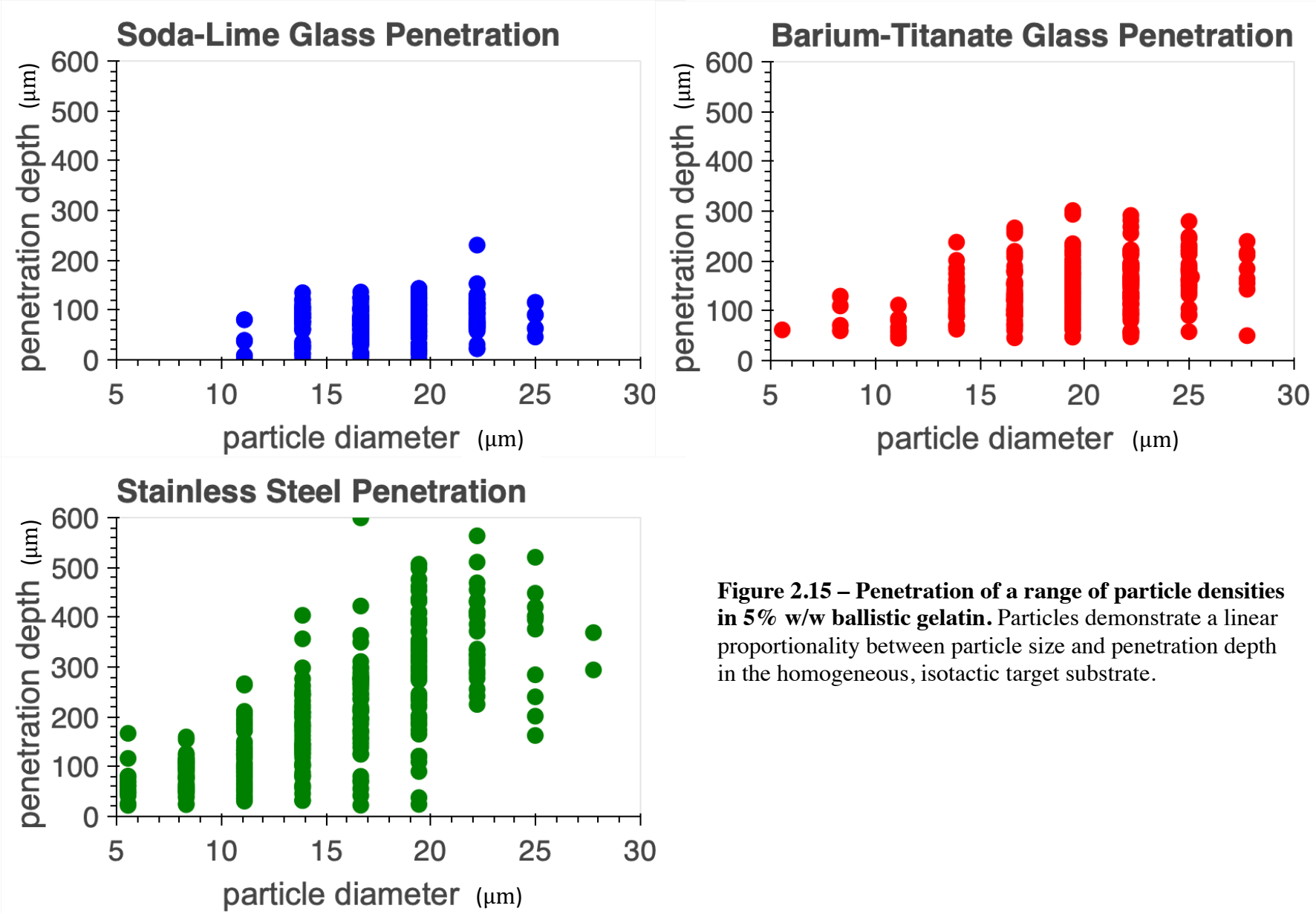

Figure 2.15 – Penetration of a range of particle densities in 5% w/w ballistic gelatin. Particles demonstrate a linear proportionality between particle size and penetration depth in the homogeneous, isotactic target substrate.

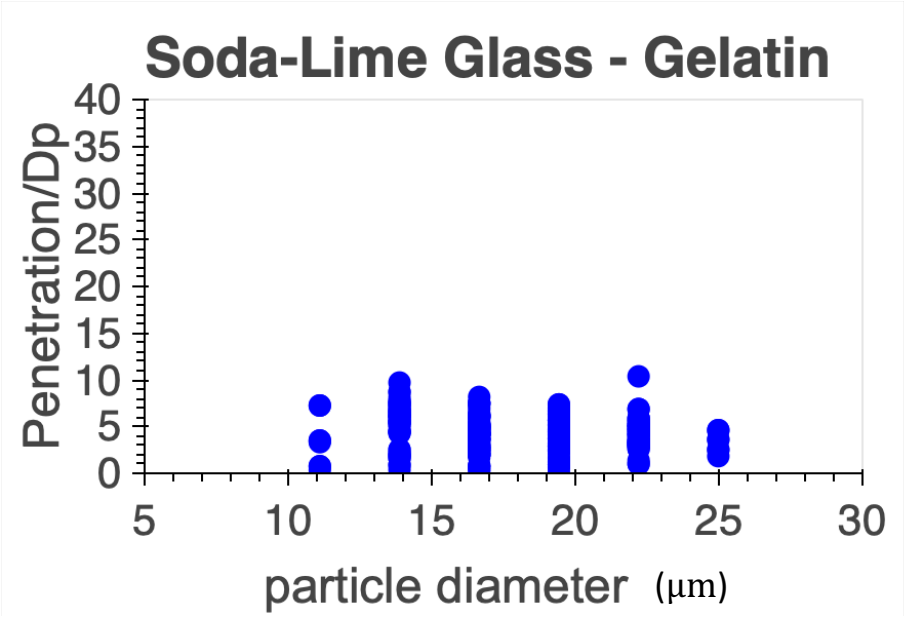

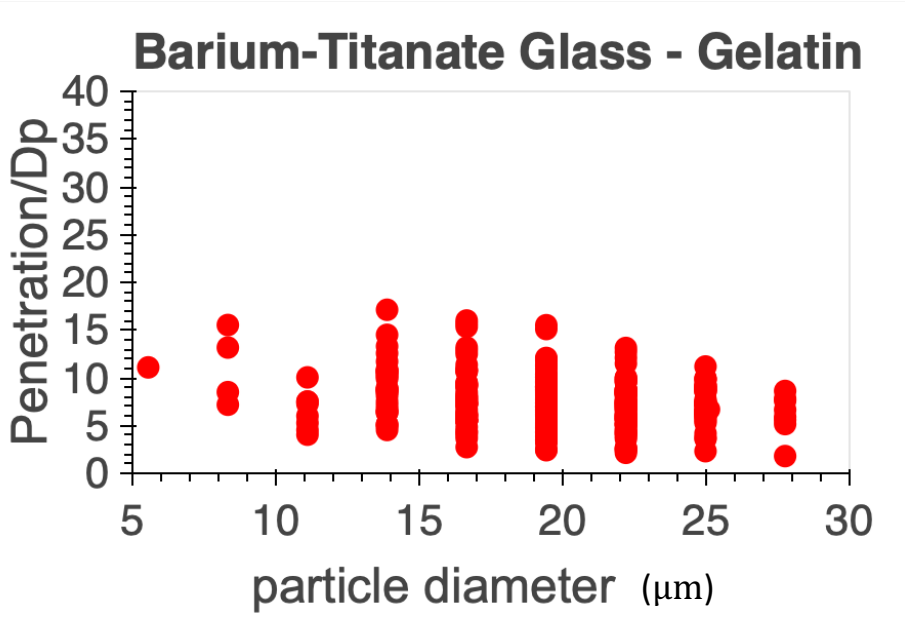

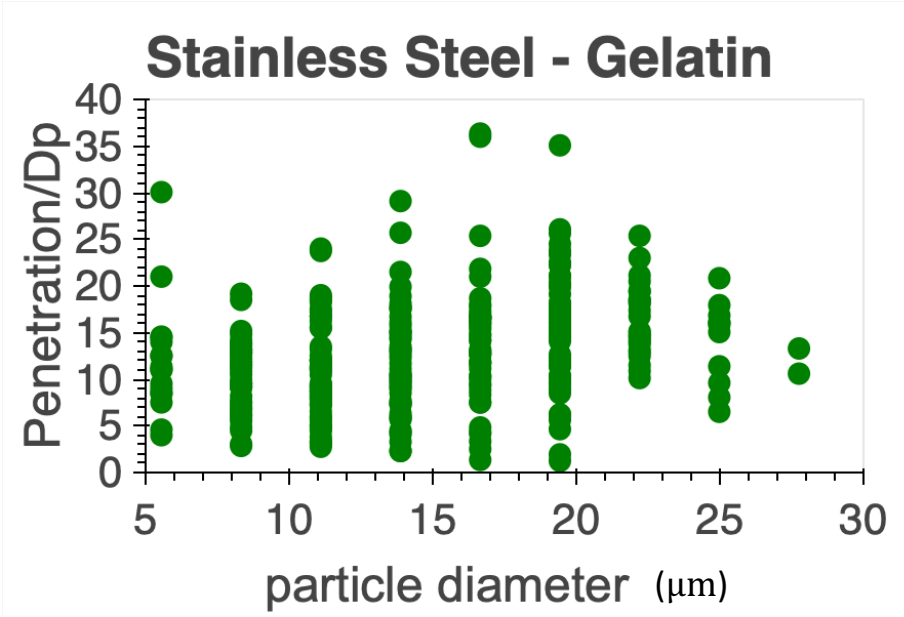

Figure 2.16 – Normalized penetration of a range of particle densities in 5% w/w ballistic gelatin. Particles' penetration normalized by dividing penetration by particle diameter. Penetration shows a flat profile.

There may be a slight downturn towards some of the larger particles in the figures, but in general, the normalized penetration depth is consistent across particle sizes tested. This observation is another indication that particle penetration in a homogeneous material is linearly proportional to particle size. This will be a useful comparison for experiments in corneal tissue.

Again, with larger projectiles than the study reported here, penetration depth (z_∞) in uniform, isotropic gel is known to scale with the Elastic Froude Number $\frac{z_\infty}{D_p} \sim \left[\frac{\Delta\rho u_o^2}{G}\right]^\gamma$, where $\Delta\rho$ indicates density difference relative to the target material, u_o is the impact velocity, G is the storage modulus of the substrate, D_p is the particle radius, and γ is an exponent empirically found to be close to one half. Penetration in the microscale, demonstrated with this dataset, is observed to scale with the Elastic Froude Number to a power of 0.8 ± 0.2, as is calculated in Appendix B.2. There is low deviation from this scaling relationship for larger particles. When smaller particles are analysed, there is more variation in the calculated fitting exponent. This may be related to the low aerodynamic relaxation time of these particles.

To test that the device was consistent, the data from different deliveries was compared. The mean and standard deviation of penetration computed for each of three replicate experiments shows good reproducibility (**Figure 2.17**): with the exception of the middle-size range for stainless steel, the mean penetration depth for each of three particle deliveries for all three size groupings are indistinguishable (no statistically significant difference from experiment-to-experiment). Using the results of Veysset et al., who show that penetration of microparticles into ballistic gelatin conforms to the Poncelét Model and provide resistance values for the three

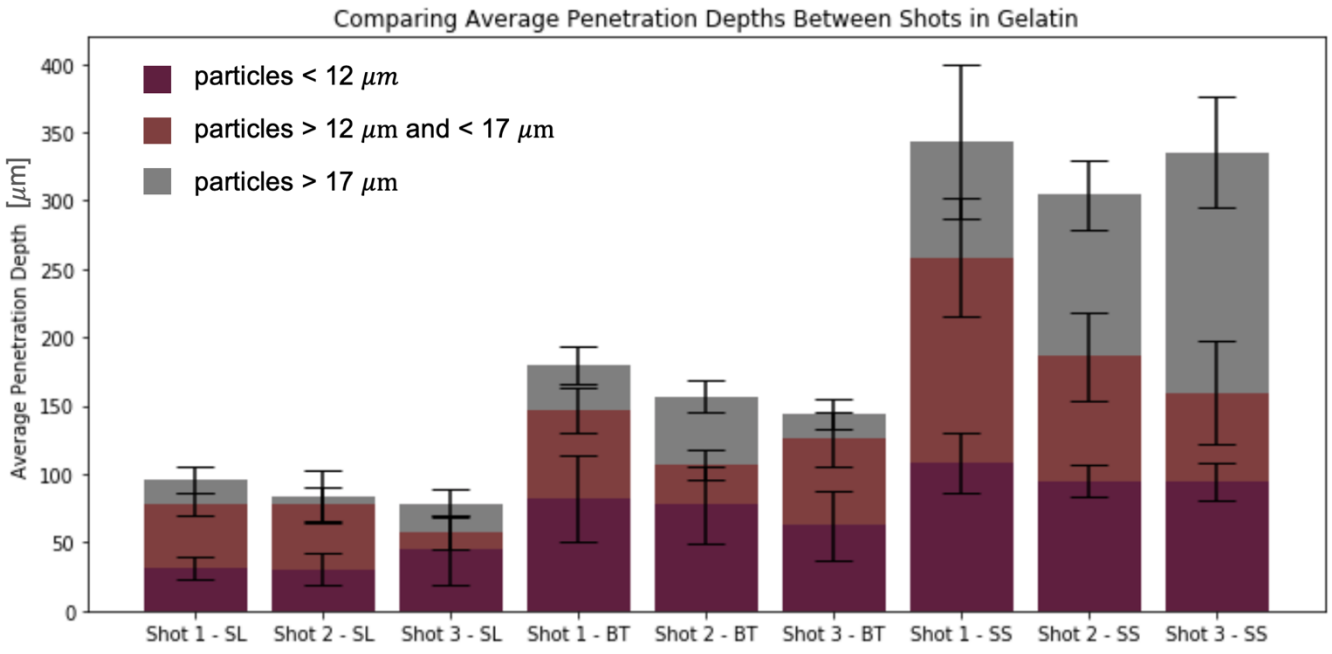

Figure 2.17 – Average penetration and standard deviation of individual particle deliveries to ballistic gelatin. Error bars show 95% confidence intervals of the penetration depth distribution. SL = soda lime, BT = barium titanate, and SS = stainless steel

concentrations examined in this work, one can infer the distribution of impact velocities (Appendix B.1). The results indicate that the velocity of most microparticles is in the range 150 to 300 m/s, with some particles having impact velocity inferred to be as high as 500 m/s.

2.3.2 – Penetrating 2.5% to 10.0% w/w Ballistic Gelatin with Range of Microparticles

To show the effect of substrate stiffness on particle penetration, microparticles were delivered to gels made with different concentrations. 2.5% and 10% w/w gels were made so that penetration models in Veysset et al. could be used to interpret the data.[7] The results of this testing are shown in **Figures 2.18**. The penetration statistics were measured for 10% w/w gel samples and not the 2.5% w/w, because the gels were too flimsy to clearly visualize the surface of the gels. From the image of the 2.5% w/w gelatin, it can be seen that some particles penetrate the gel by over a

millimeter. The 5% gelatin, which was shown in the previous section, showed penetration up to 600 μm. Last, the 10% gelatin shows penetration only from 150 to 200 μm. If the average penetration depth for particles greater than 17 μm in 5% gelatin (350 μm) is compared to the same mean value in 10% gelatin (175 μm), and data from Kiyama et al. is used (G(5% gelatin) = 5541 Pa and G(10% gelatin) = 17660 Pa), γ in $\frac{z_\infty}{d_p} \sim \left[\frac{\Delta \rho u_0^2}{G}\right]^\gamma$ comes out to ~0.6 (assuming that impact velocity is identical). This value is in the range of our previously calculated value for γ, but more data should be acquired to verify this scaling relationship, especially data that links microparticle penetration to a measurement of impact velocity.

As can be seen, penetration of the steel microparticles was progressively attenuated as the concentration of gelatin was increased. In **Figure 2.19**, the penetration depth of stainless steel microparticles is plotted for a single shot into 10% w/w ballistic gelatin. As can be seen, the penetration depth is proportional to the size of the particle, as has been previously demonstrated at lower gel concentrations. This trend is reinforced when the normalized penetration profile shows a flat response in the gel's ability to accommodate the microballistics.

Penetration depth of 5% and 10% w/w ballistic microparticles can be compared with **Figure 2.2**, which shows the expected penetration depth of stainless-steel spheres in ballistic gelatin predicted by The Poncelét Model. This is done in Appendix B.1. The mean penetration depth that is indicated by this analysis is higher than was predicted in 5% w/w gelatin. With this gel concentration, velocities inferred from the Poncelet Model from impact of soda lime, barium titanate, and stainless steel were all in agreement (mean penetration indicated an impact velocity

of 200 m/s). However, in 10% w/w gelatin, the mean penetration of stainless-steel microspheres indicated a

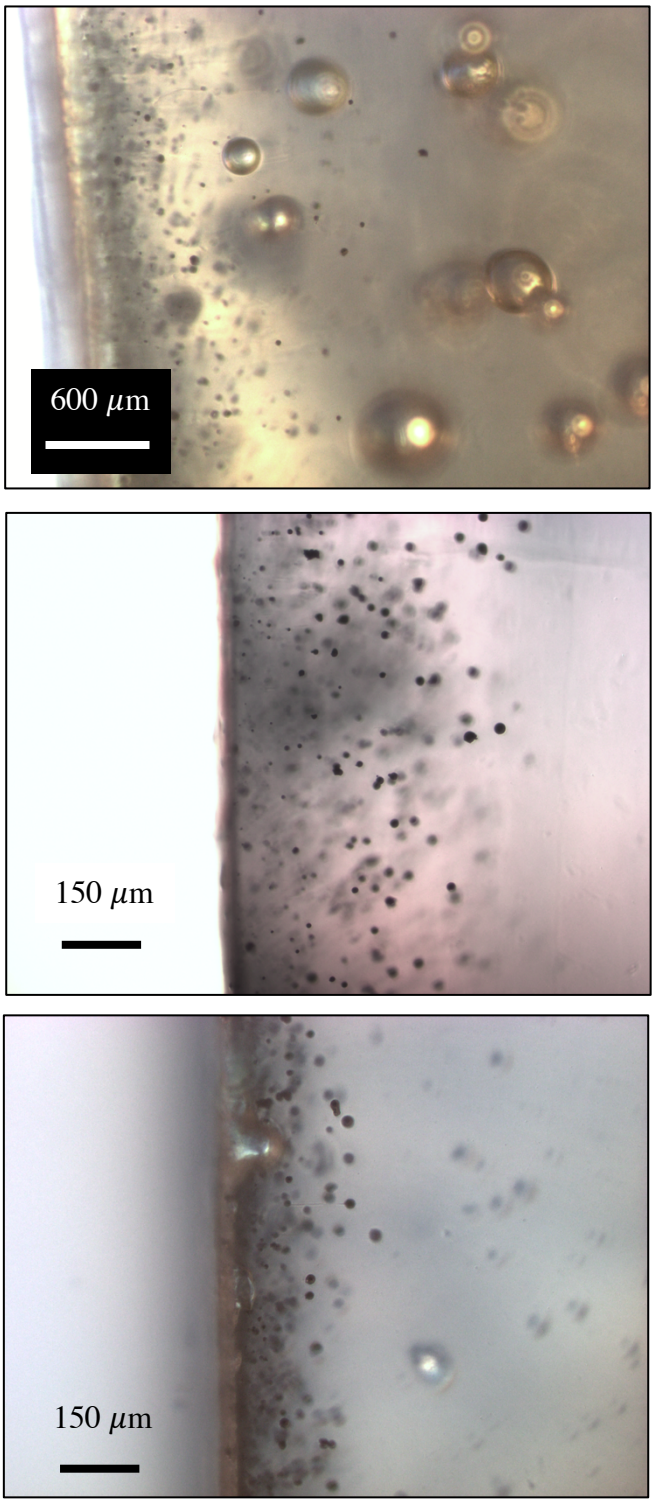

Figure 2.18 – Representative micrographs of stainless-steel microspheres in 2.5%, 5.0%, and 10.0% w/w gelatin.

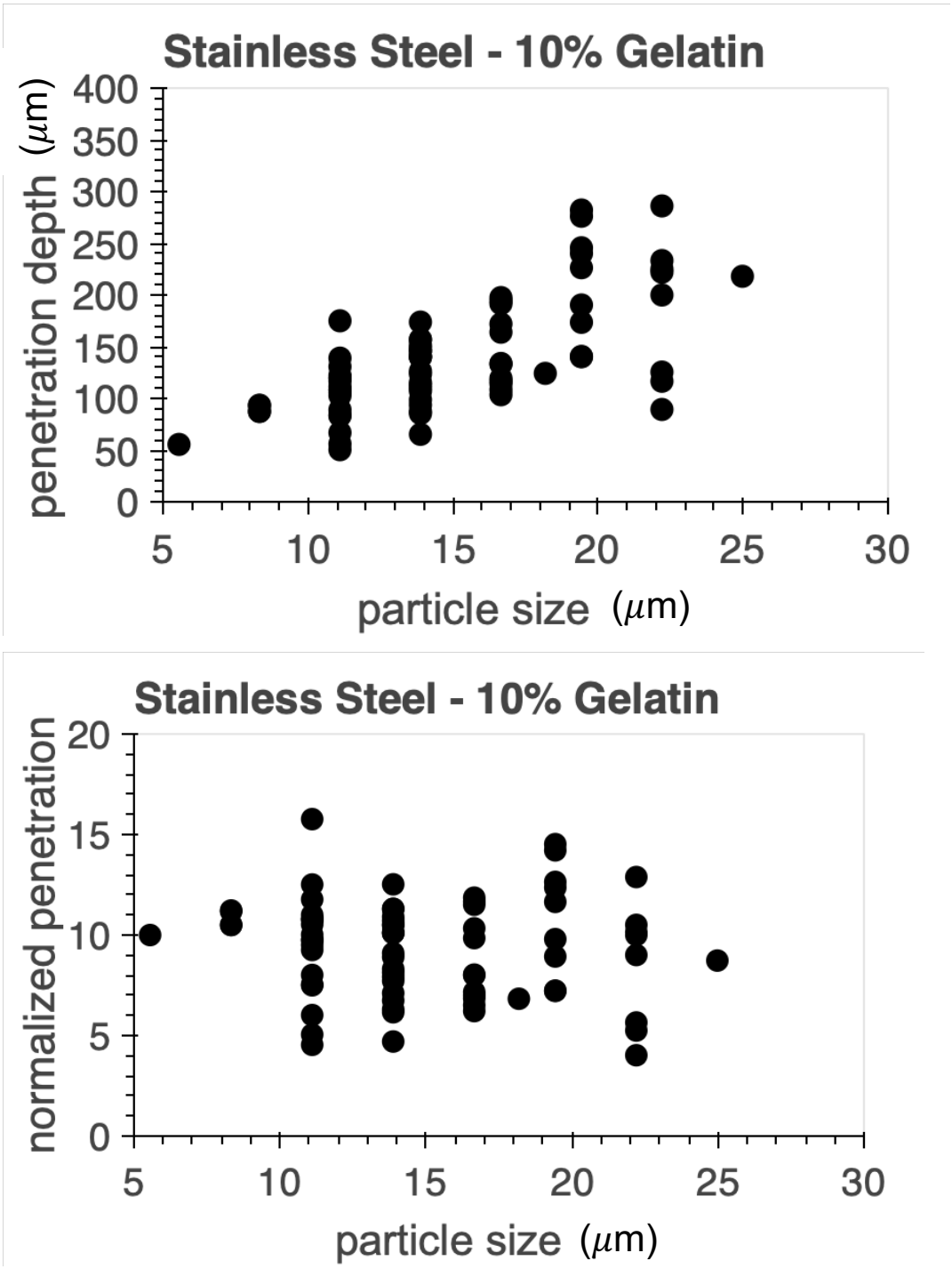

Figure 2.19 – Penetration depth (top) and normalized penetration depth (bottom) of stainless-steel microspheres in 10.0% w/w gelatin.

velocity of 300 m/s. The maximum impact velocity of microparticles, inferred from the maximum penetration depth, agreed well with the other projectile compositions tested in 5% w/w gelatin (500 m/s).

2.3.3 – *Penetrating 5% w/w Ballistic Gelatin with Tungsten Microparticles*

In addition to the range of particles tested that had densities from 1.1 to 7.8 g/cc, a final sample of microparticles was tested. Tungsten microparticles (20 – 40 μm; US Research Nanomaterials Inc.) were delivered to 5% w/w ballistic gelatin. The penetration seen was the greatest of all the ballistic materials tested. As can be seen from the image in **Figure 2.20**, some particles penetrate by over two millimeters into the gel. In addition, there were trails of bubbles left behind the tungsten particle payload. In Figure **2.25B**, there is an image recorded with a 40X objective that shows a clear trail of elliptical bubbles left behind the microparticles. Recalling the images in **Figure 2.1**, reproduced from Kiyama et al., there are long cavities which are generated from impacts that have been shown to rapidly seal up following microparticle impact in gelatin. It is unclear why the tungsten microparticles create large bubbles, but perhaps the length of the

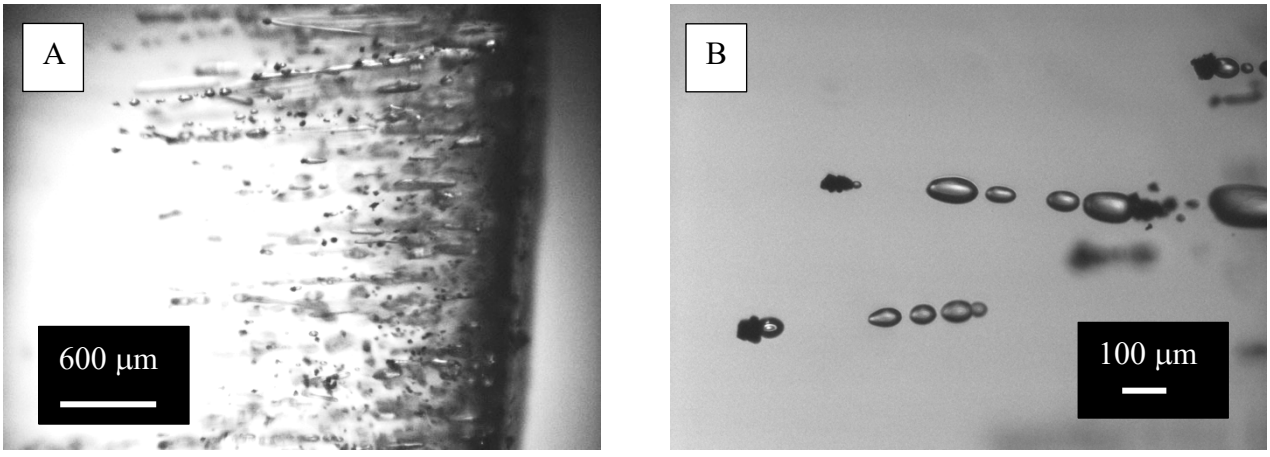

Figure 2.20 – Penetration of tungsten microparticles in 5% w/w gelatin. A) gross view of penetration. B) bubbles left behind particles.

cavities grow so quickly with the high speed of embedding that they do not have time to fully rebound elastically. Another possible explanation could be cavitation. This particle payload represents a maximum in kinetic energy that can be attained with our setup.

2.4 – Conclusions

Work with Alex Groissman's pneumatic capillary gun demonstrated that particles could be delivered under atmospheric pressure to an agarose model of the cornea with low variation in penetration depth. Penetration was shown to scale linearly with the size of microparticles. Unfortunately, the device was incompatible with denser microparticles and covers too small of a surface on the target substrate. For this reason, our group switched to the PDS1000 gene gun, which covers larger areas with microparticles and is compatible with dense ballistic materials. Using this commercial device, a broad range of kinetic embedding energies was demonstrated using projectile densities from 1.1 to 19.2 g/cc. Penetration was found to scale with Elastic Froude Number raised to a power of 0.8 ± 0.2. As gelatin stiffness was increased, penetration of microparticles was attenuated. The mean impact velocity of microparticles delivered with the gene gun was inferred to be around 200 m/s and the maximum velocity came out to around 500 m/s. This data serves as useful comparison to penetration depth in corneal tissue and demonstrates that there is a large range of kinetic energy for the embedding process accessed with the PDS1000 gene gun and the set of particles chosen.

2.5 – References

1. Kiyama, A., Mansoor, M., Speirs, N., Tagawa, Y. & Truscott, T. Gelatine cavity dynamics of high-speed sphere impact. *J. Fluid Mech.* **880**, 707–22 (2019).
2. Akers, B. & Belmonte, A. Impact dynamics of a solid sphere falling into a viscoelastic micellar fluid. *J. Nonnewton. Fluid Mech.* **135**, 97–108 (2006).
3. Swain, M., Kieser, D., Shah, S. & Kieser, J. Projectile penetration into ballistic gelatin. *J. Mech. Behav. Biomater.* **29**, 385–92 (2014).
4. Mrozek, R. *et al*. The relationship between mechanical properties and ballistic penetration depth in a viscoelastic gel. *J. Mech. Behav. Biomater.* **44**, 109–20 (2015).
5. Campbell, L. Under the hood: The physics of projectile ballistics. http://panoptesv.com/RPGs/Equipment/Weapons/Projectile_physics.php.
6. Kendall, M. A. F., Wrighton Smith, P. J. & Bellhouse, B. J. Transdermal ballistic delivery of micro-particles: Investigation into skin penetration. in *Proceedings of the 22nd Annual International Conference of the IEEE Engineering in Medicine and Biology Society* (2000).
7. Veysset, D. *et al*. High-velocity micro-particle impact on gelatin and synthetic hydrogel. *J. Mech. Behav. Biomed. Mater.* **86**, 71–76 (2018).
8. Kendall, M., Mitchell, T. & Wrighton-Smith, P. Intradermal ballistic delivery of micro-particles into excised human skin for pharmaceutical applications. *J. Biomech.* **37**, 1733–1741 (2004).
9. Kwon, J. & Subhash, G. Compressive strain rate sensitivity of ballistic gelatin. *J. Biomech.* **43**, 420–25 (2010).
10. Rinberg, D., Simonnet, C. & Groisman, A. Pneumatic capillary gun for ballistic delivery of microparticles. *Appl. Phys. Lett.* **87**, 1–3 (2005).
11. Zilony, N., Tzur-Balter, A., Segal, E. & Shefi, O. Bombarding cancer: Biolistic delivery of therapeutics using porous Si carriers. *Sci. Rep.* **3**, 1–6 (2013).
12. Mattson, M., Schwartz, D. & Kornfield, J. A mechanical measurement of sclera for screening myopia treatment. *Investig. Ophthalmol. Vis. Sci.* **46**, (2005).
13. Nickerson, C. & Kornfield, J. A 'cleat' geometry for suppressing wall slip. *J. Rheol. (N. Y. N. Y).* **46**, 5165 (2005).
14. Sharma, A. *et al*. Strain-controlled criticality governs the nonlinear mechanics of fibre

networks. *Nat. Phys.* **12**, 584–587 (2016).

15. Flagan, R. & Seinfeld, J. Noncontinuum effects. In *Air Pollution Engineering* 295 (1988).
16. Visual Acuity of the Human Eye. *Nondestructive Technology Resource Center* (2009).
17. Jin, Y., M, R., Wo, C., Han, R. & Li, B. Comparison of ballistic impact effects between biological tissue and gelatin. *J. Mech. Behav. Biomater.* **78**, 292–97 (2018).
18. Jussila, J. Preparing ballistic gelatine - Review and proposal for a standard method. *Forensic Sci. Int. 141, 91–98.* **141**, 91-98. (2004).
19. Schyma, C. & Madea, B. Evaluation of the temporary cavity in ordnance gelatine. *Forensic Sci. Int.* **214**, 82–87 (2012).
20. Große Perdekamp, M., Kneubuehl, B. P., Serr, A., Vennemann, B. & Pollak, S. Gunshot-related transport of micro-organisms from the skin of the entrance region into the bullet path. *Int. J. Legal Med.* **120**, 257–264 (2006).
21. BioRad. Performing a Bombardment in PDS-1000/He Biolistic Particle Delivery System Instruction Manual. 20–28 (2019).

Chapter 3

BALLISTIC EXPERIMENTS IN EX VIVO PORCINE CORNEA

3.1 Research on Corneal Biolistics Done by Other Labs and Plan for Experiments

While ballistic gene therapies have been developed for the corneal epithelium, to the best of our knowledge, there are no examples in literature of medicinal compounds being ballistically delivered to the epithelium or the stroma. In 2003, genes encoding GFP were first transfected biolistically using dense gold carriers that were embedded in the epitheliums of intact rabbit corneas and corneal allografts.[1,2] In Bauer et al., microballistic gene therapy was used to treat herpetic stromal keratitis. This disease, which is marked by significant inflammation of the epithelium and stroma, was treated with genes encoding protective cytokines - genes expressing interleukin-4 and interleukin-10 were delivered to the cornea and inflammation was reduced. In this study, microparticles only penetrated to the bottom of the epithelium. Since the corneal epithelium controls the stroma's immune response, this shallow penetration depth was sufficient.[3] The other instances in literature of using ballistic microparticles to deliver gene therapy to the cornea involve modulating the immune response of the corneal epithelium following penetrating keratoplasty. In these studies, a Helios Gene Gun, the most recent commercially-produced gene gun, could only make 1.5 – 3.0 μm gold particles embed to the basement membrane of the epithelium.[4,5]

While this data is at first discouraging from a standpoint of drug-delivery to the corneal stroma, the particles used in these experiments were small (≤ 3 μm) and larger particles that would still be undetectable by the eye (≤ 30 μm) had the possibility of penetrating deeper. The particles tested in our study, described in **Table 2.4**, have two to thirteen times the diameter of the largest microparticles tested in the aforementioned research. Penetration data in homogeneous gel suggested that larger ballistics could realize more penetration in the cornea. The goal of our experiments was to explore a range of particle densities and a range of particle sizes characterizing particle impacts with the anterior surface. A secondary goal of this analysis was to identify conditions that allow for particle entry into the corneal stroma.

3.2 – Initial Experiments Done with Pneumatic Capillary Gun (PCG) on Corneal Tissue

After determining penetration depth statistics in agarose for 10 to 280 μm polystyrene microspheres using the PCG, experiments were done to see if these microspheres would embed in porcine corneal tissue. This testing was done by preparing lure-lock cassettes that contain a solution of 1.5% w/w 30 μm particles with 0.5% w/w 4 μm particles. Each cassette received 2.5 μL of the solution and were dried using the freeze-drying method *(Section 2.2.4)*. 4 - μm microparticles were included to mark the surface of the tissue (due to their low impact velocities from fast deceleration rates). Similar solutions were prepared with 10 and 20 μm particles. Once cassettes were prepared, porcine eyes were trimmed of surrounding fat and muscle tunic and their surfaces were dried. Particles were delivered to the anterior surface of the tissue using an acceleration pressure of 4 bar and an injection pressure of 4.5 bar in Alex Groissman's capillary device (see **Figure2.3** for gas labelling). To image particles in tissue, transmission microscopy and confocal microscopy were performed to illuminate fluorescent microparticles. Transmission

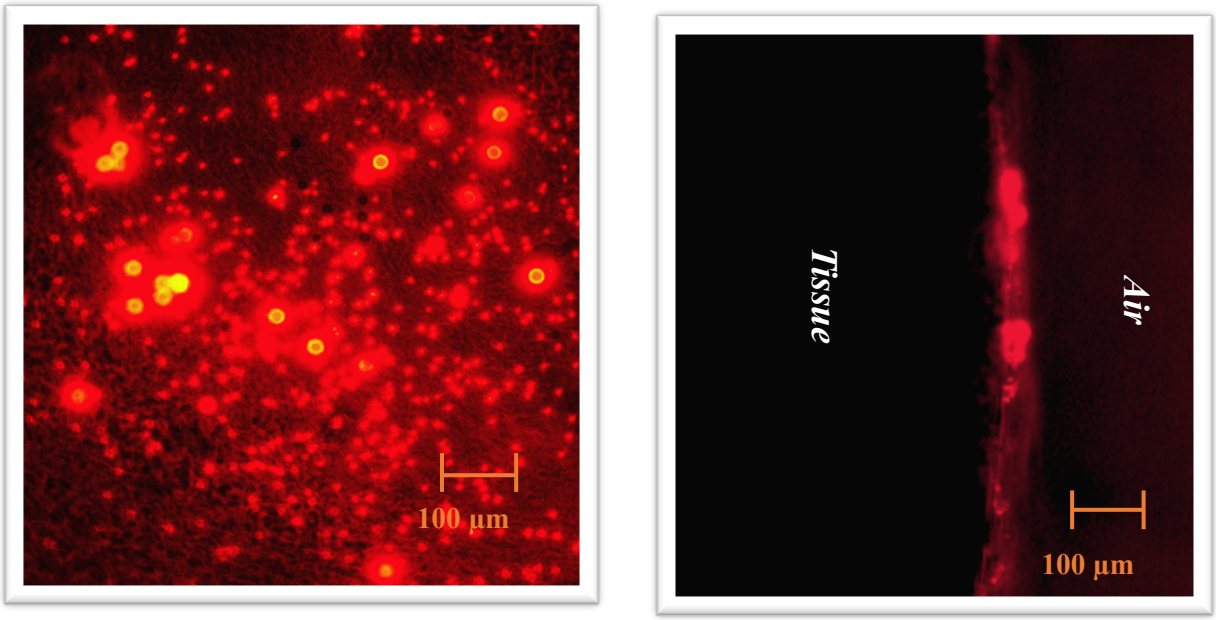

Figure 3.1 – Transmission micrographs of corneal tissue treated with 4 and 30 µm poly(styrene) spheres. Top-down view of the cornea shows all microparticles in the same plane (left). Cross-section of cornea with particles all on the surface (right).

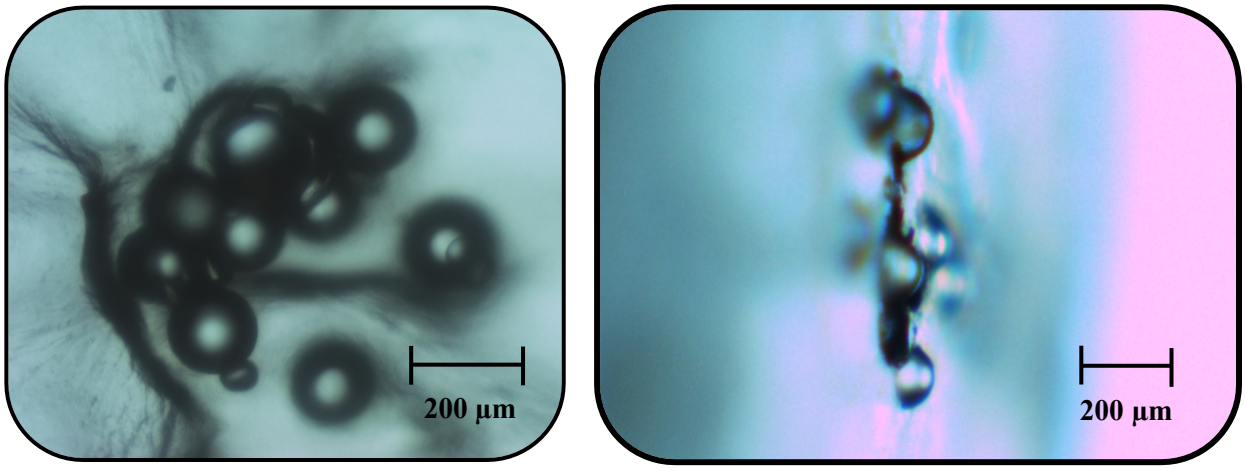

Figure 3.2 – Transmission micrographs of corneal tissue treated with 150-180 µm barium titanate spheres (4.2 g/cc). A cluster of particles indents the surface of the cornea instead of penetrating to deeper tissues (left). A group of particles has embedded by about half a diameter (right).

microscopy was performed by dissecting the cornea, placing it on a microscope slide, and tilting it to reveal the cross-section. Transmission microscopy results are shown in **Figure 3.1**. In both the top-down view of the cornea and the view of the cross-section, all microparticles appear on the anterior ocular surface in the same plane. These results indicate that the plastic spheres do not have enough kinetic energy to penetrate the surface of the cornea. **Figure 3.1** also reveals a dense network of collagen fibrils under the surface of the epithelium. This meshwork leads one to suggest that smaller microparticles may be able to get into the stroma, but these particles do not have enough energy to break through the epithelial layer. In confocal microscopy, all three particle preparations containing 10, 20, and 30 μm particles showed similar results – superficial penetration. These particle samples appeared in the same plane, just barely penetrating the surface from zero to half a diameter.

To increase the amount of kinetic energy of particles, 150-180 μm barium-titanate microspheres were delivered to the cornea. These beads, which had the ability to penetrate 1% w/v agarose gels by over two millimeters, represented the microparticle with the greatest overall kinetic embedding energy accessible with the PCG (at that time). Despite deep penetration in gel, microparticles were again found to be incapable of penetrating the cornea. Two modes of particle arrest are shown in **Figure 3.2**. Some of the microparticles were "caught" by the cornea, making an indentation on the surface of tissue. Other particles are seen embedding in the surface by as much as half a diameter. Since these particles are over three times the thickness of the epithelium, this penetration does possibly suggest penetration to the stroma. However, penetration with such large spheres in which particles may just be indenting the surface is not the kind of particle penetration sought out for (i.e. indetectable by the eye). When the PDS1000 gene

gun became available, it afforded the opportunity to test smaller, denser materials (see **Table 2.2** for reason the ballistic device is less compatible with dense particles).

3.3 – Density Ladder Study Delivering Different Microparticles to Cornea With PDS1000

3.3.1 – Methods for Measuring Penetration of Microspheres in Ex Vivo Porcine Cornea

For the following study, a new method of locating particles in tissue was needed. Since the glass and metal microparticles being used had no inherent fluorescence, the same transmission microscopy technique could not be used (tilting a cornea on a glass slide over the microscope objective and seeing where particles were by locating fluorescent regions). While confocal microscopy could have been used, it would require significant image processing and data would be confounded by the cornea's wrinkling, folding surface. As an alternative, tissue was treated with ballistic microparticles, was fixed using a paraformaldehyde solution, and then was sectioned to reveal cross-sections. This method allowed reliable measurement of penetration depths. While the microtome blade possibly moves particles, the reproducible depths observed in the research suggest that this effect was low.

To carry out experiments, porcine eyes were acquired within twelve hours of animal sacrifice (Sierra Medical Products) and were used within two hours. The eyes were stored in antibiotic media until ready for particle delivery, when the eyes were trimmed of surrounding tissue and the surface was lightly dried. Following particle delivery, porcine eyes were placed in Falcon vortex tubes filled with Davidson's Fixative Solution (DFS, as described in Shariati et al., 2008).[6] Whole eyes were allowed to be fixed for two hours so the cornea would maintain its natural shape, and then corneal tissue was dissected from intact globes, placed in DFS, and

refrigerated for 48 hours. Tissue was transferred from DFS to 10% w/w sucrose in PBS for eight hours followed by 30% w/w sucrose in PBS overnight. Fixed cornea tissue was trimmed to a 1 cm. by 1 cm. square and frozen in optimal cutting temperature (OCT) compound for 1 hour at -80 °C. Sections were prepared on a microtome in a cryostat to a thickness of 50 μm (larger than the largest particle size) and were imaged immediately to collect data on particle positioning within the tissue. To collect statistics on particle penetration into gelatin or corneal tissue, the same image processing pipeline used to analyse data from ballistic gelatin was employed to process the data from corneal tissue (pipeline described in Appendix A.1).

3.3.2 – Delivery Conditions of Different Density Microparticles to Corneal Tissue

By bombarding tissue with a set of microparticles with a broad range of densities and sizes, information about minimum kinetic embedding energies can be deduced. The following protocol for delivering microparticles to tissue was used in this study. Eyes were mounted and placed in the gene gun chamber as close as possible to the macrocarrier containment assembly. To deliver particles to tissue, 1350 PSI (91.8 bar) rupture discs were used. The gene gun bombardment chamber was evacuated to ~30 mm Hg absolute pressure. To prepare macrocarriers, the particles were placed in 96% ethanol at a concentration of 3% w/w and were vortexed immediately prior to pipetting 20 μL onto macrocarriers. Particles were allowed to dry for two-four hours before delivery to tissue. Note that experiments are analyzed one particle at a time to relate penetration depth to particle size, so the results are not affected by possible difference between the particle size distribution on the macrocarriers (suspension taken from the bottom of the test tube might be enriched in faster-settling larger particles). To quantify the impact response of the cornea to

particles, three shots of microparticles were delivered to tissue for each particle density used.

3.3.3 –Penetration of Low Density Microparticles in Corneal Tissue

Lowest-density microspheres (1.1 g/cc poly(ethylene); PE) did not penetrate the cornea deeply, but they were able to firmly embed in the apical layer of the cornea. In **Figure 2.13**, it can be seen that these projectiles only embed in 5% w/w gelatin by one to three diameters. Not surprisingly, when corneal tissue was tested with these particle payloads, penetration was superficial. **Figures 3.3A** and **3.3B** show fluorescent microparticles embedded just at the surface of tissue. While penetration was far from reaching stromal tissue, it is promising that particles can be found on tissue after three days of the tissue processing protocol. This suggests that microparticles are firmly embedded on the surface of the tissue. In addition, since the densest layer of tight protein-junctions are on the anterior surface of the cornea between stratified epithelial cells, this type of penetration may still enhance drug delivery.

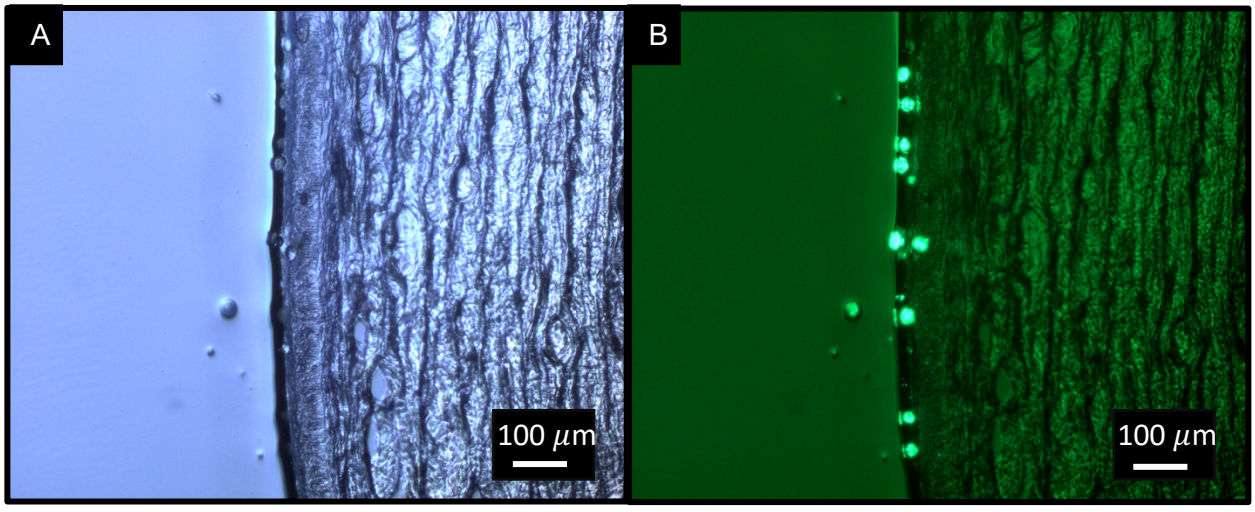

Figure 3.3 – Superficial penetration of low-density microspheres in corneal tissue . Poly(ethylene) spheres, which show low penetration in ballistic gelatin, barely penetrate corneal tissue. Fluorescent micrograph shown on the right to highlight microparticles.

3.3.3 – Resulting Penetration of 2.5 to 7.8 g/cc Microparticles in Corneal Tissue

The next particles that were tested were soda lime glass spheres (10 – 22 μm; 2.5 g/cc). These particles showed significant penetration through the corneal epithelium, and they did not penetrate any further. The penetration observed from representative micrographs shown in **Figure 3.4** indicates particles scattered throughout the epithelium. Penetration statistics for all three cornea samples treated with microparticles, shown in **Figure 3.5**, indicate similar penetration statistics from one particle delivery to another. Sample one shows only 80 particles found in the tissue (as opposed to 100 for all other samples and materials). More images were taken of the third sample to compensate. The range of particles detected by the image processing pipeline is representative of the actual range of particles reported by the vendor. Some particles are slightly larger than the expected size range, potentially due to clicking on larger diameters than actually were seen using the image processing pipeline. It is possible that deceleration of smaller particles led to a pileup at the surface of the tissue. There was a smaller quantity of particles found in the tissue sections than was seen testing higher density microspheres. It is possible that particles are embedding in the apical surface of the cornea and tissue processing is stripping particles from the surface, reducing the number of particles seen in sections. This low number of particles observation was seen with PE spheres as well.

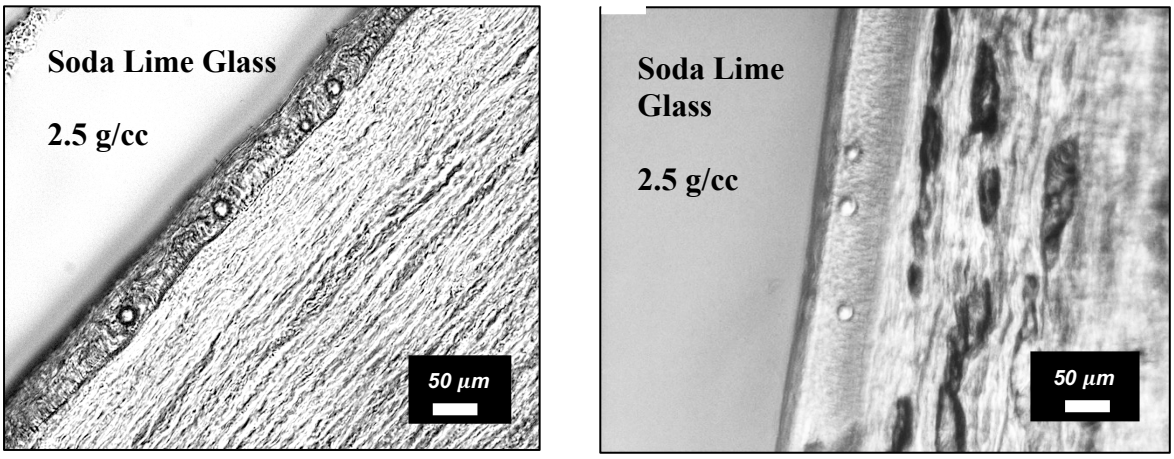

Figure 3.4 – Soda-Lime glass spheres embedded in section of corneal tissue. Tissue sections are 50 μm thick. Particles embed throughout the epithelium.

When particle density was increased, penetration depth in tissue did not significantly rise, as was expected. Barium-titanate spheres penetrated to the bottom of the corneal epithelium, but did not travel any deeper than this. While these particles were able to travel over twice the distance as soda-lime glass spheres in gelatin, **Figure 3.6** shows the particles getting stuck at the interface between the epithelial layer and stroma. What's more, stainless steel microparticles, which embedded in gelatin up to four times as much as soda-lime glass microparticles, get held back by the same interface. The full penetration statistics of the particles tested, shown in **Figure 3.7**, indicate a slight increase in penetration depth when projectile density is increased, but the penetration is similar for the three sets of particles. Data from individual deliveries of barium-titanate and steel microparticles are shown in Appendix B.3.

While embedding depth was shallow, it is interesting to note that penetration into the epithelium did not leave a visible "track." To the extent observable with optical microscopy, no evidence of

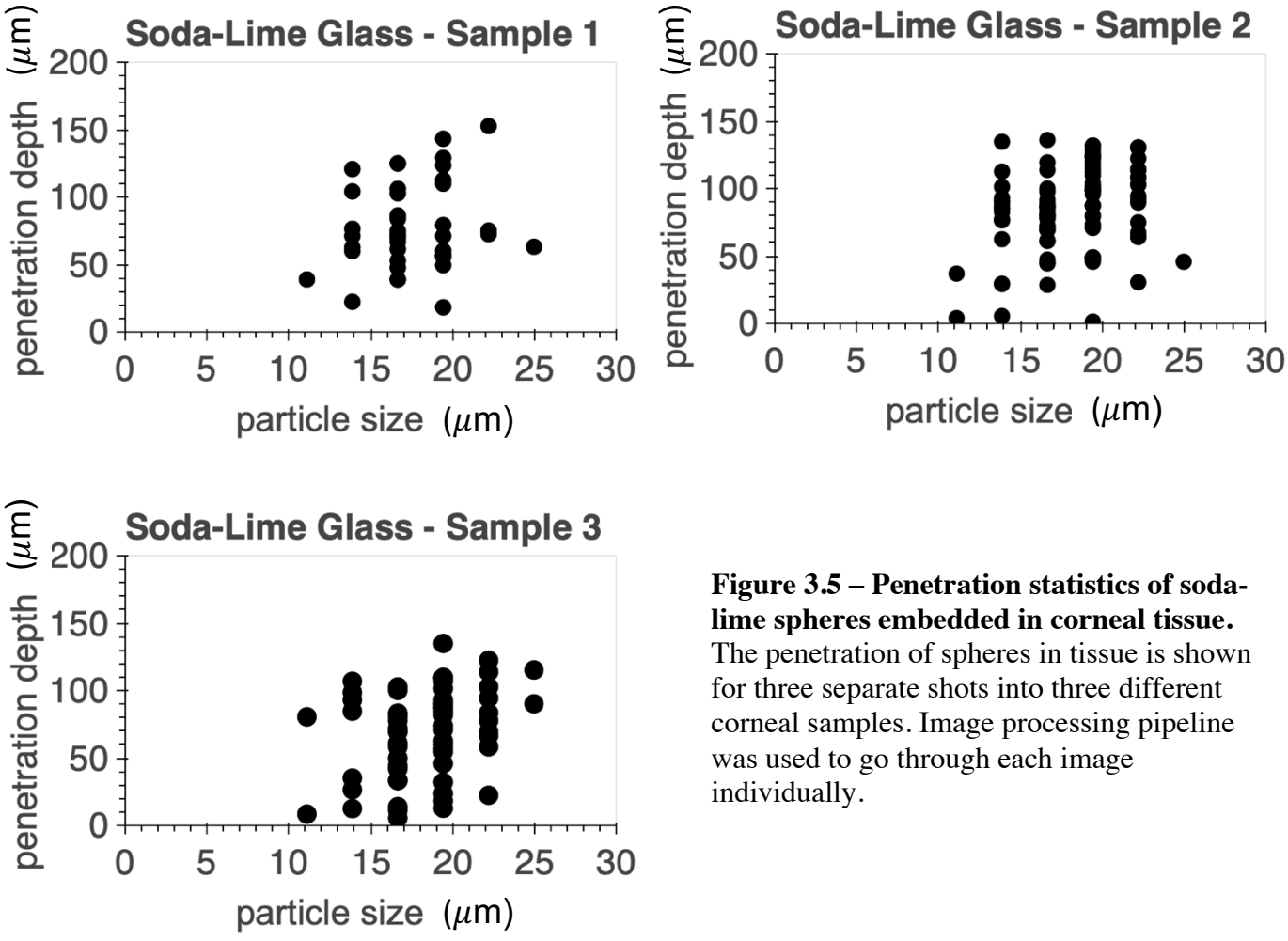

Figure 3.5 – Penetration statistics of soda-lime spheres embedded in corneal tissue. The penetration of spheres in tissue is shown for three separate shots into three different corneal samples. Image processing pipeline was used to go through each image individually.

tissue damage was seen. Confocal microscopy was done on tissue treated with stainless steel microparticles prior to staining with picosirius red (Abcam Inc.). Picosirius red is a fluorescent dye that binds strongly to collagen fibrils and is used to determine collagen type, as in Vogel et al.[7] While it was recommended that staining should be done for 1 hour, sections of tissue were stained for 5 minutes. This was sufficient to produce bright fluorescence on the stroma and the epithelium. The tissue was sectioned 30 μm thick to ensure adherence to the microscope slip during staining. When this was done, there were no observed defects in the epithelium that could have been a trail, despite there being many particles that were in the tissue (**Figure 3.8**).

There are slight variations in the thickness of the epithelium. The thickness of the epithelium was measured for 100 images of tissue sections. The mean thickness was 63.1 μm (standard dev. 9.8 μm). Despite areas where the epithelium was thinner, there is little ability for the microparticles tested to carry through the epithelium and embed into the stromal tissue of the cornea.

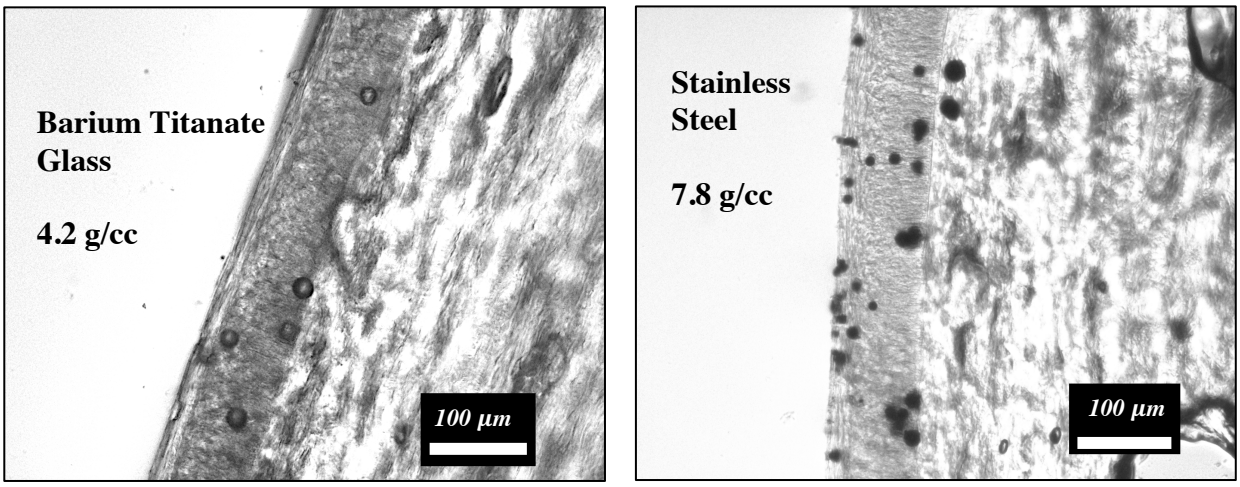

Figure 3.6 – Penetration of barium-titanate and stainless-steel microparticles in cornea. The penetration of spheres in tissue is shown in 50 μm tissue sections

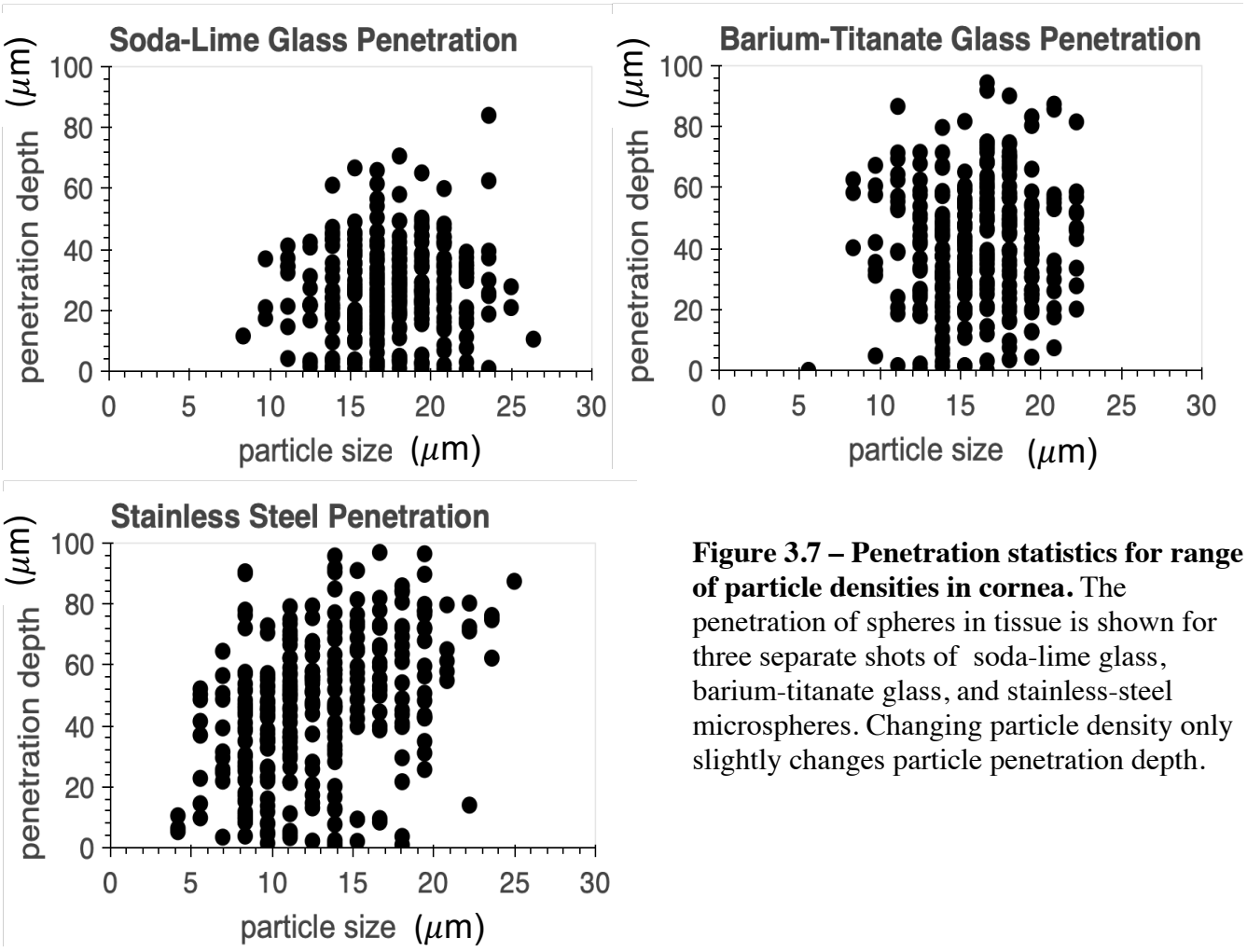

Figure 3.7 – Penetration statistics for range of particle densities in cornea. The penetration of spheres in tissue is shown for three separate shots of soda-lime glass, barium-titanate glass, and stainless-steel microspheres. Changing particle density only slightly changes particle penetration depth.

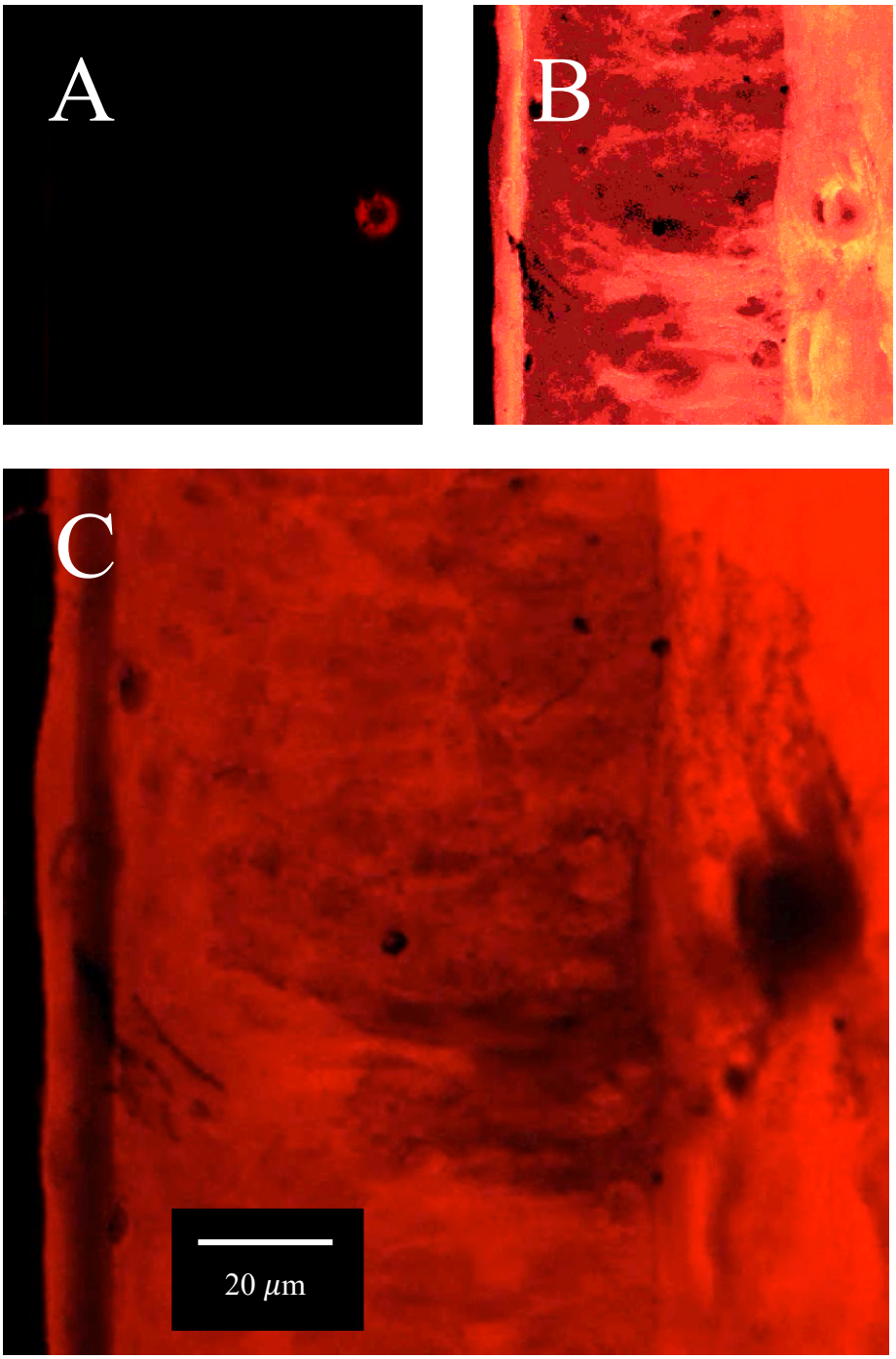

Figure 3.8 – Confocal Z-Stack showing steel particle embedded in Picosirius-Red stained corneal tissue. From A to C, depth in the z-stack is increased. The 30 μm thick section was stained for 5 minutes in Picosirius Red.

Gelatin Data:

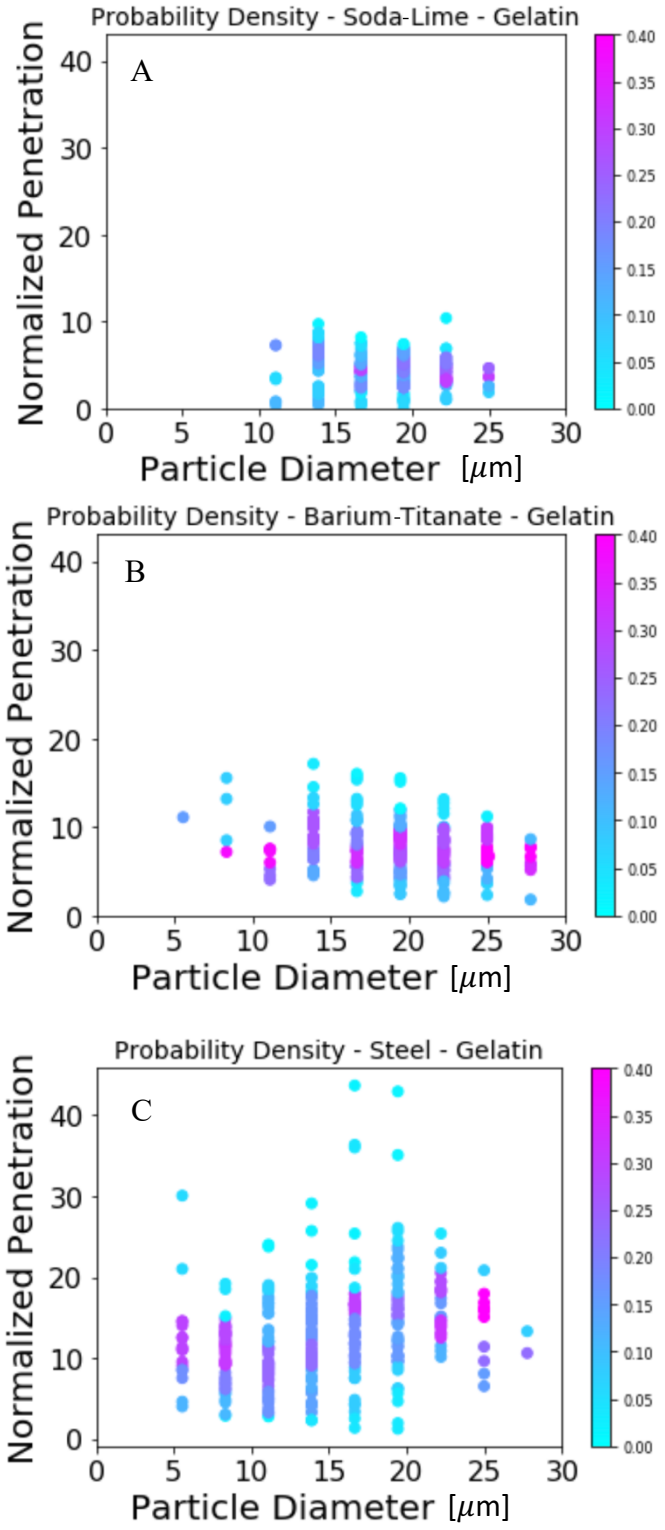

Figure 3.9 - Probability densities of range of particles in 5% w/w ballistic gelatin shown with particle penetration normalized by particle diameter. Probability density for the colormap was calculated by binning data into discreet groups along the x and y axes.

Cornea Data:

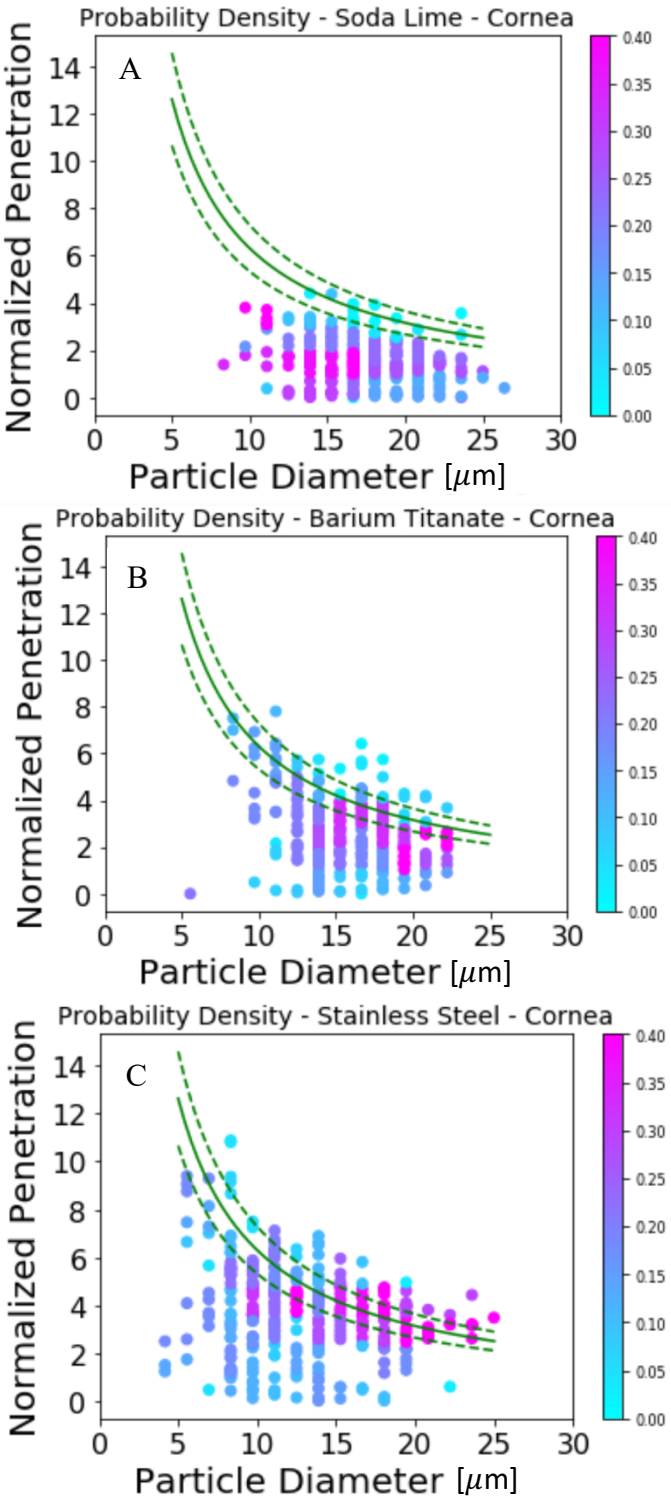

Figure 3.10 - Probability densities of range of particles in 5% w/w cornea shown with particle penetration normalized by particle diameter. The green band represents the measured average thickness of the epithelial layer bounded by a standard deviation above and below the mean value.

There is more information contained in the probability density of particle impacts (**Figures 3.9** and **3.10**). To calculate probability density, impact points are binned according to the discrete sizes shown in penetration statistics. They are binned according to their distance from the sample surface. Last, binned penetration depths are divided by the total number of observations for that particle size. Penetration depth is normalized by dividing the penetration distance by particle diameter, so the expected proportionality to particle diameter yields a constant normalized penetration depth. The probability density for the normalized penetration depth in ballistic gelatin is insensitive to particle size, as expected (**Figure 3.9**). In gelatin, increasing relative density of particles relative to the sample conforms with the expected proportional increase in normalized penetration.

In contrast, normalized penetration into the cornea is not independent of particle size and does not simply increase linearly with a particle's relative density (**Figure 3.10**). Peculiar features of the distribution of normalized penetration in the cornea include bimodal probability distributions for small, low density particles (**Figure 3.10A**, 12.5±0.7 and 14.0±0.7; for smaller particles, very few entered the epithelium and loss of particles from the surface during handling precluded quantitation). A first peak at very low penetration suggests that there is a threshold impact parameter required to pass through the apical layer of the corneal epithelium (*i.e.*, the distribution of impact parameter for small soda lime particles includes some that are so low that the particles come to rest on the epithelium). With increasing size, soda-lime particles transition to a unimodal distribution as seen in ballistic gelatin, with the most probable normalized penetration insensitive to particle size (**Figure 3.10A**, for particle diameter > 15 μm). At the opposite extreme, large, high-density particles show a penetration depth that does not increase with particle size and

normalized penetration depth actually decreases with increasing particle size (**Figure 3.10B** for particle diameter > 15 μm and **Figure 3.10C** for particle diameter > 8 μm). The peak penetration depth appears to be dictated by the thickness of the epithelium (indicated by a green band in Figure **Figure 3.10**). The limited ability of the microparticles tested to penetrate through the epithelium and embed into the stromal tissue of the cornea suggests that there is a threshold "remaining impact parameter" that must be exceeded for particles to pass through the boundary between the epithelium-stroma. In accord with this hypothesis, the distribution of penetration depths has a pronounced asymmetry, with an abrupt decrease in probability of penetration into the stroma.

When particles enter the cornea, it appears that there is a narrow range of penetration depths in which particles can embed, confined to the epithelium, for the range of impact parameter examined here. Once particles reach the epithelial-stromal boundary, their motion is essentially arrested. This behaviour accords with corneal mechanical properties in the literature. Atomic force microscopy has been applied to interrogate individual layers, leading to a Young's Modulus of 0.57 kPa for the corneal epithelium, 110 kPa for Bowman's Layer, and 33 kPa for the stroma.[8,9] While porcine corneas lack Bowman's Layer, mechanical properties within the stroma can be stiff and vary with depth. Regions where the collagen lamellae are more interwoven (the anterior stroma) are consistently found to be stiffer than the posterior cornea.[10] Such a step up in the stiffness could explain the high probability of particles halting at the boundary between the two layers. The possible role of the porcine epithelial basement membrane was considered. It was concluded that for the porcine corneas considered here it is unlikely to make a significant contribution to arresting particle penetration: it is quite thin (~100 nm thick) and is continuous with the stroma below.[11] Nonetheless, the evidence reported in this research

suggests layered heterogeneity in the mechanical properties of the tissue is what gives rise to the cornea's penetration response.

According to estimations made in Chapter 2 of this thesis, the penetration seen in gelatin indicates that impact velocities around 500 m/s can be attained with the PDS1000 gene gun. By changing particle density, our group effectively accessed a broad range of kinetic embedding energies. From the particle with the least kinetic energy (10 μm PE; 150 m/s) to the particle with the most kinetic energy (22 μm steel; 500 m/s), these experiments span almost three orders of magnitude in kinetic energy. Since this did not yield higher levels of penetration in the ex vivo model, then it is unlikely that higher velocities will yield significantly deeper penetration. Unfortunately, the cornea does an effective job of keeping particles from entering stromal tissue.

As a final test to determine minimum kinetic energy needed to break through to the stroma, penetration of tungsten microparticles with a diameter of 20 to 40 μm was investigated. Since these particles had such a high settling velocity, it was difficult to pipette mixtures of ethanol and tungsten particles. As such, tungsten was deposited dry on Kapton macrocarriers. Electrostatic forces between particles and the polymer film were enough to keep the particles in place long enough to be bombarded into tissue. The results of bombardments in corneal tissue using an 1800 PSI rupture disc were recorded. Tungsten particles embedded between 50 and 100 μm into the stroma in the two images are shown in **Figure 3.11**. As is shown, tungsten particles are firmly embedded in the tissue, with little damage or disturbance of the surrounding tissue. This data shows that in order for microparticles to traverse the epithelial layer of the cornea, they need to have exceptionally high density like tungsten.

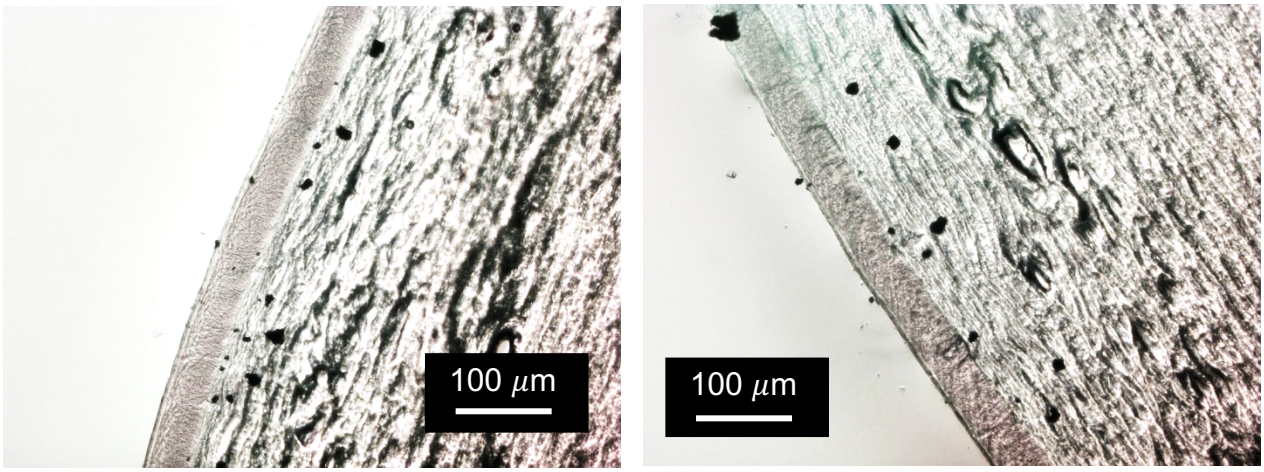

Figure 3.11 – 20 to 40 μm tungsten ballistics embedded in corneal tissue. These particles, which have 19.2 times the density of the tissue itself, are able to get all the way through the epithelium.

3.3.5 – Penetration of Microparticles in Anterior and Posterior Layers of Stromal Tissue

Tough mechanical properties of the stroma appear to be the cause of particles getting effectively stopped in corneal tissue. This would explain how small particles are able to travel freely more self-diameters in distance before getting halted at the stroma, but larger particles are halted as soon as they reach the epithelium-stroma interface. To test if the stroma was the main source of resistance to microparticle entry, corneal tissue was prepared for ballistics testing that had been debrided (epithelium removed). If particles were indeed being stopped by the thick anterior layers of the stroma, the spheres should still become arrested at superficial depth. If there is a decelerating effect of the corneal epithelium, then microparticles should travel even further without the layer of tissue intact.

The corneal epithelium can be removed by scraping the surface of the cornea with a razor blade. This was done before two preparations of particles were delivered ballistically with the PDS1000 gene gun. Soda-lime and stainless steel microparticles were prepared for the experiment. The

results of soda-lime glass spheres embedding in debrided tissue show what was expected: the particles (**Figure 3.12**) are arrested in the outermost layer of the stroma. It was also observed that fewer particles were in the cornea following the tissue processing procedures, as opposed to when the corneal epithelium is in place when particles are embedded. Perhaps this soft layer of tissue keeps particles in the sample while tissue is being fixed and protected. Only the particles that get firmly stuck in the fibers of the stroma remain when the tissue is inspected. Even when the particles are three times as dense as the stainless-steel microspheres are, **Figure 3.13** shows that microparticles are arrested in the anterior stromal surface. There are fewer microparticles embedded in the tissue than with the epithelium intact, but there are more present than with the soda-lime glass particles. It can be seen that both stainless steel microparticle sizes on the low and high end of the size spectrum show up in the images selected.

In addition to delivering microparticles to the anterior surface of the stroma, particles were also delivered to the posterior surface to assess the ability of the interface to arrest particles (**Figure 3.14**). This was done by dissecting cornea tissue from porcine eyes and using the ballistic device to treat the back surface of each sample. The endothelium is a five micron thick monolayer of cells with hexagonal packing.[12] Since it has such a low thickness, this layer's contribution to the mechanical properties relating to microparticle entry are likely small (compared to underlying posterior layers of the stroma). When posterior corneal tissue was treated with microparticles, there was a similar particle arresting response observed compared to particles embedding at the anterior surface. Particles embed in the stroma by one to two diameters, but none go deeper than this. AFM data from the literature reports that the posterior stroma has a lower Young's Modulus than the anterior stroma. Penetration observed was a bit deeper than in experiments done on the anterior stroma.

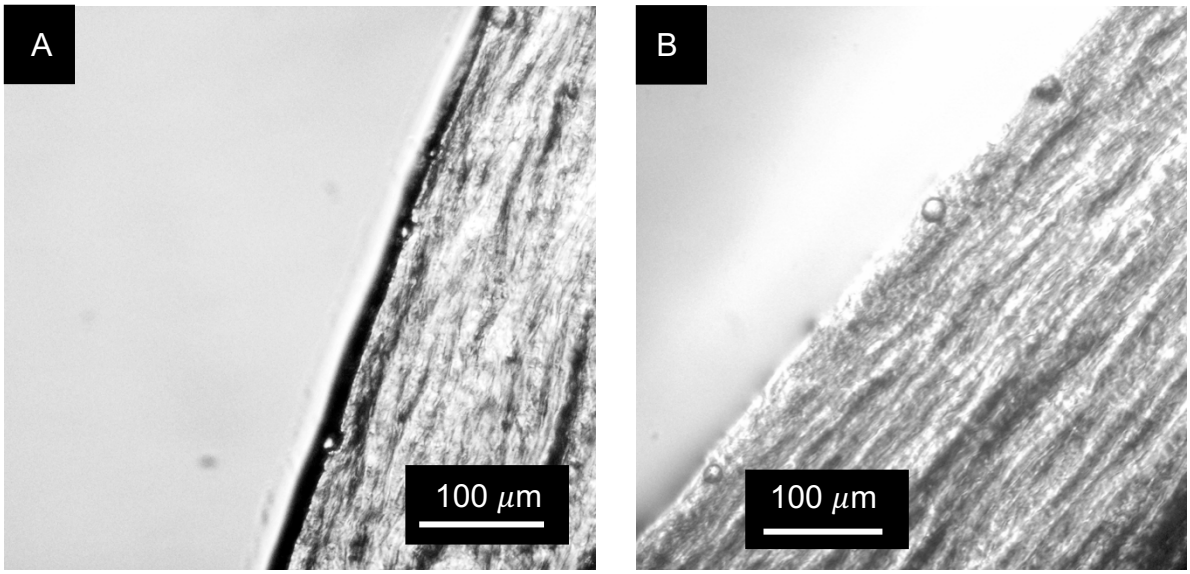

Figure 3.12 – 10-22 μm soda lime spheres embedded in debrided corneal tissue. Microparticles embed in the outermost layer of the stroma. Fewer particles found than with epithelium intact.

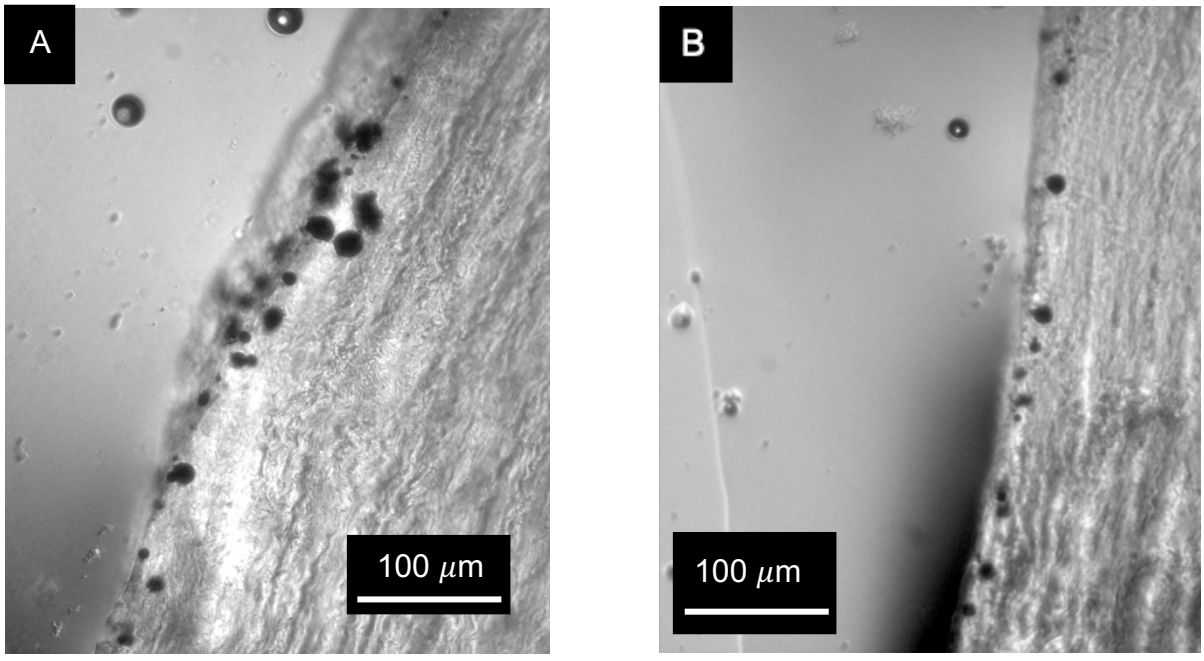

Figure 3.13 – 5-22 μm stainless steel spheres embedded in debrided corneal tissue. Microparticles embed in the outermost layer of the stroma. Particles on the large and small end of the size spectrum show up in the tissue.

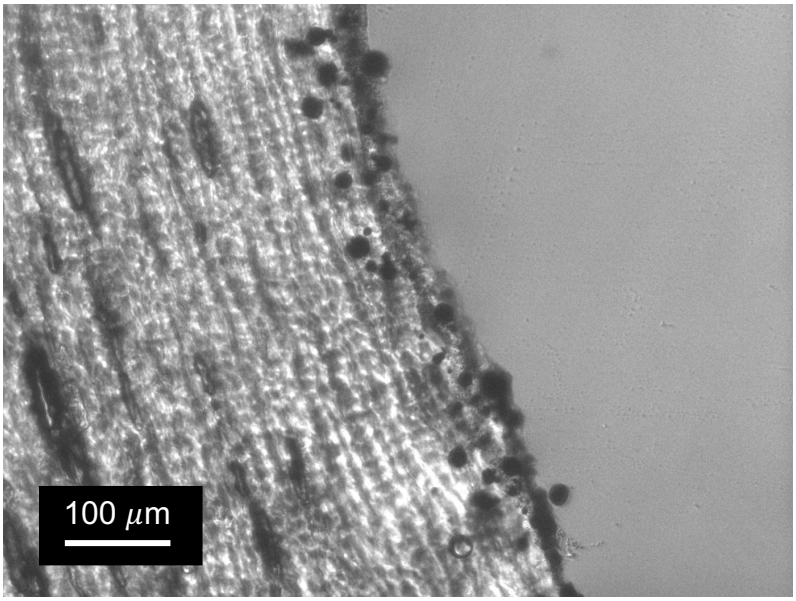

Figure 3.14 – 5 – 22 μm stainless steel spheres embedded in posterior corneal surface. Microparticles embed in the endothelium and a small distance into the underlying stroma tissue.

3.4 – Biolistic Microparticles as an Alternative to Topically Applied Ophthalmic Medicines

While it may not be possible for microparticles to traverse the cornea's epithelial layer, the technology developed in this project still has utility in the field of ophthalmology. When it comes to delivering drugs to the cornea, topically administered solutions show mass-transfer limitations. In the field of ophthalmology, this disadvantage of topically applied formulations is referred to as low ocular bioavailability. It can be attributed to numerous anatomical and physiological constraints such as tear turnover, nasolachrymal drainage, reflex blinking, and numerous static barriers (i.e. the hydrophilic corneal epithelium, tight junctions in the epithelium, and the positively charged mucin barrier). As mentioned previously, most topically administered solutions are washed away within just 15–30 s after instillation.[13]

Biolistic delivery of microparticles to the cornea has several advantages compared to standard topological solutions. First, therapeutic microparticles can be delivered to the surface of the cornea in a uniform, quantifiable layer that will not be redistributed due to gravity and the geometry of the anterior ocular surface. This could lead to much more even distribution of therapeutic compounds, which can be beneficial for treatments like corneal cross-linking surgery in which cross-linking density is affected by spatial distribution. Second, the use of ballistic microparticles likely allows for instantaneous traversal of the eye's mucin coat. This barrier can lead to rejection of many negatively charged molecules. Last, embedding a microparticle in corneal tissue allows for bioavailability of compounds for a long duration of time. Many eye-drop formulations in use today contain viscosity boosting additives to increase the exposure time of drug-material. If particles are embedded in tissue, fixing them in place, they can dissolve over a period of several hours, leading to more effective uptake of medicine. While the idea of traversing the corneal epithelium with ballistic microparticles may never be fully realized, ballistic microparticles could still be an appealing mode of corneal drug delivery. With this in mind, research was done to demonstrate the concept of ballistically applied medicine compounds. It was shown that particles could be delivered uniformly, that they would be firmly embedded in tissue, and that they would dissolve over time - leading to effective uptake of the drug.

3. 5 – Delivery of Therapeutic Payloads to Porcine Corneal Tissue

Therapeutic poly(ethylene glycol)/Eosin Y microparticles (prepared in Chapter 4 using a vibrating orifice aerosol generator and a temperature controlled column) were used as ballistic payloads in experiments with corneal tissue. The aim of this experiment was to determine ultimate penetration depth of Eosin Y and to see if microparticles could be used to uniformly distribute the therapeutic compound. To do these experiments, dry microparticles (1% Eosin Y; diameter ~ 30 to 50 μm) were deposited onto macrocarriers. Dry microparticles were used because if the particles were exposed to water or ethanol (like in the usual macrocarrier preparation procedure), they would rapidly dissolve. Using a 1350 PSI rupture disc (93 bar), microparticles were delivered to intact porcine eyes. 10 minutes after particle delivery, particles like those shown in **Figure 3.15A** and **B** are embedded in the anterior surface of the cornea. As can be seen in these brightfield and fluorescent micrographs, the particles appear uniformly distributed across the surface of the cornea. It is hard to tell if microparticles are embedded firmly in the tissue from images shown, but underneath the microscope, when tissue was slid along the surface of the petri dish it was being imaged on, particles remained in place on the tissue surface. These images were taken 10 minutes after ballistic delivery, and it can be seen that microparticles are dissolving into the surrounding tissue. Thirty minutes after particle delivery, confocal microscopy was done on the tissue. By measuring a stack of images along the z-axis of the tissue, it was determined that the Eosin dye only penetrated tissue as deep as 50 μm. A confocal image of the dye fluorescence, like that shown in **Figure 3.16**, reveals staining from Eosin Y around microparticles. Following the tissue fixation protocol (two days later), **Figures 3.17A** and **B** show the staining of the epithelium with Eosin Y. While more images of the tissue closer to the time of delivery were not acquired, microparticles appear to have fully dissolved

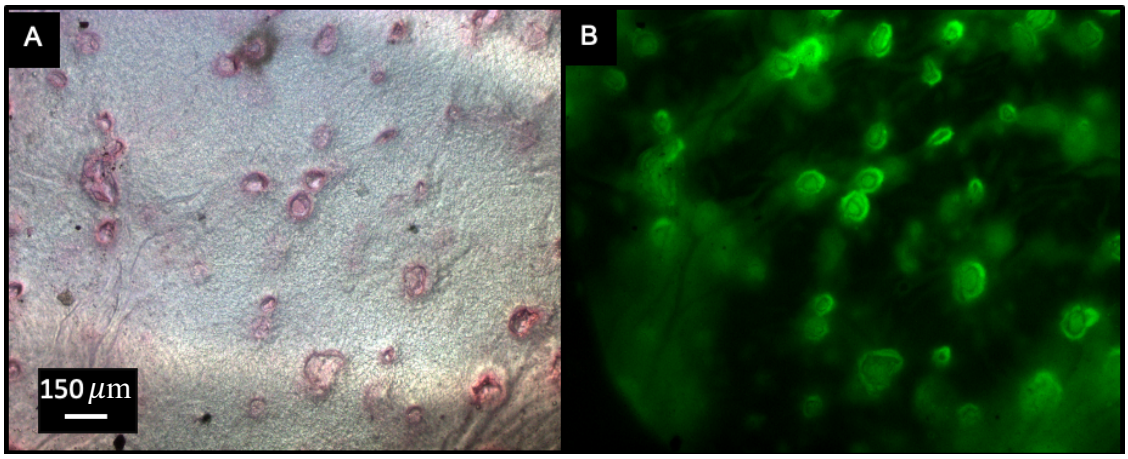

Fig. 3.15 PEG Particles with 1% w/w Eosin Y embedded in corneal tissue (transmission microscopy; 10 minutes after particle delivery). Polyethylene glycol microspheres with 1 w% EY embedded in corneal tissue. A) Brightfield microscopy showing the anterior surface of the cornea. B) Fluorescent excitation of anterior surface under 500 nm light excitation.

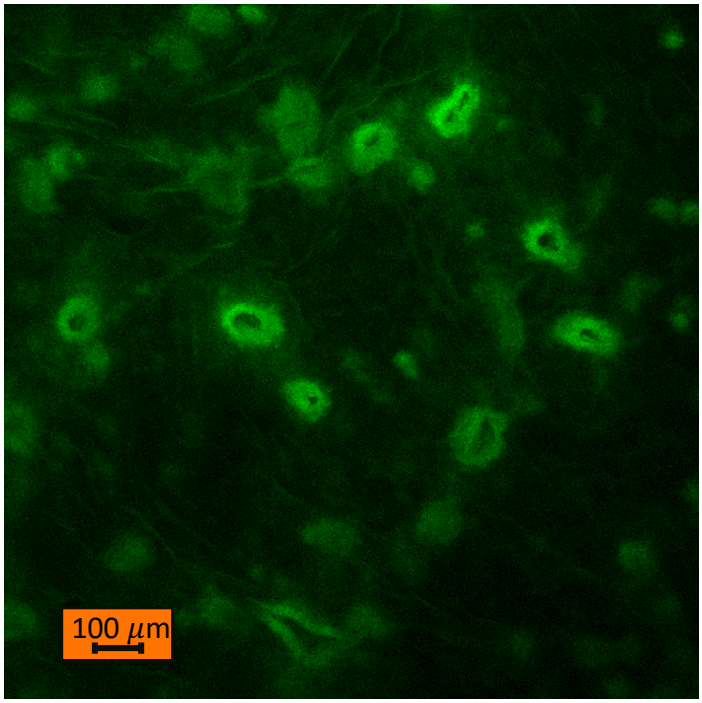

Fig. 3.16 PEG Particles with 1% w/w Eosin Y embedded in corneal tissue confocal microscopy 30 minutes after particle delivery (confocal microscopy; 30 minutes after particle delivery). Eosin Y is diffusing from microparticles into the surrounding tissue.

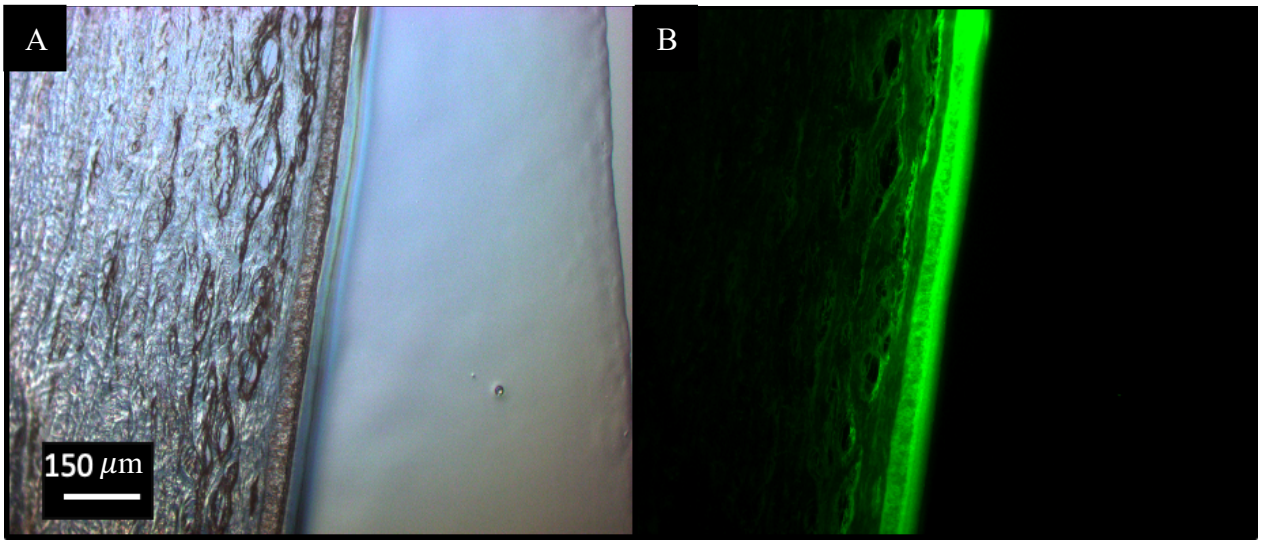

Fig. 3.17 Representative stained epithelial tissue from 1% EY microparticle delivery (transmission microscopy; 2 days after particle delivery). Eosin Y was effectively distributed throughout the cornea. The staining of the underlying stromal tissue was low.

while being exposed to fixative solutions. Solid microparticles could not be found and there was a strong staining of the corneal epithelium with the fluorescent Eosin dye. As can be seen in the images, staining of the underlying stroma was minimal. There was some evidence of stromal staining. There is impetus to more closely measure the dissolution of these microparticles.

The delivery of PEG microparticles with Eosin Y staining opens up potentially fruitful investigations for the future. While microparticles were not found in tissue after the tissue fixation protocol, the sections of corneal tissue were brightly stained (on the epithelium). Clearly, there was effective transfer of the therapeutic compound. If this drug-delivery strategy can solve the problem of low bioavailability of topically delivered solutions, it is worth more closely investigating particle dissolution in corneal tissue. Experiments were initiated to observe the effects of Eosin Y concentration on microparticle delivery to the tissue, but 10% w/w Eosin Y

had difficulties getting fully dry in the temperature-controlled column, possibly due to crystallization of the dye which appeared in dark rings on the particle's surfaces (discussed in Chapter 4). Another interesting study would be to look at microparticle dissolution efficiency over time. The eye could slowly be exposed to drops of hydrating solution to simulate physiological conditions, and the time it takes for particles of different size to be fully dissolved could be studied. This work could also be expanded to involve investigating PEG particles made with different compositions (e.g. polymers of different molecular weight). Unfortunately, microparticle preparation was a difficult process. Long times for the column to heat up, problems with condensation in particle collection chambers, and frequent obstructions of pinholes made the materials that can be accessed for these experiments difficult to produce quickly enough.

3.6 – Conclusions

In this research, it was shown that the corneal stroma has considerable stopping power when it comes to ballistic microparticles. Research on the *ex vivo* model began with using the pneumatic capillary gun to deliver microparticles to the surface of the cornea. Microparticles were only able to embed to superficial depths with this device. With the PDS1000, it was possible to more fully map out penetration mechanics in the cornea. The dramatic difference in penetration distribution seen in corneal tissue compared to gelatin provides clear evidence of enhanced barrier function at the anterior surface of the corneal epithelium and especially at the interface between the epithelium and the stroma. Using a ladder of particle densities expanded the range of impact parameters to span from values low enough that a significant fraction of particles halt at the anterior surface up to values that result in a majority of particles penetrating entirely through the epithelium and coming to a halt at or near the interface between the cornea and the stroma. By

delivering microparticles to surfaces of debrided corneal tissue and by plotting the probability density of microparticle impacts, it was suggested that the cornea has multiple kinetic energy thresholds necessary to embed in tissue: 1) to get through the apical epithelial surface and 2) to get through the interface between the epithelium and the stroma.

While this study did not uncover facile uptake of microparticles in the stroma, useful information was uncovered about just how well the cornea is protected from high velocity microparticles. This material responds as well, if not better, than skin tissue as a stopping medium.[14] Toughness demonstrated by this tissue is even more surprising, considering the cornea has a higher water constant than skin tissue. The cornea has a reported water content of 76% by mass, much higher than the exposed surface of the skin's stratum corneum, which contains 40% water at the surface and increases to 70% water by the stratum granulosum.[15,16]

The penetration measured in our tissue model was lower than desired, but the therapeutic microballistics developed in our research proved to be able to decorate the surface of the cornea uniformly. When these particles were delivered to tissue, it was shown that they could rapidly and quantifiably embed in the cornea. It is hypothesized that delivering these discrete particles can provide a potential solution for the problem of low bioavailability of topically administered compounds. Over a period of two days, the particles dissolved to stain the tissue with the dissolved Eosin Y payload. While Eosin Y is a hydrophilic compound and the epithelium is a hydrophobic cell layer, the instantaneous delivery of microparticles was able to stain the epithelial tissue effectively. Now that delivery of therapeutic microparticles to corneal tissue has

been achieved using the PDS1000, it is a next logical step to find ways to deliver particles to corneal tissue effectively with samples under ambient pressure.

3.7 – References

1. Lu, W. N. *et al*. Gene transfer into corneal endothelial cells by Helios gene gun. *Nihon. Ganka Gakkai Zasshi* **107**, 189–195 (2003).
2. Tanelian, D. L., Barry, M. A., Johnston, S. A., Le, T. & Smith, G. Controlled gene gun delivery and expression of DNA within the cornea. *Biotechniques* **23**, 484–488 (1997).
3. Bauer, D. *et al*. Immunomodulation by topical particle-mediated administration of cytokine plasmid DNA suppresses herpetic stromal keratitis without impairment of antiviral defense. *Graefe's Arch. Clin. Exp. Ophthalmol.* **244**, 216–225 (2006).
4. Merediz, S. A. K., Zhang, E. P., Wittig, B. & Hoffmann, F. Ballistic transfer of minimalistic immunologically defined expression constructs for IL4 and CTLA4 into the corneal epithelium in mice after orthotopic corneal allograft transplantation. *Graefe's Arch. Clin. Exp. Ophthalmol.* **238**, 701–707 (2000).
5. Zhang, E. P. *et al*. Minimizing side effects of ballistic gene transfer into the murine corneal epithelium. *Graefe's Arch. Clin. Exp. Ophthalmol.* **240**, 114–119 (2002).
6. Shariati, A., Ameri, H. ., Hinton, D. . & Humayun, M. The effects of davidson's fixative solution in preserving the rabbit eye. *Investig. Opthalmology Vis. Sci.* **49**, (2008).
7. Vogel, B., Siebert, H., Hofmann, U. & Frantz, S. Determination of collagen content within picrosirius red stained paraffin-embedded tissue sections using fluorescence microscopy. *MethodsX* **2**, 124–134 (2015).
8. Last, J. A., Thomasy, S. M., Croasdale, C. R., Russell, P. & Murphy, C. J. Compliance profile of the human cornea as measured by atomic force microscopy. *Micron* **43**, 1293–1298 (2012).
9. Thomasy, S., Raghunathan, V. & Winkler, M. Elastic modulus and collagen organization of the rabbit cornea: epithelium to endothelium. *Acta Biomater.* **10**, 785–91 (2014).
10. Blackburn, B. J., Jenkins, M. W., Rollins, A. M. & Dupps, W. J. A review of structural and biomechanical changes in the cornea in aging, disease, and photochemical crosslinking. *Front. Bioeng. Biotechnol.* **7**, (2019).
11. Abhari, S. *et al*. Anatomic studies of the miniature swine cornea. *Anat. Rec.* **301**, 1955–1967 (2018).
12. Sridhar, M. Anatomy of cornea and ocular surface. *Indian J. Opthalmology* **66**, 190–94

(2018).

13. Ahmed, I. The noncorneal route in ocular drug delivery. In *Ophthalmic drug delivery systems* 335–63 (2003).
14. Kendall, M., Mitchell, T. & Wrighton-Smith, P. Intradermal ballistic delivery of micro-particles into excised human skin for pharmaceutical applications. *J. Biomech.* **37**, 1733–1741 (2004).
15. Taylor, Z., Garritano, J., Sung, S. & Bajwa, N. THz and mm-wave sensing of corneal tissue water content: electromagnetic modeling and analysis. *IEEE Trans Terahertz Sci Technol.* **5**, 170–183 (2015).
16. Warner, R., Myers, M. & Taylor, D. Electron probe analysis of human skin: Determination of the water contration profile. *J. Invest. Dermatol.* **90**, 218–224 (1988).

Chapter 4

VIBRATING ORIFICE GENERATOR RESEARCH AND THERAPEUTIC MICROPARTICLE PRODUCTION

4.1 Background on the VOAG and Plan to Produce Solid Microparticles

Vibrating orifice aerosol generators (VOAGs) are devices which create monodisperse droplets. They use pressure pulses from a piezoelectric element to modulate the size of droplets formed during the breakup of a liquid capillary jet.[1] VOAGs have previously been used to generate droplets with a range of compositions, from aqueous salt solutions and organic mixtures for the study of aerosol thermodynamics, to the production of uniform glassy-carbon spheres containing dispersed carbon-black nanoparticles for the study of char oxidation in coal combustion.[2–4] In the latter application, a heated column was used to produce solid microparticles. In Alemrayat et al., a VOAG was used for the preparation of monodisperse drug particles.[5] Spheres of poly(caprolactone) and poly(lactic acid) were prepared to carry the breast cancer drug letrozole. Instead of using a drying column, polymers and drug were dissolved in dichloromethane (DCM) and were sprayed into an aqueous solution of 0.5-1.0% w/w poly(vinyl alcohol). Following evaporation of DCM, stable, solid microspheres were formed.

The goal of our research was to use a VOAG to prepare solid microparticles containing a base polymer and Eosin Y as the active photosensitizing agent. The calculations for numbers of particles needed are based on Joyce Huynh's work cross-linking the ocular coat. In her research, sufficient cross-linking of the cornea was achieved by dissolving 8 mg/mm^2 of Eosin Y and then

exposing tissue to 15 minutes of green light (523 nm; 6 mW/cm^2).[6] **Table 4.1** shows required particle payloads for pure Eosin Y microparticles based on Dr. Huynh's work.

Table 4.1 – Required solid Eosin Y particles needed for effective CXL therapy

Eosin Y Particle Diameter	**# Particles Required Per mm^2**
6 μm	7300
10 μm	1600
15 μm	470
20 μm	200
30 μm	60

With these statistics in mind, 30 μm particles were targeted as a desired drug-delivery particle size (diameter). 1) This is around the size of the smallest detectable object by the human eye (.03 mm) [7], 2) a low number of these particles would need to be delivered to the cornea (roughly 6000 per cm^2 of the cornea), and 3) 30 μm particles have a long aerodynamic relaxation time needed to keep their velocity in ballistics experiments done at ambient pressure (τ = 2.8 msec).

4.1.1 – Theory Behind Operation of the VOAG

The initial goal of this project was to make solid microparticles in a hot column by drying droplets emitted from the VOAG. Before attempting to make solid particles, a characterization of solution flowrates for different operating conditions was required in order to avoid excess

solvent evaporation. Flow through a pinhole is typically normalized from orifice to orifice using Bernoulli's Equation with a discharge coefficient C_D introduced to account for resistance to flow:

$$\dot{m} = C_D A_o \sqrt{2\rho_l \Delta P} \tag{1}$$

where $\dot{m}$ is the mass flowrate, A_o is the area of the orifice, ρ_l is the density of the atomized fluid, and ΔP is the pressure drop experienced as fluid traverses the outlet. At low pressure drops, liquid pools on the outside of the orifice, but at high enough pressures, liquid-capillary jets are formed. As such, minimum fluid velocity (v_{min}) at which a jet can be formed has been tabulated. Lindblad and Schneider found that v_{min} scales inversely with jet diameter D_j, density ρ, and the liquid's surface tension in ambient air σ.[8] They reported the following:

$$v_{min} = \sqrt{\frac{8\sigma}{\rho_l D_j}}\,. \tag{2}$$

In combination with Equation 1 and suitable data on C_D, this expression is helpful in determining minimum jet discharge pressures of low viscosity fluids. When predicting excitation frequencies that lead to controlled capillary-jet breakup, disturbance wavelength λ is a frequently used parameter. It is defined as:

$$\lambda = \frac{v_{jet}}{f} \tag{3}$$

where v_{jet} is the velocity of the capillary jet and f is the frequency of piezoelectric excitation. Schneider and Hendricks found that the range of disturbance wavelengths that lead to monodisperse droplet breakup of a jet of water is given by the following relation:[9]

$$3D_j \leq \lambda \leq 7D_j\,. \tag{4}$$

The droplet size for a given frequency is given by the following mass conservation equation

$$D_d = \sqrt[3]{\frac{6Q}{\pi f}}\,. \tag{5}$$

4.1.2 – Reasoning for Testing Viscosity Compatibility with the VOAG

There is impetus to study making aerosols using viscous liquids. Information gathered in this research has informed our aerosolization of drug and excipient solutions. This work could also enable the use of tools frequently used on aerosols, like scattering-based techniques, for the study of polymeric liquids. Options available for aerosolization of polymer solutions, including electrospray and hydraulic atomization, typically do not have the sensitivity to create monodisperse droplet streams. Certain techniques, like measurement of Mie-Scattering patterns, benefit from having monodisperse droplet size. Unfortunately, little work has been done to interrogate performance of the VOAG with high-viscosity solutions. The functional range of viscosities compatible with the VOAG is unknown and it is also uncertain how viscosity affects droplet-size distributions.

There is evidence in literature that suggests that even moderate viscosities can present considerable challenges to working with the VOAG. Aerosolizers which use single-phase flow require exceedingly high pressures when ejecting fluids with a viscosity between 50 and 100 centipoise [cP]. Leahy and Kimmel used 204 bar to aerosolize oil with viscosity of 83 cP using a 203-μm-diameter nozzle.[10] Wolf developed an aerosol generator which successfully atomized fluids with viscosities in the 60-75 cP range, using pressures between 6 and 20 bar.[11]

The disintegration of a liquid-capillary jet from a VOAG for a given fluid is unpredictable and the effect of viscosity on droplet-size distribution is poorly understood.[12] Sutherland found that there was little effect of viscosity on droplet-size when using a hydraulic atomizer.[13] On the other hand, Broniarz found that the aerosol size-distribution increased significantly when

atomizing emulsions of high viscosity (Sauter Mean Diameter for oil-water emulsion a factor of 1.5 greater than water alone).[14] Surface-tension has received more research interest for its effects on capillary-jet breakup, but viscosity also appears to be a major player in droplet breakup dynamics. Brenn and Lackermeyer found that droplet size was a function of the ratio of Weber to Reynold's numbers, but only looked at viscosities from 1 to 3 cP.[15] In order to make more fluids compatible with the VOAG, research was done to see which viscosities could be aerosolized and how droplet-size is affected by solution viscosity.

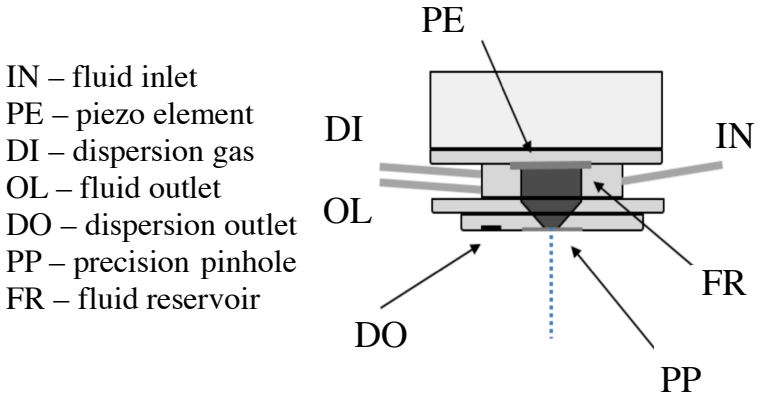

Figure 4.1 - Schematic of custom VOAG. The device has an inlet, an outlet, and a conduit for dispersion gas. The precision pinhole which forms the outlet of the device and the piezoelectric element are both interchangeable. Cartoon prepared by Isabella Pestana.

4.2 Materials and Methods for Aerosol Measurements

4.2.1 – Monodisperse Aerosol Generator

Figure 4.1 shows a schematic of the vibrating orifice generator used in this study. The orifice is made of a precision pinhole laser-drilled into a thin foil disc (Edmund Optics). It is an element that can be interchanged when a different outlet size is required or when the orifice has become obstructed. The piezoelectric element is a 2.5-cm-diameter disc punched out of 75-μm-thick steel shim stock fixed to a piezoelectric ceramic (7x8 mm; Stem Inc.) using silver epoxy. When initiating a jet, the tubing which carries fluid away from the device is capped, introducing a step

change in pressure. The piezoelectric ceramic is controlled using a function generator (Agilent 33220a) with sinusoidal waveforms oscillating between positive and negative five volts. There is an input for compressed air on the device that disperses microparticles ejected into the particle drying column.

4.2.2 - Oscillatory Shear Rheology

To measure the viscosity of PEG solutions, a strain-controlled oscillatory shear rheometer was used (ARES 4100). An 80 mm cone-shaped geometry (4° degree cone angle) was used with a 50 μm gap. Samples were tested on the rheometer with low strain rates compared to particle impacts (from 1 to 100 1/s) and n = 5 measurements were recorded per solution.

4.2.3 - Aerosol Flowrate Measurement

To measure the flowrate of fluid ejected from orifice pinholes, liquid was collected in 1.5 mL conical microcentrifuge tubes for thirty seconds. At the end of collection times, the mass ejected from the pinhole was measured. Using the diameter of the pinhole, the velocity of incompressible fluid exiting the orifice was calculated. Measurements were recorded six times for each viscosity of fluid tested.

4.2.4 – Custom High-Speed Imaging System

When imaging aerosols, the set-up shown in **Figure 4.2** was used to record images of shadows cast by moving droplets. The VOAG was mounted on top of a hollow poly(ethylene) cylinder. Aerosols were illuminated with either a continuous lamp or a bright pulsed-LED (VLP-4830-2S;

VAL Electronics). The former was used to measure broad polydisperse size distributions. The pulsed-LED was used to visualize monodisperse size distributions when more resolution was desired. Aerosols were imaged three centimeters from the outlet of the VOAG. A Chronos 2.1-HD high speed camera (Krontech) was used for these studies. It was run at 1024 frames per second to maximize camera resolution (1.3 megapixels). There were two separate microscope objectives used in this study, 2X and 10X magnification lenses (Mitutoyo). The lenses have a 33.5 mm working distance. The 2X objective was used to measure aerosols not being exposed to piezoelectric agitation (with the continuous light source and a 1 μsec exposure time). The 10X objective was used for monodisperse aerosols (with the pulsed light source). The LED flashes for a duration of 10 μsec at the start of every ten milliseconds.

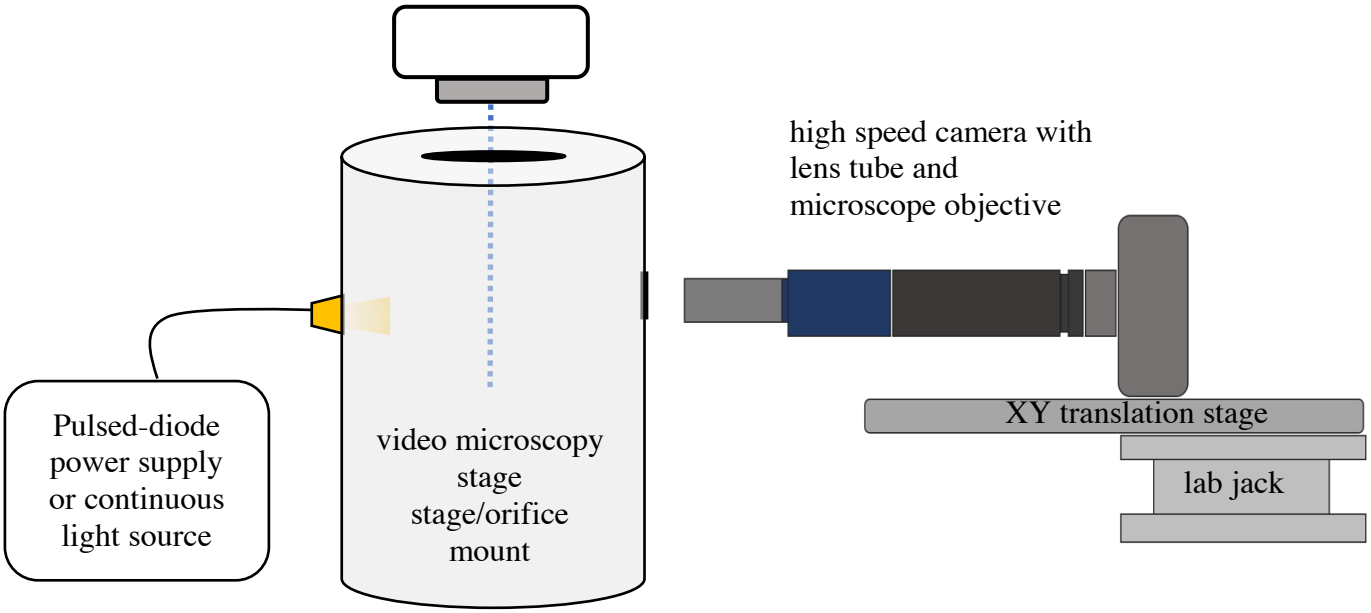

Figure 4.2 – High-speed imaging system for droplet train emission. The VOAG is mounted on a cylinder of polyethylene, which has been hollowed out. The block has a window for the high-speed camera and a pocket to mount a light source. The light can be continuous or a pulsed-LED that fires with 10 µsec pulse-time. The camera used is mounted on a lab-jack with XYZ-position control.

4.2.5 - Image Processing Pipeline

To record droplet size distributions from high-speed video, an image processing pipeline was written in Python (Appendix A.2). Binary images were generated that turned camera frames into 2D plots that show information describing what pixels contain outlines of droplets. Since droplet data often had different degrees of background lighting, threshold pixel values were chosen on a video-by-video basis. Threshold values were increased until droplet objects no longer increased in size. Once masks were generated from image data, regionprops, an open-source Python function, was used to locate objects and record their major and minor axis dimensions. The major axis was indicated by where the droplet was at its widest and the minor axis was where it was the smallest. Droplet diameters (major axes) were recorded if major:minor axis ratios were less than 1.3 and droplets were not connected. These criteria were included to reject droplets that had not yet relaxed after breaking up from the capillary jet, to reject droplets that had not yet broken up, and to reject droplets colliding. Data from individual frames were saved and plotted. Droplet size-distributions of polydisperse aerosol trains were reduced to whisker plots using bokeh, another open-source Python package.

4. 3 High-Viscosity Aerosolization Study

4.3.1 - Flowrate Characterization

The results of flow characterization studies are shown in **Figure 4.3** and the viscosities measured for solutions tested in this study are shown in **Figure 4.4**. Solution viscosity follows the following power law expression, where c is the weight fraction of PEG in solution.

(6)

$$\mu = 1955.2c^3 - 368.7c^2 + 61.0c + 0.3 .$$

The power law expression is plotted along with viscosity data in Appendix C.2. 50 and 75 μm pinholes were used to aerosolize solutions that have viscosities from 1 to 40 centipoise.

The data for the 50 μm pinhole shows that when solution viscosity reaches 20 cP, the lowest aerosolization pressure tested increases slightly from 5 to 7.5 PSI. This is because, at 5 PSI, the aerosol could not be initiated and maintained for more than a few seconds. When testing 30% PEG, the minimum pressure tested increases further to 10 PSI. This behavior suggests that a minimum pressure isneeded for aerosol formation. **Figure 4.3** also plots the ejection velocity.

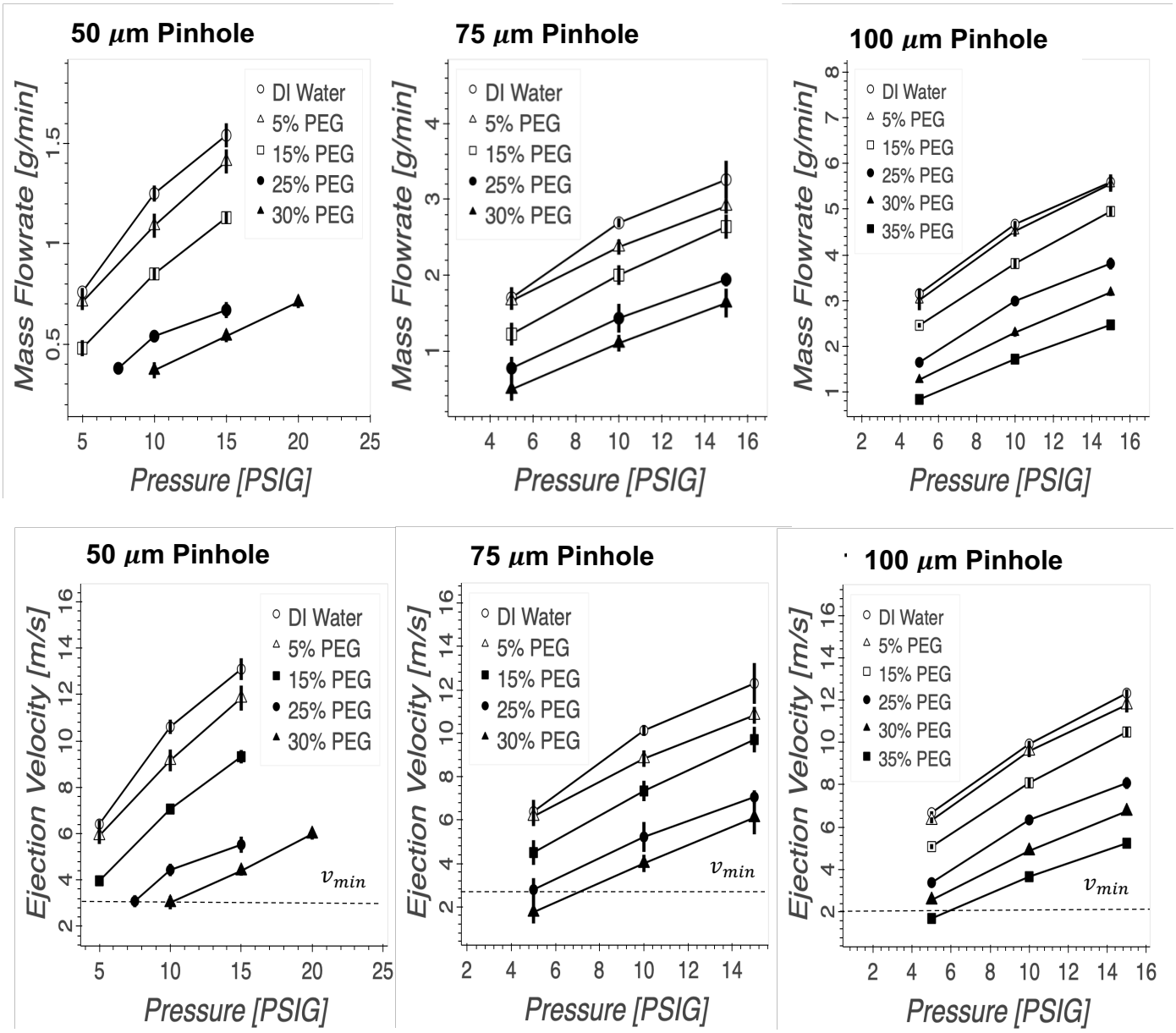

Figure 4.3 – Mass flowrate and ejection velocity for different pinholes with PEG solutions of different concentration. The mass flow rate (top) and ejection velocity (bottom) for three pinholes is plotted for a set of different PEG solutions. N = 6 measurements. Error bars show 95% confidence intervals. Dotted lines show v_{min}, predicted by Equation 2.

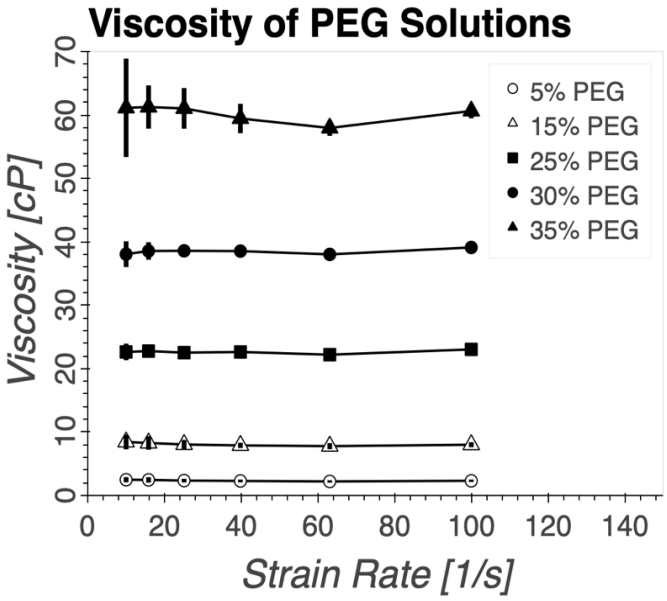

Figure 4.4 – Oscillatory shear rheology of PEG solutions. Strain sweeps for five different PEG solutions from 10 to 100 1/s. Each point is from n = 5 tests. Error bars show 95% confidence intervals.

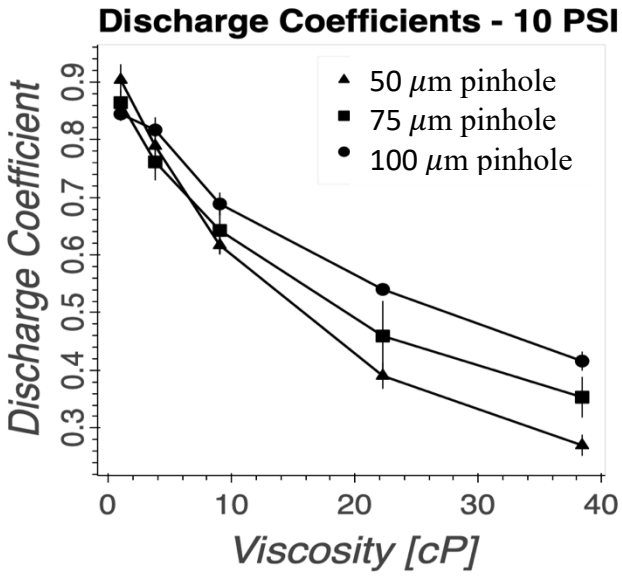

Figure 4.5 – Discharge coefficient as a function of viscosity. At 10 PSI, the discharge coefficient of each pinhole is recorded. N = 6 samples per data point. Error bars show 95% confidence intervals.

Ejection velocity for a given pressure is similar between pinholes. Dotted lines indicate the theoretical minimum jet velocity predicted by Equation 2. The theoretical minimum ejection velocity was predicted accurately for the 50 μm pinhole, but jet velocities below the predicted value were measured for data with the 75 and 100 μm pinholes.

Solutions were tested with higher viscosity (60 and 80 cP), but they were found to be exceedingly difficult to form droplet trains. When pinhole size was increased to 100 μm, the VOAG was able to aerosolize a 60 cP solution. The range of viscosities reported represent a range that can be aerosolized reliably with the VOAG used in this study. Higher pressures were tried (up to 60 PSI; 4.21 bar), but they did not lead to jet initiation when viscosities were greater than 60 cP. **Figure 4.5** shows how C_D changes in the aerosol generator.

4.3.2 - High-Speed Microscopy of Aerosols Formed from Different Viscosities

To measure the size distributions of viscous solutions aerosolized by the VOAG, the image processing pipeline (Appendix A.2) went through frames one by one thresholding and acquiring droplet data. Representative images of aqueous aerosols measured with 10X and 2X objectives are shown in **Figures 4.6** and **4.7** respectively. These figures indicate the dichotomy between monodisperse and polydisperse aerosol size-distributions. Monodisperse aerosols show identically sized objects with uniform spacing. Polydisperse distributions are characterized by nonuniform spacing between droplets and aspherical shapes, which are formed from insufficient time for drops to relax following droplet breakup or collisions between droplets of different size/characteristic acceleration times. The 10X objective which produced **Figure 4.6** was used to

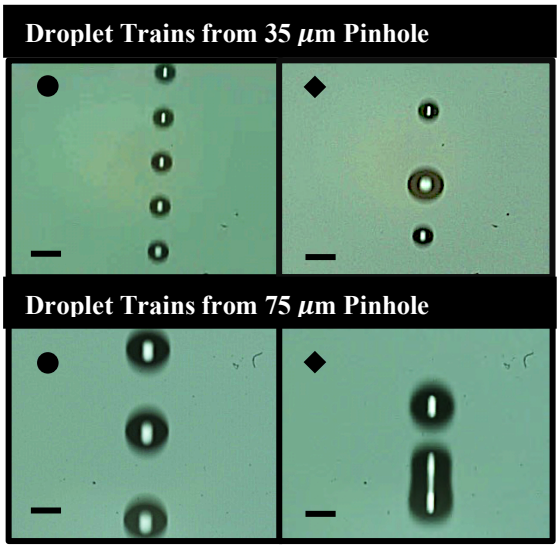

Figure 4.6 – Representative micrographs of aerosols emitted from different pinholes (10X Objective; strobing light – 1 msec exposure time). Light exposure is 10 microseconds when recording of trains of ♦ monodisperse and • polydisperse droplet trains. 100 μm bar shown.

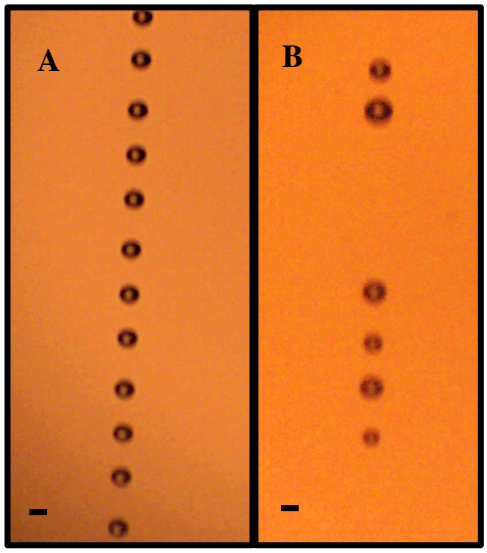

Figure 4.7 – Micrographs of aerosols emitted from a 35 μm pinhole (2X Objective; bright continuous light source – 1 μsec exposure time). A) Monodisperse aerosol excited at 35 kHz and B) Polydisperse aerosol excited at 60 kHz. 100 μm error bars shown.

measure droplet size from monodisperse aerosols (for better size resolution than the 2X objective). Despite slight motion blur in the images, this study was capable of measuring diameters accurately by recording the major axis perpendicular to the velocity vector. Size distributions, like those shown in **Figure 4.8**, were recorded for a range of viscosities using a 75 μm pinhole. These graphs, which show individual droplet size over time (denoted by Droplet ID number - a sequential numerical marker), describe the same monodisperse and polydisperse aerosols shown in **Figure 4.7**. Using Image J on **Figure 4.7A**, droplet size measured around 110μm, indicating good accuracy of the image processing pipeline. **Figure 4.8B** shows a polydisperse distribution, with high number density around two different sizes.

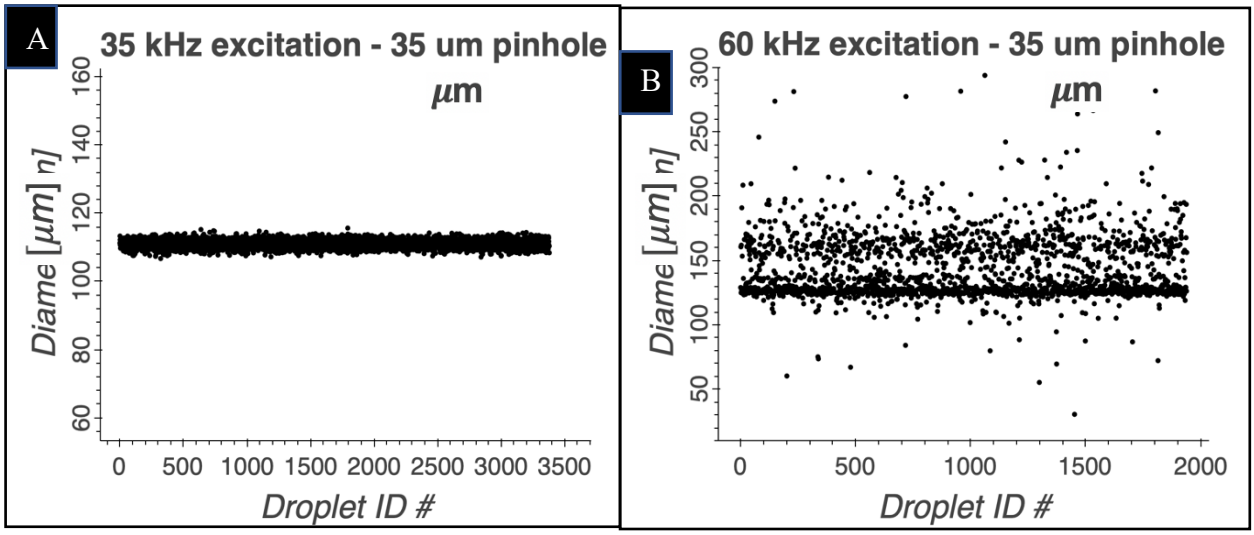

Figure 4.8 – Size distribution for aerosol formed from water emitted by a 35 μm pinhole. Size distributions show the droplet-sizes recorded from two separate high-speed videos (three and two seconds long). The x-axis shows the droplet ID number from videos which increases with elapsed time. A) Droplets from an aerosol excited at 35 kHz. B) Droplets from an aerosol excited at 60 kHz, outside of the monodisperse regime. Water was used as opposed to ethanol, which is used in later sections.

4.3.3 - Effect of Viscosity on Droplet Sizes Produced with Unexcited Pinhole

The size distribution of polydisperse, non-excited droplet-trains was recorded. The data is represented using a boxplot in **Figure 4.9**. Boxes show the interquartile range (IQR), and whiskers show the lowest datapoint still within 1.5 times the IQR. Black points on these figures indicate outliers in the dataset. The data shows significant increases in droplet-size as viscosity is increased. Using the power law expression in Equation (5), an increase in viscosity from 1 to 3.4 cP for the 35 μm pinhole (using 7 % PEG as the weight fraction) results in a significant increase in droplet size. The mean droplet size increases from 148.3 μm to 173.5 μm and the IQR shifts as well. Thus, an increase in viscosity, which has minimal effect on the mass flowrate of a given pinhole, can still have a significant effect on the breakup of a capillary jet into droplets. The effects seen in 50 and 75 μm pinholes also show significant changes with increased viscosity. Using a 13% w/w PEG solution (6.3 cP), the mean droplet size shifts from 162 μm to 181 μm. When a 22% w/w solution is used (16.7 cP), the mean droplet size shifts to 241 μm and the IQR shifts from 3 to 4 pinhole diameters to between 4.5 and 5.5 orifice diameters. The 75 μm pinhole showed a large range in droplets produced. Testing the solution that was ~40 cP in viscosity, droplets were made that were five to six times the diameter of the orifice. These data indicate that the VOAG is sensitive to changes in viscosity and altering solution viscosity can lead to a much wider range of droplet sizes that can be used.

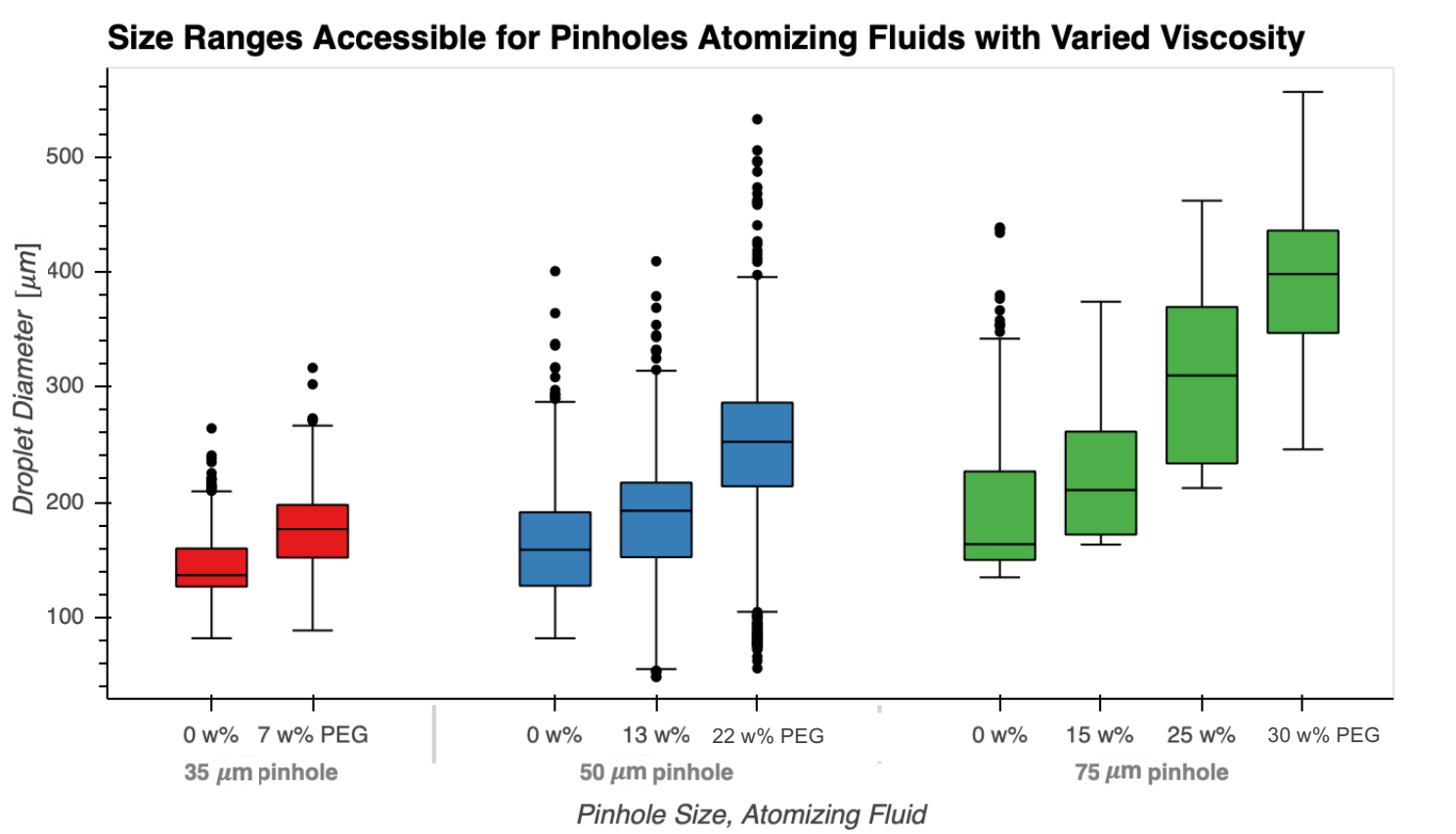

Figure 4.9 – Size distribution of viscous aerosol droplets from orifice pinholes without piezoelectric excitation. Box-plots summarize the size-distribution of aerosols emitted from three different pinholes with a range of PEG solutions. Driving force for aerosolization was 0.3 bar.

4.3.4. Discussion of VOAG Performance with Viscous Liquids

The data presented in this study is useful for anyone using a flat orifice VOAG, and it also shows interesting dynamics in droplet breakup phenomenon. The information about flowrates presented shows deviations from inviscid flow that are necessary for using these devices in experiments requiring precise flow. Using driving pressures from 0.3 to 1 bar (5-15 PSI) and 50-100 μm pinholes, solution viscosities up to 40 cP could reliably be used to form droplet trains. However, as viscosity was increased, there were significant deviations from inviscid flow (represented by C_D in Bernouli's corrected equation). The discharge coefficient calculated has a common value for all the pinholes when tested at low viscosity. However, as viscosity goes up, there is a sharp reduction in the discharge coefficient. This reduction becomes even more pronounced the smaller the pinhole is that is being tested.

The minimum ejection velocity predicted by Equation (2) was in good agreement with the data in this study. Using the 50 μm pinhole, there was a clear minimum velocity established when 25% PEG and 30% PEG solutions were aerosolized. At 3 m/s for these two solutions, if the pressure was lowered, the jet would immediately collapse. This suggests that surface tension, which shows up in Equation (2), could be a dominant parameter in jet initiation, as opposed to viscosity. Viscosity, of course, plays a significant role in minimum pressures for jet initiation.

Unlike flow initiation velocity, the dynamics of droplet breakup are significantly affected by viscosity. When analyzing the size distribution of capillary jets breaking up without controlled excitation, it can be seen that slight changes in viscosity bring about large shifts in the droplet-size distribution. As viscosity increases, the IQR of distributions goes up as well. In the case of

the 35 μm pinhole, a rise in viscosity of just 3.4 cP shifts the IQR with an increase of about 40 μm. We thought that this trend could possibly be explained by the effects of elongational viscosity. Elongational viscosity can be several orders of magnitude higher than viscosities measured with steady-state shear-flow rheology.[16] However, based on the small size of our polymers and their low concentration, the momentum relaxation time of the polymer is very low, negating the possibility of increased viscosity during elongation. A more likely explanation comes from the damping effects of viscosity for a wave propagating in a cylindrical jet. According to Frankel and Weihs, the flow field of an elongating capillary jet depends on three characteristic timescales associated with the growth of perturbations (due essentially to the effect of the surface tension), the elongation of the jet, and the inward diffusion of vorticity. While there are several effects at play, the diffusion of vorticity appears to be reduced by increased viscosity. The effect of increased viscosity is a dampening of the ability of a pressure wave to lead to instabilities. Only at longer length-scales can the instabilities lead to droplet break-up.[17]

What is most surprising of all is the continued efficacy of vibrational excitation over a broad range of viscosity. Equation (4), which suggests that the range monodisperse disturbance wavelengths likely exist, indicates a narrow range of droplets that can be produced with a monodisperse size distribution. The data presented in Appendix C.3, in combination with ejection velocity data, suggests that disturbance wavelengths over 40 times the diameter of the pinhole can be used to generate monodisperse aerosol standards (when fluid viscosity is altered). With disturbance wavelengths over 3 mm, the orifice is still able to produce monodisperse droplets.

These data indicate that higher viscosity fluids can be used with the VOAG, but one must anticipate the larger diameters of droplets that will be produced. The standard deviation of droplet distributions produced also seems related to fluid viscosity (Appendix C.3). This may have to do with the ability of polymers to stabilize liquid jets at low concentrations. When jets exhibit a strong elastic response to deformation, even when polymers are in the dilute regime, there can be a stabilizing effect on a resulting capillary jet.[18]

4. 4 Producing Aerosol Droplets for Microparticle Preparation

The work done aerosolizing fluids of different viscosity is compelling from a fluid dynamics perspective and can be useful to aerosol researchers. It also taught our group to be wary of the effect of polymers on droplet size production. To make solid microparticles, precise size control over low-viscosity, high-volatility liquids was desired. Based on heat-mass transfer modeling (discussed in section 3.6), it was found that it would be difficult to fully dry aerosol droplets made from an aqueous liquid at the max temperature of our drying column (100 °C). The volatility of liquid water is too low to really produce solid microparticles at the heat duties accessed by our drying column. Instead, our modeling suggested that volatile organics, like ethanol and acetone, would have better chances of fully drying to create solid microparticles. Since acetone has a deleterious effect on the Buna rubber used to make o-rings in our aerosol generator, it was decided to use ethanol as a solvent to form microparticles. To check compatibility of ethanol with our aerosolizer, a study was done with various pinholes to see what ethanol droplet sizes could be prepared in a monodisperse manner.

4.4.1 – Procedure for Measuring Excitation Regimes That Lead to Monodisperse Production

When measuring droplet-size distributions, the key to collecting reliable data was ensuring that solutions were clear of impurities and the pinhole was not obstructed. Obstructed pinholes affect the ability to create a monodisperse aerosol. To avoid obstruction, 100 mL of solution were filtered using 0.45 μm cutoff syringe filters (Thermofischer). Then to check for obstructions, the mass of fluid ejected from the aerosolizer was measured. Once average mass flow was calculated, the average ejection velocity was calculated using the dimensions of the pinhole and this value was compared to the data in **Figure 4.3**. If the velocity measured was comparable to what was measured in our previous testing, it would be assumed that our pinhole was clean and unobstructed. From here, the expected range of frequencies leading to monodisperse production (predicted by Equation (4)) was calculated. Then, size distributions were measured with the high-speed microscopy system for frequencies below, within, and above the expected range of monodispersity. This procedure is presented in the following section.

4.4.2 – Production of 70 to 175 µm Droplets Using Atomization of Alcohols

To test low-viscosity, high-volatility liquids like ethanol and isopropanol, a 75 μm pinhole was first used. Isopropanol was filtered and then the flowrate was measured using a pressure of 0.34 bar. The average volumetric flowrate of isopropanol was measured to be 1.49 cc/min. This corresponds to an ejection velocity of $v = \frac{\dot{Q}}{\frac{\pi}{4}D_o} = \frac{\left(1.49\frac{cm^3}{min}\frac{1min}{60\ sec}\right)}{\frac{\pi}{4}(.0075\ cm)^2}\frac{1\ m}{100\ cm} = 5.6\ m/s$, where $\dot{Q}$ is the volumetric flowrate and D_o is the orifice diameter. When comparing this with the data shown in **Figure 4.3**, it can be seen that the expected ejection velocity was 6.0 m/s $\pm$ 0.5 m/s, so the

pinhole was considered to be clear and unobstructed. Next, the expected range of frequencies leading to monodispersity was calculated. The high-end range of frequencies is given by $\lambda = 3D_j$ in Equation (4), where D_j is the jet diameter, which is approximated using the diameter of the orifice. This disturbance wavelength leads to a frequency of $f = \frac{v}{3D_o} = 25.0\ kHz$. The low end of expected monodisperse frequencies is 10.7 kHz. Based on these calculations, frequencies were chosen below this range (6 and 8 kHz), within this range (10, 12, 14, and 18 kHz), as well as size distributions greater than this range of frequencies (25 kHz and 50 kHz). The size distributions measured in this analysis are shown in **Figures 4.10 and 4.11.**

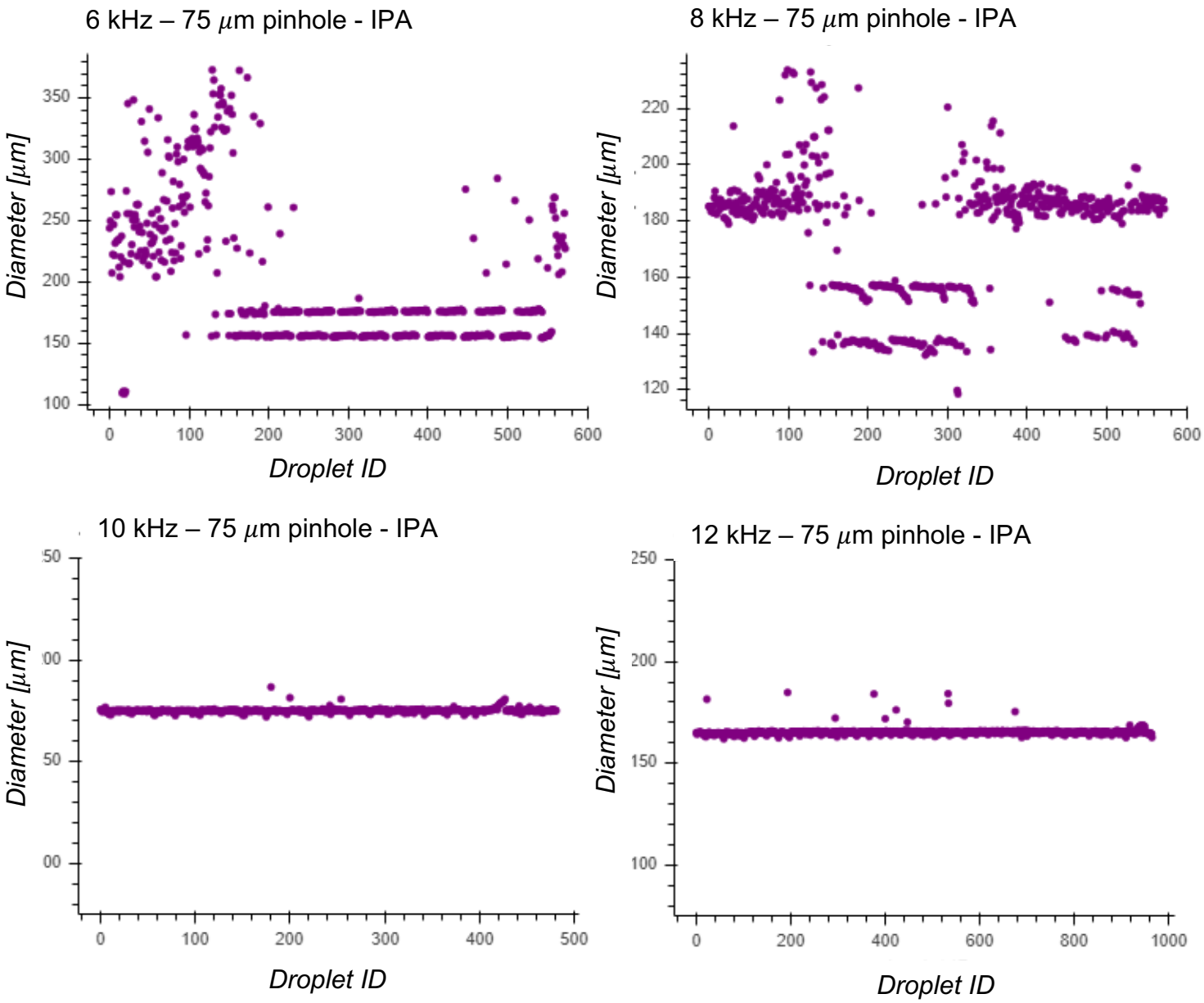

Figure 4.10 – Size distribution of isopropanol ejected from a 75 μm pinhole (6 to 12 kHz). Lower frequencies show bimodal and even trimodal distributions of droplet size. Then, when the expected region of monodisperse frequencies is entered, there is a shift to monodisperse droplet production.

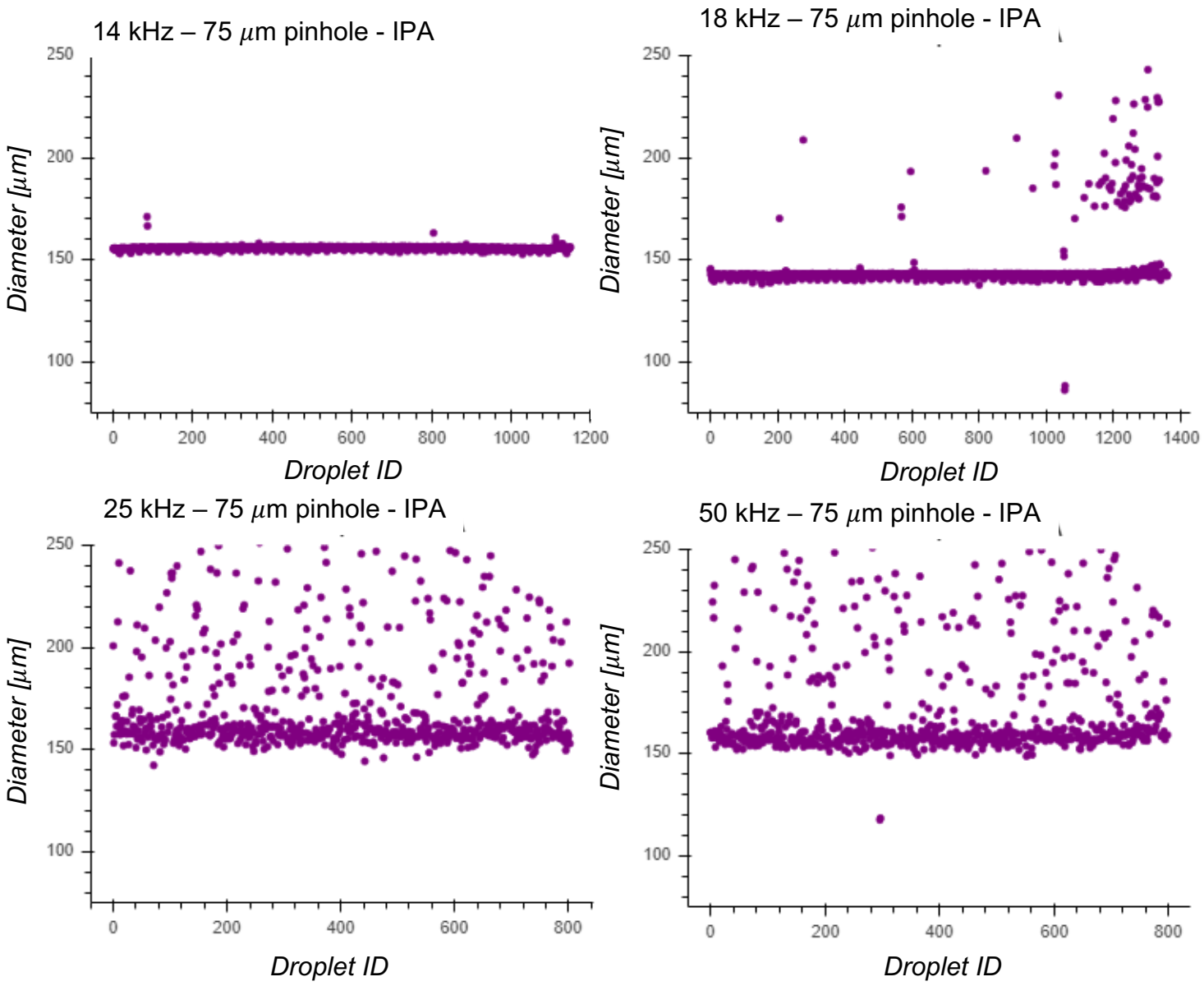

Figure 4.11 – Size distribution of isopropanol ejected from a 75 μm pinhole (14 to 50 kHz) – monodisperse production occurs up until 18/19 kHz. Then at 25 kHz and 50 kHz, the production of droplets is essentially the same as if the orifice were not being excited at all.

By plotting size distributions, it was shown that the control of droplet size using the 75 μm pinhole was a richer experiment than expected. The range of monodisperse frequencies recorded in this experiment spans from 10 kHz to 18 kHz. This is within the expected range that was calculated previously using Equation (4). 20 to 25 kHz frequencies did not result in monodisperse aerosols, even though they were within the predicted range. An aspect of the data which was not expected was the response of the aerosol to lower frequencies that were not supposed to be monodisperse. In **Figure 4.11**, it can be seen that 6 and 8 kHz frequencies resulted in clear bidisperse and tridisperse distributions of droplet sizes. While the goal of this work was monodisperse distributions of size, it was helpful to know that low frequencies can provide two, or even three, discrete modes of droplet sizes. The diameter of monodisperse drops that can be prepared using the 75 μm pinhole is between 175-140 μm as shown in **Figure 4.12**.

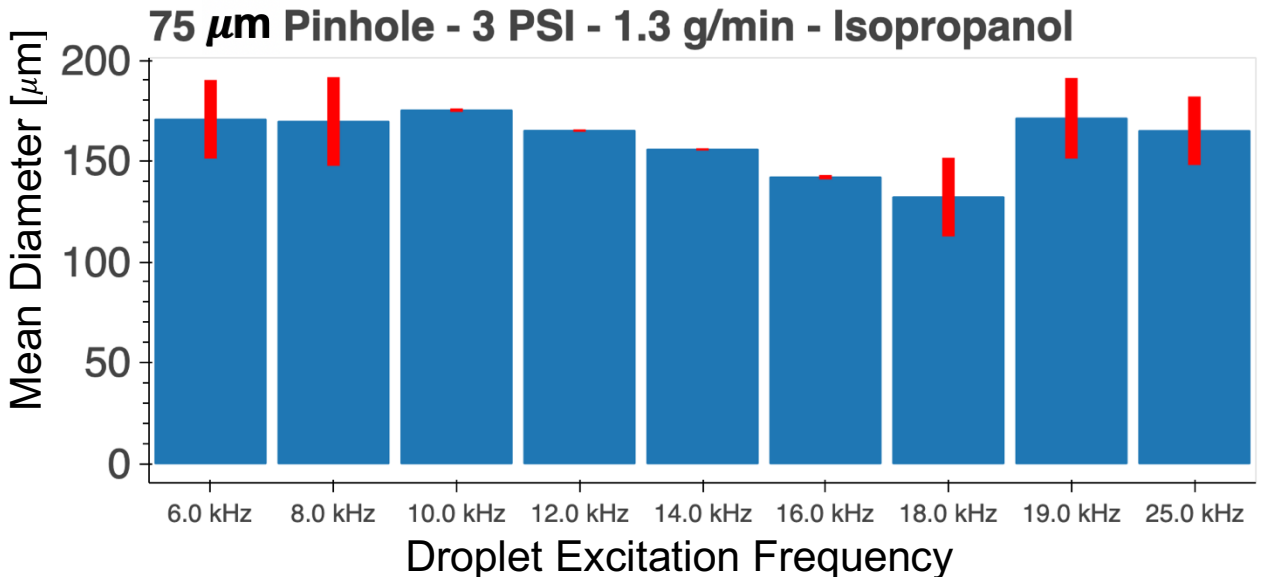

Figure 4.12 – Mean and standard deviation of size-distributions of isopropanol ejected from a 75 μm pinhole. Average droplet size plotted with 95% confidence intervals.

A smaller 50 μm pinhole was investigated for its ability to make droplets with lower diameter and settling velocity. Ethanol was chosen for these studies because it was found to dissolve our base polymer poly(ethylene glycol) at room temperature, whereas isopropanol solutions that contained dissolved PEG (5 w%) would show solute crystallization upon cooling. The procedure used to measure aerosol size distributions with this pinhole and resulting data are shown in Appendix C.1. In **Figure 4.13**, the resulting mean and standard deviation from our frequency-sweep measurement of aerosol-size distributions are shown (for the 50 μm pinhole). As can be seen, 100 to 125 μm droplets can be prepared in a monodisperse manner. Ultimately, our group wanted to produce smaller droplet sizes than this, so a 35 μm pinhole was investigated for its ability to produce monodisperse droplets. Again, look to Appendix C.1 for the results of testing. Data summarized in **Figure 4.14** show that the 35 μm pinhole can produce monodisperse droplets in a much broader range of diameters than the other two pinholes. The 35 μm pinhole can create monodisperse drops from 70 to 120 μm, which is twice the breadth of the range achieved by the other pinholes.

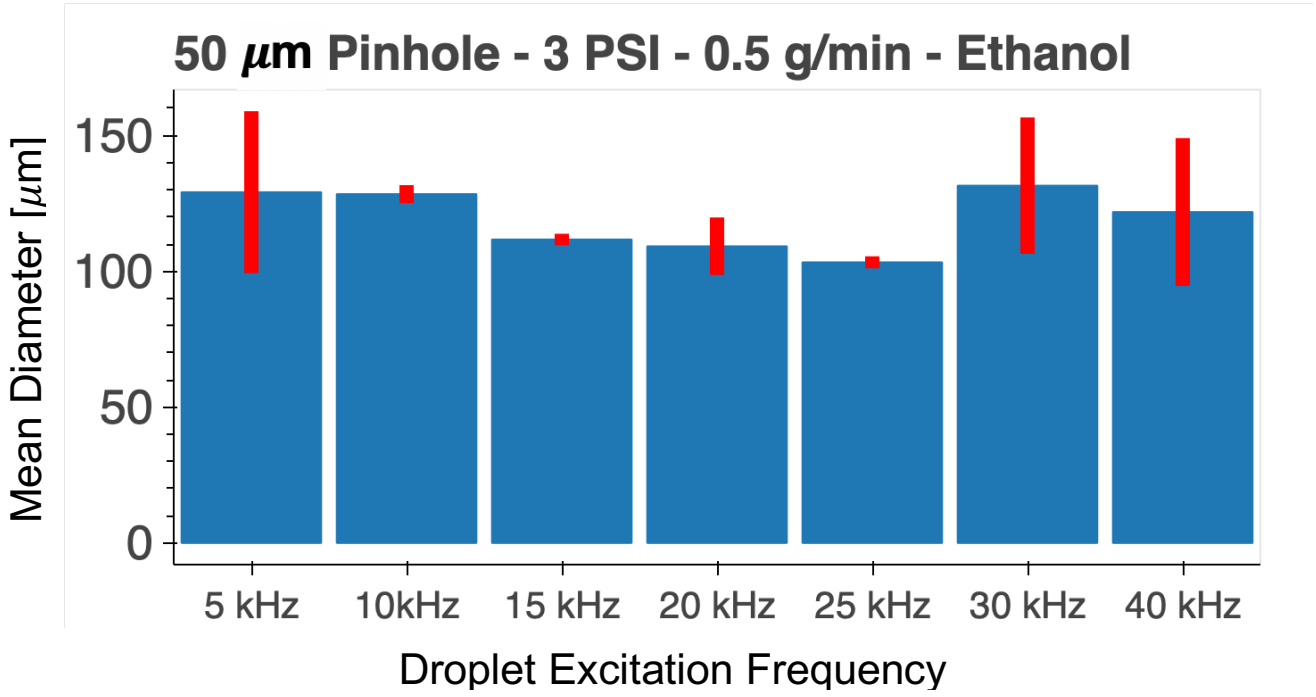

Figure 4.13 – Size distribution statistics of ethanol ejected from a 50 μm pinhole. Monodisperse production occurs from 10 to 25 kHz. Error bars show 95% confidence intervals about the mean diameter.

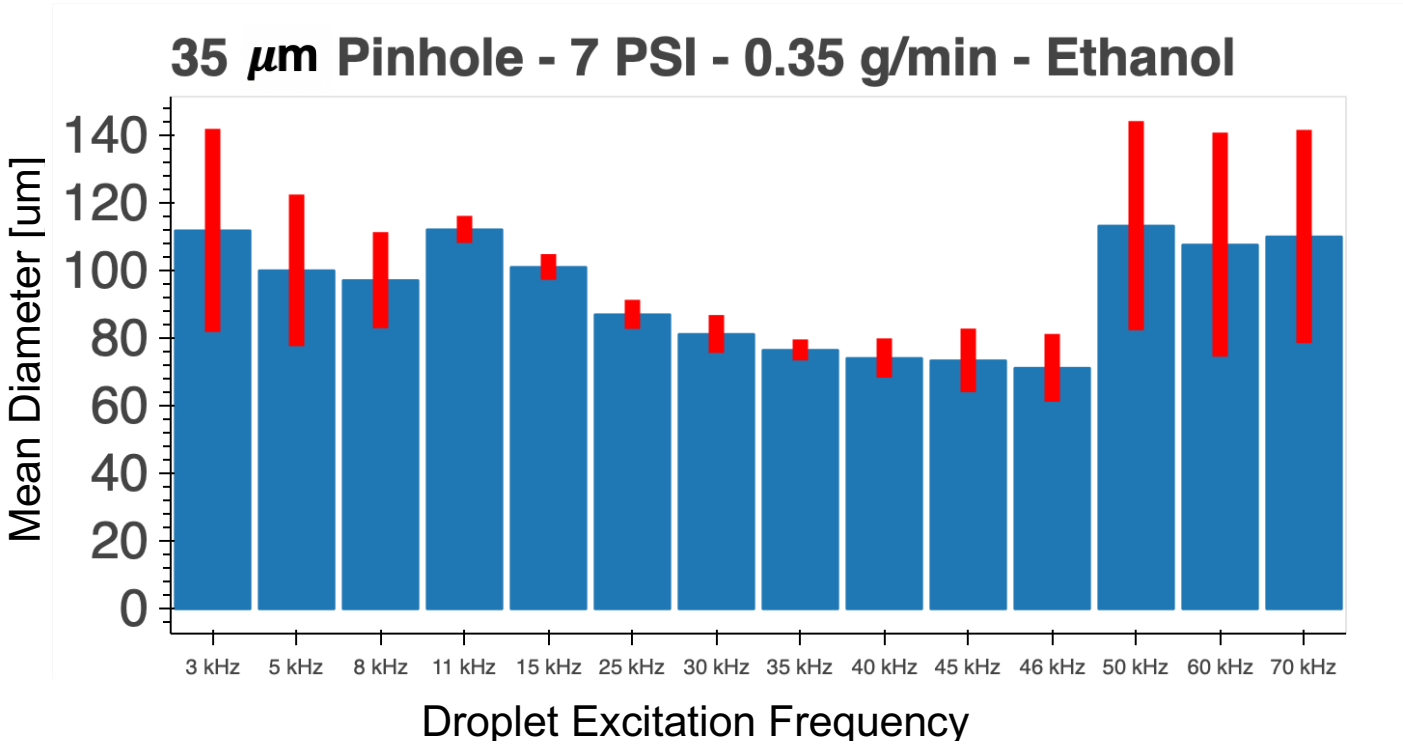

Figure 4.14 – Size distribution statistics of ethanol ejected from a 35 μm pinhole. Monodisperse production occurs from 11 to 46 kHz. Error bars show 95% confidence intervals about the mean diameter.

Table 4.2 - Monodisperse droplet data for VOAG atomizing isopropanol and ethanol

Pinhole Size	*Range of Droplet Sizes that Can Be Monodisperse*	*Functional Frequency Range*	*Flowrate*	*Range of Expected Settling Velocities in Air*
75 μm	150 to 175 μm	10 – 18 kHz	1.5 cc/min (5 PSI) IPA	66 to 90 cm/s
50 μm	100 to 125 μm	10 - 25 kHz	0.5 cc/min (3 PSI) EtOH	29 to 45 cm/s
35 μm	70 to 120 μm	11 – 46 kHz	0.35 cc/min (5 PSI) EtOH	14 to 42 cm/s

Ultimately, the settling velocity of our aerosolized droplets is the key parameter which determines the ability to form solid particles in the drying column. When ejected into a heated atmosphere, the droplet will immediately begin to evaporate and size will change, but first the droplet rapidly decelerates to its settling velocity. The initial settling velocity has to be low enough to ensure the droplet will have a long enough residence time in the column. The 35 μm pinhole is the only orifice which has the ability to produce droplets with an initial settling time < 20 cm/s, as is shown in **Table 4.3**. This information shows that there is a broad range of droplets that can be produced (70 to 175 μm), but the high settling velocity of droplets produced by the larger pinholes makes them likely incompatible with our 1-meter-tall drying column.

4.5 – Drying Column Used for Microparticle Preparations

A drying column was built in many stages for the production of solid polymeric microparticles. To dry the particles, the column was heated using heat tape, inline heaters, and two temperature controllers. Initially an acrylic column was used, as shown in **Figure 4.15A**. This material was not heat resistant enough, so a glass column was used instead (1 meter x 10 cm. diameter). The column was first placed in a fume hood in the lab like in **Figure 4.15B**, but it was difficult to operate the column when the VOAG had to be mounted roughly 2.5 meters off of the ground. Ultimately, the drying column was placed in a ventilated tent enclosure. There were multiple heated-gas connections made to the column so that gas carrying particles in the column could be sufficiently diluted before reaching the particle collection chamber, which is shown in **Figures 4.15 D** through **F**. Gas enters a concentric cone with holes drilled into a cover for the second cone (to relieve pressure) and particles are left to settle into a collection chamber. A petri dish is placed in the collection chamber to collect microparticles.

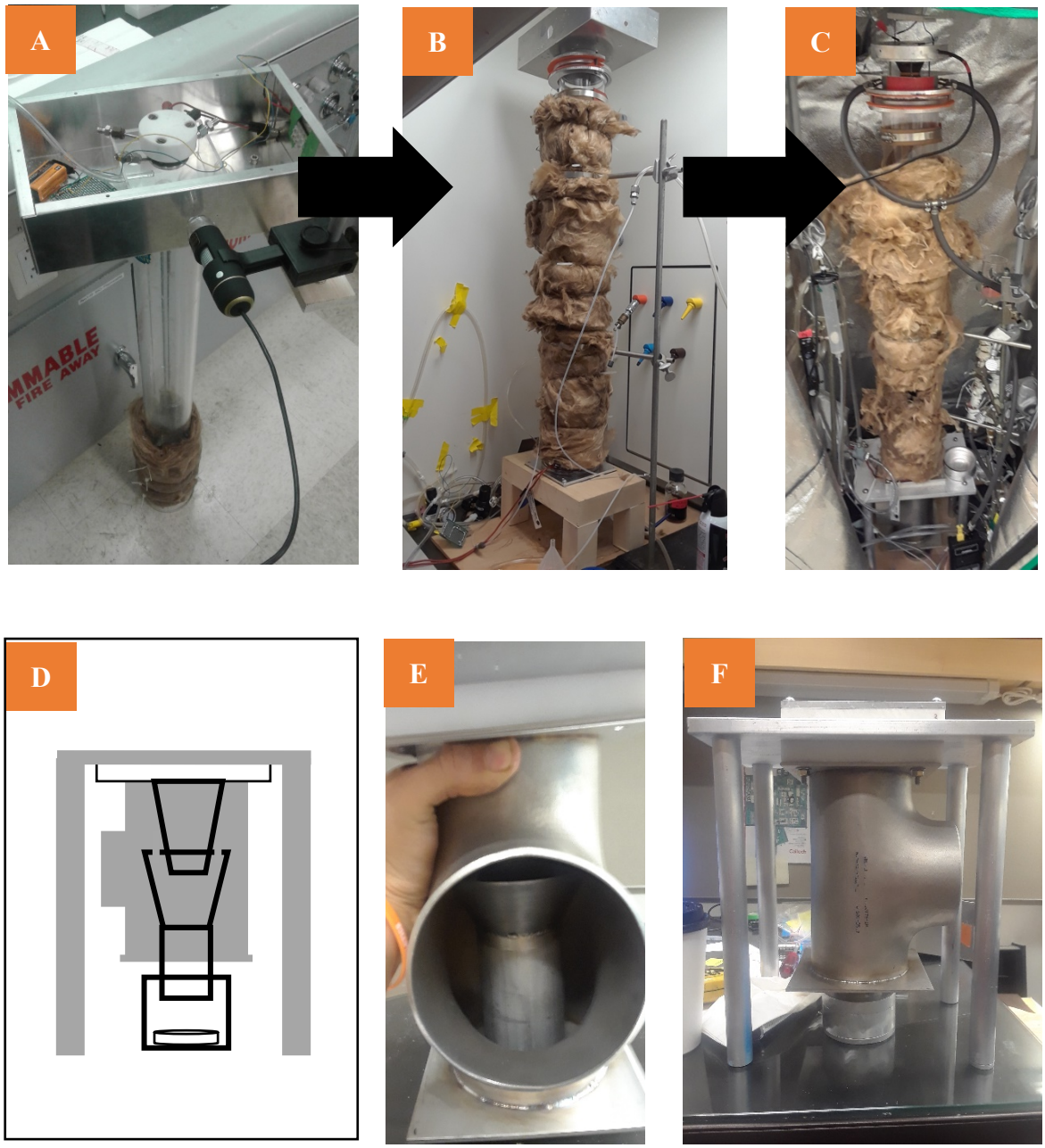

Figure 4.15 – Evolution of the drying column and particle trap. A) The drying column started out as an acrylic column. B) When higher temperatures were needed, the column was switched to a 1-meter-tall by 10 cm. diameter column. C) The column was connected to inline furnaces and placed in a tent enclosure. D) Schematic of the particle collection trap. Gas flows from the column into two concentric cones. The receiving cone has holes drilled in its top to relieve the pressure drop at the bottom of the column. Ideally, particles settle down into the bottom of the collection chamber where a petri dish is placed. E) At the bottom of the column is the receiving cone. F) The overall assembly of the particle trap can support the heavy column.

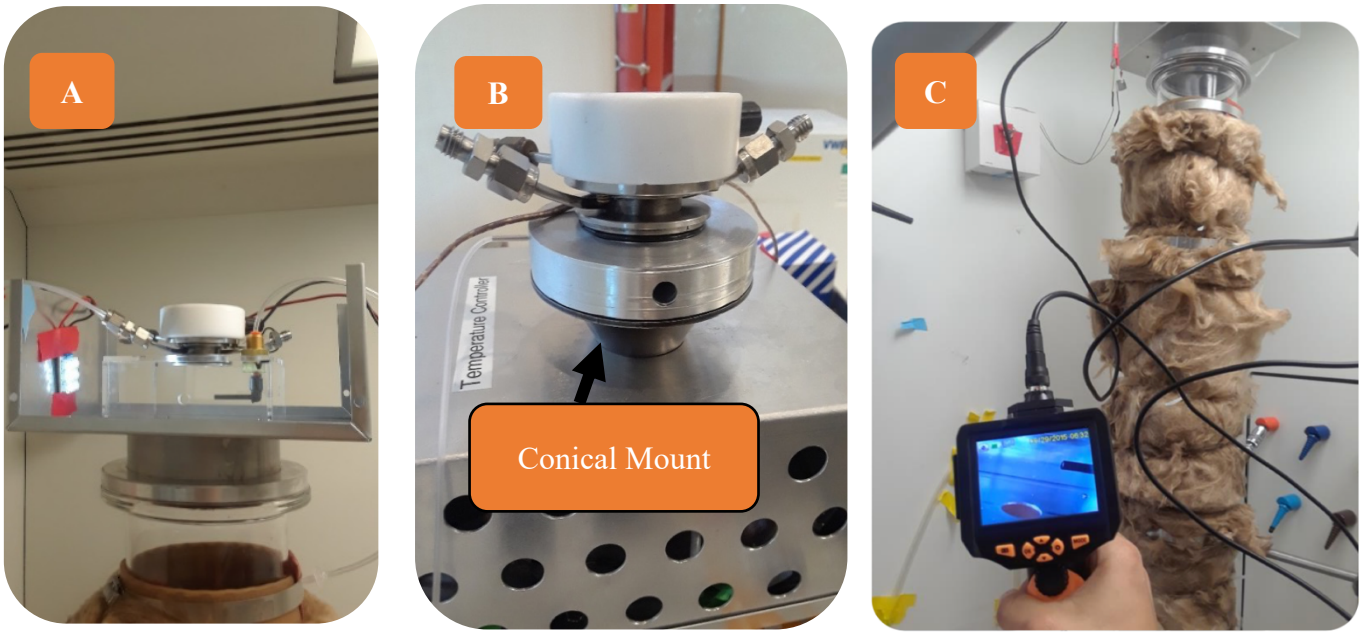

Figure 4.16 – Mounts used for the VOAG. Various mounts were used to keep the VOAG positioned over the column and to disperse droplets before entry. A) An acrylic mount was used with an orthogonal gas jet positioned in order to check for monodispersity. B) An aluminum mount replaced the acrylic mount. The benefit of this part is that there was a nozzle heading into the column that could be used to help focus particles as they travel and disperse into the column. C) There is also a viewport for a boroscope to check and see if aerosols are flowing and to check for monodispersity.

The mount used to place the VOAG on top of the column centered and helped disperse the aerosol being fed to the drying column. Mounts were built that used a quick, diagnostic test to see if droplets were being produced in a monodisperse manner (**Figure 4.16**). With the jet initiated, a stream of gas was directed orthogonally at the droplet-train. If the flow of the gas was laminar and the frequencies being provided to the VOAG were in the range of monodisperse breakup, then the liquid would be deflected as a kinked ray, instead of a spray. This phenomenon is demonstrated in **Figure 4.17**. With no excitation, particles are deflected in a spray because the

distribution is polydisperse and droplets have different characteristic aerodynamic relaxation times. When a 19 kHz signal is applied to the microjet, a clean ray of particles is deflected.

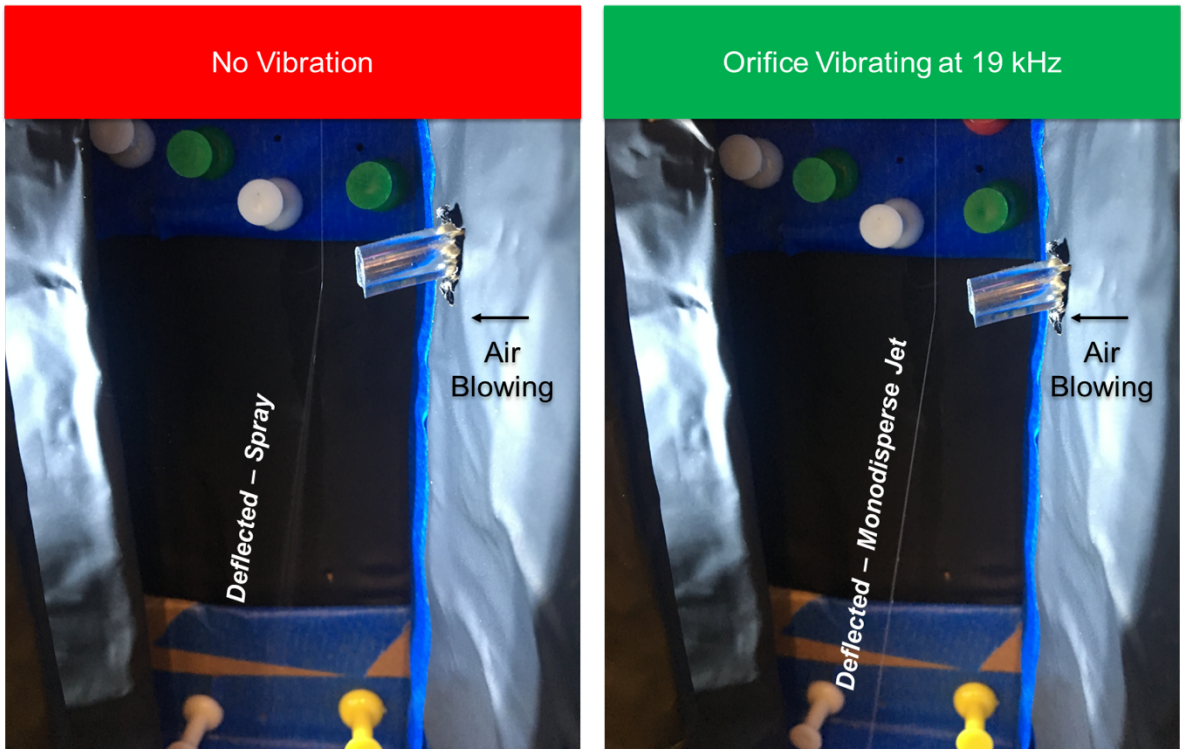

Figure 4.17 – Diagnostic test for monodispersity. (Left) no excitation leads to a deflected spray of polydisperse droplets. (Right) 19 kHz excitation leads to a deflected ray, indicating monodispersity has been achieved.

4.5.1 – Mass-Heat and Momentum Transfer on Drying Microparticles

In order to find conditions for solid microparticle production, a model was built to track the evaporation of droplets in the column. Several assumptions were made: 1) air entering the column was at 50% humidity, 2) there was no droplet coagulation, 3) there was ideal plug flow in the column, and 4) the temperature of the particle was constant throughout. The fourth assumption was valid since the Biot Number of 100 μm droplets in air is far less than one (resistance to heat transfer is convection limited). The differential equations used to track particle temperature, position, velocity, and diameter are shown in **Table 4.4**. The equations in this table

Table 4.3 – Model equations for drying-column model.

Dependent variable	Gradient Equation
velocity	$m_p \frac{dv}{dt} = m_p g - 3\pi\mu \left(\frac{6m_p}{\pi\rho_p}\right)^{\frac{1}{3}} \left(\frac{Q}{A_{col}} - v\right)$
position	$\frac{dx}{dt} = v$
particle temperature	$\frac{dT_p}{dt} = \frac{1}{m_p C_p}\left[\frac{dm_p}{dt} H_v + 4h\left(\frac{6m_p}{\pi\rho_p}\right)^{\frac{2}{3}} (T_\infty - T_P)\right]$
column temperature	$\frac{dT_\infty}{dt} = 0$
convective heat transfer coefficient	$h = \frac{.59(Gr * \Pr)^{\frac{1}{4}}}{\left(\frac{6m_p}{\pi\rho_p}\right)^{\frac{1}{3}}} k_{air}$
particle mass	$\frac{dm_p}{dt} = -\pi\left(\frac{6m_p}{\pi\rho_p}\right)^{\frac{2}{3}} \rho_g k_{H2O,air}\left(X_{SAT,T_p} - X_\infty\right)$
mass fraction of water in column air	$\frac{dX_\infty}{dt} = \left(-\frac{f}{\rho_g Q}\right)\frac{dm_p}{dt}$
convective mass transfer coefficient	$k_{H2O,air} = \frac{Sh * D_{H2O,air}}{\left(\frac{6m_p}{\pi\rho_p}\right)^{\frac{1}{3}}}$

m_p= particle mass, v = velocity, g = gravitational constanty, μ = dynamic viscosity of air, ρ_p= particle density, Q = carrier gas flow rate, A_{col} = column area, x = particle postion, T_p = paticle temperature, C_p= the heat capacity of the liquid in the particle, H_v is the heat of vaporization, h is the convective heat transfer coefficient, T_∞ = the column steady state temperature, Gr is the Grasshoff Number, Pr is the Prandtl Number, k_{air} is the thermal conductivity of air, $k_{H2O,air}$ is the convective mass transfer coefficient, X_{SAT,T_p} is the saturation mass fraction of water vapor in air at T_p, X_∞= the mass fraction of water in the column air, f = the frequency of droplet generation, Sh is the Sherwood Number, and $D_{H2O,air}$ is the diffusivity of water in air.

come from Bird, Stewart, and Lightfoot and Levendis.[19,20] Using the numerical integration suite in MatLab, ODE15s, models were built for the evaporative process going on within the column. For momentum transfer, particles are assumed to be falling with the force of gravity, but eventually (when small enough) are pulled by the drag of a carrier gas. For heat transfer, droplets are modelled to be heating in the hot column atmosphere, but they are also rapidly cooled by evaporative effects. The heat transfer coefficient is calculated using a heat transfer expression with Prandtl and Grasshoff Numbers. These dimensionless groups are only slightly affected by temperature and are coded into our modeling equations. In mass transfer equations, the mass fraction of water vapor in air is assumed to be a result of perfect plug-flow with no back mixing in the column. The convective mass transfer coefficient is calculated using a correlation that is a function of the Sherwood Number and the diffusivity of the vapor, both of which are coded into the model.

4.5.2 – Investigating Drying Rates Using Model of Heat and Mass Transfer

To prepare solid microparticles in a drying column, our group wanted to figure out what temperature the column should be maintained at, what solvent the droplets should be made with, and what initial size the droplets should have. To answer these questions, a mass, momentum, and energy balance was coded in Matlab for droplets settling in an infinitely long column (Appendix A.3). Particles will ultimately be formed with solutions that are 1% to 5% w/w nonvolatile polymer, assuming the droplet was entirely composed of water simplified calculations. The initial mass fraction of water-vapor entering the column was taken to be X_o = .015 (50% relative humidity) and the flowrate of gas through the column was 30 standard

cubic feet per hour. Saturation vapor pressure of the liquid was calculated using Antoine's Equation with NIST data.[21]

Using the simulation, it was found early on that aqueous solutions needed too much time to become fully dry in the column. 100 μm droplets needed around 25 seconds to reduce in mass by 95% in a 100 °C column. 55 μm droplets needed about half of this time. However, when ethanol was used in the simulation, there were greatly improved drying rates attributed to the higher volatility of ethanol. 100 μm droplets made of ethanol only needed 5 seconds in the column to become fully dry. The full drying process is shown in **Figure 4.18**. With ethanol ejected into the column at 25 °C, there was a pronounced evaporative cooling effect from the high initial speed of the droplet and the high volatility of ethanol. The droplet cools by over 20 °C and then steadily begins to raise in temperature. The rapid drop in temperature corresponds with the time the droplet is still moving several meters per second. With high Sherwood Numbers, the droplet rapidly evaporates and decreases the temperature of the liquid. After taking 20 cm to come to a lower settling velocity, the droplets evaporate for around 5 seconds. In this time, they settle 60 cm more while they dry. Based on these calculations, our group had confidence in making solid microparticles using ethanol as a solvent because procedures were ready to make monodisperse droplets that were 100 μm in diameter and smaller (Section 4.5.2).

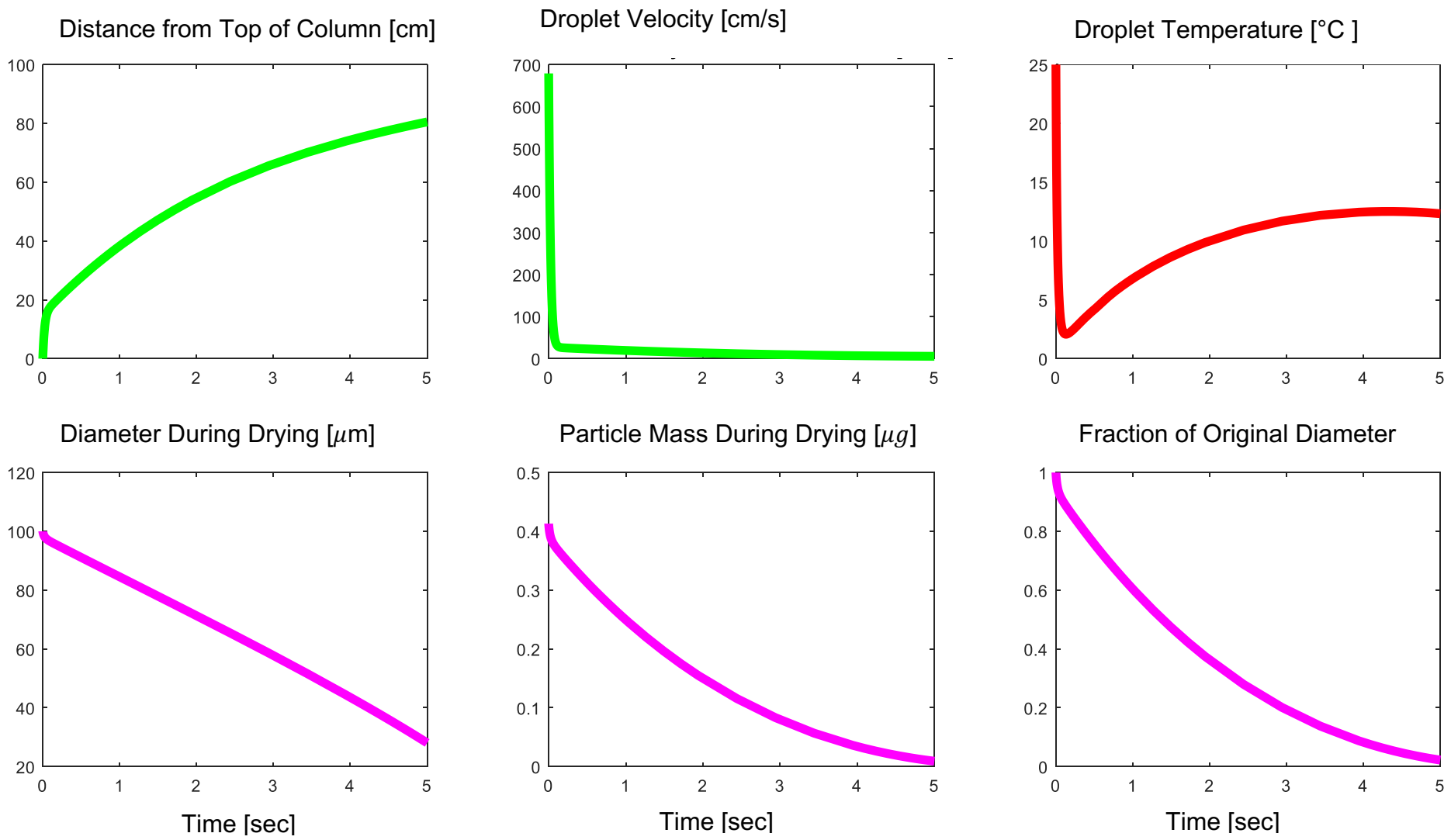

Figure 4.18 – Drying of a 100 µm ethanol droplet in a 100 °C drying column. With an ethanol composed droplet, the column should able to dry microparticles fully at this temperature. There is a large initial evaporative cooling effect. The particle travels roughly 15 cm while decelerating. It then decelerates at settling velocity for around 5 seconds while the particle fully dries.

4.5.3 – Suggested Drying Column Parameters

The drying simulation suggested that if droplets made of ethanol could be aerosolized with diameters less than or equal to 100 μm, then solid microparticles could be formed in the one-meter-tall drying column. A 35 μm pinhole was chosen so monodisperse aerosols could be produced, like the ones described in Figure 4.15. This figure shows that this pinhole can be used to produce 70 μm to 120 μm droplets that can be formed with ethanol. If the generator was operated at around 35 kHz, 70 μm droplets could be produced by the VOAG. With this droplet size, an expected final particle diameter can be calculated using the following conservation equation:

$$D_p = C_v^{1/3} D_d \tag{6}$$

where D_p is the diameter of the particle, D_d the diameter of the droplet, and C_v is the volumetric concentration of solute. For a 70 μm droplet with concentration of 1% to 5% w/w, the expected final droplet size comes out to 15 to 26 μm. For a 100 μm particle, the expected final particle size comes out to 21 to 36 μm. This size range is in the range of previously tested ballistics, so these conditions were thought to be ideal for our particle preparations.

4.5.4 – Final Design of Drying Column and Parameters for Making Microparticles

The final design of the drying column was made to effectively dry microparticles, to dilute the vapors exiting the bottom of the column, and to fully contain the aerosols produced within. The one-meter-tall 10-cm-diameter drying column was wrapped in heater tape (about 3.6 meters of tape with a width of 5 cm; McMaster Carr). The tape was controlled with a CN142 temperature controller (Omega Engineering) that was used to drive a solid-state relay controlling power to the

heater. The temperature controller was receiving input from a K-Type thermocouple attached between the heat tape and the wall of the glass column. This allowed us to have more control over heat tape, preventing overheating. Two T-Type Process Heaters (Omega Engineering; Item# AHP-5052) were used to heat the carrier gas (fed to the top of the column) and the dilution gas (fed to the bottom of the column). The carrier gas was used to dilute the air in the column and to carry the particles gently to the particle trap. The dilution gas was fed directly to the particle trap to dilute vapor in the column and prevent condensation. Another CN142 temperature controller was used to control the temperature of the inline heater feeding the carrier gas to the column. The other inline heater was wired in series with the first heater, giving it indirect temperature control.

Three flow control-valves with rotameters were used to control 1) the carrier gas flow, 2) the dilution gas flow, and 3) the dispersion gas flow being sent directly to the VOAG (gases labelled in **Figure 4.20**). The dispersion gas was meant to disperse droplets radially as they enter the column, thus improving drying and hopefully reducing droplet coagulation. Since the column would be producing respirable microparticles and vapors from organic solvents, the entire apparatus was placed inside a tent enclosure with a duct connected to the house ventilation system (**Figure 4.19**). This setup allowed for containment of hazardous materials, and also kept the column at a workable height.

While there was no optimization procedure (e.g. design of experiment) run to determine optimal parameters, eventually a procedure was developed that produced satisfactory microparticles. The flowrates of gas flowing into the column in **Figure 4.20** were used for each particle preparation.

The dispersion gas flow was set by monitoring the state of the aerosol jet at the top of the column using a borescope. The flow was increased to 10 SCFH until the jet just started to move with the dispersion gas. A flowrate of 30 SCFH was chosen for the carrier gas. This resulted in an approximate velocity of gas moving through the column of 3 cm/s. Dilution gas was set to 10 SCFH. For particle preparations, the temperature of the heat tape wrapped around the column was set to 170 °C. At steady state with a 35 μm pinhole ejecting fluid into the column at 0.1 g/min, the column gas temperature was 100 °C (measured 2/3rd's of the way up the column with a temperature probe). The inline heaters were set to 250 °C, resulting in a steady state gas temperature of 80 °C for the nitrogen going into the column. The VOAG using a 35 μm pinhole was excited at 35 kHz to try and produce droplets that were around 70 μm. These are the typical conditions at which particle preparations were run at.

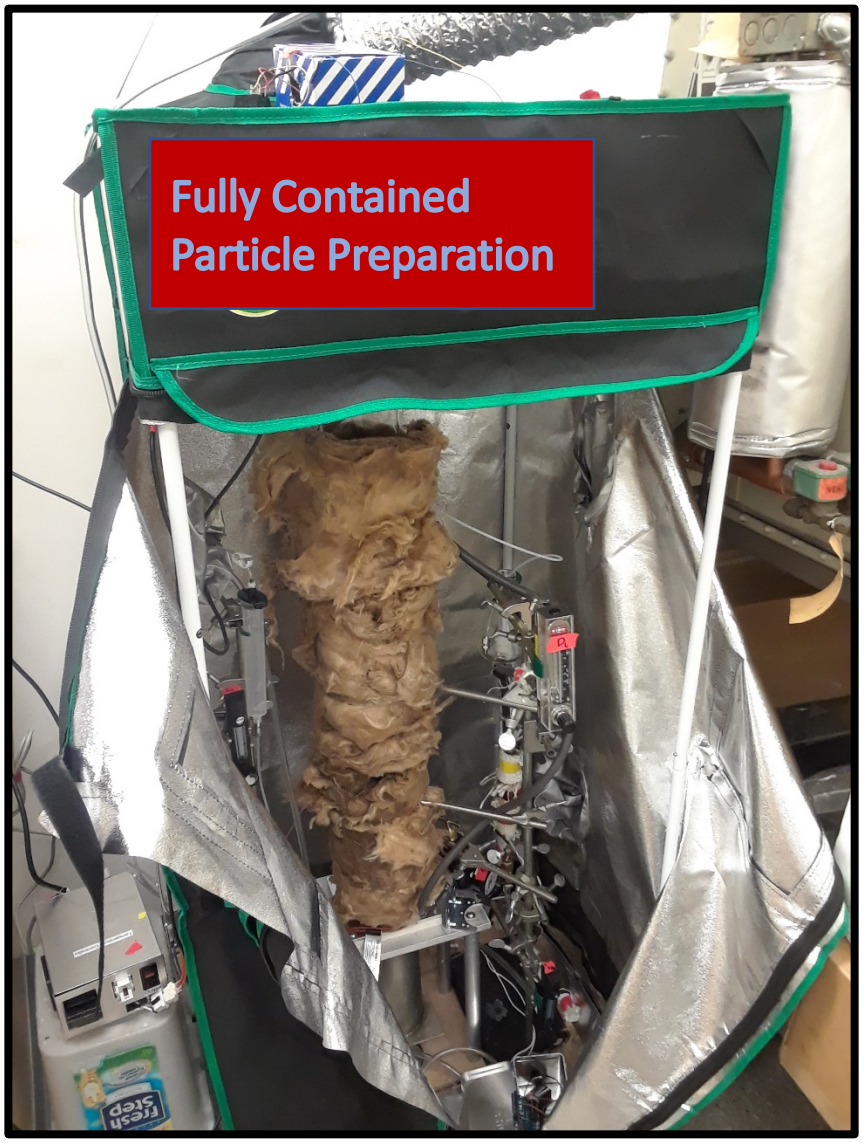

Figure 4.19 - Fully enclosed drying column. The column along with all flow meters and heating elements were placed in a tent enclosure. The enclosure allows for containment of microparticles and vapors.

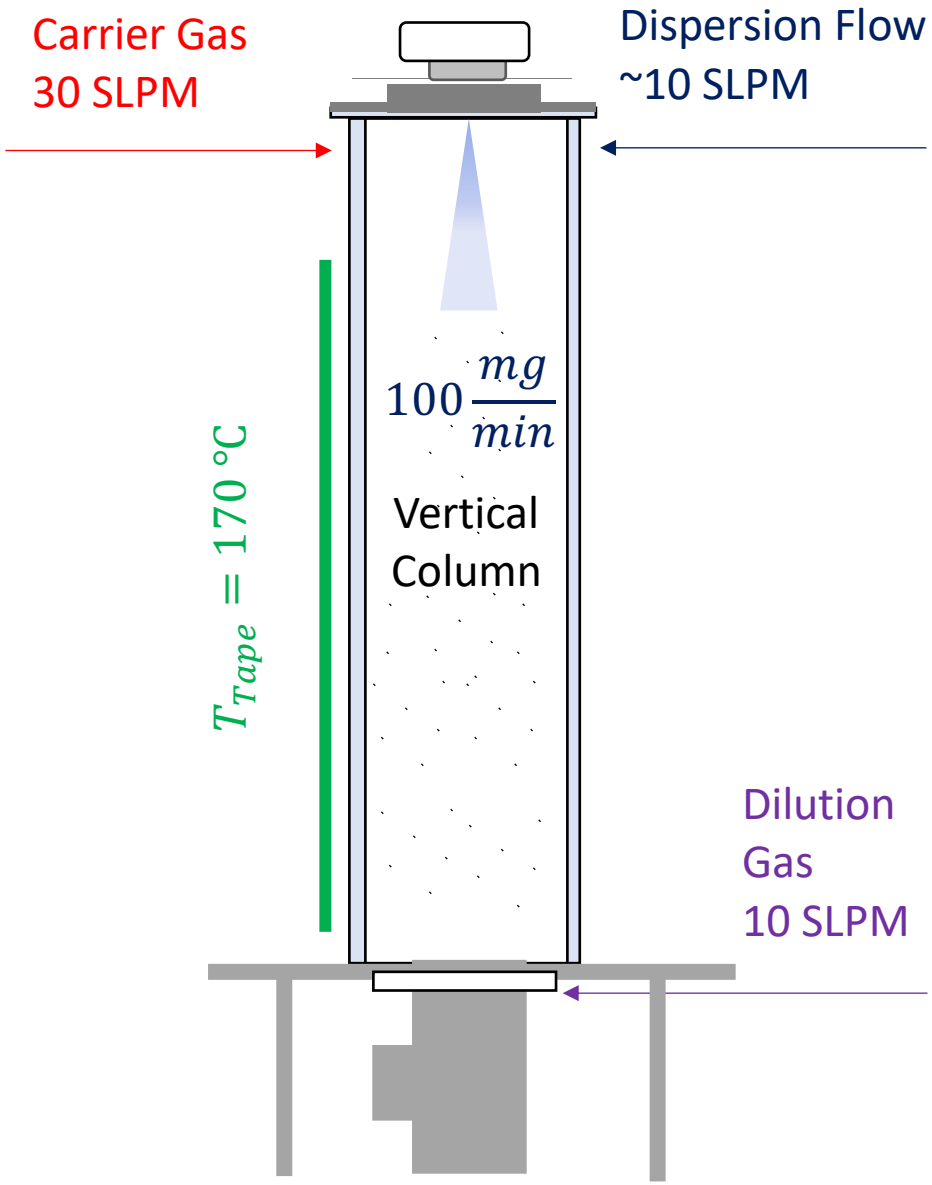

Figure 4.20 – Typical conditions for microparticle preparation. Nitrogen is fed to the VOAG (dispersion gas), to the top of the column (carrier gas), and to the particle trap (dilution gas). The column walls are heated to a certain temperature and the VOAG usually ejects a ~200 mgs of solution a minute, if the 35 μm pinhole is used.

4.6 – Preparation of Solid Microparticles Using Custom Drying Column

4.6.1 – Procedure for Microparticle Preparation

To form particles in the drying column, the following procedure was developed. A solution of poly(ethylene glycol) (PEG 10 kDa M_w; Alpha Aesar) was prepared by heating and stirring in 96% ethanol (VWR) until the solution reached 35 °C and was stirred for another half hour. In the case of 1% w/w Eosin Y microparticles, 3.96 grams of PEG was dissolved in 96 grams ethanol along with 40 mgs of Eosin Y salt (Sigma Aldrich). The solution was cooled to room temperature and filtered with a 0.45 μm cutoff syringe filter. The solution was loaded into the VOAG and a microjet was initiated. After checking monodispersity of the aerosol stream using the impinging jet method (**Figure 4.7**), the VOAG was mounted on top of the column without having engaged any heating. Once the aerosolizer was mounted, temperature controllers were turned on along with gas inputs. While the column was heating up, the bottom of the particle trap was left open so vapor and condensed liquid could drip out. After one hour of heating and feeding the aerosol jet into the column, the particle trap was connected to the collection chamber and a glass petri dish was inserted to collect settling particles. The column was run for one-hour intervals, at which time dried particles would be collected and a fresh petri dish would be placed in the collection chamber. With low flowrates of 0.1 to 0.2 mL/min, the 50 mL fluid reservoir would last for a few hours. If solution ran out, fresh solution would be refilled, but often this would lead to obstructions building up in the pinhole during column downtime. The petri dishes were placed in a vacuum oven at ambient temperature and vacuumed down to 125 mmHg. After drying overnight, the particles were scraped up using a razor blade and stored in a scintillation vial. In general, the yields were low. About 40 mgs of particles could be collected over a preparation that lasted four hours and used 100 mL of particle solution (1% yield).

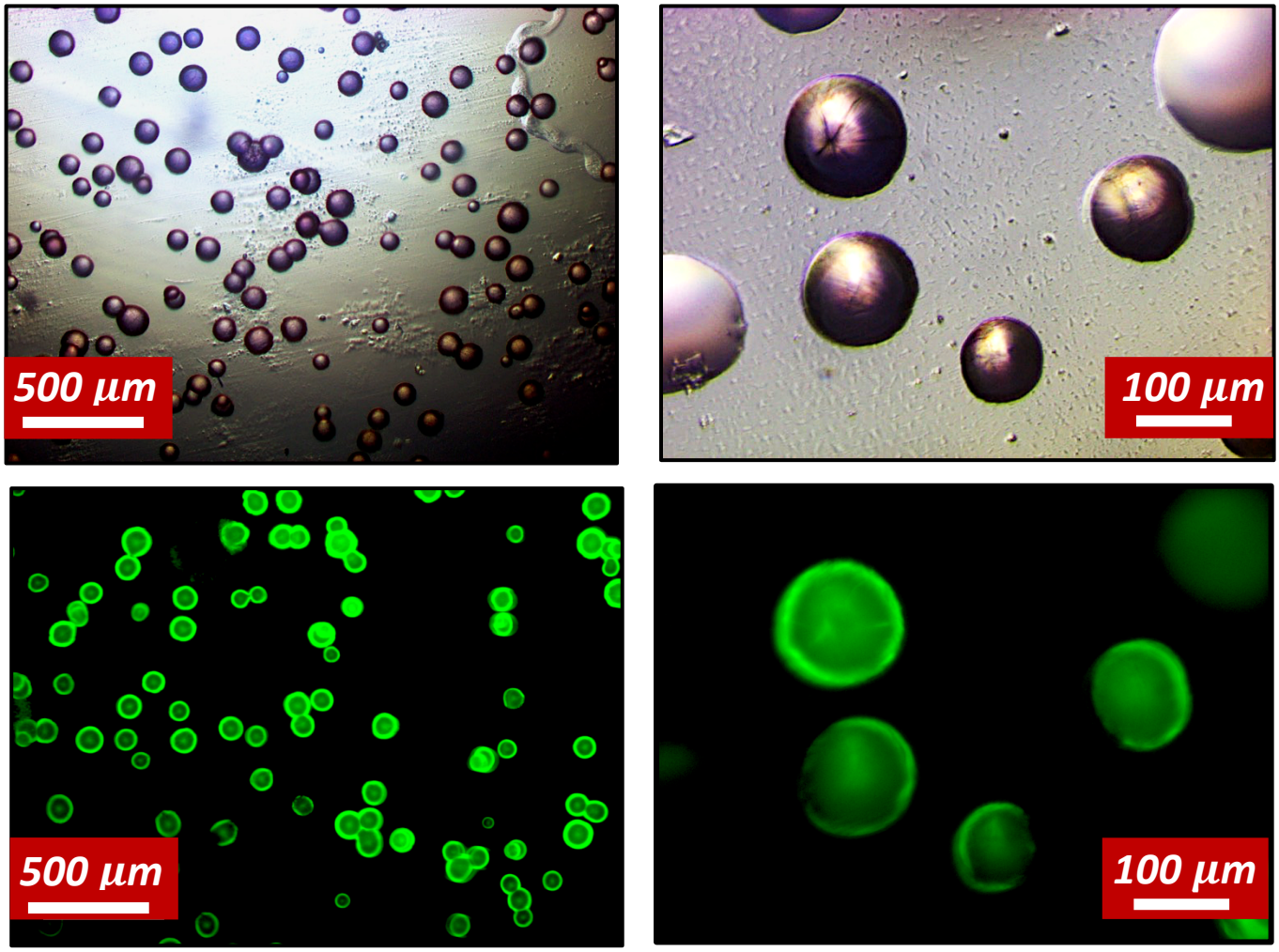

Figure 4.21 – PEG microparticles made with 1% w/w EosinY using 50 µm pinhole. These microparticles were formed using the protocol described in section 7.1. The particles had a flattened morphology from relaxing on the bottom of the petri dish. As seen in the top-right image, particles were not fully dried in the process.

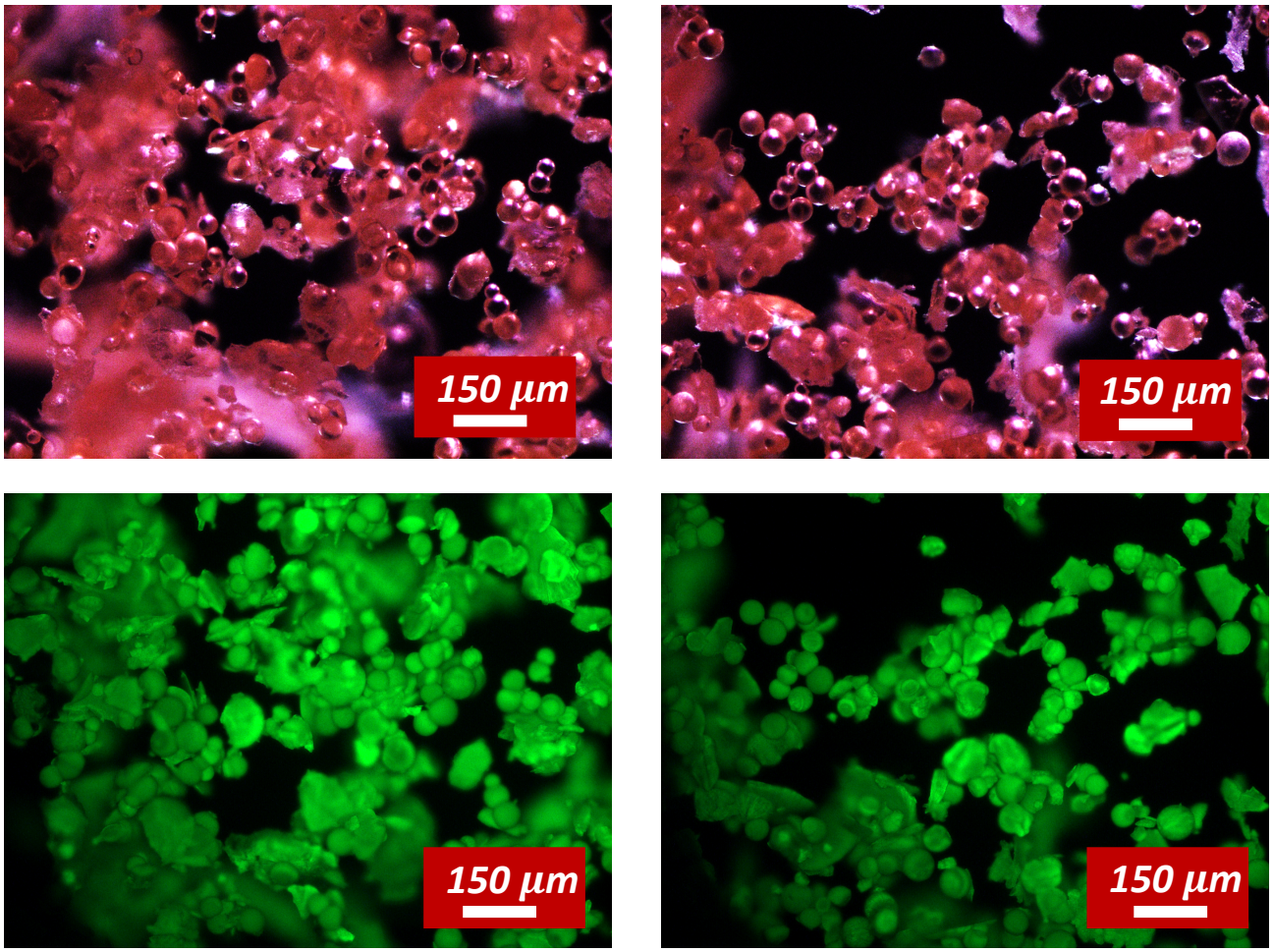

Figure 4.22 – PEG microparticles made with 1% w/w Eosin Y using 35 µm pinhole. The particles were smaller than those formed with the 50 µm pinhole. The particles are round, solid, and stick to one another.

4.6.2 – Description of Microparticles Formed

Using the drying column, several samples of PEG microparticles were prepared. PEG was used due to its biocompatibility and its relatively high density for a polymer (1.125 g/cc). **Figure 4.21** shows the particles that are produced using the 50 μm pinhole, which may not be fully dry. The microparticles formed in this particle preparation were made using a 50 μm pinhole receiving excitation at 17.5 kHz. These images show a distribution of particles that is polydisperse. The microbeads that appear dry are 50-80 μm. The polydispersity is likely due to a distribution of residence times in the column and potential coagulation of droplets. In addition, while monodispersity is checked at the beginning of runs, it is quite likely that particulate matter builds up on the orifice leading to periods where the aerosol is no longer monodisperse. One other interesting facet of these images is the dark stained ring surrounding particles. In many particle preparations that resulted in wet microparticles, this ring phenomenon is observed. The predominant theory for this observation involves the diffusion of charged solutes in wet droplets to the interface between droplet and air. This can lead to subsequent crystallization on the surface, poor drying, and hollow morphologies.[22]

When a smaller pinhole was used, particles like those shown in **Figure 4.22**, were formed. In these figures, clusters of particles can be shown sticking together. There is no discernible Eosin Y ring on these particles, possibly because charged solutes do not have enough time to diffuse to the surface of the droplet before drying. The solid microparticles are all under 50 μm. There was also a good amount of PEG that crystallized on the bottom of petri dishes. This material was scraped up with the rest of the microparticles. Nonetheless, this particle preparation was a success, because it achieved essentially dry microparticles that are in the same size range as our

previous ballistics testing. With these particles set aside and stored under vacuum, they were ready to be placed on macrocarriers and used in our *ex vivo* ballistics experiments.

4.6.3 – Attempts at Making Microparticles with Altered Density

One particle preparation which was never fully realized was the tungsten-loaded, density-modified microparticle. Since the results of Chapter 2 indicate that density is a determining factor in resulting penetration depth, there was impetus to be able to increase the density of our projectiles. To do this, 60 nm tungsten particles (density of 19.2 g/cc) were included in our particle preparation solutions. Solutions were prepared to make 10% w/w tungsten loaded microparticles. This may seem like a high concentration, but since the initial concentration of our base polymer is low, the amount of solids added is low as well. The actual formulation prepared contained 3.6 grams of PEG dissolved in 96 grams of ethanol with 400 milligrams of tungsten particles. Assuming the solution could be kept well homogenized, then our resulting particle density would be $0.9\rho_{PEG} + 0.1\rho_{Tungsten} = 2.93\ g/cc$. Unfortunately, a microparticle preparation with the tungsten solution was not realized. While a stable microjet was initiated with the previously described solution and was imaged for a half hour, each time the solution was tried on the drying column obstructions in the orifice prevented particle preparation, even with the solution reservoir kept homogenized with a sonicating bath. The group is still confident that a solution can be aerosolized into the column using tungsten, acoustic agitation, and a larger pinhole, but the heat duty of the column is going to need to be increased to dry the larger droplets.

4.7 – Conclusions

The work in this chapter spans from testing fundamental operating behavior of a VOAG to the theory and practice of using this technology to form solid microparticles. In order to have information about aerosol feedrates and droplet generation rates, this study required an initial characterization of flow through the VOAG. In addition to typically low operating viscosities, the limitations of instrument operation were pushed using a range of PEG solutions of different viscosity. Once microscopy technology was developed to visualize high-speed droplet trains, our group was able to study the droplet size of trains emitted by the aerosol generator. Size distributions were measured for a range of pinholes over a range of different excitation frequencies. This work was expanded to solutions of PEG, and it was demonstrated how sensitive the VOAG is to changes in viscosity. It was also shown that the device maintains monodisperse production capability for a range of solution viscosities.

Once the group had an understanding of expected solution feed rates for a given pressure and pinhole geometry, and once the frequency ranges were determined that would result in monodisperse droplet production, solid particle preparation was attempted with the custom-built drying column (following heat and mass transfer modeling). It was observed that the 35 μm orifice was able to produce small enough droplets to become fully dry in the column. Despite checks to see if monodisperse droplet streams were being emitted during particle preparations, particle productions came out with polydisperse size ranges. High deviation in particle size is attributed to coagulation in the column and aerosol production where droplets were not monodisperse. Nonetheless, the group was successful in preparing 1% w/w Eosin Y particles with PEG as the base polymer. The size distributions of this particle preparation resulted in

particles of sizes 30 to 50 μm. In the end, the broad library of microparticle size and composition that was desired could not be produced, due to time constraints and difficulties avoiding pinhole obstruction. With higher heat duties to the column, slightly larger pinholes, and improved dispersion of droplet trains entering the column, it is expected that it will become easier to make dry microparticles. A rich potential research project involves making particles containing density-boosting metal nanoparticles to increase the embedding energy of therapeutic microparticles.

4.9 References

1. Berglund, R. N. & Liu, B. Y. H. Generation of monodisperse aerosol standards. *Environ. Sci. Technol.* **7**, 147–153 (1973).
2. Jayanthi, G. V., Zhang, S. C. & Messing, G. L. Modeling of solid particle formation during solution aerosol thermolysis: The evaporation stage. *Aerosol Sci. Technol.* **19**, 478–490 (1993).
3. Levendis, Y. & Flagan, R. Comustion of uniformly sized glassy-carbon particles. *Combust. Sci. Technol.* **53**, 117–36 (1987).
4. Levendis, Y. & Flagan, R. Synthesis, formation and characterization of micron-sized glassy-carbon spheres of controlled porous structure. *Carbon N. Y.* **27**, 265–83. (1989).
5. Alemrayat, B., Elrayess, M. A., Alany, R. G., Elhissi, A. & Younes, H. M. Preparation and optimization of monodisperse polymeric microparticles using modified vibrating orifice aerosol generator for controlled delivery of letrozole in breast cancer therapy. *Drug Dev. Ind. Pharm.* **44**, 1953–1965 (2018).
6. Huynh, J. Factors Governing Photodynamic Cross-Linking of Ocular Coat (2011).
7. AliceD. What's the smallest size a human eye can see? *stackexchange.com.biology* (2014).
8. Lindblad, R. & Schneider, J. Production of uniform-sized liquid droplets. *J. Sci. Instrum.* **42**, 635–638 (1965).
9. Schneider, J. & Hendricks, D. Source of uniform-sized liquid droplets. *Rev. Sci. Instrum.* **35**, 1349–1350 (1964).
10. Kimmel, E. C. & Leahy, H. F. & Carpenter, R. L. A high pressure aerosol generator for viscous fluids. *Nav. Med. Res. Inst. Armstrong Lab.* 1–33 (1991).
11. Wolf, K. P. W. & Groves, W. United States Patent (19). (1994).
12. Reitz, R. D. Modeling atomization processes in high-pressure vaporizing sprays. *At. Spray Technol.* **3**, 309–337 (1987).
13. Sutherland, J., Sojka, P. & Plesniak, M. Ligament-controlled effervescent atomization. *At. Sprays* **7**, 383–406 (1997).
14. Broniarz-Press, L., Ochowiak, M., Rozanski, J. & Woziwodzki, S. The atomization of water-oil emulsions. *Exp. Therm. Fluid Sci.* (2009). doi:10.1016/j.expthermflusci.2009.04.002

15. Brenn, G. & Lackermeier, U. Drop formation from a vibrating orifice generator driven by modulated electrical signals. *Phys. Fluids* **9**, 3658–3669 (1996).
16. Lindner, A., Vermant, J. & Bonn, D. How to obtain the elongational viscosity of dilute polymer solutions? *Phys. A Stat. Mech. its Appl.* **319**, 125–133 (2003).
17. Frankel, I. & Weihs, D. Influence of viscosity on the capillary instability of a stretching jet. *J. Fluid Mech.* **185**, 361–383 (1987).
18. Yu, J. H., Fridrikh, S. V. & Rutledge, G. C. The role of elasticity in the formation of electrospun fibers. *Polymer (Guildf).* **47**, 4789–4797 (2006).
19. Bird, R., Stewart, W. & Lightfoot, E. *Transport Phenomena*. (1960).
20. Levendis, Y. A fundamental study of char oxidation kinetics using model materials. (1988).
21. Ethanol: Antoine Equation Parameters. *NIST Webbook* (2018).
22. Emami, F., Vatanara, A., Park, E. J. & Na, D. H. Drying technologies for the stability and bioavailability of biopharmaceuticals. *Pharmaceutics* **10**, 1–22 (2018).

Chapter 5

TECHNOLOGY DEVELOPED AND DIRECTIONS FOR THE FUTURE

5.1 – Plans for Future Experiments

Work done to further develop this technology first and foremost involves delivering microparticles to gel and tissue under atmospheric pressure. While the PDS1000 was a helpful tool in that it delivers particles at high velocity and with uniform coverage of the target substrate, it uses an evacuated chamber to embed microparticles. The device likely uses an evacuated chamber to increase the speed of the microcarrier (throttling from a high pressure to a low one increases the overall velocity during an isentropic expansion). Aerodynamic relaxation of a microparticle is not affected by pressure, so it should be investigated whether particles can be delivered at atmospheric pressure by carefully controlling microparticle acceleration. Towards this goal, a device was built that aerodynamically focuses particles into a narrow acceleration capillary. This device was built to accelerate microparticles with a low collision rate and a low volume of gas that can be easily diverted.

In addition, it is also of interest to characterize tissue damage in response to biolistic particle embedding and to test various particle formulations on *ex vivo* corneal tissue. Experiments should be done to assess tissue damage in response to different particle sizes and velocities. Using fluorescein isocyanate solutions, damage to the corneal epithelium can be quantified and tracked over time. An animal model can be used to track inflammation induced from the ballistic

treatment. Different microparticle compositions and morphologies should be investigated for their ability to embed and dissolve in tissue. In addition to testing therapeutic microparticles with increased density, it would be interesting to test the effect of microparticle aspect ratio on embedding depth. Ultimately, our group wants to know if there are ways to cause deeper penetration than what has been observed, if there is a deleterious effect of ballistic particles on tissue, and if compounds can be delivered to tissue with high bioavailability.

5.2 – Ballistic Delivery of Model Microparticles Under Atmospheric Pressure Using an Aerodynamically Lensed Particle Acceleration Device

Moving away from the PDS1000 gene gun, our group decided to build a custom device which had interchangeable parts that could be used to optimize particle ejection velocity. There were two major constraints in our design of a particle delivery device. First, particles were desired that had at least the embedding power observed using the PDS1000. To this aim, a device with interchangeable components was conceived to find design parameters (e.g. barrel length and diameter) that would allow for optimal ejection velocity. Second, our device was built with the goal of eliminating compressed-gas shockwave emission that can be harmful to tissue. Our design was made to use a low volume of gas, which would be easily diverted from exposed tissue. The device incorporated an aerodynamic lens to more carefully feed microparticles to the acceleration capillary. This initial focusing will hopefully lead to lower amounts of particle-wall and particle-particle collisions. To build a device with dose-control, our group also meant to incorporate a pressurized microparticle feeder, but this was never realized.

5.2.1 – Theory Behind Operation and Examples of Aerodynamic Lens Devices

Aerodynamic lenses are used to concentrate streams of microparticles or nanoparticles into thin beams for sample enrichment in aerosol mass spectrometry and preparation of patterned microstructures.[1,2] Aerodynamic lenses are formed by combinations of properly designed axisymmetric contractions and expansions. A key feature of most aerodynamic lenses is that they operate at low pressures (typically <100 mtorr). These low pressures are chosen to decrease the Stokes Number of a microparticle traveling through the lens system and also because most applications of aerodynamic lenses require low pressures (i.e. aerosol mass spec.). The Stokes Number relates the relaxation time of a microparticle's momentum to the relaxation time of the surrounding fluid. Having a Stokes Number that is too high will result in a particle that impacts aperture walls instead of following fluid streamlines. Having a Stokes Number that is too low results in particle defocusing soon after exiting the lens orifice. A Stokes Number equal to unity results in optimal focusing. The aerodynamic relaxation time of a microparticle assuming Stokes Drag has already been shown in Chapter 2. The Stokes' Number is the ratio of this value to the relaxation time of the fluid $\tau_f = \frac{d_o}{U}$, resulting in the following expression:

$$St = \frac{C_d \rho_p D_p^2 U}{18 \mu d_o} = \frac{C_d \rho_p D_p^2}{18 \mu D_o} \left(\frac{\dot{m}}{\rho_g \pi D_o^2} \right) = \frac{C_d \rho_p D_p^2 \dot{m}}{18 \mu \rho_g \pi D_o^3} \quad (1)$$

where U is the gas velocity, C_d is the drag coefficient, ρ_p is the particle density, D_p is the particle diameter, μ is the dynamic viscosity, d_o is the orifice diameter, $\dot{m}$ is mass flowrate through the orifice, and ρ_g is the density of the flowing gas. To calculate aerodynamic relaxation times of the fluid as a function of pressure, an empirical expression accounting for mass flow through the orifice has to be introduced. In this expression both the total pressure of the system and the pressure drop across the orifice are critical[3]:

$$\dot{m} = A_o \frac{C_D Y}{\sqrt{1-\beta^4}} p_1 \sqrt{\frac{2M}{RT_1}\frac{(p_1 - p_2)}{p_1}} \quad (2)$$

where A_o is the area of the orifice, β is the contraction factor equal to the orifice diameter divided by the spacer diameter, Y is an expansion factor which accounts for the effect of compressibility on the flowrate, p_1 is the upstream pressure, p_2 the downstream pressure, M is the molar mass of the gas, R is the gas constant, and T is the upstream pressure. Since total pressure is a variable that drives up Stokes Numbers, it makes sense that most aerodynamic lenses are operated at such low pressures. An example of an aerodynamic lens is described in Benner et al. In this paper, the total pressure drop from particle collection inlet to detector is from atmospheric pressure to 10^{-6} torr. However, between these two elements is an aerodynamic lens train which uses differential pumping. Particles enter through a filter and into a chamber evacuated down to 1-15 torr. Particles get concentrated through a 2 mm ID tube with a series of six increasingly-narrow orifice discs (1.93, 1.76, 1.61, 1.48, 1.37, and 0.966 mm orifice diameters). Across these lens elements, the total pressure drop is low (1-15 torr). Finally, particles pass an orifice disc into a chamber evacuated to 10^{-6} torr and on to pass two charged aerosol detectors. From this example, it can be learned that both total pressure and pressure drops across orifices in aerodynamic lens trains are typically low.[4]

While aerodynamic focusing is possible at higher pressures, there are certain design constraints regarding turbulent flow that must be considered. Mainly, at atmospheric pressure, there is a limitation to how many aerodynamic constrictions can be used, their spacing, and their width (they cannot be too narrow if multiple discs are used; $\beta < 0.5$). This limitation has to do with the formation of jets in narrow orifices. Throttling from a high pressure to a low pressure is

associated with a Reynold's Number and the higher the Reynold's Number, the more jet-like and turbulent flow becomes. Reynold's number through an orifice is directly proportional to particle pressure:

$$Re = \frac{dv\rho}{\mu} = \frac{dvPM}{\mu RT}. \quad (3)$$

Reynold's Numbers were calculated at the beginning of our investigation to characterize turbulent behavior of gas traveling through tubing in the aerodynamic lens. An inner diameter of a lensing orifice of 0.75 mm was considered to greatly lower the Reynold's Number and to represent a design for an aerodynamic lens discussed shortly. A low expected helium flowrate of 1 standard liter per minute was assumed. The raise in the expected Reynold's Numbers for a range of pressures is shown in Table 5.1:

Table 5.1 – Reynold's Number of gas flowing at 1 SLPM through a 0.75 mm tube

Pressure [torr]	Reynold's Number
1500	494.0
760	250.0
100	32.9
10	3.3
1	0.3

As can be seen, by using atmospheric lenses at higher pressures, the Reynold's Number of flow through the orifice approaches the laminar to turbulent transmission regime. While focusing is still possible, the existence of high Reynold's Number flows through the orifice is indicative of a more jet-like flow than is typically found in aerodynamic lenses. The presence of high Reynold's

Number flows assures transition of a jet to turbulent flow in the transient, latter portion of the jet. Higher Reynold's Number flows display a quicker transition from laminar to turbulent flow downstream of the orifice. For this reason, successive narrow orifices, as used in the previously described aerodynamic lens train example, cannot be usefully employed. If lenses were spaced far apart to allow for redevelopment of laminar streamlines, particles would be defocused by transience in the jet-like flow. If lenses were placed close together, there would be a series of jets feeding through the orifices without development of the lensing streamlines needed for focusing. While orifices with several relatively wide orifices can be used with one narrow orifice, once a jet-like flow is encountered, putting multiple lensing discs in series will only act to defocus the particles.

An example of an aerodynamic lens designed by another lab that operates at close to atmospheric pressure (730 to 760 torr) is in Deng et al. In this work, a single aerodynamic constriction was used to create the desired lensing effect. 1 to 10 μm particles were charged through a 1.6 mm ID tube with a 0.75 mm outlet. Particles were lensed to beams of diameters down to 500 μm using a differential pressure drop of 5 to 25 torr.[5] The low pressure-drop results in Stokes Numbers close to one needed for particles to be aerodynamically focused in the particle diameter range of interest. In addition to the high lensing effect reported in this paper, the transmission efficiency (the percentage of particles that make it through the aerodynamic lens) was high as well. The transmission efficiency was 90% for 2 μm particles and dropped to 60% for 8 μm particles. The aerodynamic lens was designed to have Stokes Numbers, shown in Table 5.2 (calculated with Equation (1)), that are close to unity. These values indicate that if flow gets higher than 1 SLPM, particle Stokes Numbers will get larger and lensing quality will degrade.

Table 5.2 – Stokes Number of different particles flowing through a 0.75 mm orifice at a flowrate of 1 SLPM

Dp [μm]	Stokes Number
1	0.2
3	1.4
5	3.8
8	9.7
10	15.1

5.2.2 – Design of Device for Ballistics Experiments at Atmospheric Pressure

Our group incorporated the geometry of the aerodynamic lens in Deng et al. into a design for a ballistic device. A schematic of the ballistic device which uses readily purchased tubing and easily machined components is shown in **Figure 5.1**. The device works such that a pressure drop can be controlled across an aerodynamic lens component. A continuous stream of gas flows through the device until it is discharged immediately over an orifice disc. The space between the outlet and the orifice disc is small (~ 1 mm), to maintain lensing streamlines in the flow of gas (magnified portion of Figure 5.1). The pressure drop is controlled by using an outlet for gas connected to vacuum, a proportional valve to control P_1, and an inlet for compressed gas connected to a proportional valve to control P_2. For particles that make it through the orifice disc, there is a piece of capillary tubing (1.6 mm OD; 0.1 to 0.5 mm ID) that accepts microparticles and accelerates them for a length of about 15 centimeters. This tubing is interchangeable, so the ideal acceleration barrel can be incorporated into the device by using iterative design optimization.

The aerodynamic lens in Deng et al. was demonstrated using ten-micron microparticles and smaller. To determine compatibility with our new device design, computational fluid dynamics calculations were run in ANSYS Fluent to generate expected flow fields within the device. Then, particles were seeded into the regions of flow upstream of the lensing tube and trajectories were calculated, using an empirical expression for drag and Newton's Second Law of Motion. As a first step of our analysis, a geometry was built using a 1.6 mm tube discharging into a much larger atmosphere. The geometry conceived, which is shown in **Figure 5.2,** reveals a 1.6-mm-diameter tube discharging into an atmosphere with a diameter of 3 centimeters. The gas chosen in our simulations was helium for its ability to reduce Reynold's Numbers (due to its low density as a function of pressure) and for its high speed of sound. A low pressure-drop was chosen from tube to expansion chamber (10 torr), but a turbulent model was used to account for momentum dissipation. As can be seen in Table 1, even low flowrates for a gas flowing through a small geometry (1 SLPM) have Reynold's Numbers that indicate turbulence. The orifice was constructed with 0.25-mm-radius rounded fillets and high mesh density in the throat of the model orifice. A $k-\epsilon$ model was used to account for momentum dissipation. When the velocity magnitude for this steady-state simulation is plotted, it can be seen that there is a jet-like structure to flow through the orifice. Examining the Reynold's Numbers for this situation, it is seen that in the throat of the orifice, values can be found that are greater than 2300, the cut-off between laminar and turbulent flow.

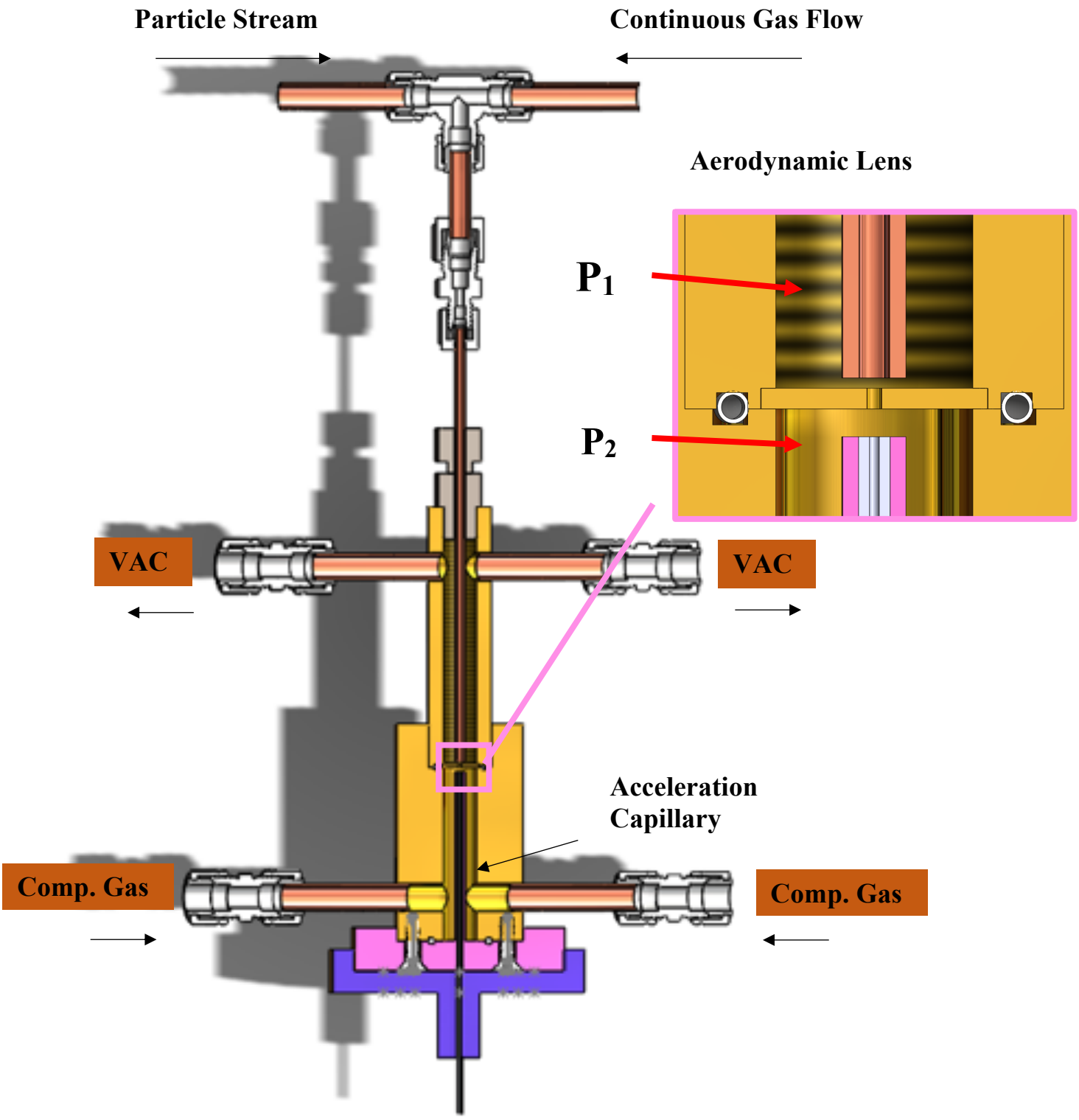

Figure 5.1 Design of aerodynamic-lens-assisted micropowder ejector. The device works by using a continuous stream of gas that is lensed across an interchangeable orifice disc. A valve is opened to introduce particles into the device. Two proportional valves control the pressure in the lensing region at P_1 and P_2. Particles are lensed into an interchangeable acceleration capillary.

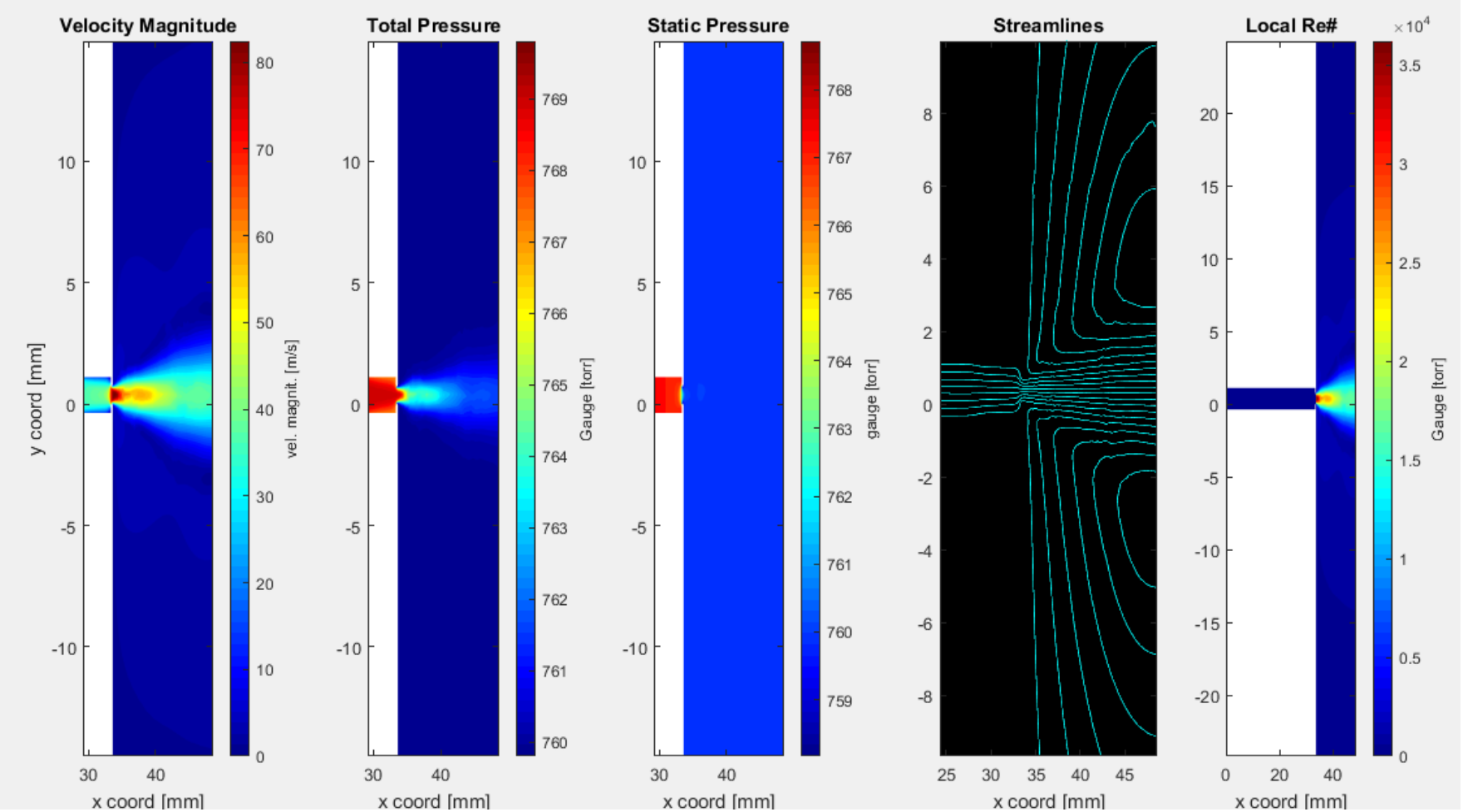

Figure 5.2 CFD calculation for a 1/16th in tube discharging into a larger atmosphere. The heat map of the gas velocity magnitude shows a jet-like structure as compressed gas flows through a narrow orifice. Total pressure is the sum of dynamic and static pressure. The streamlines in flow reveal lensing structures. Turbulent models for momentum dissipation must be used, due to high Reynold's Numbers in the throat of the orifice.

Despite these signs that indicate that the flow is jet-like, when streamlines are plotted in the throat of the orifice, the quickly converging and slowly diverging streamlines associated with an effectively designed aerodynamic lens can still be seen. In addition, there are zones of gas recirculation flanking the jet exiting the orifice. To determine how long jets can be made before becoming unsteady, the simulation was extended such that the relaxation chamber was longer. It was found that after about 1.5 centimeters, the jet starts to diverge and flow along one side of the chamber wall. From this analysis, it was concluded that a jet could be kept steady for about 1.5 centimeters.

After showing that lensing structures in the flow streamlines could be generated in a CFD simulation, it was next investigated to see what would happen when particles larger than 10 μm

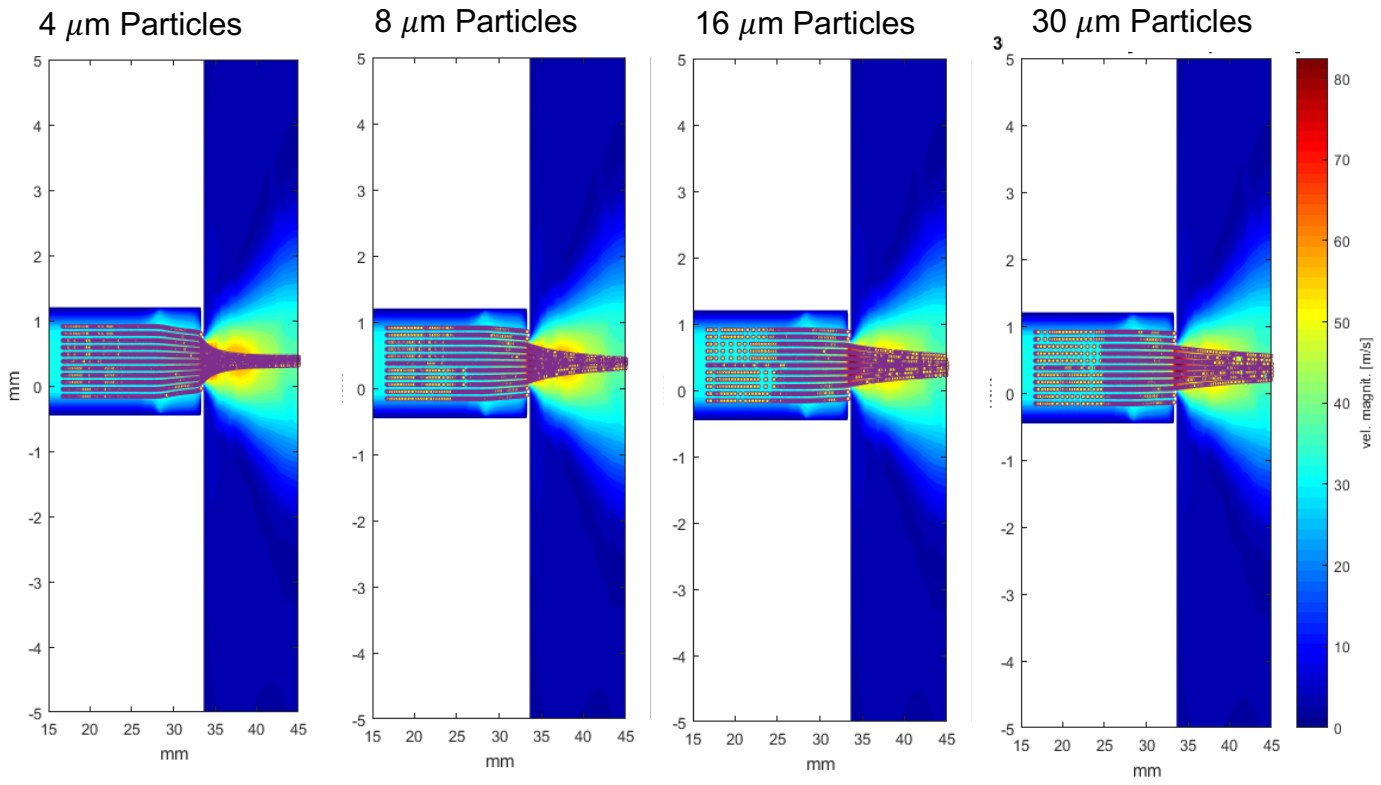

Figure 5.3 Trajectories of different particle sizes in the aerodynamic lens. 4, 8, 16, and 30 μm particles are seeded in the lensing tube. When particles collide with a wall, their trajectory stops. Particles are lensed to lesser extents as particle size is increased.

microparticles were introduced into the tube. Particles were seeded at different values of $\alpha = r_{pi}/r_t$, where r_{pi} is the upstream radial component of the particle's position and r_t is the tube radius. **Figure 5.3** reveals the results of our analysis in which larger microparticles are focused to lesser extents 1 cm outside of the orifice disc. In this figure, the 4 μm microparticles show ideal focusing. All microparticles, with $-0.3 \leq \alpha \leq 0.3$, have low enough Stokes' Numbers to get through the orifice without impacting the walls. The generated beam is thin, around 250 μm in diameter. As particles get larger, there are more impacts with the walls and the focused beam starts to get wider. 8 μm microparticles show impacts with $\alpha > 0.2$ and with $\alpha < -0.2$, but a thin beam is still generated as particles flow through the orifice. When particles are 30 μm, the particle beam has grown to a diameter slightly less than 500 μm. The results of this analysis show that while transmission efficiency may be affected by particle size, particles can still be effectively lensed to a beam < 500 μm in diameter using this geometry and a low pressure drop.

After assessing the performance of the lens on its own, our group wanted to see how it would perform when placed in series with an acceleration capillary. To do this, the geometry described in Deng et al. was constructed in ANSYS Fluent. The jet was set up to discharge into a 0.25 mm ID capillary that is 15 cm long. Boundary conditions were set such that the lens tube was kept at 1 bar, the ends of the expansion chamber were set at .987 bar (-10 torr gauge pressure), and the end of the acceleration capillary was at atmospheric pressure. The results of the simulation in **Figure 5.4** show particles getting focused at a point close to the orifice outlet, and then the beam begins to diverge. Before the beam fully diverges, the converging streamlines entering the acceleration capillary work to refocus the particles before they travel down the length of the tube.

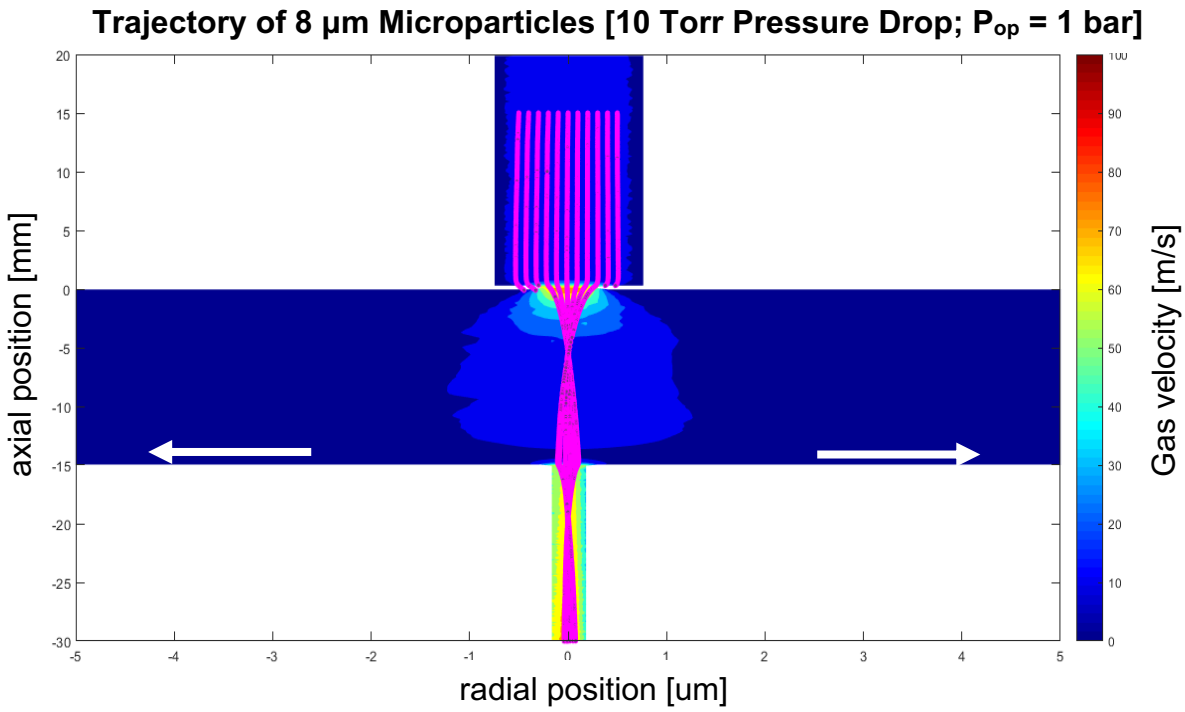

Figure 5.4 - Trajectories of 8 µm particles in series with acceleration capillary (10 torr Δ*P*). The particles are lensed into a beam that then diverges slightly before entering the acceleration capillary, where it is again focused by converging gas streamlines.

The flow field attained in these simulations does not show smooth transitions in the magnitude of gas velocity - contours shown in **Figure 5.4** are not smooth like they should be. The reason for this was the mesh density in the expansion chamber being too low to show smooth transitions.

The rest of the simulations show sufficient lensing when the orifice disc is put in series with an acceleration capillary. Simulations for particles smaller than 8 µm and larger are shown in Appendix D.1. Down to 4 µm particle diameters, focusing is effective. Below this size threshold, defocusing occurs and the effects of the lensing disc are nullified. Increasing particle size from 8 µm leads to a streamline cross-over point that moves further and further from the orifice disc. **Figure 5.5** shows the trajectory of 30 µm particles. While collisions with the orifice walls are

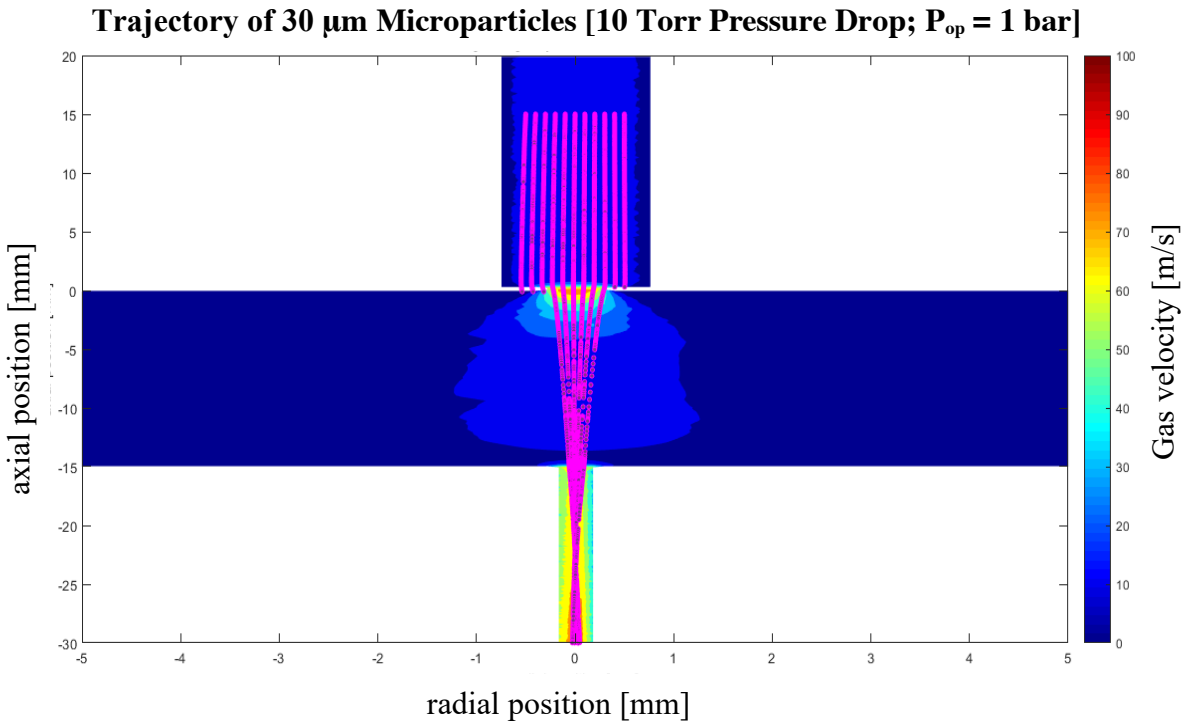

Fig.ure5.5 - Trajectories of 30 µm particles in series with acceleration capillary (10 torr Δ*P*). The particles are lensed into a beam that focuses part of the way down the acceleration capillary.

high, there is still effective focusing that creates a cross-over point about a centimeter down the length of the acceleration capillary. When particles enter the acceleration capillary, they have a high enough Stokes Number such that their trajectory is undisturbed by gas entering the narrow acceleration tube.

In addition to testing a range of particle sizes, different pressure drops were tested across the acceleration capillary. With higher pressure drops comes a greater mass flowrate of air moving through the tube. This creates a potential for collisions with tube walls when they enter the acceleration capillary. **Figure 5.6** reveals what happens when particles are not lensed into the acceleration capillary with a higher operating pressure. After particles travel through the orifice,

the particle beam defocuses and particles spread out radially around the inlet of the acceleration capillary. Then when particles enter the acceleration capillary, the converging streamlines of gas lead to a transfer of radial momentum and collisions between particles and the walls of the capillary. One of the benefits of using an aerodynamic lens in a ballistic device is reduction of these particle collisions. In Appendix D.1, the data charting particle trajectories shows that severe delensing occurs for particles less than 12 in diameter. The focusing effect for particles 12 μm and larger is still effective in threading particles down the centerline of the acceleration capillary. However, this exercise reveals the importance of controlling the pressure drop across the aerodynamic lens and effectively lensing particles.

After determining that the aerodynamic lens would work with the range of particles selected, it was investigated how well microparticles could be accelerated using a 15 cm acceleration capillary. To do this, particles were seeded in the flow fields of our CFD calculations and acceleration was assessed along the length of a capillary. Pressure drops across the acceleration capillary were selected to be 1 and 2 bar. The results of simulations showed that small microparticles could be accelerated efficiently. In **Figure 5.7**, it is shown that 4 μm microparticles are ejected from the capillary at 200 m/s with a driving pressure of 1 bar and at 250 m/s with a driving pressure of 2 bar. On the other hand, 30 μm microparticles would have an ejection velocity of 60 m/s with driving pressures of 1 bar, and only 80 m/s with driving pressures of 2 bar. In between this size range, particles still have high velocity, but it is worth noting that as larger particles are used, slower ejection velocities are realized. It is interesting to note that velocity drops linearly with particle diameter, in contrast to Equation (17) in Chapter 2.

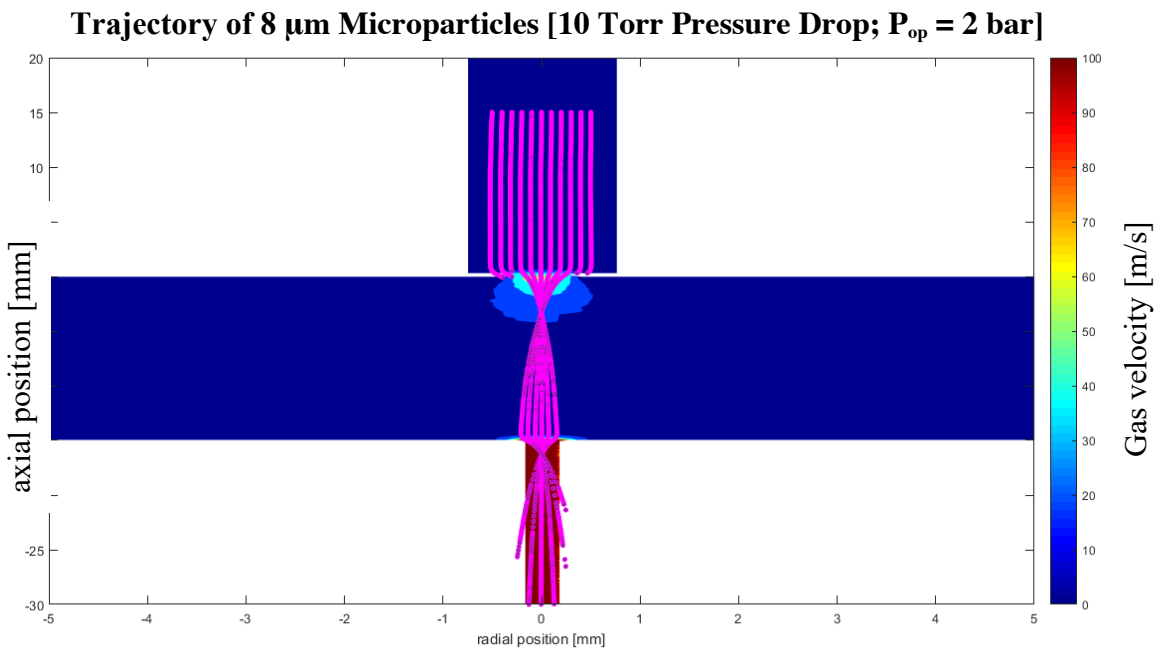

radial position [mm]

Figure 5.6 - Trajectories of 8 µm particles in series with acceleration capillary (10 torr ΔP; 2 bar operating pressure). The particles defocused using a higher pressure drop across the aerodynamic lens.

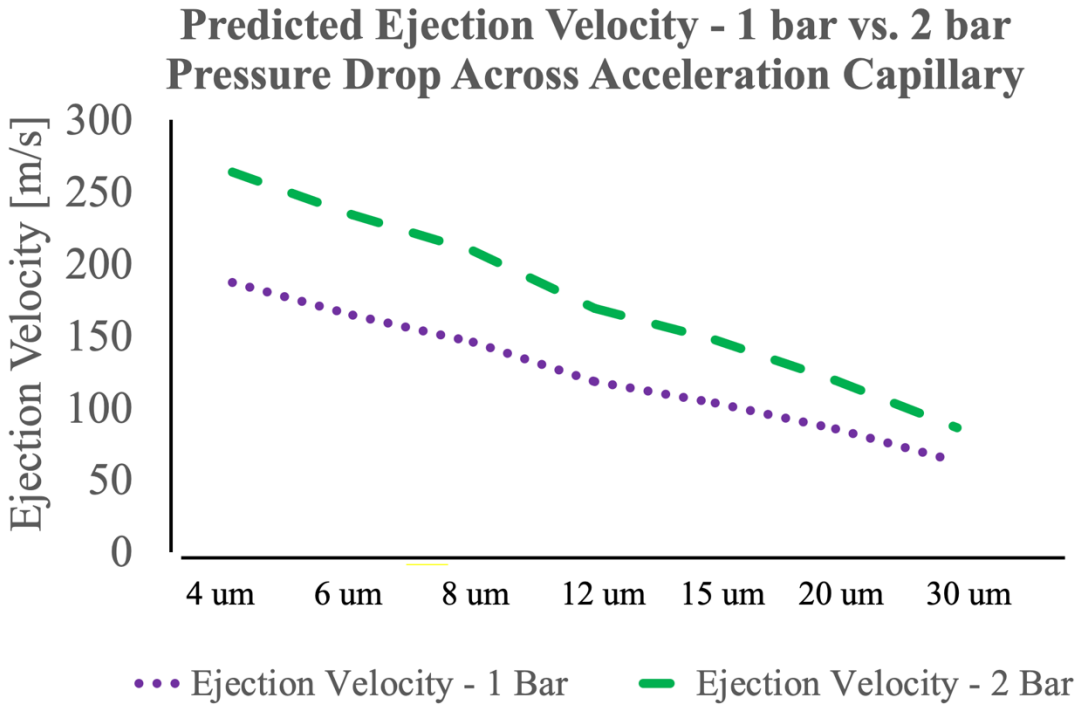

Figure 5.7 – Expected ejection velocities in custom ballistic device. Using the CFD calculated flow field, the expected ejection velocity of microparticles traveling through the device was calculated.

5.2.3 – Design of Experiment to Optimize the Device

In order to relate how the device should be optimized, the possible benefits of using aerodynamic lensing in our ballistic device should first be discussed. The following are hypotheses about potential device performance when using aerodynamic lensing:

1. By focusing microparticles into thin beams that can be adjusted using proportional valves, more consistent particle feedrates can potentially be achieved. With the use of a charged aerosol detector and a more reproducible method to feed particles to the device, particle efflux rates can be correlated to pressure drop across the aerodynamic lens with monodisperse beads. Consistent beam widths could translate to consistent particle flux.
2. Aerodynamic lenses could have the ability to "thread the needle" of thin capillaries - to feed focused beams down the centerline of acceleration tubes. As seen in previous simulations of particle trajectories, an unfocused particle stream is more likely to collide with the walls of the capillary, especially in the entrance to the tube. If collisions can be reduced using aerodynamic focusing, it is possible that higher velocities can be attained.
3. By concentrating microparticles into a beam, there could be higher amounts of penetration in tissue. In the work of Veysset et al, it was shown that when microparticles embed in a soft substrate, there is a thin, capillary shaped depression that forms continuous with the surface of the material.[6] This cavity, which is many times longer than the particle radius, quickly rebounds and yields around the particle after a maximum penetration depth has been achieved. It is possible that if many particles are colliding with a surface at once, these zones of depression will overlap and there will be a synergistic effect on particle penetration depth.

In order to determine if these potential benefits can be realized, there are several investments in equipment that should be made. As stated above, in order to determine particle efflux rates, a measurement device needs to be used to count the number of particles exiting the ballistic device every time it is actuated. A condensation particle counter can be used, which uses aerosol particles as droplet nuclei and then detects them using a laser and a photodiode. The particles used in our research may be large enough to count using laser beam interaction without condensation, but this device can be used regardless. Another option would be to use a charged aerosol detector, which is frequently used in HPLC applications. In these devices, aerosolized solutions flow past a corona needle, picking up charge, and then an electrometer determines the amount of charged material in the gas flow.

In order to determine if aerodynamic focusing improves particle acceleration, and to ultimately optimize the device, a robust way of measuring particle velocity should be developed. In **Figure 5.8**, relatively large microparticles (150 – 180 μm) were imaged using a highspeed camera and an exposure time of 1 μsec. If exposure times are adjusted, then velocities can be inferred based on the changing lengths of streaks. However, there really should be a quicker, more reliable way than this to measure particle velocity (especially for smaller projectiles). For example, if a Laser Doppler Anemometer (LDA) is used, then particle velocity distributions can be recorded instantaneously. The detector will need to be tuned so that the velocity of microparticles is measured, and not the velocity of the gas, but with a measurement device from Measurement Science Enterprises, LLC, which is used frequently to measure the velocity of microparticles, this should not be a problem.

Last, a method should be used to determine penetration depth more quickly than looking at substrate cross-sections. In the past year, a method has been devised that involves using optical coherence tomography (OCT) to map particles in a gel volume. While a visual defect called autocorrelation can occur, this problem can likely be solved by coating treated gels with a layer of agarose to cover the particle treated surface. Using this method along with three-dimensional thresholding software will result in a rapid way to compare particle penetration depths, especially when different particle efflux rates are chosen using the aerodynamic lens.

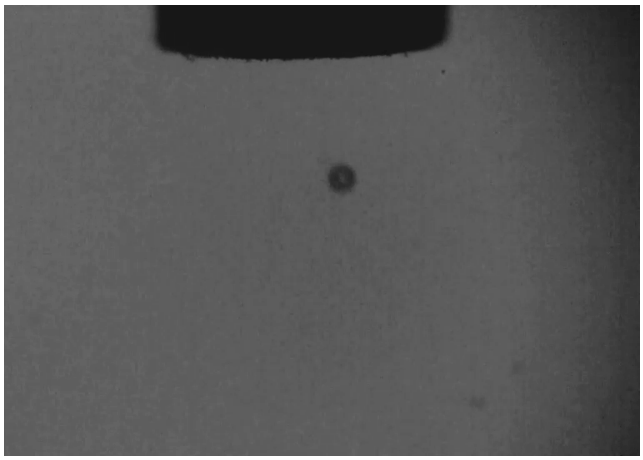

Figure 5.8 – 180 µm soda-lime glass microparticle filmed with highspeed camera. Ejection event filmed using camera at 1024 frames per second. Exposure time of camera was 1 microsecond and particles were illuminated with rear halogen lamp.

In addition to testing these potential benefits of the aerodynamic lens, it is necessary to run a multifactorial design of experiment analysis (DOE) to optimize the embedding power of the ballistic device. The two response variables which will be used in the DOE will be average speed calculated from the particle velocity distribution (measured with the LDA) and particle efflux rate (measured with a charged aerosol detector). In general, the average particle velocity will be used to optimize the device, but the particle efflux rate will be considered as well. There are five design variables that can be quickly changed due to the modularity of the ballistic device. The

first variable is the operating pressure of the device, the pressure at the top of the acceleration capillary. This pressure is altered using a combination of proportional valves and an upstream gas regulator. The second variable is the lensing pressure drop across the aerodynamic lens. Third is the diameter of the aerodynamic lens orifice. This can be changed by switching out the lensing inserts in the device. Last, the diameter and length of the acceleration capillary can be changed just by switching the tubing in the device. By iteratively changing all of these parameters, and by using monodisperse, consistent particle standards charged at different pressures, the ballistic device can be optimized by maximizing ejection velocity. One thing that the DOE analysis will be dependent on is a more reproducible method to feed microparticles into the device.

5.2.4 – Final augmentations of the ballistic device

There are three essential augmentations that must be completed before meaningful optimization and research can be done with the ballistic device shown in **Figure 5.9**. First, in order to perform a DOE and also to control rates of particle delivery to target substrates, there needs to be a more reproducible way to feed microparticles to the ballistic device. Second, in order to have reproducible lensing pressures, there should be a PID control scheme introduced to modulate aerodynamic lens pressures. Third, in order to protect the surface of target substrates, to maximize particle impact velocities, and to control the ultimate comfort of patients treated with this device, a strategy needs to be implemented to divert compressed gas from the outlet of the device.

Figure 5.9 – Assembled ballistic device with connections for controlling aerodynamic lens. The pressure drop across the aerodynamic lens is regulated by two inlets for compressed gas on the bottom of the lensing chamber and two outlets connected to vacuum on the top lensing chamber.

Currently, to load particles into the ballistic setup, either particle-coated tubes are nested in the plumbing of the device, or ~ 1 mg quantities of particles are emptied into the device above a closed valve (prior to actuation). In order to determine if aerodynamic lensing is working, a more reproducible way to introduce particles must be incorporated. In addition to this, the number density of particles in pulses emitted by the device is currently too high. Our group ran preliminary experiments using the new ballistic apparatus on corneal tissue. When 10-22 μm soda-lime spheres were ejected using the ballistic device with helium pressurized at 5 bar (without aerodynamic lensing), there was considerable penetration, but as **Figure 5.10** shows, there is a pile-up of microparticles in the corneal epithelium. Since the highest penetration of microparticles were found in these areas where the particle density was high, as opposed to areas in the periphery of the particle delivery zone, this data suggests that there may be synergistic effects leading to improved penetration by having a high number density of particles hit a surface at once.

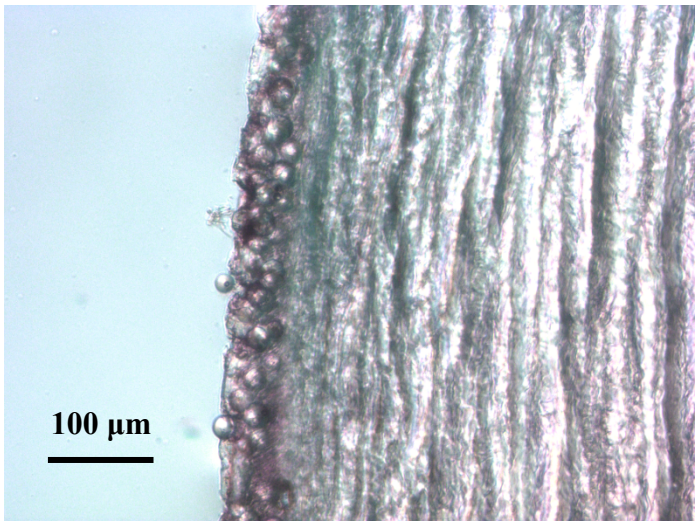

Figure 5.10 – 10-22 μm soda-lime microspheres ejected with custom ballistic device into porcine cornea. Particles pile up in a thick layer on the corneal epithelium when delivered under atmospheric pressure.

This data also suggests that the ballistic device requires an improved mechanism to feed particles and limit such high ejection rates. There are many potential strategies to fluidize micropowders that can be borrowed from literature. The goal is to introduce particles in a way that the duration of pulse injections and the concentration of particle feeds can be adjusted. In Yang et al., micropowders were fluidized using a combination of mechanical agitation and acoustic vibration. This design allows for different particle feed rates by extracting microparticles from different points along the axis parallel to the particle fluidization direction.[7] Our own microparticle feed chamber would have to be raised to high enough pressure in order to inject particles into the ballistic device, but with mechanical agitation and a solenoid valve timed to control pulse duration, it is likely that a much more reproducible form of particle introduction into the device could be achieved.

Similarly, the procedure used to set the pressure across the aerodynamic lens orifice makes it hard to dial in to exact pressures. The procedure starts by opening several valves that are displayed in **Figure 5.11**. Valves one and three are opened sequentially, then valves four and five are opened simultaneously. Suddenly exposing the membrane which transduces pressure to too high of a pressure drop can cause damage to the sensor. With this valve arrangement, the pressure in the top of the lensing chamber can be fed such that equal pressures are exposed to each side of the pressure transducing membrane. In **Figure 5.11C**, the pressure drop across the aerodynamic lens is plotted. It is first shown that there is a slight pressure drop even when the two sides of the sensor are reading the same pressure. This is indicative of a small leak in the plumbing of the system. Regardless, with the absolute pressure read simultaneously (using the digital absolute pressure gauge), a pressure that is ~0.3 bar lower than this is regulated and sent

to the proportional valve controlling the pressure in the bottom of the lensing chamber. Following this pressure input, valve two is opened and valve three is closed to begin reading the difference in pressure between the top and bottom of the aerodynamic lens. After preprogrammed proportional valves are switched on, the pressure-drop across the aerodynamic lens drops to ~25 torr. When particles are injected into the device, there is a quick, unexplained drop in pressure, but then the differential pressure drop rises to ~28 torr. Then, valves can be returned to their original configuration and the process started over again.

While differential pressure drops can be selected by manually tuning the proportional valves, it is difficult to get the exact pressure drop desired because the gain of changing a proportional valve is too high to make precise inputs. In addition, the system is vulnerable to perturbations. To enable more precise control of the aerodynamic lens, a PID control loop should be integrated into the proportional valves used to modulate aerodynamic lens pressure drop. With the differential pressure transducer feeding a control signal to a digital-to-analog converter, a control scheme can be devised to send 0 to 30 V signals to proportional valves. While both proportional valves control the differential pressure drop, drawing gas away from the top lens chamber with vacuum has low gain when it comes to manipulating the differential pressure drop. For this reason, the proportional valve feeding gas into the bottom lensing chamber will be the main manipulated variable. Once a PID control scheme is introduced to the ballistic device, our group will be able to input desired pressure drops and have consistent conditions from experiment to experiment.

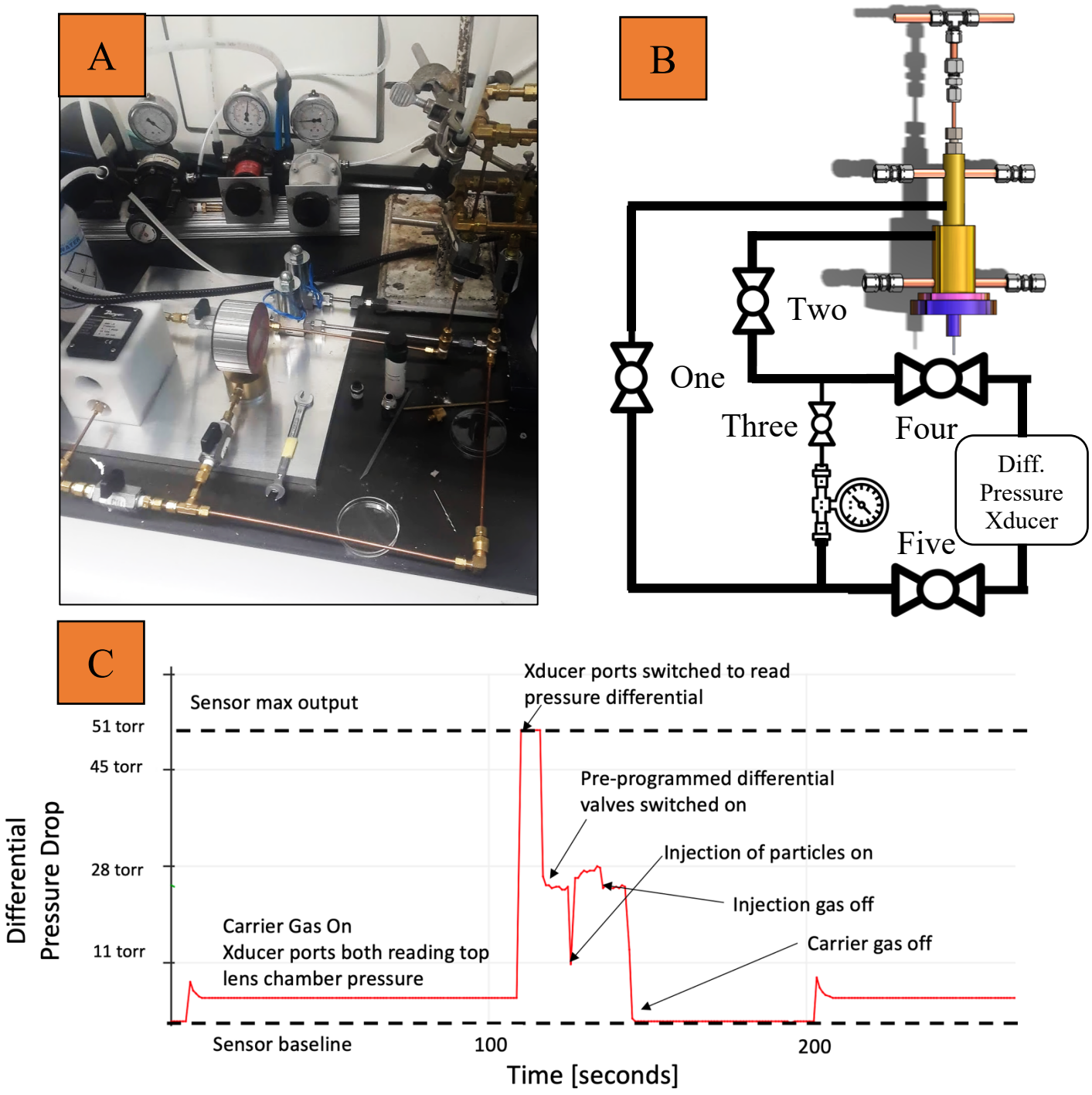

Figure 5.11 Plumbing and sensors for differential pressure drop measurement.
A) Image of plumbing connected to lensing chambers of ballistic device B) Schematic showing connections to the ballistic device, ball valves, a pressure gauge, and the differential sensor. C) Representative signal from differential pressure transducer during delivery of microparticles.

While the new ballistic device was designed to use a low volume of gas to accelerate microparticles (with a 0.1 to 1.0 mm ID capillary), there is still a compressed gas jet released from the device when using a 0.5 mm ID capillary, especially with operating pressures above three bar in the lensing chamber. This compressed gas poses two problems. First, when gas impinges on a surface, the angle of incidence for particle impacts can be altered, especially for smaller particles with low Stokes Numbers. This can potentially impact penetration depth of microparticles. Second, the compressed gas jet can create deformation in gel substrates and would cause significant discomfort or damage to patients receiving ballistic therapies. As an initial solution to this problem, a basic insert was machined to divert gas away from the substrate. The insert slides over the 1.6 mm OD acceleration capillary. At the bottom of the insert (**Figure 5.12**), there is a 1-mm hole that is meant to release particles and small amounts of gas. Within the insert, the compressed gas jet expands and impinges on the surface containing a 1-mm bored outlet. Gas is diverted out of eight holes on the insert away from the substrate, and small volumes of gas are released out of the 1 mm hole. This device works well up to pressures of 5 bar, but considerable gas is released above this pressure. To make the ballistic device more robust, an insert should be machined that uses vacuum to increase the amount of gas diverted away from the tissue sample.

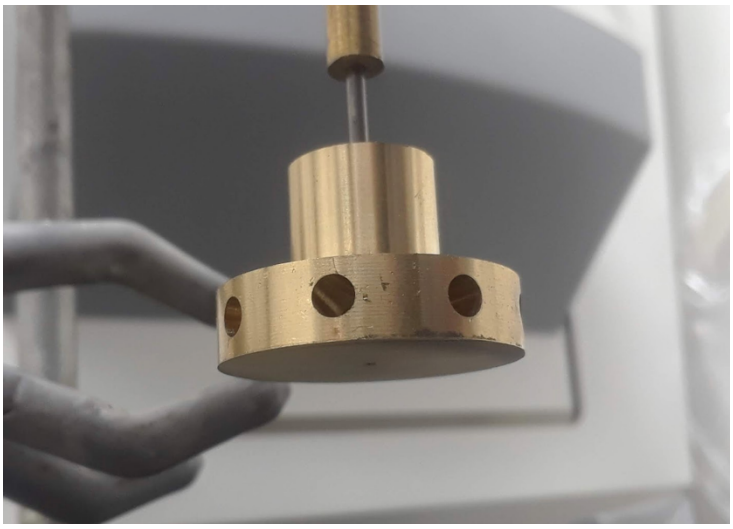

Figure 5.12 – Insert for gas diversion at the bottom device's acceleration capillary. A small (1 mm) hole at the bottom of the insert releases particles and small amounts of gas. Holes around the insert divert gas away from the substrate.

5.2.5 – Future Experiments for Ballistic Delivery at Atmospheric Pressure

Following the installation of the necessary augmentations for ballistic device improvement and also the DOE used to optimize ballistic device performance, there are several experiments that should be done to advance the research of ballistic delivery at atmospheric pressure. First, the penetration of ballistic microparticles should be measured in ballistic gelatin to make comparisons to research done with the PDS1000 with substrates under vacuum. Initial work has been done to determine the performance of the ballistic device using 1% w/v agarose gels. This work, which is shown in Appendix D.2, was done in the agarose model because these gels are much more quickly prepared than ballistic gelatin and initial results in 5% w/w ballistic gelatin showed low penetration. In this work, it was found that penetration in the gel model was sensitive to pressure used to accelerate microparticles, with penetration increasing until operating pressures of 5 bar were used. Higher pressures resulted in diminished returns in penetration. The device also showed improved performance with helium as a carrier gas instead of nitrogen. The

device was found to be insensitive to acceleration barrel length, but the data suggested that aerodynamic lensing had a small effect on the penetration of microparticles. Once a DOE has been performed, penetration of microparticles in ballistic gelatin should be assessed and compared to the results acquired using the PDS1000 gene gun.

Following this study, ballistic delivery to the cornea should be assessed. The results of initial testing, shown in Figure 5.10, show that significant penetration is possible. A detailed study should be done in which particle efflux rates and operating pressure are changed and penetration depth in the cornea is measured. Finally, a study should be run in which therapeutic microparticles loaded with Eosin Y are delivered to the cornea. Since microparticle payloads are produced with relatively low yield, this study will require a microparticle feeder, like the one discussed in Section 5.2.5, in order to sufficiently cover the cornea with small amounts of particles. By moving the cornea underneath the ejection point of the ballistic device in between shots, an attempt can be made to evenly cover the surface of the cornea with microparticles. After particle delivery, corneas should be dissected and particle dissolution on the surface of the cornea should be charted over time. To simulate natural lacrimation of the eye, PBS should be applied to the cornea dropwise. Using standard fluorescent transmission microscopy, particles can be imaged and their dissolution over time charted. Corneal tissue can be sectioned and compared to eyes that have an equivalent dose of Eosin Y applied topically to see if ballistic therapies can deliver drugs with higher bioavailability than standard topical delivery. Additional investigations can be done, like the use of a tapered acceleration capillary, but these studies will go a long way to characterize the ability to deliver ballistic microparticles under standard atmospheric pressure.

5.3 – Investigation of Effect of Particle Morphology on Particle Impacts

While there have been many studies demonstrating the penetration of microparticles with different sizes and densities in gels and tissue, there have been few studies which explore the effect of microparticle morphology. In the field of ballistics research, the aspect ratio of a projectile, its length divided by its diameter, has a significant effect on penetration depth in semi-infinite media. The transient stress field within the target is significantly higher peaked as penetrators get longer, leading to higher velocities during embedment.[8,9] Ultimately, increasing aspect ratio for penetrators leads to decreases in penetration, due to bending and rotational displacement of the projectile.[10] While aspect ratio is frequently changed in ballistics research of macroscopic projectiles, this topic has received little attention in the microballistics community. In Zhang et al., the penetration of spherical and aspherical steel powders was compared using an agarose target.[11] While the two experimental groups showed no statistical significance between one another (95% confidence intervals overlap), these results compared projectiles that were spherical and aspherical. The aspect ratio of the projectiles was left more or less unchanged. The effect of using projectiles with high aspect ratios is appealing when considering the stromal layer of the cornea, which is a dense, fibrous network. We hypothesize that projectiles may be able to move between fibers in the stroma more effectively than spherical projectiles. Whatever is the case, modern ballistic projectiles have changed their aspect ratios over the years (e.g. musket balls vs. modern armor piercing bullets). A study which looks at the effect of projectile aspect ratio on penetration at the microscale could be helpful in attaining greater penetration in the cornea.

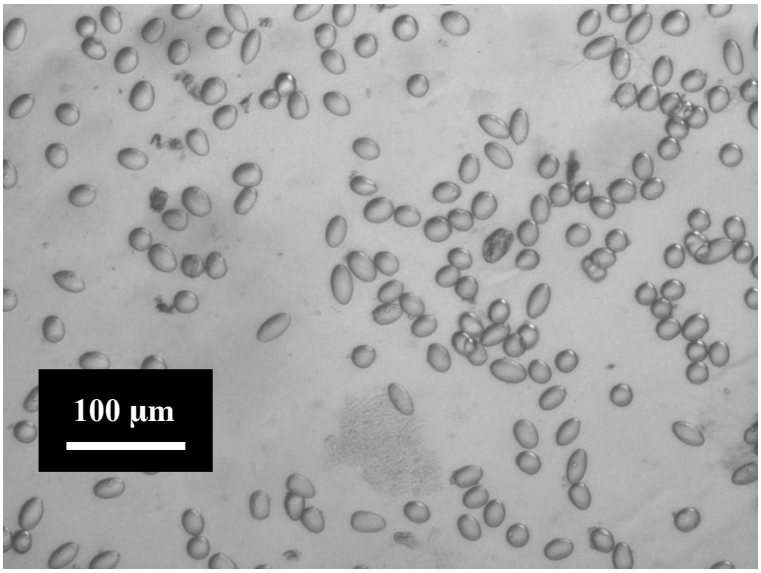

Figure 5.13 – Anisotropic poly(lactic acid) microparticles.
PLLA microparticles were stretched in PVA films that were then dissolved in water to extract particles.

To make stretched microparticles, poly(lactic acid) (PLA) is a good choice for both biomedical and ballistic applications. An example of research that uses stretched microparticles is in Sharma et al. In this work, microparticles with different aspect ratios demonstrated reduced rates of binding and uptake by macrophages.[12] PLA is biocompatible, there are readily available methods for PLA microparticle preparation, and the material has a low glass-transition temperature (60-65 °C). For these reasons, it is frequently used in stretched particle applications. The relatively high density of this polymer (~1.25 g/cc) makes it an appealing choice for microballistic therapies.

Using the protocol laid out in Champion et al. for poly(styrene) microspheres, our group made our own stretched microparticles.[13] 5 mL of 20 µm PLA particles (1% w/w; Cospheric) were centrifuged and suspended in 1 mL of water. This was added to the 39 mL of 10% w/w poly(vinyl alcohol) (PVA) as is laid out in the Champion protocol. The PVA solution was poured

into a mold and allowed to dry into a clear film over 48 hours. Our microparticles were stretched at 90 °C in an oil bath to a total strain of around 250% using a film-stretching device fabricated by The Tirrel Lab (**Figure 5.14**). Particles were removed from PVA films by letting them soak in room temperature water on a wrist-action shaker overnight. Particles were centrifuged and this process was repeated three times. Ultimately, the microparticles shown in **Figure 5.13** were produced from this process. As can be seen, there is a broad distribution in microparticle aspect ratios. Upon inspection of PVA films, it was revealed that particles closest to the end of the films that was stationary during the uniaxial stretching process contained spherical particles. On the other end of the film, microparticles were stretched with high aspect ratios (between two and three). In future studies, either two-directional uniaxial stretch should be employed, or strips of PVA should be cut out based on the aspect ratio of the particles contained. If several particle stretching procedures are run with identical total amounts of strain applied to the PVA films, then the strips can be cut out and dissolved separately such that a large number of particles with nearly identical aspect ratios can be accumulated. In the end, enough particles should be prepared to perform ballistics testing in both gelatin and corneal tissue. Using the PDS1000, rice-shaped microparticles can be prepared to deliver spherical particles of the same mass to gelatin. Our group was limited on time and resources to build up enough particles for these experiments.

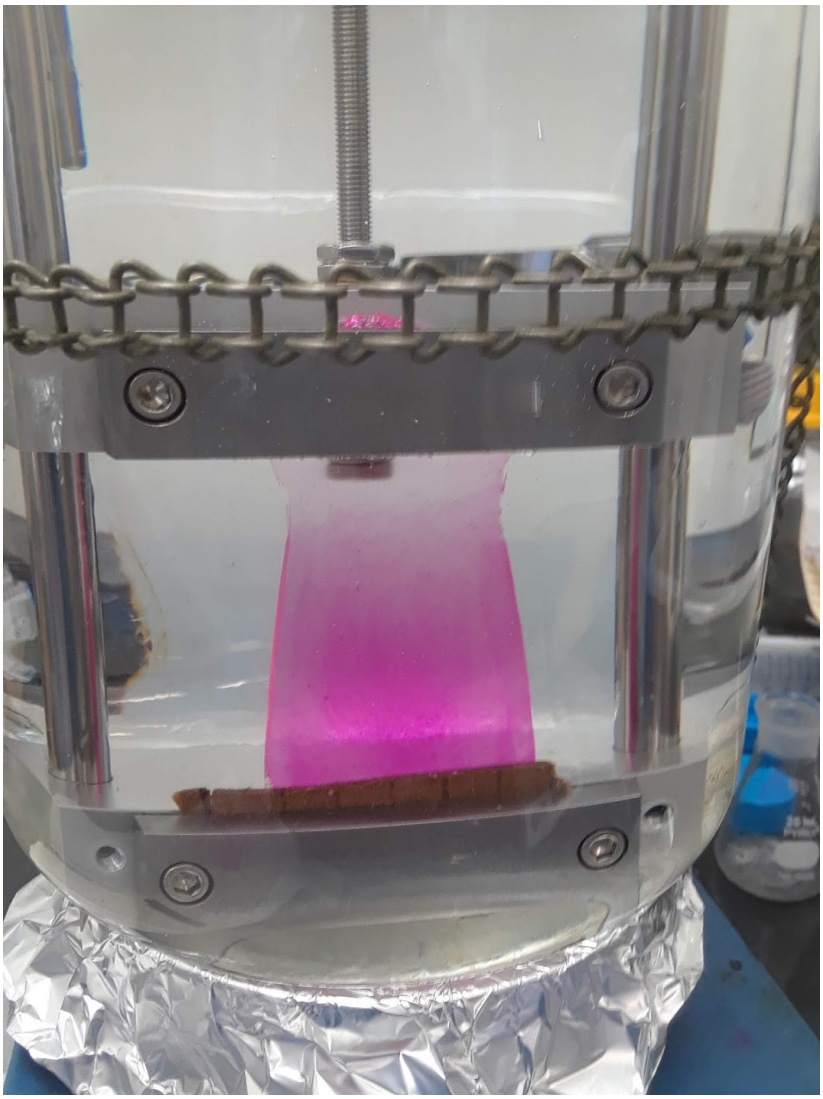

Figure 5.14 – Poly(vinyl alcohol) film with poly(lactic acid) microparticles and rhodamine B. Particles are stretched in an oil bath at 90 °C. One side stretches more than the other.

The platform of using PLA particles also offers a potential way to change particle density. In Guo et al., polymer entanglements left over from stretching PDLLA microparticles close to the glass transition temperature of the polymer lead to shape memory particles when heated back to the glass transition temperature. This response lead researchers to load microparticles with gold nanoparticles so that laser excitation at 530 nm could be used to heat particles locally and induce the shape-memory transition.[14] While the researchers in the study loaded gold nanoparticles in low concentration (~.05% w/w), it is possible that higher concentrations can be reached. This may be worth investigating for making our own density-modified microparticles. If particles can be loaded with gold by as much as 10% w/w, then ballistic studies can be run with these new PLA microparticles (that have a density of ~ 3 g/cc). These experiments would open up the way to anisotropic particles that have increased density as well.

5.4 – Assessing Damage From Ballistic Delivery and Toxicity Of Microparticles

To assess the damage left by microballistic particles, barium-titanate spheres will be delivered to corneal tissue using the PDS1000. These spheres will work best because they display high embedding depth in the corneal epithelium, and they will not oxidize corneal tissue like stainless steel particles will.[15] To incubate corneal tissue, a protocol will be used by Evans and coworkers, ultimately modified by Amy Fu.[16,17] Corneas will be dissected so 5 mm of scleral rim is intact. Equal volumes of 1% w/w agarose and tissue culture media will be mixed and allowed to solidify on the inside of the tissue sample. Tissue will be placed in well plates filled with media just up to the scleral rim of the cornea. Corneas will be incubated at 37 ° C under 5% CO_2. Every day, the tissue will be treated with fluorescein drops and imaged under cobalt blue light using a camera (with 4X magnification should be sufficient). Under this lighting, areas of the epithelium

that have been wounded will show up as bright green.[18] While it is expected that the damage from microparticles will be low, if there is any damage, it will be highlighted with the fluorescein and increased magnification of the camera.

To assess toxicity to the cornea, microparticles will have to be delivered to an animal model. Albino rabbits (New Zealand White Rabbits) are typically used in animal models of the human cornea. To maximize comfort of animals tested, the ballistic device used should be fitted with mounts for the resting animal. After delivery of therapeutic microparticles, The Draize Eye Irritation Test will be applied at timepoints of 1, 4, 24, 48, and 72 hours, and then 4, 7, and 21 days. This test allows researchers to weigh and sum six components of directly observable changes on the anterior segment of the eye, including the density and area of corneal opacification, the severity of iritis, conjunctival redness, edema, and discharge. An illustrated standard guide is used to score irritancy.[19]

5.5 – Delivering Custom Therapeutic Microparticles

Final experiments that could be done on this project involve building therapeutic microparticles with ideal penetration characteristics. Some work will have to be done to use the VOAG to produce droplets loaded with metal nanoparticles, including increasing the heat duty of the drying column so larger pinholes can be used. Another option would be to use an electrospray setup like in Cam et al.[20] Whatever method is used, the ultimate particle prepared should be around 10% w/w metal nanoparticle. Depending on the base polymer chosen, this would result in a particle that is around 2.9 g/cc. This density would likely result in penetration to the bottom of the corneal epithelium, as was seen with soda-lime microparticles. An ideal particle for

penetration studies would include 88% w/w PEG, 10% w/w tungsten nanoparticles, 1% w/w Eosin Y, and 1% w/w benzalkonium chloride. The final component, benzalkonium chloride (BAC), is a component of all multidose eyedrop formulas (e.g. for glaucoma). It is known to induce the lysis of cell membranes at the ocular surface, even at very low doses.[21] This compound has been used to effectively increase imbibition of riboflavin in rabbit stromal tissue in epithelium-on corneal cross-linking surgery.[22] Our group wants to avoid the damage of tissue with our drug delivery strategy, but since this compound is so widely used in medications, it would be interesting to see if it had any effect. To compare the efficacy of these ballistic microparticles, particles that are 99% w/w PEG with 1% Eosin Y and particles that are 89% w/w PEG, 1% Eosin Y, and 10% metal nanoparticle will be compared to our custom particles. Corneal tissue will be kept hydrated by topically applying PBS drops onto the surface of the tissue for up to a day to model diffusion of drugs into the surrounding tissue medium. Tissue will be processed and sectioned to compare the penetration of Eosin Y into the cornea. It is expected that the addition of metal nanoparticles and BAC will have a positive effect on the uptake of Eosin Y in tissue.

5.6 – References

1. Ziemann, P. J., Liu, P., Rao, N. P., Kittelson, D. B. & McMurry, P. H. Particle beam mass spectrometry of submicron particles charged to saturation in an electron beam. *J. Aerosol Sci.* **26**, 745–756 (1995).
2. Di Fonzo, F. *et al*. Focused nanoparticle-beam deposition of patterned microstructures. *Appl. Phys. Lett.* **77**, 910–912 (2000).
3. Wang, X., Kruis, F. E. & McMurry, P. H. Aerodynamic focusing of nanoparticles: I. Guidelines for designing aerodynamic lenses for nanoparticles. *Aerosol Sci. Technol.* **39**, 611–623 (2005).
4. Benner, W. H. *et al*. Non-destructive characterization and alignment of aerodynamically focused particle beams using single particle charge detection. *J. Aerosol Sci.* **39**, 917–928 (2008).
5. Deng, R. *et al*. Focusing particles with diameters of 1 to 10 microns into beams at atmospheric pressure. *Aerosol Sci. Technol.* **42**, 899–915 (2008).
6. Veysset, D. *et al*. High-velocity micro-particle impact on gelatin and synthetic hydrogel. *J. Mech. Behav. Biomed. Mater.* **86**, 71–76 (2018).
7. Yang, Y. & Li, X. Experimental and analytical study of ultrasonic micro powder feeding. *J. Phys. D. Appl. Phys.* **36**, 1349–1354 (2003).
8. Lynch, N. J., Subramanian, R., Brown, S. & Alston, J. The influence of penetrator geometry and impact velocity on the formation of crater volume in semi-infinite targets. *Int. Symp. Ballist.* **May 7-11**, (2001).
9. Zhang, W. *et al*. Experimental investigation on ballistic stability of high-speed projectile in sand. *AIP Conf. Proc.* **1793**, (2017).
10. Vahedi, K., Zohoor, H., Nezamabadi, A. & Zolfaghari, M. Performance optimization of a long rod penetrator penetrating into a semi-infinite target considering bending characteristics. *Turkish J. Eng. Environ. Sci.* **33**, 9–20 (2009).
11. Zhang, D., Rielly, C. D. & Das, D. B. Microneedle-assisted microparticle delivery by gene guns : experiments and modeling on the effects of particle characteristics and modeling on the effects of particle characteristics. *Drug Deliv.* **22**, 334–350 (2015).
12. Sharma, G. *et al*. Polymer particle shape independently in fl uences binding and internalization by macrophages. *J. Control. Release* **147**, 408–412 (2010).

13. Champion, J. A. & Mitragotri, S. Role of target geometry in phagocytosis. *PNAS* **103**, 4930–34 (2006).
14. Guo, Q. *et al*. Entanglement-based thermoplastic shape memory polymeric particles with photothermal actuation for biomedical applications. (2018). doi:10.1021/acsami.8b01582
15. DeBroff, B. *et al*. Clinical characteristics of corneal foreign bodies and their associated culture results. *CLAO J*. **20**, 128-130. (1994).
16. Evans, M. *et al*. The use of corneal organ culture in biocompatibility studies. *Biomaterials* **23**, 1359-1367. (2002).
17. Fu, A. Mitigating scarring and inflammation during corneal wound healing using nanofiber-hydrogel scaffolds. (2015).
18. Wipperman, J. L. & Dorsch, J. N. Evaluation and management of corneal abrasions. *American Family Physician* (2013).
19. Huhtala, A., Salminen, L., Tahti, H. & Uusitalo, H. Corneal models for the toxicity testing of drugs and drug releasing materials. in *Multifunctional Biomaterials and Devices* 4–5 (2008).
20. Cam, M. E., Zhang, Y. & Edirisinghe, M. Electrosprayed microparticles: A novel drug delivery method. *Expert Opin. Drug Deliv*. **16**, 895–901 (2019).
21. Droy-Lefaix, M. T., Bueno, L., Caron, P., Belot, E. & Roche, O. Ocular inflammation and corneal permeability alteration by benzalkonium chloride in rats: A protective effect of a myosin light chain kinase inhibitor. *Investig. Ophthalmol. Vis. Sci*. **54**, 2705–2710 (2013).
22. Singh, V., Grossman, G. H., Agrawal, V. & Sinha, A. Techniques in Rabbits. **29**, 332–341 (2018).

Appendix A

CODE USED IN STUDY

A.1 - Particle Penetration Depth Image Processing Pipeline

Pseudo Code:

1. Load images into a directory
2. Import necessary Python packages
3. Input filepath for calibration dot to calculate interpixel distance
4. Use record clicks kwarg in bebi103 function to measure the pixel length of the calibration dot
5. Store interpixel length
6. Open selected image with "record clicks" kwarg activated. Click on each side of selected particle and then click on the point closest to the surface from the particle
7. Take pixel data in array form and input it into for loop to do statistical analysis
8. For (number of particles)

   Calculate particle penetration depth measured from center of the particle to the surface of the material

   Print diameter
9. For (number of particles) → print penetration depth

10. Store output penetration data in .csv file

Representative Image of Interface:

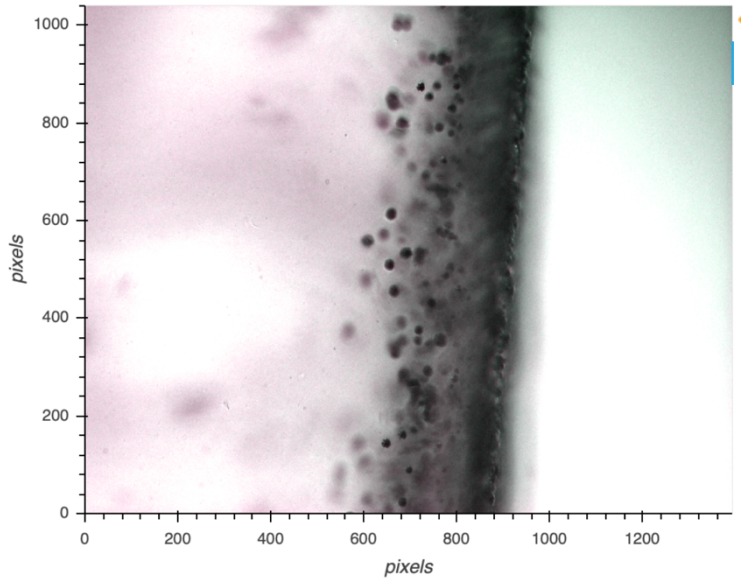

Figure A1 - Interface used in Jupyter Notebook to measure particles. User clicks on microparticles in order to record points on each side of the particle as well as points on the surface. These coordinates were fed to the end of the image process pipeline and penetration statistics were generated. Here is shown penetration of stainless steel microspheres in 10% w/w gelatin.

A.2 – Droplet-Train Image Processing Pipeline

Pseudo Code:

1. Import necessary packages, including the Python skimage package for image processing
2. Load frames in video using OpenCV CV2 function
3. Set the interpixel distance by using the pixel dimensions of the frame and the field of view reported by the camera vendor
4. Look at a histogram of pixel intensity values for the first image. Sometimes we were using videos illuminated by a strobing LED, so the first few frames would be blank, but this histogram can be used on exposed frames to set thresholds on a mask.
5. Use frameextractor function to pull out frames that are not blank. The threshold used is that the picture has at least 100,000 pixels with an intensity over 10.
    a. Create array to store histogram data
    b. Read in first frame and store true Boolean in success variable so you can enter the while loop.
    c. While (next frame contains data and is not empty)
        →load in the next frame and the success Boolean variable
        →if you want to limit the data to extract one of five frames, fiver checkvariable can be used. This can be helpful when there are thousands of frames
        →check if the image contains at least 100,000 frames with intensity greater than 10
        → if yes, write the image into a file in the current directory
        → store histogram data
6. Print number of frames extracted and the total number of frames analysed
7. Take the frames just extracted and manually put them in a folder
8. Import several functions, including regionprops, which will generate data on object sizes
9. Open the file holding frames and store frames in a stack

10. Look at any images to explore the data set
11. Set image threshold value and begin processing statistics on first image. This is where one can determine what threshold value will result in the most accurate mask.
    a. Set the threshold value
    b. Produce falsecolor image
    c. Calculate regionprops data on image
    d. For (every object read by regionprops)

    → check that the centroid is within the ROI and check that the area of the droplet is large enough

    → check that the diameter of the particle is in the right range

    → check that the aspect ratio is below a certain value

    → check that the droplets are not too close together, indicating that they have not broken apart yet or have just collided with one another

    → if all these conditions are met, store the major axis, the minor axis, the area, and the aspect ratio

    → plot red lines to indicate the major and minor axes

    → plot blue box around the droplet
12. Once the image thresholding is satisfactory, repeat the previous process for all of the images, storing penetration statistics as the code progresses
13. Plot the data from all of the images in the file in a scatterplot
14. Store the data in an .xslx file

Representative Images from Image Processing Pipeline

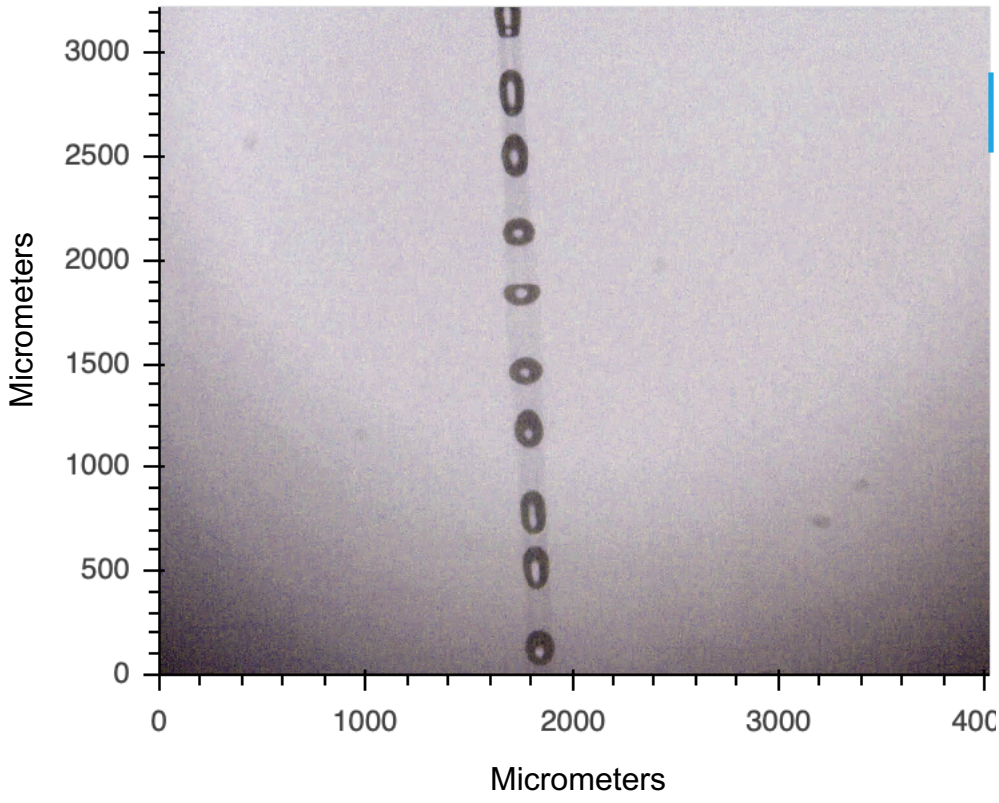

Figure A2 - High-speed video frame of an aerosol ejected from a 75 μm pinhole (2.5X). The axes label show the size of the image in micrometers.

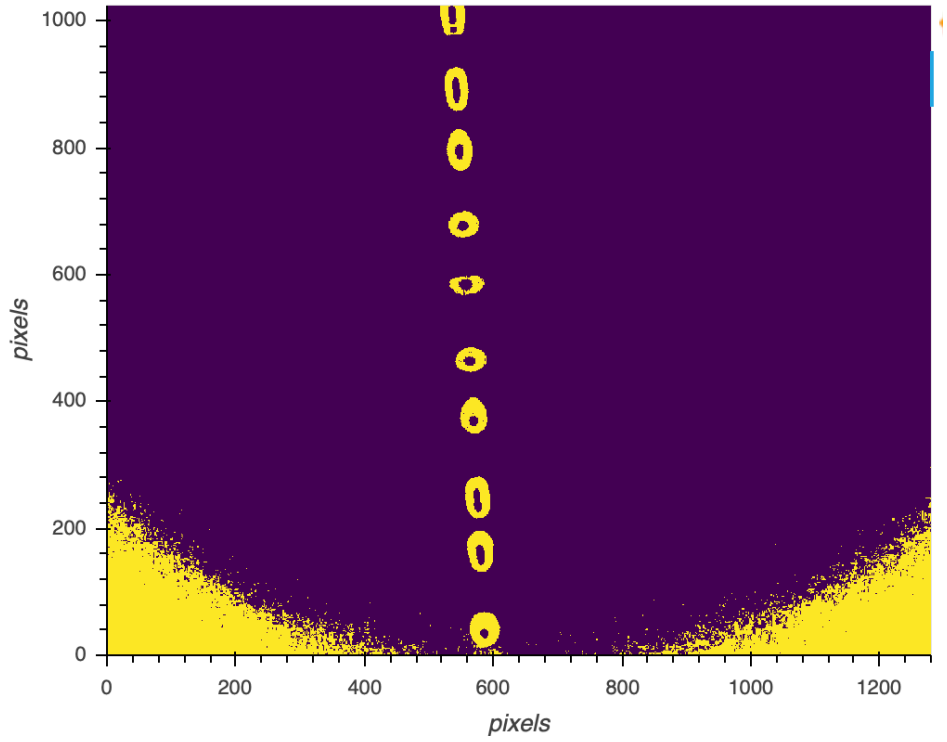

Figure A3 - **Mask of an aerosol ejected from a 75 μm pinhole.** The droplets are outlined effectively by the thresholding operation. The bottom corners of the image show up highlighted like the droplets do, since there was uneven background lighting in the image.

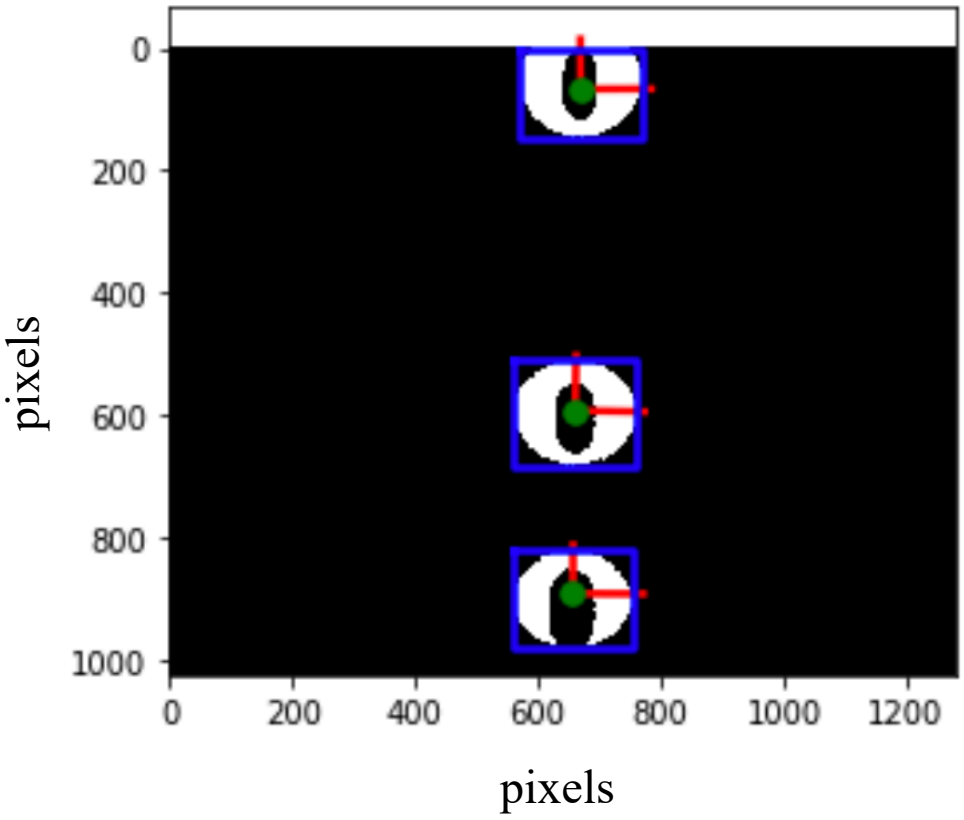

Figure A4 – Image processed by code (10X). The droplets have their major and minor axes read by the regionprops function. The horizontal axis is selected and stored as the diameter.

A.3 – Code to Predict Evaporation Rates in Drying Column

Pseudocode

1. Store variables about the gas in the column
2. Program flowrate of gas that gives a total flowrate of 5 cm/s for the carrier gas in the column
3. Ask the user for initial diameter of the particle
4. Ask the user for the mass flowrate of aerosol coming from the VOAG
5. Ask the user what solvent is being used
6. Calculate the initial volume, mass, terminal velocity, and initial velocity
7. Estimate the drying time by calculating the initial drying rate. Use this to determine the time limit of integration
8. Call ODE15s to integrate the transport equation shown in Table 3.4
9. Calculate the time to dry
10. Plot the data for the velocity, droplet size, and temperature over time
11. Plot heat and mass transfer coefficients. Plot the mass fraction of solvent vapor in the column as a function of position along the length of the column

Appendix B

INTERPRETING PENETRATION IN GEL AND CORNEA

B.1 – Inferring Impact Velocities from The Poncelét Model

Using our normalized penetration depth data in Chapter 2, the penetration observed in ballistic gelatin can be compared with the Poncelet Model to estimate impact velocity. To do this, the mean particle penetration was calculated as well as the maximum penetration depth. By plotting the data in **Figures B1** to **B2** on curves showing the expected penetration in 5% w/w gelatin (as predicted by the model), a range of impact velocities can be inferred using data from soda-lime glass and barium-titanate glass penetration. In both figures, the mean penetration of the sample shows up with normalized penetration depth indicating a velocity of a little over 200 m/s. Standard deviation of the data set indicates that most particles have velocities from 150 to 300 m/s. The maximum penetration depth in the figures comes out to around 500 m/s. Data from stainless steel impacts in 5% and 10% w/w ballistic gelatin shown in **Figure B3** indicates slightly different impact velocities. The mdata from 5% w/w gelatin compared to the Poncelet Model indicates a mean impact velocity of around 200 m/s, but the data from impacts in 10% w/w gelatin indicates a mean impact velocity of 300 m/s. The maximum penetration for both datasets indicates a maximum impact velocity of around 500 m/s. The reason that the 10% w/w gelatin compares differently to the Poncelet Model may have to do with using a lower number of penetration statistics to calculate mean values.

Based on this analysis, a range of microparticle velocities is expected to be between 150 and 500 m/s, with most microparticles having a velocity of 150 to 300 m/s. This range is not only broad, it is likely an underestimation due to the elastic recoil in gel as is demonstrated in Veysset et al. The fact that the three different sets of

penetration data for soda-lime, barium-titanate, and stainless steel microparticles show similar predicted impact velocities suggests that the Poncelét Model fits the data well. While our prediction of velocity is broad, it at least indicates that the microparticles tested in this study had impact velocities on the order of hundreds of meters per second.

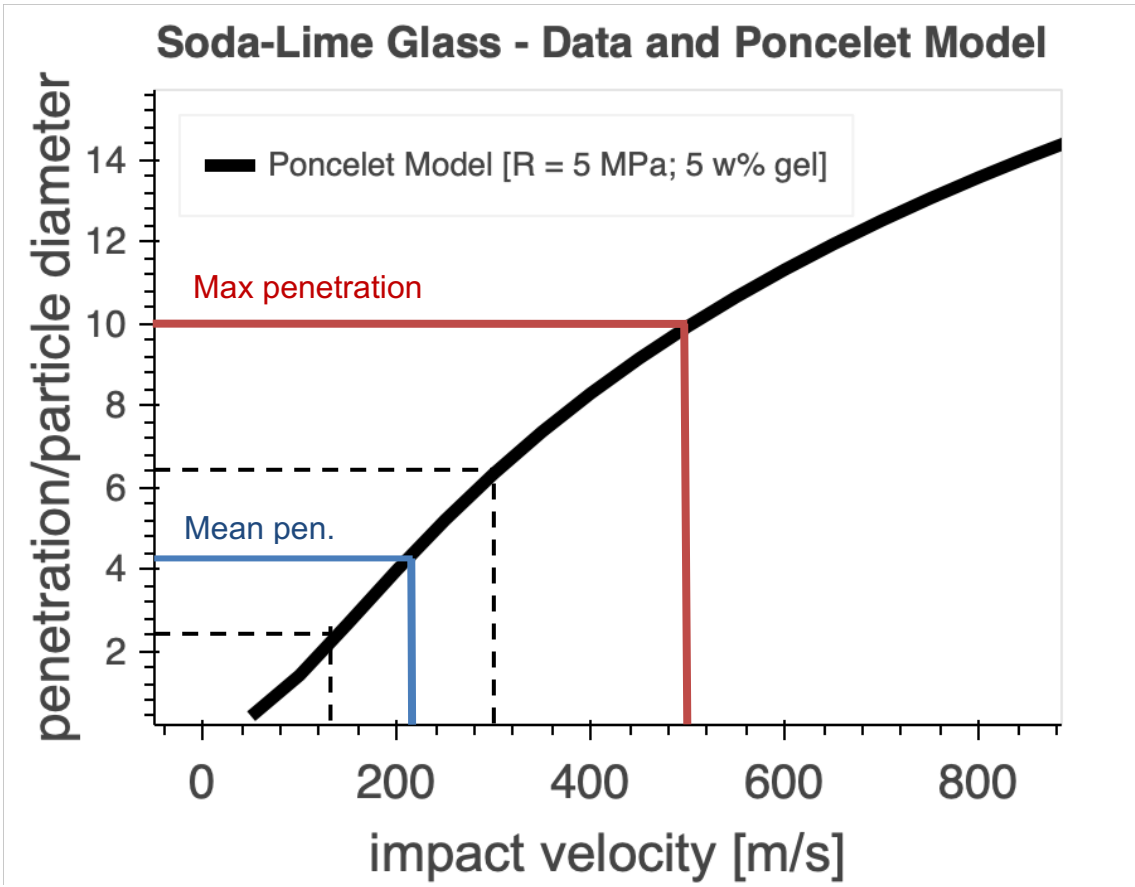

Figure B1 – Poncelet Model for maximum penetration of spheres with density of 2.5 g/cc. Blue line shows average measured penetration depth of soda-lime spheres embedded in 5% w/w gelatin. Dotted lines show one standard deviation above and below the mean. Red line shows the penetration depth and the corresponding impact velocity of a microparticle embedding at the maximum recorded normalized penetration.

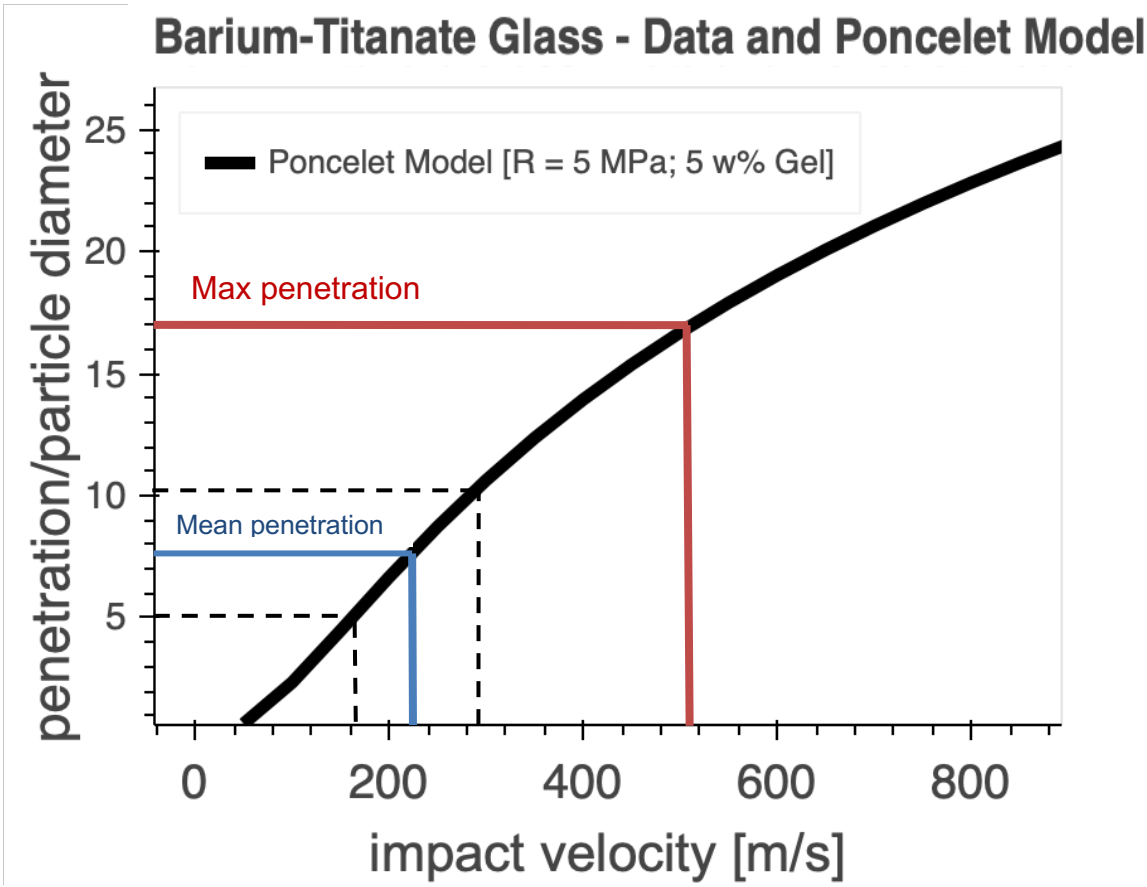

Figure B2 – Poncelet Model for maximum penetration of spheres with density of 4.2 g/cc. Blue line shows average measured penetration depth of barium titanate spheres embedded in 5% w/w gelatin. Dotted lines show one standard deviation above and below the mean. Red line shows the penetration depth and the corresponding impact velocity of a microparticle embedding at the maximum recorded normalized penetration.

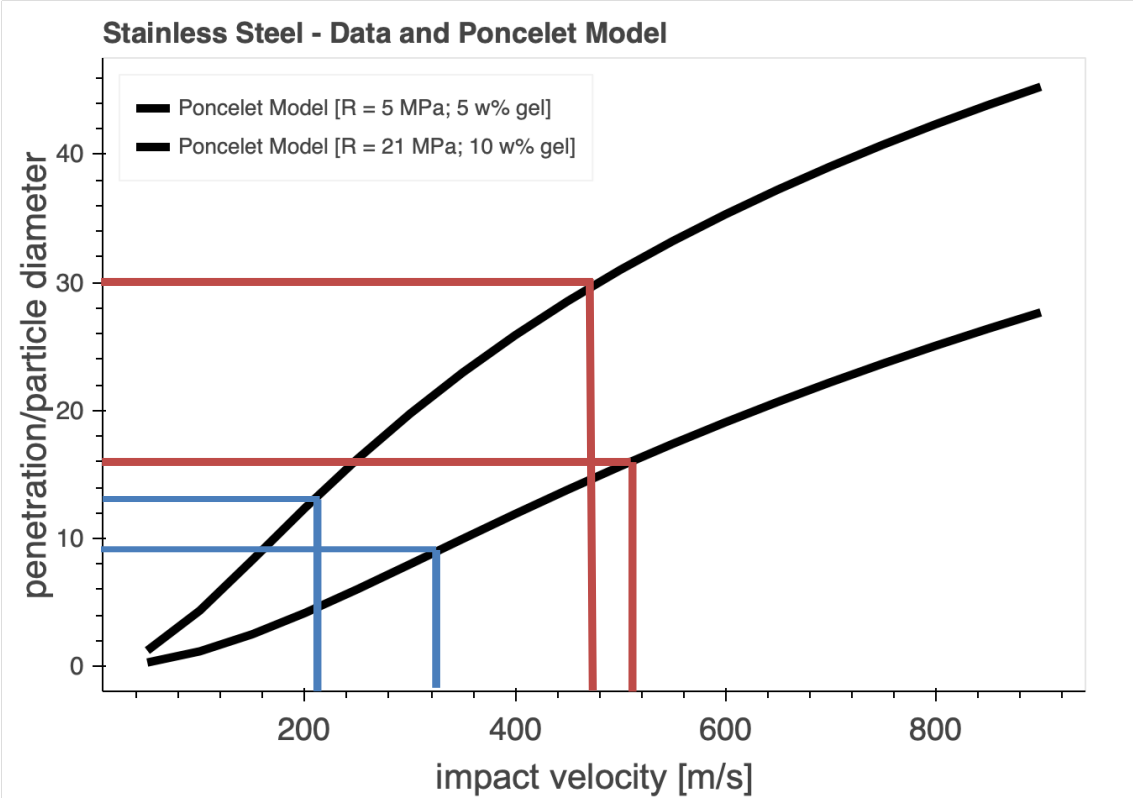

Figure B3 – Poncelet Model for maximum penetration of spheres with density of 7.8 g/cc. Blue lines show average measured penetration depths of stainless steel spheres embedded in 5% w/w and 10% w/w gelatin. Red line shows the penetration depth and the corresponding impact velocity of a microparticle embedding at the maximum recorded normalized penetration.

Appendix B.2 – Elastic Froude Number Based Scaling Relationship for Penetration in Gel

In previous ballistics research, penetration of millimeter-sized projectiles has been shown to scale with the Elastic Froude Number to some power. In Akers and Belmonte, spheres penetrating a viscoelastic, micellar fluid were shown to display maximum penetration depth scaling with $z_\infty \sim \left[\frac{\Delta\rho u_O^2}{G}\right]^{1/3}$. In Swain et al., the penetration of steel spheres in ballistic gelatin was shown to scale with $z_\infty \sim \left[\frac{\Delta\rho u_O^2}{G}\right]^{1/2}$. In Table B2-1, the ratio of density differences between target and substrate is compared to the ratio of penetration depths. This was done for small particles (< 12 um), medium sized particles (12 um ≤ Particles ≤ 17 um), and large particles (17 um < Particles). The value of $\boldsymbol{\gamma}$ in $\boldsymbol{\Delta\rho_1^\gamma/\Delta\rho_2^\gamma}$ that fit the data best was 0.8 ± 0.2. There is considerable variation in the value of $\boldsymbol{\gamma_{min}}$.

Table B1 - Comparing Ratio of Mean Penetration Depths to Ratio of Densities with Exponent γ

	Particles < 12 um			12 um ≤ Particles ≤ 17 um			Particles > 17 um		
	$\Delta\rho_{BT}/\Delta\rho_{SL}$	$\Delta\rho_{SS}/\Delta\rho_{BT}$	$\Delta\rho_{SS}/\Delta\rho_{SL}$	$\Delta\rho_{BT}/\Delta\rho_{SL}$	$\Delta\rho_{SS}/\Delta\rho_{BT}$	$\Delta\rho_{SS}/\Delta\rho_{SL}$	$\Delta\rho_{BT}/\Delta\rho_{SL}$	$\Delta\rho_{SS}/\Delta\rho_{BT}$	$\Delta\rho_{SS}/\Delta\rho_{SL}$
experimental - $z_{\infty 1}/z_{\infty 2}$	2.10	1.34	2.81	1.77	1.59	2.81	1.86	2.05	3.81
theoretical - $\Delta\rho_1^{\gamma min}/\Delta\rho_2^{\gamma min}$	2.10	1.33	2.79	1.77	1.59	2.79	1.86	2.05	3.84
abs(experimental - theoretical)	0.00	0.00	0.01	0.00	0.00	0.02	0.01	0.00	0.02
$\boldsymbol{\gamma_{min}}$	0.96	0.39	0.68	0.74	0.99	0.68	0.8	0.97	0.89
								$\boldsymbol{\gamma_{AVG}}$	0.8
								standard deviation	0.2

Appendix B.3 – Individual Deliveries of Microparticles to Corneal Tissue

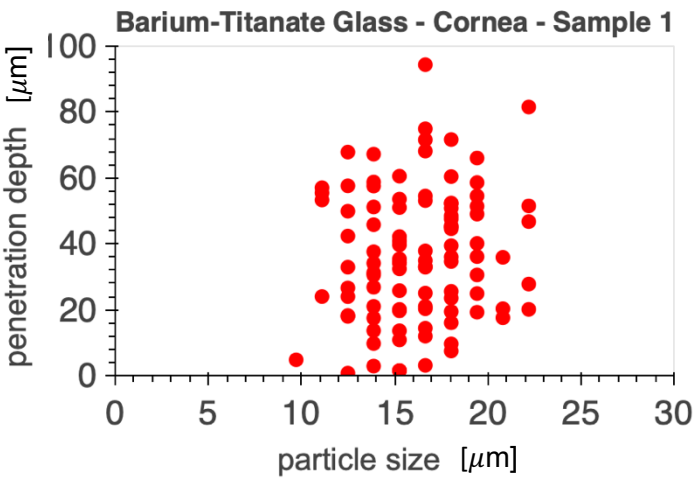

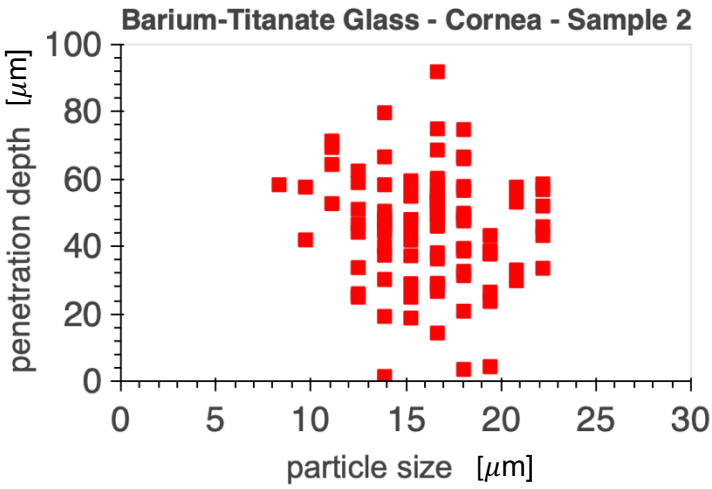

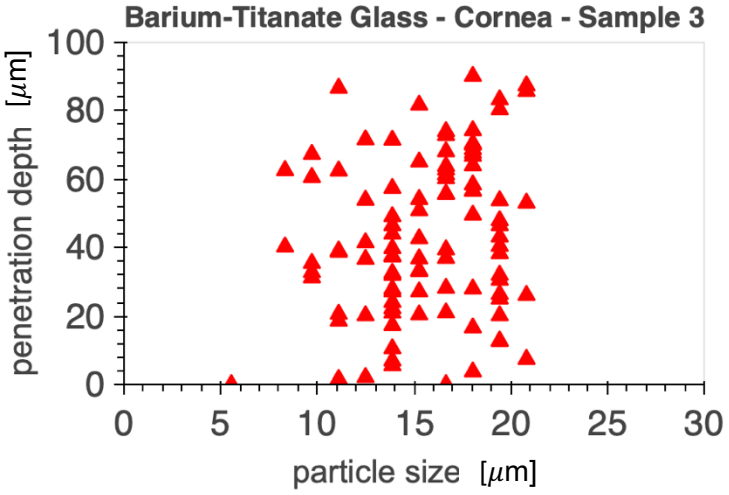

Figure B4 – Individual deliveries of barium-titanate microparticles to corneal tissue. Device is consistent from shot to shot.

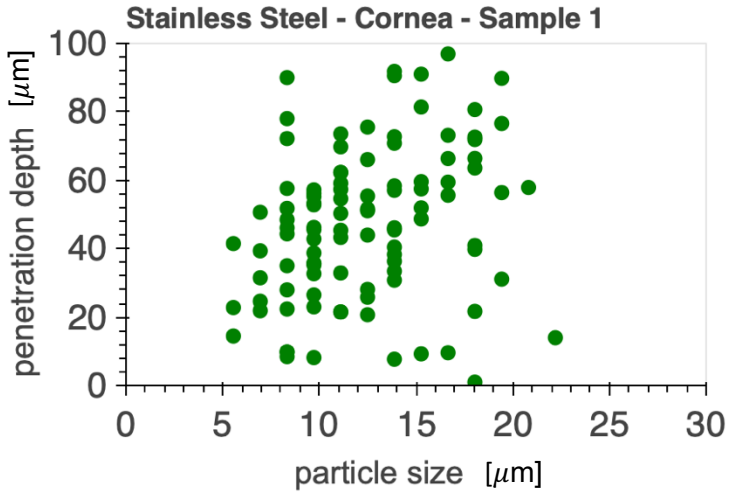

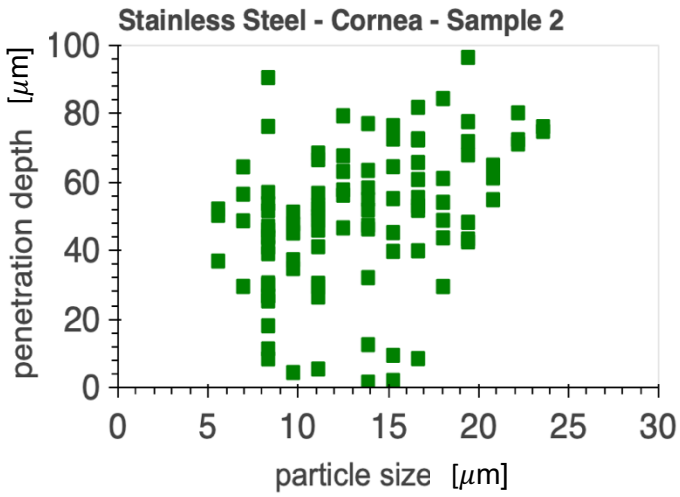

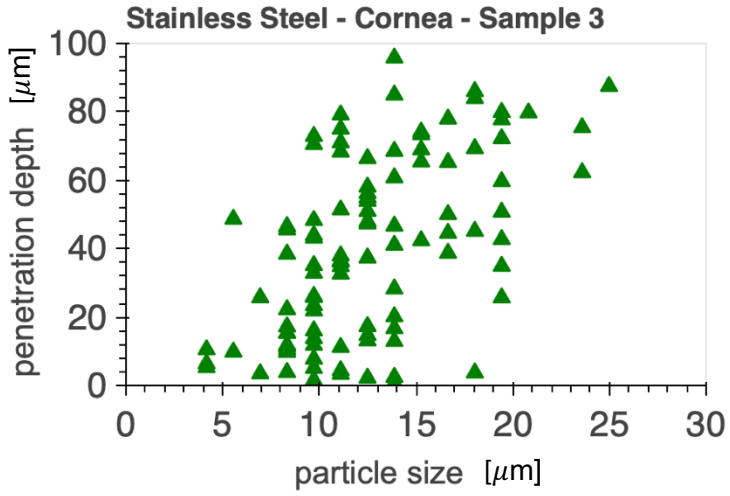

Figure B5 – Individual deliveries of stainless steel microparticles to corneal tissue. Penetration proportional to particle size.

Appendix C

DROPLET-SIZE DISTRIBUTION ANALYSIS

C.1 – Production of Monodisperse Aerosols Using 50 and 35 μm Pinholes

50 μm pinholes were tested using our standard protocol for measuring monodisperse droplet size-distributions. Ethanol was filtered and then flowrate was measured using a pressure of 0.22 bar. The average volumetric flowrate of ethanol was measured to be 0.5 cc/min. This corresponds to an ejection velocity of $v = \frac{\dot{Q}}{\frac{\pi}{4}D_o} = \frac{\left(0.5\frac{cm^3}{min}\frac{1min}{60\ sec}\right)}{\frac{\pi}{4}(.005\ cm)^2}\frac{1\ m}{100\ cm} = 4.2\ m/s$, where $\dot{Q}$ is the volumetric flowrate and D_o is the orifice diameter. This data compares well with the data in Figure 3.3 for a pressure of 3 PSI. Next, we calculated the expected range of frequencies leading to monodispersity. The high-end disturbance wavelength leading to monodispersity is expected to be $f = \frac{v}{3D_o} = 28.3\ kHz$. The low end of expected monodisperse frequencies is 12.1 kHz. Based on these calculations, frequencies were chosen from 5 to 40 kHz. The size distributions measured in this analysis are shown in **Figures C1** and **C2**. The resulting size distributions show that monodispersity can be achieved for 100 to 125 μm droplets. Monodisperse frequencies occurred from 10 to 25 kHz, which is close to the expected range predicted by Equation 3.4.

To produce even smaller droplets, a 35 μm pinhole was also used. Using such a small pinhole, it starts to become a challenge to avoid impurities and particulate matter that can obstruct the orifice. Nonetheless, monodisperse aerosols were recorded at 0.22 bar with an ejection velocity of about 4 m/s. The high-end disturbance wavelength leading to monodispersity is expected to be $f = \frac{v}{3D_o} = 38.1\ kHz$. The low end of expected monodisperse frequencies is 16.3 kHz. Results of droplet-train size-distribution measurements are shown in **Figures C3** and **C4**.

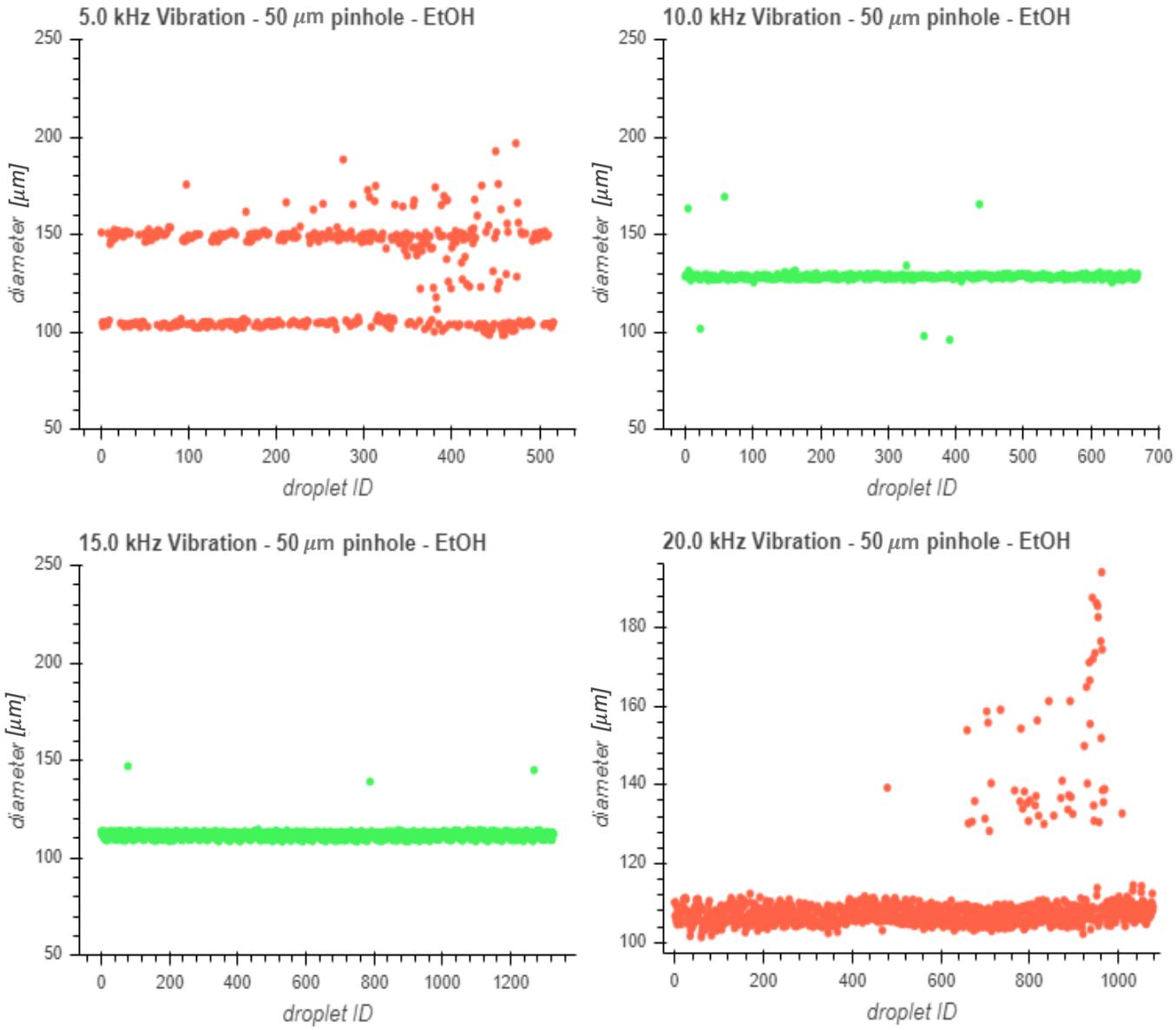

Figure C1 – Size distribution of ethanol ejected from a 50 μm pinhole. Monodisperse production occurs once the jet gets up to 10 kHz. When the 20 kHz aerosol was filmed, there was a momentary production of high-viscosity droplets.

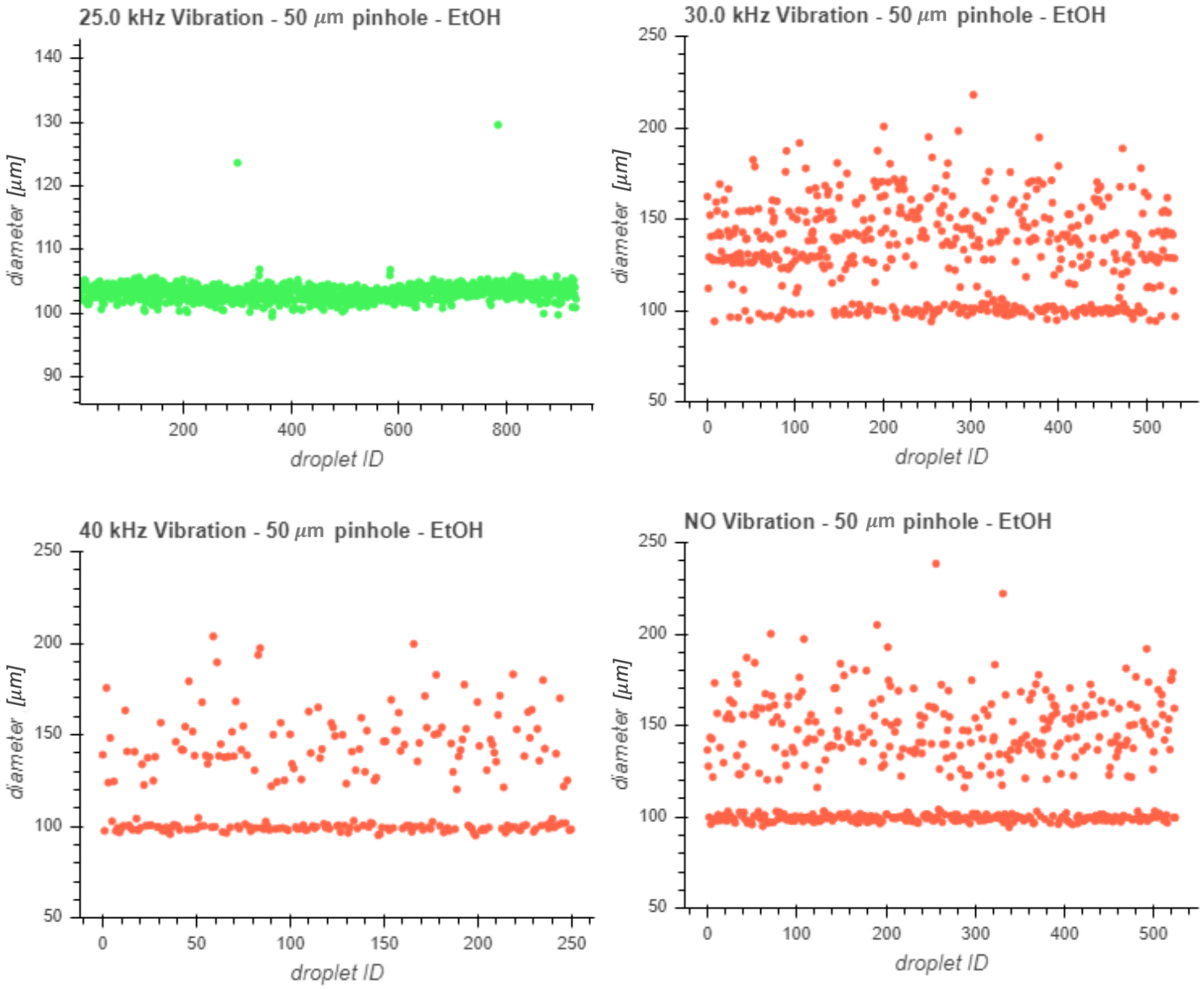

Figure C2 – Size distribution of ethanol ejected from a 50 μm pinhole. Monodisperse production occurs up to 25 kHz. When the 20 kHz aerosol was filmed, there was a momentary production of high-viscosity droplets.

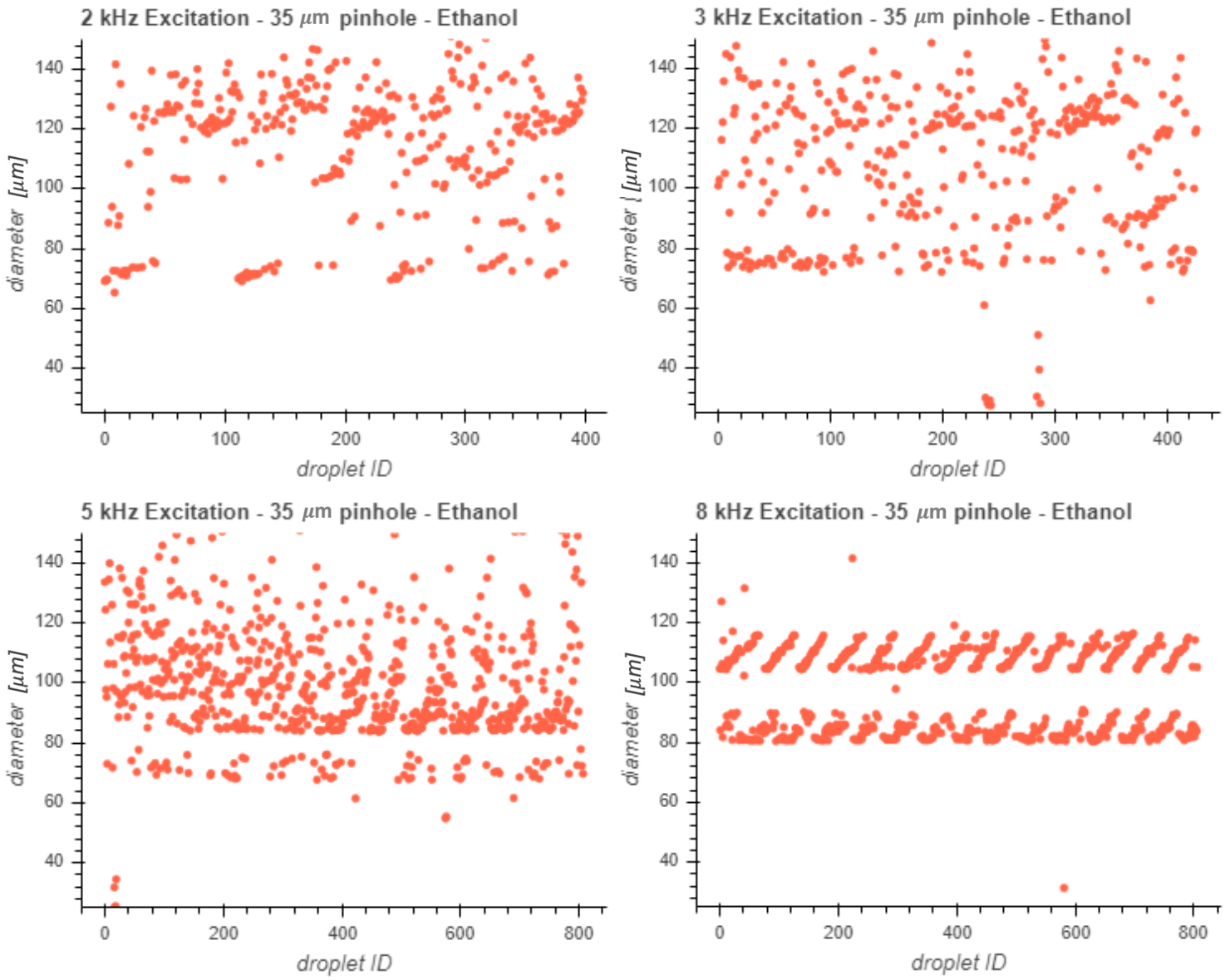

Figure C3 – Size distributions of ethanol ejected from a 35 μm pinhole. There is polydisperse production up to 8 kHz, and then the distribution shifts to bimodal.

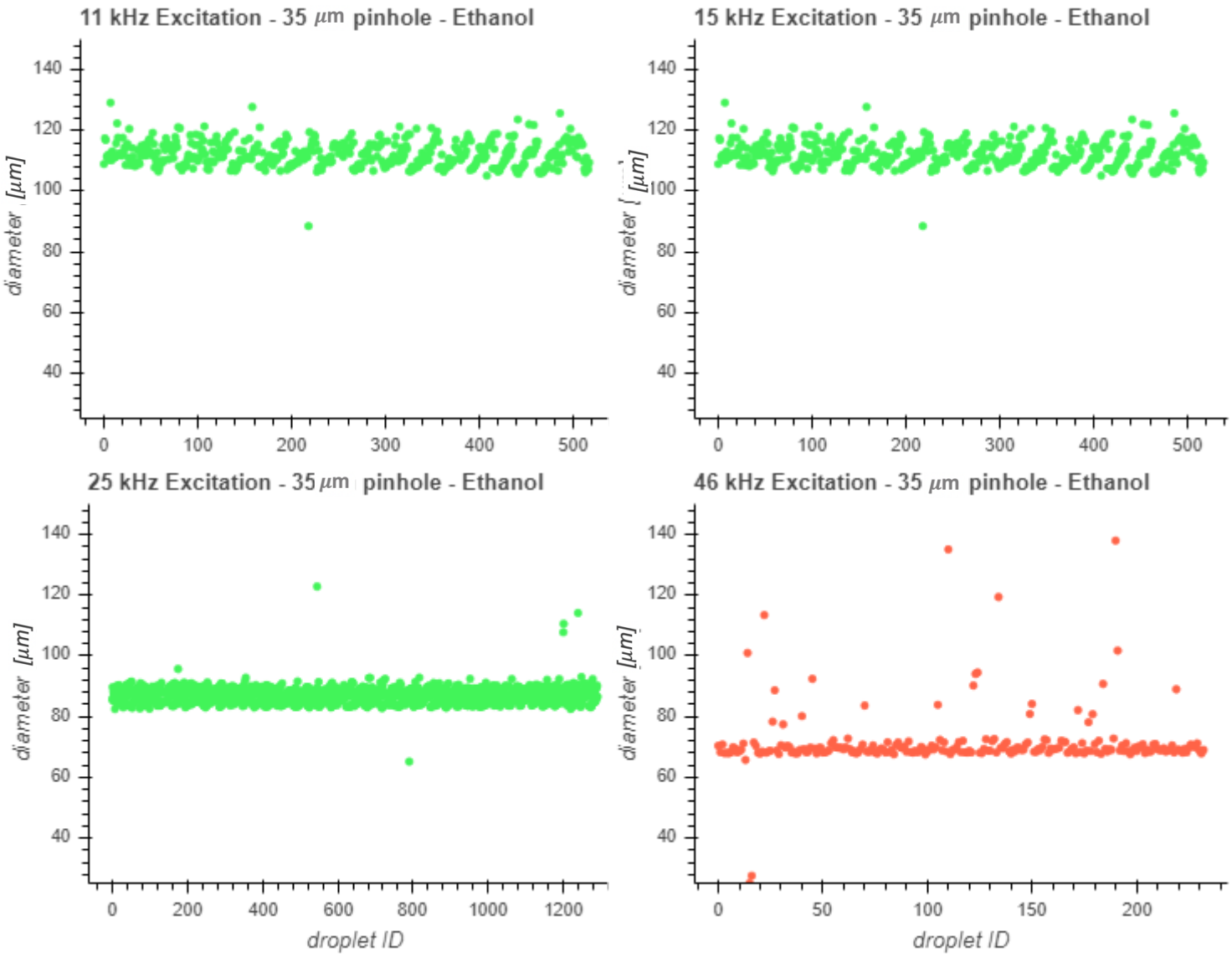

Figure C4 – Size distributions of ethanol ejected from a 35 μm pinhole at higher frequencies. Monodisperse production occurs from 11 kHz (120 μm) to 46 kHz (70 μm). The data is from high-speed video with different video lengths. Fourth figure is red because it has a considerably higher standard deviation than the other samples.

Appendix C.2 – Viscosity of PEG Solutions and Fit of Power-Law Equation

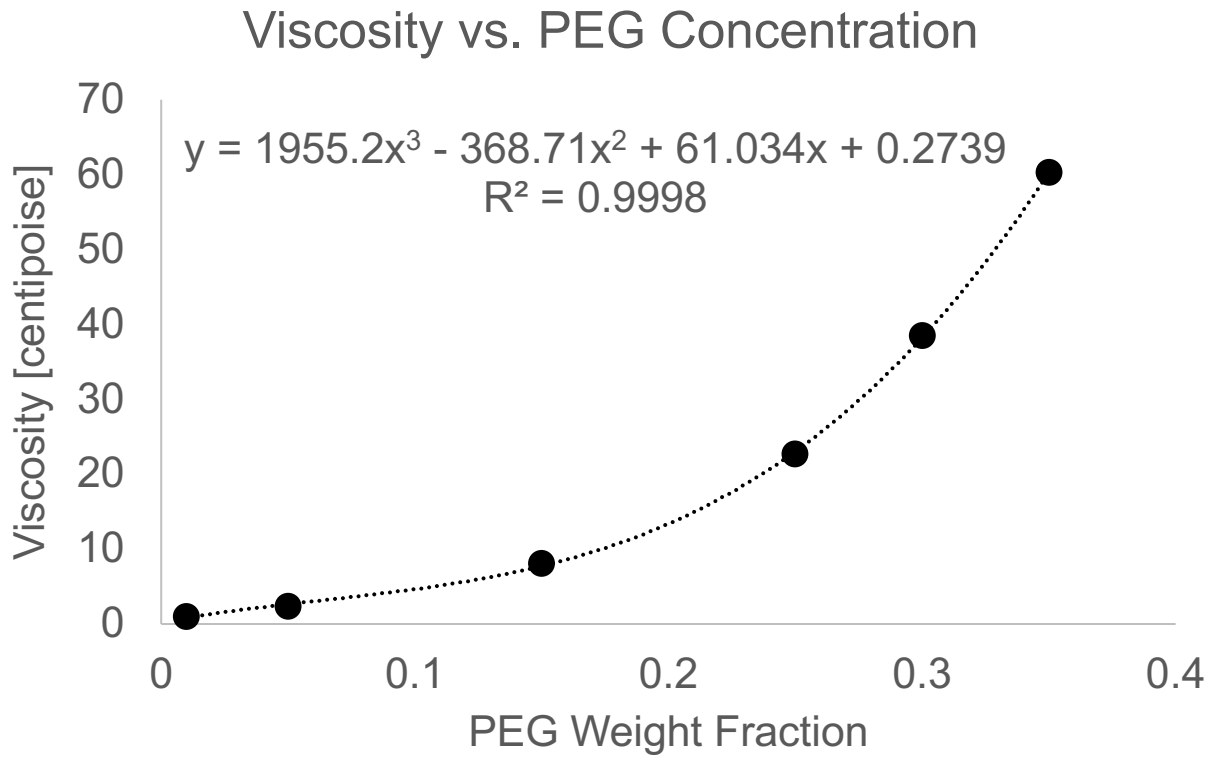

Figure C5 – Mean viscosity of PEG solutions measured with oscillatory shear rheology. A trinomial is used to fit the data.

Appendix C.3 - Performance of VOAG with Viscous Fluids

Within a viscosity range of 1 to 20 cP, the functionality of monodisperse aerosol production is maintained. In **Figure 3.10**, five different size distributions produced using a 75 μm precision pinhole are shown. First, a monodisperse aerosol is produced using water with an excitation frequency of 13 kHz (pressurized at 5 PSI), corresponding to a disturbance wavelength of 460 μm (about 6 orifice diameters). Above this, two aerosols are shown made using a 15% PEG solution (also at 5 PSI). 4 kHz and 3 kHz are the lowest frequencies that produced monodisperse aerosols. The corresponding disturbance wavelengths are 1.0 and 1.3 mm, respectively. At this elevated viscosity, the monodispersity of the aerosol produced is also improved when using the 15 cP fluid (**Table C1**). The standard deviation of the 3 and 4 kHz droplet-trains are 2.9 and 1.8 μm, respectively, compared to a value of 5.6 μm when using the pinhole to aerosolize water. Finally, at a pressure of 10 PSI, a 25% PEG solution was excited at 1.5 kHz and 2 kHz. 1.5 kHz corresponds to a disturbance wavelength of around 3.5 mm, and the standard deviation starts to broaden. This data shows that with a single pinhole, the range of monodisperse droplets that can be produced is increased to between 2 and 3.75 times the diameter of the pinhole, with disturbance wavelengths that are 6 to 45 times this pinhole diameter. This increased control over droplet size comes from changing solution viscosity.

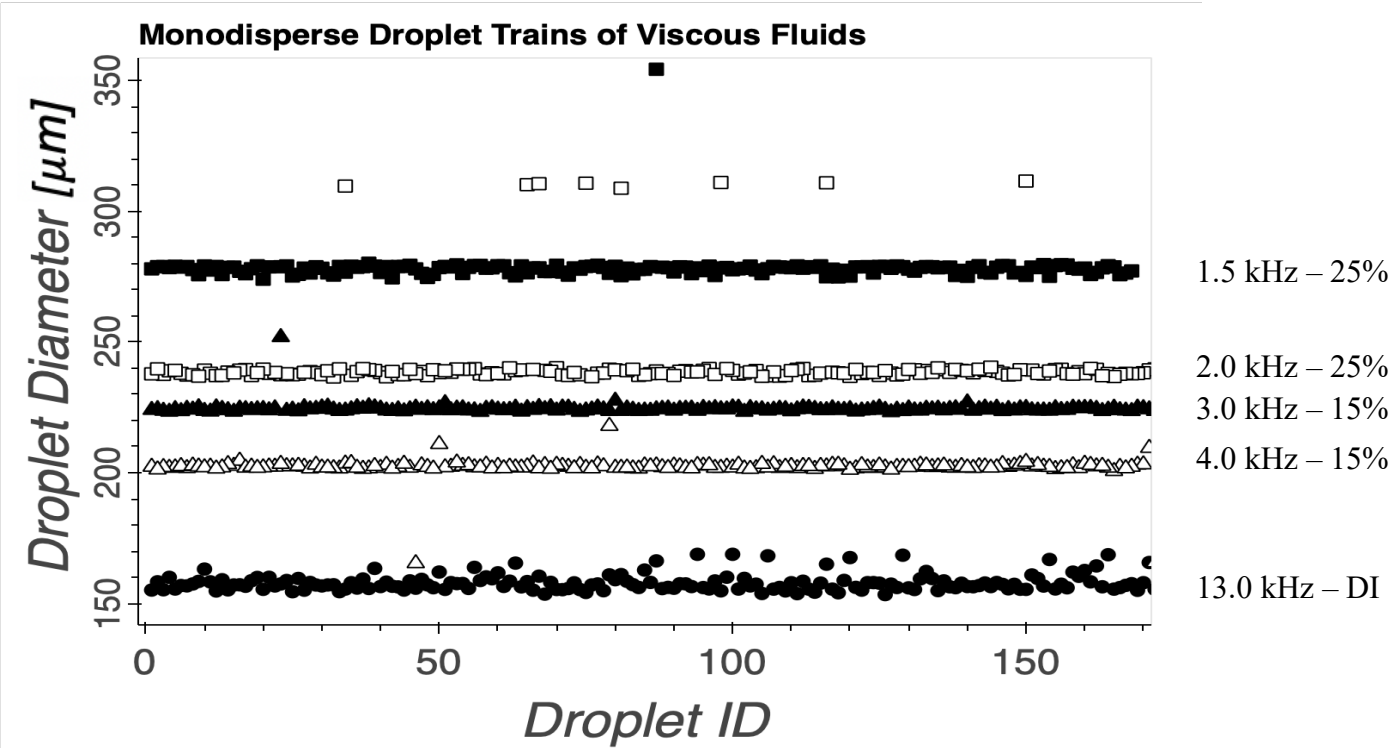

Figure C6 - Size distribution of monodisperse, viscous aerosol trains (75 μm Pinhole). Using one 75 μm pinhole, five separate monodisperse droplet trains are generated by changing the fluid being atomized. Changing solution viscosity from 1 to 20 cP results in droplets that are 2 to 3.75 times the size of the orifice.

Table C.1 – Mean diameters and standard deviation of aerosols produced with 75 μm pinhole and different peg solutions

Fluid	Excitation Frequency	Standard Deviation	Mean Diameter
DI Water	13.5 kHz	5.6 μm	157.9 μm
15 w% PEG	4.0 kHz	2.9 μm	202.2 μm
15 w% PEG	3.0 kHz	1.8 μm	224.4 μm
25 w% PEG	2.0 kHz	14.7 μm	241.5 μm
25 w% PEG	1.5 kHz	10.9 μm	279.0 μm

Appendix D

SIMULATIONS FROM DESIGN OF BALLISTIC DEVICE AND INITIAL DATA FROM TESTING

D.1 – Simulations of Particles Moving Through Aerodynamic Lens and Acceleration Capillary in Series

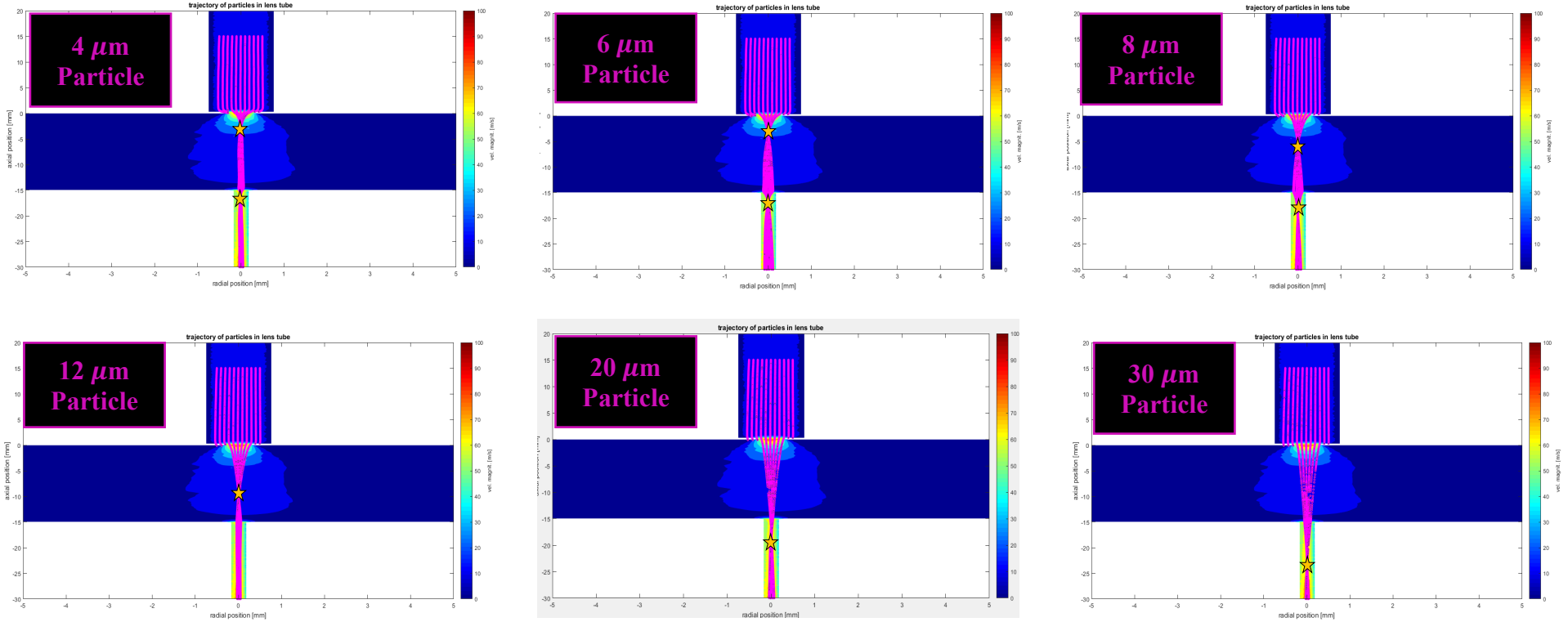

Figure D1 – Trajectories of particles placed in aerodynamic lens with helium flowfield ($\Delta P = 10\ torr$). Particles 4 μm and greater show effective lensing through the acceleration capillary with this low pressure drop. Pressure in lens tube is 1 bar.

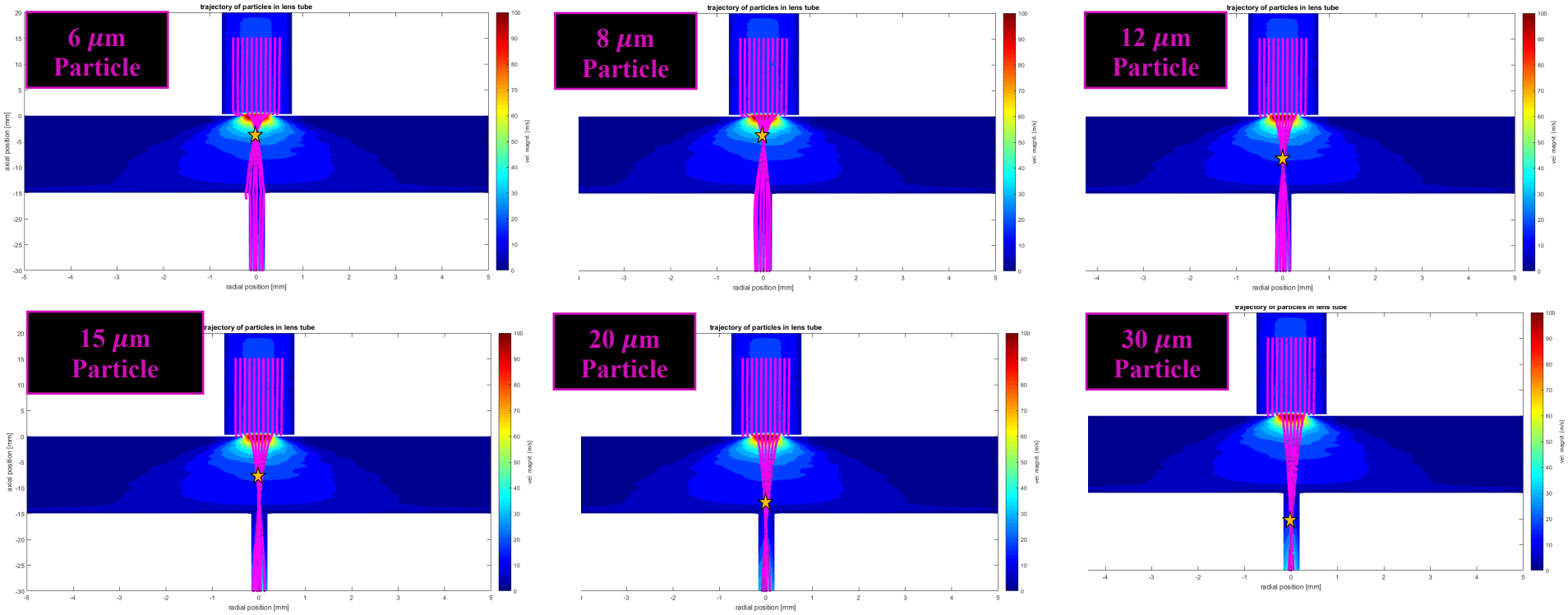

Figure D2 – Trajectories of particles placed in aerodynamic lens with helium flowfield ($\Delta P = 25\ torr$). Particles 4 μm and greater show effective lensing through the acceleration capillary with this low pressure drop. Pressure in lens tube is 1 bar.

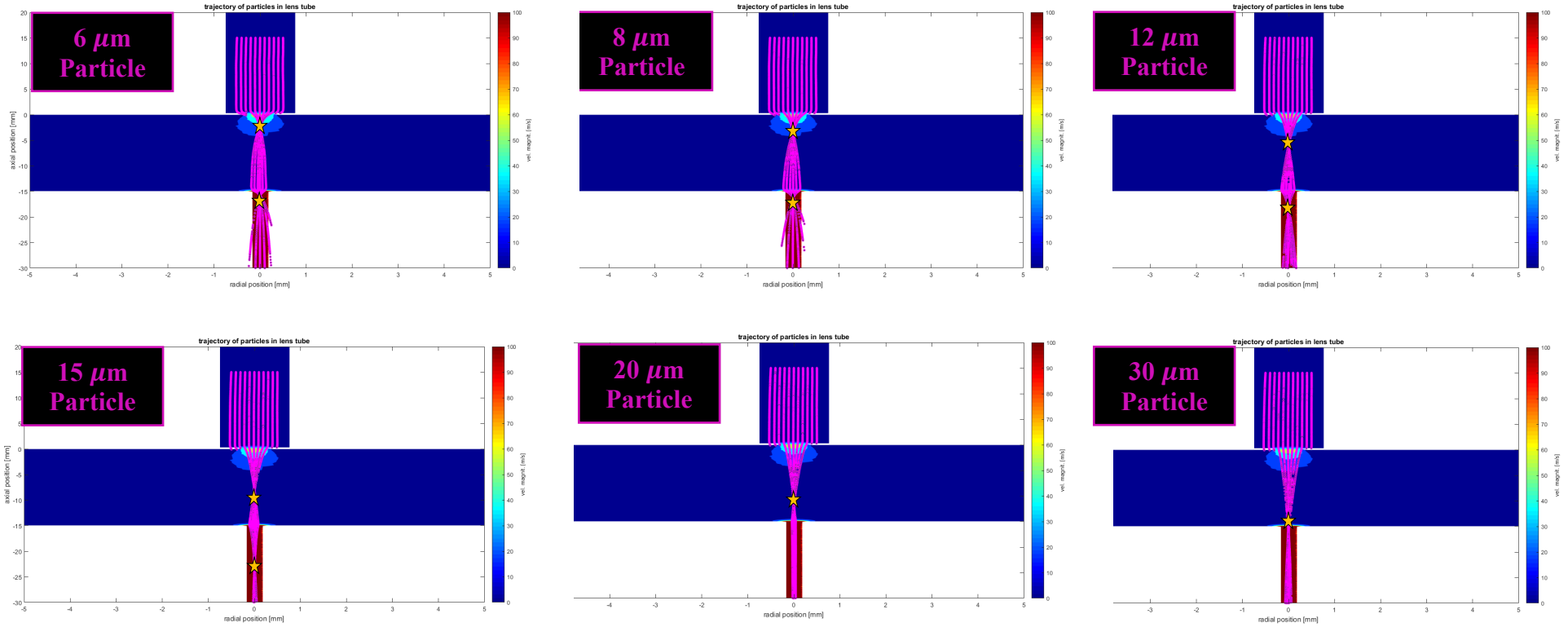

Figure D3 – Trajectories of particles placed in aerodynamic lens with helium flowfield ($\Delta P = 10\ torr\ P_{op} = 2bar$). Particles 4 μm and greater show effective lensing through the acceleration capillary with this low pressure drop. Pressure in lens tube is 2 bar.

D.2 – Penetration Data Measured with Custom-Built Ballistic Device

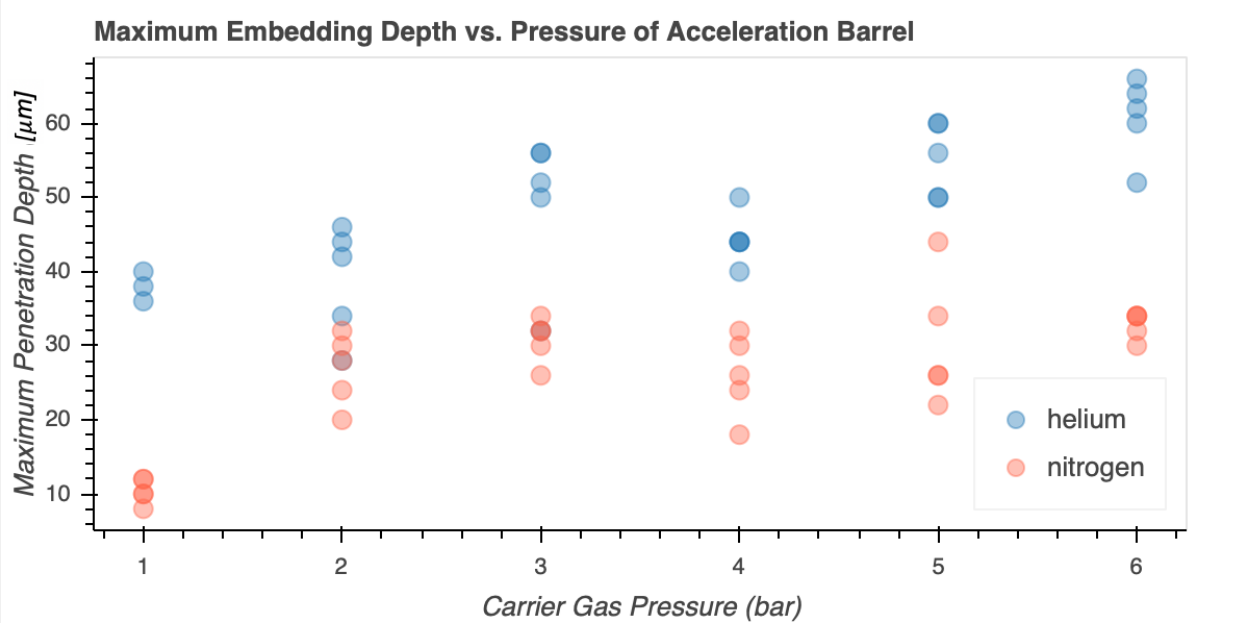

Figure D4 – 10 – 22 μm soda-lime spheres ejected from custom-built ballistic device in 1% w/v agarose (helium vs. nitrogen accelerating gas). n is 5 shots per gel.

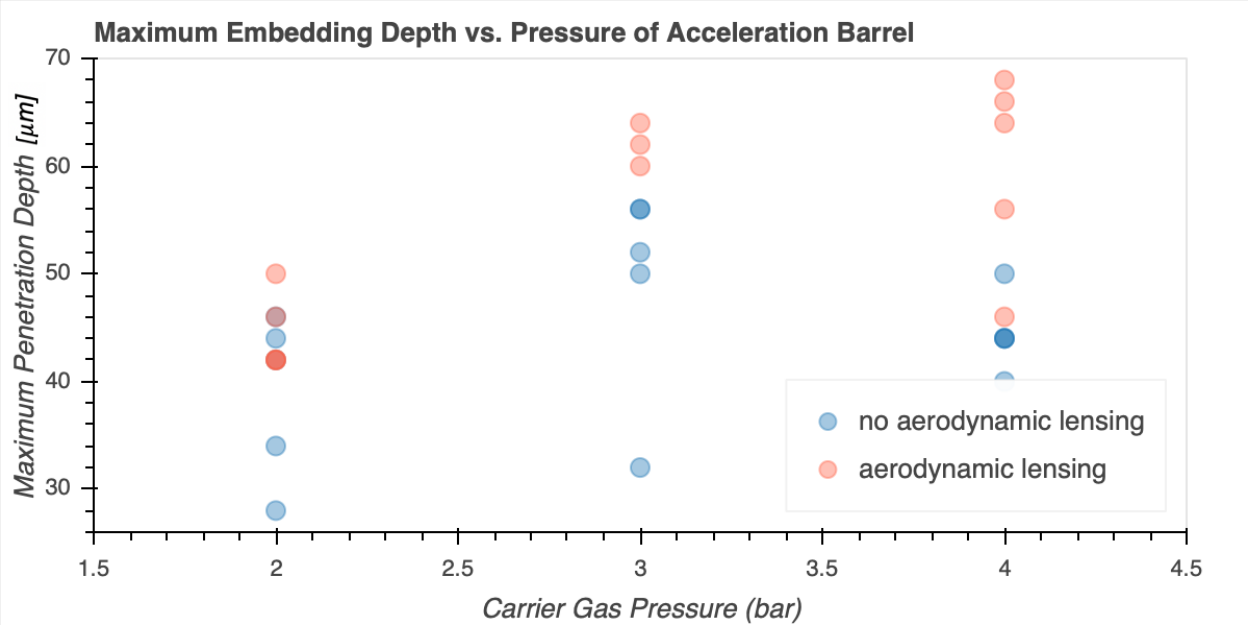

Figure D5 – 10 – 22 μm soda-lime spheres ejected from custom-built ballistic device in 1% w/v agarose (effect of aerodynamic lensing). n is 4 shots to gel.

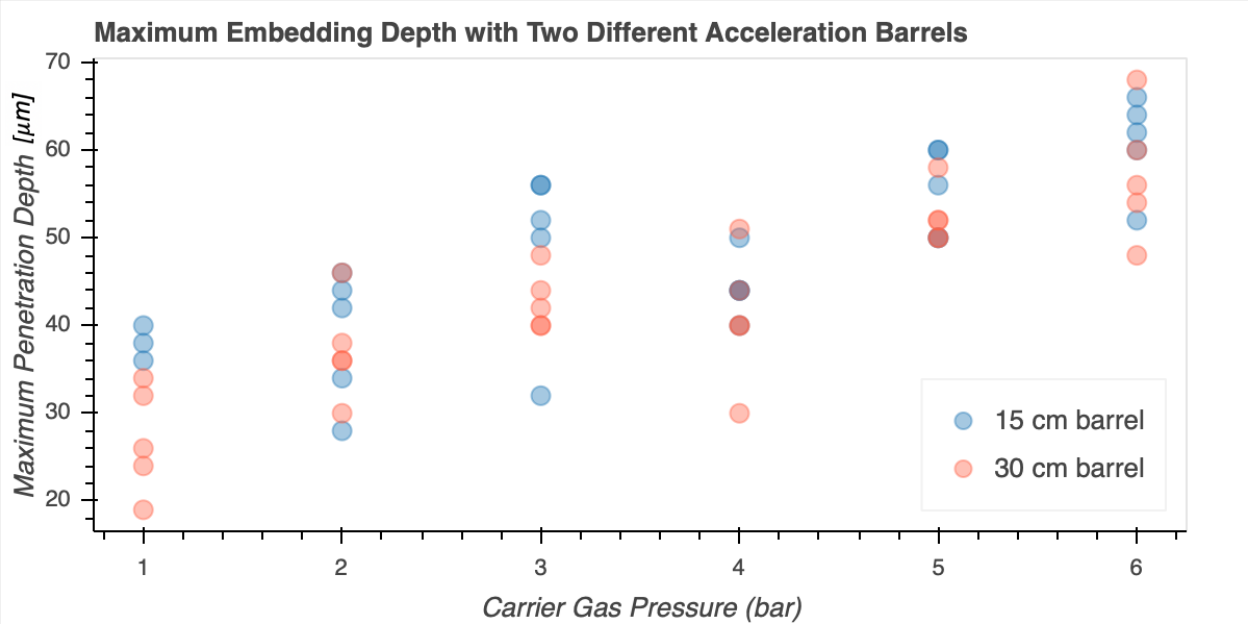

Figure D6 – 10 – 22 μm soda-lime spheres ejected from custom-built ballistic device in 1% w/v agarose (effect of acceleration barrel length). n is 4 shots to gel.